UNIVERSITÉ DU QUÉBEC À MONTRÉAL

SYSTÈMES FLUVIAUX TEMPÉRÉS FROIDS: APPROCHE CONCEPTUELLE ET MODÉLISATION INTÉGRÉE DES DYNAMIQUES SÉDIMENTAIRES, DES CRUES ET DES SÉCHERESSES

THÈSE

PRÉSENTÉE

COMME EXIGENCE PARTIELLE

DU DOCTORAT EN SCIENCES DE L'ENVIRONNEMENT

PAR

ALI FAGHFOURI

MAI 2026

REMERCIEMENTS

Je tiens avant tout à exprimer ma profonde gratitude à mon directeur de recherche, le Professeur Daniel Germain, pour ses conseils inestimables, son soutien constant et ses retours éclairés à chaque étape de ce travail. Sa patience, son encouragement et son dévouement ont non seulement façonné cette thèse, mais m'ont également inspiré à progresser en tant que chercheur indépendant. Sa capacité à allier rigueur et générosité a été une source permanente de motivation, et ses conseils avisés m'ont guidé à travers les phases les plus exigeantes de cette recherche.

Je suis également très reconnaissant à mon co-directeur, le Professeur Guillaume Fortin, pour ses conseils constructifs, sa disponibilité constante et son encadrement académique, qui ont grandement enrichi la profondeur et la qualité de cette thèse. Ses analyses critiques, son souci méticuleux du détail et ses suggestions pertinentes ont renforcé la solidité de mon travail et m'ont encouragé à affiner mon approche analytique. Je lui suis aussi reconnaissant pour son encouragement et sa disponibilité à engager des discussions stimulantes, qui ont élargi mes perspectives et approfondi ma compréhension du sujet.

J'aimerais également exprimer ma sincère gratitude au Professeur Olivier Caron et au Professeur Vincent Dubreuil pour leurs suggestions précieuses, leurs recommandations constructives et leur soutien continu lors des étapes de collecte et de traitement des données. Leur expertise et leurs conseils éclairés ont joué un rôle déterminant dans la rigueur et la fiabilité de cette recherche.

Je tiens aussi à remercier chaleureusement mes co-auteurs, Albin Ullmann, Florian Raymond, Charlotte Poirier et Achraf Hentati, pour leurs contributions significatives, leur engagement scientifique et les discussions enrichissantes que nous avons partagées. Leur collaboration, leurs perspectives critiques et leur volonté commune de faire progresser la recherche ont considérablement amélioré la qualité, la profondeur et la clarté de ce travail.

Enfin, j'adresse mes plus vifs remerciements aux membres de notre groupe de recherche — Jo-Annie, Marie-Hélène, Mehrnoosh, Valentin, Louna, Charline et Jean-François — pour leurs encouragements constants, leurs retours positifs et leur esprit de soutien tout au long de ce parcours. Leur motivation et leurs paroles bienveillantes m'ont donné confiance et inspiration, rendant cette aventure académique à la fois enrichissante et agréable.

DÉDICACE

Cette thèse est dédiée à ma bien-aimée, dont l'amour, la patience et le soutien indéfectible ont été une source constante de force; à ma famille, pour son amour et son soutien inconditionnels; et à mes mentors, pour leurs conseils et leur inspiration qui ont façonné à la fois mon parcours académique et mon développement personnel.

TABLE DES MATIÈRES

LISTE DES FIGURES

LISTE DES TABLEAUX

LISTE DES ABRÉVIATIONS, DES SIGLES ET DES ACRONYMES

(AD) Anderson-Darling

(AET) Actual Evapotranspiration

(ANN) Artificial Neural Network

(CANGRD) Canadian Gridded Temperature and Precipitation Anomalies

(CCCma) Canadian Centre for Climate Modelling and Analysis

(CDF) Cumulative Density Function

(CGCM) Second-generation Canadian Earth System Model

(CGCM3) 3rd generation or the Coupled Global Climate Model

(CGM) Climate Change Model

(CS) Chi-square

(DEM) Digital Elevation Model

(DL) Deep Learning

(DoD) DEM of Difference

(DSAS) Digital Shoreline Analysis System

(DSM) Digital Surface Model

(DTM) Digital Terrain Model

(DWPR) Designated Watershed Protected Area

(EMA) Equal Mobility Approach

(ESA) Energy Slope Approach

(FDCs) Flow Duration Curves

(FFA) Flood Frequency Analysis

(GCPs) Ground Control Points

(GCM) General Circulation Model

(GEV) Generalized Extreme Value

(GIS) Geographic Information System

(GOF) goodness-of-fit

(GSD) Grain Size Distribution

(HSFM) Historical Structure from Motion

(IC) Index of Connectivity

(IHC) Index of Hydrosedimentological Connectivity

(IPCC) Intergovernmental Panel on Climate Change

(IVW) inverse-variance weighted average method

(LiDAR) Light Detection and Ranging

(LN3) three-parameter lognormal

(LoD) Level of Detection

(LULC) Land use/Land cover

(MCMC) Markov Chain Monte Carlo

(MIEM) Multiple Imputation Estimation Method

(MK) Mann-Kendall

(ML) Machine Learning

(MPM) Meyer-Peter & Müller

(MSE) Mean Squared Error

(NB) New Brunswick

(NDVI) Normalized Difference Vegetation Index

(PA) Probabilistic Approach

(PD) Probability Distributions

(PDF) Probability Density Function

(PET) Potential Evapotranspiration

(PDSI) Palmer Drought Severity Index

(PMR) product-moment ratio

(PWMs) probability-weighted moments

(RA) Regression-based Approach

(RCP) Representative Concentration Pathway

(RCP 4.5) Representative Concentration Pathway 4.5

(RCP 8.5) Representative Concentration Pathway 8.5

(RHBN) Hydrometric Basin Network

(S.M.) Spencer's method

(sc-PDSI) self-calibrated Palmer Drought Severity Index

(SCA) Snow Cover Area

(SDR) Sediment Delivery Ratio

(SEDI) Standardized Evapotranspiration Deficit Index

(SfM) Structure-from-Motion

(SI) Sinuosity Index

(SPEI) Standardized Precipitation Evapotranspiration Index

(SPI) Stream Power Index

(SPI) Standardized Precipitation Index

(SSA) Shear Stress Approach

(STI) Sediment Transport Index

(UAV) Unmanned Aerial Vehicle

(USDA) US Department of Agriculture

LISTE DES SYMBOLES

($\overline{E_i}$) Water fluxes

($\overline{L_i}$) Runoff and water loss to the soil layers

($\overline{PEi}$) Potential evapotranspiration

($\overline{PL_i}$) Potential loss

($\overline{PR_i}$) Potential recharge

($\overline{PRO_i}$) Potential runoff

($\overline{R_i}$) Denoting evapotranspiration

($\overline{Ro_i}$) Recharge to soils

(A) Cross-sectional area

(Ad) Area of the basin

(As) The upslope contributing area per unit width

(B) Top width of river

(CO2) Carbon dioxide

(D) The straight-line distance between endpoints

(d) Moisture departure

(d50) Median grain size

(D90, D75, D25, D10) Percentile-based indices

(d90/d10 and d75/d25) Sorting rations

(g) Gravitational acceleration

(Gs) Specific gravity of sediment

(h) Flow depth

(H0) Null hypothesis

(Ha) Alternative hypothesis

(K) Climatic characteristic

(L) Length

(n) Manning's roughness Coefficient

(P new) Modified monthly precipitation

(P) Wetted perimeter

(Pfact) The ratio of the CGM simulated mean precipitation in the future time relative to the historical mean precipitation

(Q) Discharge

(q) Unit discharge

(Qavg) Mean monthly

(Qd) Daily maximum discharges

(Qobs) Daily observed discharge

(R) Hydraulic radius

(R) coefficient of correlation

(S) Channel slope

(Tdelta) The difference between the climate change model's (CGM) simulated mean temperature (projected in the future) and the historical mean temperature

(Tmax new) Modified monthly maximum temperature

(Tmin new) Modified monthly minimum temperature

(u) Shear velocity

(uc) Critical shear velocity

(v) Flow velocity

(W) Average channel width

(β) Local slope

(γ) Specific weight of water

(γ_s) Specific weight of sediment

(ΔSB) Sediment budget

(θ) Shields stress

(θ) The slope angle

(θc) Critical shields criterion

(ρ and ρw) Density of water

(ρ_s) Density of sediment

(τ) Shear bed stress

(τ) Kendall's Tau

(τ_b) Kendall's correlation coefficient

(τc) Critical bed shear stress

(Φ) Dimensionless transport rate

(φ) Empirical coefficient

(Φ_{90}) Coarser grain fraction

(ω) Stream power per unit width

(ωc) critical stream power threshold

RÉSUMÉ

Cette thèse présente une investigation détaillée et multi-échelle des dynamiques sédimentaires, des extrêmes hydrologiques et des contraintes hydroclimatiques dans des systèmes fluviaux tempérés froids. En intégrant synthèse conceptuelle, modélisation statistique climatologie et hydrologie, télédétection, observations de terrain et formulations multiples du transport sédimentaire, ce travail élabore des outils et diagnostics transférables visant à améliorer la prévision et la gestion des risques liés aux sédiments, aux crues et aux sécheresses dans des bassins versants influencés par la cryosphère. La recherche s'articule autour de quatre composantes complémentaires.

Premièrement, un cadre conceptuel spécifiquement conçu pour la connectivité sédimentaire en régions froides intègre et synthétise approches indexées, réseaux, perspectives morphologiques et méthodes numériques, en incorporant explicitement les forçages cryosphériques (cycles gel–dégel, pulsations de fonte nivale, processus de glace), les héritages géomorphologiques, les couplages biotique–géomorphique et les modifications anthropiques (chapitre 1). Le cadre met l'accent sur la fragmentation des voies sédimentaires, la réactivation différée des stocks, les mécanismes de transport hivernal et les rétroactions entre offre sédimentaire, forçage hydraulique et compartiments de stockage, formulant ainsi des hypothèses testables pour des analyses empiriques ultérieures.

Deuxièmement, un réseau de neurones artificiels modifié (RNA ; rétropropagation optimisée par la méthode de Levenberg–Marquardt), implémenté sous MATLAB, a été développé pour projeter les débits moyens mensuels (Qavg) et les débits maximaux journaliers (Qd) du bassin versant de la rivière Eel (Nouveau-Brunswick- chapitre 2). Les entrées comprenaient les précipitations journalières observées, les températures maximales et minimales de l'air et les débits (1967–1983) agrégés en valeurs mensuelles, complétées par les projections climatiques mensuelles CanESM2 pour 1996–2099 sous RCP4.5 et RCP8.5. Les sorties du RNA ont été soumises à une analyse de fréquence des crues (FFA) utilisant les lois de valeur extrême généralisée (GEV) et log-normale à trois paramètres (LN3) ; l'ajustement et la performance ont été évalués par les tests d'Anderson–Darling et du χ^2 pour la FFA, et par le coefficient de corrélation (R) et l'erreur quadratique moyenne (EQM) pour le RNA. Les projections identifient plusieurs fenêtres futures critiques de hausse de l'intensité et de la fréquence des crues (notamment 2022–2038, 2056–2072, 2073–2089 pour RCP4.5 ; 2039–2055, 2073–2089, 2083–2099 pour RCP8.5) et indiquent une augmentation d'environ 50 % du débit moyen durant les périodes les plus critiques, accompagnée d'une amplification marquée des magnitudes de crue centennale estimées.

Troisièmement, une reconstruction géomorphologique intégrée sur sept décennies de la rivière du Diable (1949–2019) a combiné photographies aériennes historiques, MNT (modèles numériques de terrain) à haute résolution dérivés de LiDAR et bilans sédimentaires volumétriques (chapitre 3). L'analyse granulométrique (32 échantillons de falaises et de plages) et les mesures hydrauliques ont été associées à cinq approches complémentaires d'estimation du transport (relations sans dimension pour le transport de fond) : méthode par contrainte de cisaillement (SSA), méthode énergie-pente (ESA), méthode de régression (RA), approche probabiliste (PA) et approche d'égalité de mobilité (EMA) (chapitre 4). Les analyses comparatives révèlent une hétérogénéité

spatiale et temporelle marquée : export net maximal de sédiment entre 1980–2001 (−142,5 $m^3\ km^{-1}\ an^{-1}$), épisode de stockage net en 2001–2007 (+70,8 $m^3\ km^{-1}\ an^{-1}$) et mobilisations répétées lors des fontes printanières et des années de crues exceptionnelles (notamment 2011 et 2017–2019). Les falaises constituent des sources persistantes de sédiments grossiers tandis que les plages agissent comme des zones de remaniement à court terme ; les cartographies de l'Indice de Transport Sédimentaire (STI) et de l'Indice de Puissance du Cours d'Eau (SPI) dérivées des MNT coïncident étroitement avec les zones névralgiques prédites par les modèles, démontrant un couplage robuste entre topographie, énergie hydraulique et disponibilité sédimentaire.

Quatrièmement, la variabilité régionale des sécheresses au Nouveau-Brunswick (1971–2020) a été évaluée par les indices stationnels Palmer Drought Severity Index (PDSI) et Standardized Evapotranspiration Deficit Index (SEDI) sur dix stations météorologiques, complétés par les anomalies température–précipitation du produit gridded CANGRD (1979–2014) (chapitre 5). La détection de tendances non paramétrique (test de Mann–Kendall et estimateur de la pente de Sen) met en évidence une intensification des épisodes de sécheresse extrême et une hétérogénéité spatiale de la vulnérabilité, les zones côtières du sud présentant une susceptibilité accrue liée à la diminution de la fréquence des jours pluvieux et des totaux de précipitation.

Dans son ensemble, la thèse (i) fait progresser la compréhension théorique de la connectivité sédimentaire en environnements froids, (ii) propose une approche rigoureuse fondée sur les RNA pour la projection des crues sous contrainte climatique, (iii) démontre un protocole multi-méthode pour quantifier le transport sédimentaire et l'évolution géomorphologique à l'échelle décennale, et (iv) diagnose les tendances régionales de sécheresse utiles pour la planification des ressources en eau. Les résultats produisent des livrables opérationnels — priorisation spatiale des zones d'érosion et de fourniture sédimentaire, estimations de risque de crue fondées sur des scénarios, et cartes de vulnérabilité à la sécheresse directement exploitables pour la gestion des bassins versants, la priorisation de la restauration et les stratégies d'adaptation climatique. La thèse se conclut par des recommandations pour intégrer des métriques de connectivité sensibles à la cryosphère dans les modèles prédictifs, renforcer la couverture d'observation hivernale et coupler approches processuelles et approches fondées sur les données pour améliorer la planification de la résilience.

Mots-clés : connectivité sédimentaire en régions froides, réseau de neurones artificiels (RNA), projection des crues, bilan sédimentaire, LiDAR, estimation du transport de fond, puissance de cours d'eau, PDSI, tendances de sécheresse

Introduction Générale

Les systèmes fluviaux en climat tempéré froid présentent des dynamiques hydro-sédimentaires particulièrement sensibles aux contraintes saisonnières, aux événements extrêmes et aux forçages anthropiques. Dans ces environnements, le transport sédimentaire, l'évolution morphologique des chenaux et la connectivité entre les composantes du paysage — versants, chenaux secondaires, plaines inondables — sont modulés par la variabilité climatique interannuelle, la couverture de glace, la fonte nivale et les apports soudains associés aux crues printanières ou aux pluies intenses. Ces dynamiques s'inscrivent dans le cadre plus large des changements globaux, où les aléas hydro-climatiques, tels que les inondations et les sécheresses, évoluent en fréquence, en intensité, en durée, et dans leur répartition spatio-temporelle.

Dynamiques fluviales en régions tempérées froides

Les rivières des zones tempérées froides, notamment dans les environnements boréaux et alpins du Canada, sont dominées par des processus fluviaux et se révèlent particulièrement sensibles aux variations saisonnières comme aux perturbations naturelles et anthropiques. Comme l'indiquent Orwin et al. (2010), « *fluvial processes dominate sediment flux from most cold environments and as such are particularly sensitive to environmental change* ». Ces systèmes réagissent non seulement à la variabilité climatique interannuelle et décennale (Vincent et al., 2015; Aygün et al., 2020), mais constituent également des laboratoires privilégiés pour analyser l'influence du changement global sur les dynamiques hydrologiques et sédimentaires.

La présence saisonnière de neige et de glace exerce un contrôle fondamental sur les régimes fluviaux (Beltaos, 2008). Le cycle annuel — prise des glaces, couverture hivernale, débâcle printanière — impose un rythme marqué aux débits et à la mobilisation des sédiments, structurant un patron bimodal d'activité géomorphologique. En hiver, les faibles débits combinés à la couverture de glace limitent l'érosion; toutefois, même de modestes écoulements peuvent transporter des sédiments si la glace est mobile (Turcotte et al., 2011). Au printemps, la fonte nivale concentre l'essentiel du travail géomorphologique et sédimentaire. En somme, les contrôles saisonniers — accumulation nivale, fonte et redoux hivernaux — régulent de manière critique les écoulements, les pulsations sédimentaires et les ajustements géomorphologiques dans ces environnements (Orwin et al., 2010; Turcotte et al., 2011).

Les transitions saisonnières influencent également fortement l'apport sédimentaire et l'évolution du chenal. En hiver, la formation d'un couvert de glace modifie profondément l'hydraulique fluviale : elle réduit la vitesse des écoulements et la capacité de transport (Shen, 2010), favorisant l'accumulation de sédiments fins et altérant la qualité des habitats aquatiques (Turcotte et al., 2011). Lors de la débâcle, qu'elle survienne au printemps ou au cours de redoux hivernaux, la montée des eaux combinée au déplacement de la glace engendre une érosion latérale intense et le transport de volumes considérables de sédiments et de débris ligneux (Beltaos, 2008). Des observations sur la rivière Liard, dans les Territoires du Nord-Ouest, ont montré des hausses de plus d'un ordre de grandeur des concentrations de sédiments en suspension lors de la débâcle (Prowse, 1993). Ces épisodes illustrent le rôle déterminant des processus liés à la glace dans les bilans sédimentaires

annuels. Turcotte et al. (2011) rappellent que la glace d'ancrage, la glace de rive et les embâcles préparent le terrain à d'importantes pulsations printanières, tandis que Beltaos & Burrell (2021) notent que les pics de sédiments en suspension précèdent souvent le débit maximal. Dans de nombreux cours d'eau canadiens, comme la Saint-John ou l'Athabasca, les ruptures d'embâcles génèrent des charges extrêmes. La crue nivale printanière constitue donc la principale période de travail géomorphologique (Church, 2006), mais son régime évolue déjà sous l'effet du réchauffement climatique, caractérisé par des fontes plus précoces, des pics parfois moins intenses et une multiplication des épisodes liés aux redoux hivernaux (Déry et al., 2009).

Connectivité hydro-sédimentaire

La connectivité entre versants, chenaux secondaires et plaine d'inondation constitue un déterminant majeur des dynamiques sédimentaires en climat froid. Dans les bassins à régime nival, le dégel saisonnier et les épisodes de pluie sur neige favorisent le transfert de débris depuis les versants vers le chenal principal, directement ou via des ravines et affluents (Pomeroy et al., 2016; Jiang et al., 2020). En amont, les processus érosifs dominent, tandis qu'en aval, les débordements dans la plaine inondable et les chenaux secondaires favorisent le dépôt des sédiments fins lors de la décrue (Morin et al., 2015). Les différentes unités paysagères — pentes raides, cônes colluviaux, chenaux, plaines alluviales — fonctionnent ainsi comme sources ou comme puits de sédiments, avec une connectivité qui varie d'une année à l'autre selon les conditions hydrologiques. Dans ce contexte, les réseaux hydro-sédimentaires apparaissent hautement dynamiques : les connexions versant-chenal se réactivent rapidement lors des crues, mais se déconnectent tout aussi vite en périodes sèches.

Perturbations anthropiques

Les activités humaines modifient profondément les rythmes hydro-sédimentaires des cours d'eau en climat froid. L'exploitation forestière, par exemple, tend à accroître l'écoulement et l'érosion (Moore & Wondzell, 2005; Champagne et al., 2020). En Colombie-Britannique, la déforestation et les routes d'accès peuvent non seulement amplifier significativement les débits annuels, mais aussi amplifier les crues printanières (Buttle et al., 2000), ce qui accentue l'érosion des berges et du lit. Les routes concentrent également le ruissellement et accroissent l'apport de particules fines, avec des effets négatifs sur la qualité de l'eau, les habitats de fraie et la macrofaune benthique (Jordan, 2006). Même si des bandes riveraines sont instaurées comme mesure d'atténuation, leur efficacité demeure variable et l'héritage des pratiques anciennes reste perceptible (Richardson et al., 2012).

Dans d'autres contextes, les activités minières et les coupes en zone boréale créent de nouvelles sources sédimentaires (Macklin et al., 2006), tandis que les barrages hydroélectriques interrompent la continuité des flux en piégeant les sédiments et en privant les tronçons aval d'apports essentiels. Dans les Prairies, l'irrigation et le drainage intensif modifient la connectivité hydrologique et augmentent les charges sédimentaires et nutritives (Rashmi et al., 2022). Le drainage des milieux humides et la construction de barrages de castors illustrent également la forte sensibilité des réseaux fluviaux aux perturbations locales (Dumanski et al., 2015). Globalement, les changements d'usage du territoire tendent soit à accélérer l'érosion et le transfert sédimentaire (routes, coupes, déboisement riverain), soit, au contraire, à provoquer un découplage des flux par la création de zones artificielles de stockage (barrages, canalisations).

Changements climatiques et extrêmes hydrologiques

Le réchauffement climatique transforme en profondeur les régimes fluviaux en climat tempéré froid. Des pluies plus fréquentes et plus intenses, particulièrement en été et en automne, déclenchent des crues éclair à fort pourvoir érosif, surtout dans les petits bassins très réactifs (Mailhot et al., 2010; Kingumbi et al., 2010). Plusieurs études documentent également des fontes nivales plus précoces, une augmentation des précipitations liquides en hiver et une variabilité accrue des crues (Déry et al., 2009; Whitfield & Shook, 2019; Fang et al., 2015; Aygün et al., 2020; Zhang et al., 2023). Dans certains bassins, des analyses dendrochronologiques révèlent que des crues récentes dépassent les maxima historiques (Nolin et al., 2021; Burn & Whitfield, 2015). À l'inverse, des étés plus chauds et plus secs favorisent des étiages prolongés et des sécheresses récurrentes (Champagne et al., 2020; CCR, 2019; Pestal & Carr-Harris, 2025). Ces évolutions combinées accentuent l'instabilité hydro-sédimentaire des rivières tempérées froides et soulignent l'importance de mieux comprendre leurs réponses dans un contexte de changements globaux.

Problématique de recherche

Malgré une reconnaissance accrue du rôle des événements extrêmes dans la dynamique hydrologique et sédimentaire des systèmes fluviaux, plusieurs lacunes majeures subsistent. Elles concernent :

1. La quantification des transformations morphologiques à long terme des rivières en milieux froids ;
2. La modélisation du transport sédimentaire à partir d'équations adaptées aux distributions granulométriques réelles ;
3. L'intégration de la connectivité sédimentaire dans des cadres conceptuels véritablement opérationnels ;
4. L'anticipation des effets des changements climatiques sur les régimes hydrologiques futurs au moyen de méthodes statistiques robustes.

Cette thèse de doctorat vise à répondre à ces enjeux en combinant approches empiriques, conceptuelles, et modélisations, appliquées à deux bassins représentatifs de l'Est du Canada, la rivière Eel (Nouveau-Brunswick) et la rivière du Diable (Québec).

Transformations morphologiques à long terme en milieux froids

Les processus hivernaux (englacement, cycles gel–dégel, crues de débâcle, et embâcles) influencent fortement la morphologie et la dynamique des chenaux, mais demeurent peu intégrés aux analyses à long terme. Prugne et al. (2024) soulignent que plusieurs concepts fondamentaux de la biogéomorphologie fluviale « restent à appliquer en milieux froids », tandis que Chassiot et al. (2020) recensent de nombreuses questions ouvertes concernant l'érosion de berges, notamment liées à l'affaiblissement thermique ou à l'arrachage par glace d'ancrage. Les principales identifiées concernent: i) la sous-représentation des processus hivernaux, difficiles à mesurer mais déterminants; ii) les interactions encore mal connues entre la végétation riveraine et la dynamique géomorphologique; iii) la calibration et le changement d'échelle des modèles physiques développés en climat tempéré; iv) le rôle cumulatif et mal quantifié des événements extrêmes.

Répondre à ces enjeux exige des suivis multi-décennaux à haute résolution, des expérimentations ciblées et des modèles capables d'intégrer la physique de la glace et son couplage avec les processus sédimentaires.

Modélisation du transport sédimentaire

L'application des formules mathématiques classiques du transport sédimentaire (p. ex. Meyer-Peter & Müller, Engelund–Hansen) aux rivières naturelles à granulométrie mixte demeure problématique (Andualem et al., 2023). La plupart des modèles considèrent une taille représentative unique, souvent le d50, ce qui néglige le tri sélectif des particules et la complexité des lits naturels. Les défis actuels concernent: i) la représentation des lits hétérogènes et les mécanismes d'entraînement sélectif; ii) l'absence de modèles prédictifs robustes et validés capables de traiter des distributions

granulométriques multi-classes; iii) l'extrapolation incertaine des relations de transport vers des crues extrêmes, rarement observées et difficiles à calibrer.

Pour progresser, il est nécessaire de développer des modèles multi-fractions mieux paramétrés, appuyés par des données de terrain et de laboratoire permettant de représenter fidèlement la variabilité granulométrique et les conditions hydrauliques en milieux froids.

Dynamique de connectivité sédimentaire

La connectivité sédimentaire décrit le transfert de matériaux depuis les sources (versants) jusqu'aux zones de stockage ou d'exportation en passant par le réseau hydrographique. Bien que plusieurs cadres conceptuels aient été proposés, aucun modèle intégré et multi-échelles n'a encore été opérationnalisé pour les rivières en climat froid. Cho et al. (2023) appellent ainsi au développement d'un cadre véritablement intégré, couplant connectivité structurelle (morphologie, topographie) et connectivité fonctionnelle (flux et événements), tout en tenant compte de la dynamique temporelle et des régimes saisonniers de type « on/off ». Les principaux obstacles sont : i) la fragmentation des approches existantes, souvent centrées sur des indices ou sur des processus sans réelle intégration; ii) la faible prise en compte de la variabilité temporelle des connexions; iii) le biais marqué vers des contextes non fluviaux; iv) la rareté d'outils prédictifs adaptés aux réseaux hydro-sédimentaires froids.

Changements climatiques et régimes hydrologiques futurs

La projection de l'évolution des régimes hydrologiques (saisonnalité, extrêmes, volumes) demeure un défi scientifique majeur. Une difficulté centrale réside dans l'écart d'échelle entre les modèles climatiques globaux (GCM) et les bassins versants, dont les dynamiques nécessitent des résolutions fines. Comme le notent Kour et al. (2016), les sorties des GCM sont trop grossières pour être directement intégrées aux modèles hydrologiques.

Le recours à la descente d'échelle (désagrégation spatiale) et aux corrections de biais s'avère incontournable, mais introduit lui-même d'importantes incertitudes. Celles-ci proviennent : i) des méthodes utilisées (statistiques vs dynamiques, choix des algorithmes de correction de biais); ii) de la difficulté à intégrer la non-stationnarité des extrêmes hydrologiques; iii) de l'incertitude persistante concernant la fréquence et l'intensité des événements rares, même en approche multi-modèles; iv) du manque d'attention portée aux bassins des environnements froids et non jaugés, particulièrement sensibles aux changements; v) d'une communication insuffisante des incertitudes, qui gagnerait à s'appuyer sur des approches probabilistes ou bayésiennes.

Réduire ces incertitudes exige le développement de schémas avancés de descente d'échelle, l'adoption de statistiques non-stationnaires adaptées aux extrêmes, et une meilleure quantification de la propagation des incertitudes à travers les chaînes de modèles climatiques et hydrologiques. Ces améliorations apparaissent cruciales pour anticiper l'évolution future des régimes fluviaux en climat froid.

Cadre théorique et conceptuel

Cette thèse s'appuie sur la géomorphologie fluviale et s'articule autour de trois piliers conceptuels complémentaires:

1. **La connectivité sédimentaire,** qui croise approches structurelles et fonctionnelles (Fryirs & Brierley, 2013; Bracken et al., 2015), et intègre la variabilité saisonnière propre aux environnements froids.
2. **Les bilans sédimentaires à long terme**, qui permettent d'évaluer les transformations fluviales et de diagnostiquer les phases d'aggradation ou d'incision (Slaymaker, 2003; Reid & Dunne, 2016).
3. **La modélisation statistique et par réseaux de neurones**, incluant l'usage d'indices de sécheresse pour caractériser les extrêmes hydro-climatiques et projeter les risques futurs (Zhang et al., 2020; Burn & Whitfield, 2015).

Chacun de ces piliers soutient directement un ou plusieurs chapitres : la connectivité (Chapitres 1 et 4), les bilans sédimentaires (Chapitre 3), et la modélisation statistique et neuronale (Chapitres 2 et 5).

Connectivité sédimentaire

La connectivité désigne le degré de liaison entre sources, voies et puits (Fryirs & Brierley, 2013), résultant de l'interaction entre structure (morphologie) et fonction (énergie et transport). López-Vicente & Ben-Salem (2018) distinguent la connectivité structurelle, qui traduit le potentiel de mouvement selon les propriétés du système, et la connectivité fonctionnelle, correspondant au transfert effectif lors d'un événement. Fryirs (2013) met en avant l'importance des « *buffers* », « *barriers* » et « *blankets* » qui peuvent activer ou désactiver certaines portions du bassin. Bracken et al. (2015) insistent sur une approche multi-échelles articulant structure et processus. En milieux froids, la saisonnalité module fortement ces connexions, le cadre proposé dans cette thèse adapte donc ces concepts aux rivières tempérées froides en intégrant explicitement les états saisonniers de connectivité.

Bilans sédimentaires et transformation fluviale

Les bilans sédimentaires quantifient les sources, les stockages et les sorties de sédiments à l'échelle décennale ou séculaire. Ils révèlent l'empreinte cumulée des forçages naturels et anthropiques et permettent de diagnostiquer des phases d'aggradation ou d'incision (Slaymaker, 2003; Reid & Dunne, 2016). Dans cette thèse, la notion de bilan sédimentaire est mobilisée pour reconstruire la dynamique spatio-temporelle de la rivière du Diable (Québec) entre 1949 et 2019 (Chapitre 3), à partir de photographies aériennes, de modèles LiDAR et de bilans volumétriques.

Modélisation statistique et réseaux de neurones

Les approches statistiques et d'apprentissage (régressions, séries temporelles, ANN) offrent des outils pour capturer des relations non linéaires entre variables climatiques et réponses hydrologiques. Les réseaux de neurones artificiels sont particulièrement efficaces lorsque la

relation explicite entre variables est complexe ou inconnue. Ils ont déjà été appliqués avec succès à la prévision de crues sous différents scénarios climatiques (Brandão et al., 2025; Hassanjabbar et al., 2022), en complément des modèles physiques. Dans cette thèse, ils constituent un pilier méthodologique pour développer des outils prospectifs de prévision des crues (Chapitre 2) et d'évaluation des sécheresses (Chapitre 5).

Synthèse

Ces trois piliers — connectivité, bilans et modélisation — structurent la démarche de recherche. La connectivité fournit le cadre conceptuel (Chapitres 1 et 4), les bilans sédimentaires ancrent l'analyse dans le temps long (Chapitre 3), et la modélisation statistique et neuronale permet d'anticiper les régimes futurs (Chapitres 2 et 5). Ensemble, ils assurent la cohérence des cinq chapitres et apportent des réponses directes aux lacunes identifiées dans la problématique.

Objectifs de la thèse

Cette recherche vise à améliorer la compréhension des processus fluviaux et des extrêmes hydrologiques dans les systèmes tempérés froids de l'Est canadien à travers cinq objectifs interreliés. Chaque objectif correspond à un chapitre, intégrant un cadre conceptuel, des approches de modélisation, des analyses empiriques et des diagnostics climatiques :

1. **Proposer un cadre conceptuel intégratif de la connectivité sédimentaire** adapté aux rivières tempérées froides, tenant compte des cycles gel–dégel, des crues nivales et des impacts anthropiques.

2. **Développer un modèle statistique de prévision des crues basé sur un réseau de neurones artificiels (ANN),** appliqué au bassin de la rivière Eel (Nouveau-Brunswick) et calibré sous scénarios climatiques RCP 4.5 et 8.5.

3. **Reconstruire l'évolution morphologique et les bilans sédimentaires de la rivière du Diable (Québec) de 1949 à 2019**, à partir de photographies aériennes, de MNT LiDAR et de bilans volumétriques.

4. **Évaluer les taux de transport sédimentaire au moyen de cinq approches complémentaires** (*Shear Stress, Energy Slope, Probabilistic, Regression, Equal Mobility*), en mobilisant des données granulométriques et hydrauliques, afin d'identifier les zones d'activité géomorphologiques « hotspot » liés à la fonte nivale et aux crues épisodiques.

5. **Documenter les régimes historiques de sécheresse au Nouveau-Brunswick (1971–2020)** à partir des indices PDSI et SEDI et de données climatiques maillées, et en analyser les implications pour l'hydrologie régionale et la gestion des ressources en eau.

Structure de la thèse

La thèse adopte une progression allant du cadre conceptuel général vers des analyses spécifiques et appliquées. Elle est organisée en cinq chapitres complémentaires, chacun rédigé sous la forme d'un article scientifique :

Chapter 1 – *Rethinking Sediment Connectivity in Cold Regions: Towards an Integrated Framework for Fluvial Systems.*

À soumettre. Ce chapitre développe un cadre conceptuel novateur de la connectivité sédimentaire adapté aux rivières tempérées froides.

Chapter 2 – *A novel statistical model for flood prediction in the Eel River watershed, New Brunswick, Canada.*

Faghfouri, A., Hentati, A., Fortin, G. & Germain, D. (2023) A novel statistical model for flood prediction in the Eel River watershed, New Brunswick, Canada. *Water Science*, 37:1, 251-268, DOI: 10.1080/23570008.2023.2243693

Ce chapitre présente un modèle statistique innovant basé sur un réseau de neurones artificiels (ANN) pour la prévision des crues.

Chapter 3 – *Seven Decades of River Change: Sediment Dynamics in the Diable River, Quebec.*

Faghfouri, A., Germain, D. & Fortin, G. (2025). Seven Decades of River Change: Sediment Dynamics in the Diable River, Quebec. *Geosciences*, 15, 388. https://doi.org/10.3390/geosciences15100388

Ce chapitre reconstitue l'évolution morphologique et les bilans sédimentaires de la rivière du Diable (Québec) sur sept décennies à partir de données historiques et LiDAR.

Chapter 4 – *A Multi-Method Statistical Framework for Quantifying Fluvial Sediment Transport and Geomorphic Dynamics in a Cold-Region River System.*

À soumettre. Ce chapitre applique un cadre multiméthodes pour quantifier le transport sédimentaire et identifier les zones d'activité géomorphologique.

Chapter 5 – *Trends and historical patterns of meteorological droughts in New Brunswick, Canada, using PDSI and SEDI indices.*

Faghfouri, A., Fortin, G., Ullmann, A., Raymond, F., Poirier, C., Dubreuil, V., & Germain, D. (2025). Trends and historical patterns of meteorological droughts in New Brunswick, Canada, using PDSI and SEDI indices. *Theoretical and Applied Climatology*, *156*(5), 257.

Ce chapitre analyse les tendances et régimes historiques de sécheresse au Nouveau-Brunswick et leurs implications hydrologiques régionales.

CHAPTER 1

Rethinking Sediment Connectivity in Cold Regions: Towards an Integrated Framework for Fluvial Systems

Ali Faghfouri[1], Daniel Germain[2], Guillaume Fortin[3]

[1]*Institute of Environmental Sciences, Université du Québec à Montréal, Québec, Canada.*

https://orcid.org/0000-0001-6418-5436

faghfouri.ali@courrier.uqam.ca

[2]*Department of Geography, Université du Québec à Montréal, Québec, Canada.*

https://orcid.org/0000-0003-4757-3124

germain.daniel@uqam.ca

[3]*Department of History and Geography, Université de Moncton, New Brunswick, Canada.*

https://orcid.org/0000-0002-9583-9188

guillaume.fortin@umoncton.ca

The paper is to be submitted soon.

Résumé

La compréhension du transfert sédimentaire à l'échelle des paysages est devenue une préoccupation centrale en géomorphologie fluviale, le concept de connectivité sédimentaire offrant un cadre d'analyse puissant pour examiner la manière dont les sédiments se déplacent des sources vers les exutoires. Cependant, les modèles et cadres existants demeurent peu adaptés aux conditions particulières des systèmes fluviaux froids. Ces environnements sont façonnés par des facteurs saisonniers et épisodiques, notamment les cycles de gel–dégel, les crues de fonte nivale, la formation de glace et les perturbations écologiques qui fragmentent les voies sédimentaires et introduisent une forte variabilité dans les processus de transport. Dans cet article, nous réévaluons de manière critique l'applicabilité des approches actuelles de connectivité sédimentaire aux systèmes fluviaux des régions froides, en passant en revue les méthodes conceptuelles, morphologiques, indiciaires, numériques et orientées réseaux. À partir de cette analyse, nous proposons un modèle conceptuel global et multi-couches, spécifiquement adapté aux réalités des systèmes fluviaux froids. Ce modèle intègre quatre dimensions interconnectées : les facteurs environnementaux externes, les contrôles structurels, les processus fonctionnels et les rétroactions du système. En tenant explicitement compte des dynamiques cryosphériques, des effets hérités de la géomorphologie passée et des influences anthropiques, notre modèle offre une compréhension plus réaliste et flexible du transfert sédimentaire en climat froid. Ce cadre vise à soutenir à la fois les avancées théoriques et les stratégies appliquées dans les bassins versants des régions froides, notamment en matière de modélisation par scénarios, de gestion des risques sédimentaires et de planification de la restauration. Une attention particulière est accordée aux processus hivernaux, aux interactions biotico-géomorphologiques et à la réactivation différée des sédiments stockés.

Mots-clés : géomorphologie fluviale, connectivité sédimentaire, systèmes fluviaux froids, voies sédimentaires, modèle conceptuel multi-couches, modélisation par scénarios

Abstract:

Understanding sediment transfer across landscapes has become a central concern in fluvial geomorphology, with the concept of sediment connectivity offering a powerful lens to examine how sediments move from sources to sinks. Yet, existing models and frameworks remain poorly suited to the distinctive conditions of cold river systems. These environments are shaped by seasonal and episodic drivers, including freeze–thaw cycles, snowmelt floods, ice formation, and ecological disturbances that fragment sediment pathways and introduce high variability in transport processes. In this paper, we critically reassess the applicability of current sediment connectivity approaches to cold-region fluvial systems, reviewing conceptual, morphological, index-based, numerical, and network-oriented methods. Drawing from this review, we introduce a comprehensive, multi-layered conceptual model tailored to the realities of cold-region fluvial systems. The model integrates four interconnected dimensions: external environmental drivers, structural controls, functional processes, and system feedback. By explicitly accounting for cryospheric dynamics, geomorphic legacy effects, and anthropogenic influences, it provides a more realistic and flexible understanding of sediment transfer in cold climates. This framework intends to support both theoretical advances and applied strategies in cold-region watersheds, particularly in scenario-based modeling, sediment risk management, and restoration planning. Special emphasis is placed on winter processes, biotic–geomorphic interactions, and the delayed reactivation of stored sediments.

Keywords: Fluvial geomorphology, Sediment connectivity, Cold river systems, Sediment pathways, Multi-layered conceptual model, Scenario-based modeling

1.1. Introduction

Over the past two decades, sediment connectivity has become central in geomorphic theory and applied watershed management (Poeppl et al., 2017; Fryirs, 2013). This concept captures how sediments are routed through landscapes across multiple spatial and temporal scales (Andreazzini et al., 2021; Wohl, 2017; Bracken et al., 2015). By moving beyond site-based assessments of erosion or deposition, sediment connectivity provides a framework for diagnosing flux imbalance and sensitive areas and guiding restoration or hazard mitigation strategies. This dynamic is shaped by a complex interplay of topography, hydrology, climate, vegetation, land use, and disturbance regimes.

In cold regions, however, sediment connectivity is strongly modulated by cryospheric and ecological processes. Freeze-thaw cycles, snowmelt floods, droughts, permafrost degradation, wildfire, and beaver activity create threshold-sensitive and fragmented sediment pathways that often elude conventional modeling approaches. These processes generate acute, punctual, episodic sediment events (pulses) and long-lasting, persistent, continuous events through time (press), which are responsible for disconnections between sources and channels (Ettema and Daly, 2004; Fryirs, 2017; Beltaos and Burrell, 2021; Prowse, 2001; Zhao et al., 2022). Although a wide range of methodological approaches has been developed from morphological sediment budgets (Toone et al., 2014) and connectivity indices (Borselli et al., 2008; Cavalli et al., 2013) to network-based models (Heckmann and Schwanghart, 2013), most remain either narrow in scope or poorly adapted to the specific conditions of cold-region catchments. This gap is especially problematic given accelerating climate extremes, ecological pressures, and land use/land cover (LULC) change in northern rivers (Rathburn et al., 2018; Owens, 2020; Zhang et al., 2022).

This paper proposes a holistic, multi-layered conceptual model of sediment connectivity, designed explicitly for cold-region rivers. The objectives of this work are fourfold: i) to clarify foundational concepts related to sediment connectivity and sediment budgeting in cold-climate fluvial systems; ii) to critically examine existing methodological approaches including conceptual models, morphological budgets, sediment connectivity indices, numerical simulations, and network-based analysis; iii) to analyze key environmental drivers (e.g., seasonality, ice-related processes, ecological disturbances, and anthropogenic changes) that govern sediment transfer in cold regions; and iv) to introduce an integrative conceptual framework that synthesizes these elements and provides a foundation for both research and management applications.

1.1.1 Conceptual Foundations of Sediment Connectivity in River Systems

Sediment connectivity has gained increasing attention as a key concept for understanding how sediment is transferred across landscapes and within river systems. At its core, the idea captures the degree to which sediment can move from sources, through transfer zones, to depositional areas within a catchment (Bracken et al., 2015; Poeppl et al., 2017; Shi et al., 2025). This perspective improves both geomorphic interpretation and applied watershed management.

Two main dimensions of sediment connectivity are typically distinguished: structural and functional (Cho et al. 2023) (Figure. 1.1). Structural connectivity refers to the spatial configuration

of the landscape (e.g., slope composition, form and gradients, surface roughness, drainage density, vegetation cover) that either facilitates or impedes sediment transport. It is often evaluated using topographic metrics derived from digital elevation models (DEMs), digital terrain model (DTM), and GIS-based analyses, with tools like the Index of Connectivity (IC) serving as prominent examples (Borselli et al., 2008; Cavalli et al., 2013; Gay et al., 2016). Functional connectivity, in contrast, reflects the actual transfer of sediment under given hydrological and geomorphic conditions. It is shaped by sediment availability, flow energy, and disturbance regimes (Czuba & Foufoula-Georgiou, 2015; Bracken et al., 2015). However, it remains more elusive and is often inferred from indirect evidence rather than directly observed. This has led researchers to rely on structural proxies, despite their limited ability to capture dynamic sediment behavior (Najafi et al., 2021). Yet, when analyzed jointly, structural and functional perspectives provide a more complete understanding of sediment transfer mechanisms. Their integration is now widely regarded as critical for interpreting sediment pathways in complex, disturbance-prone systems. Still, their operationalization remains challenging, particularly in cold-region catchments where data are scarce, and processes are often nonlinear or delayed.

1.1.1.1 From Concept to Application: The Sediment Budget Perspective

Closely related to the notion of connectivity, the sediment budget framework offers a quantitative lens through which sediment production, storage, and export can be evaluated within defined spatial units such as catchments or river segments (Figure. 1.1; Dietrich & Dunne, 1978; Slaymaker, 2003; Frings & Ten Brinke, 2018). It enables researchers and managers to identify sediment sources, sinks, and routing pathways, thereby supporting diagnoses of imbalance or bottlenecks in sediment fluxes. However, building reliable sediment budgets is no simple task. The spatial heterogeneity and temporal variability inherent to fluvial systems, combined with data scarcity and the complexity of non-linear sediment responses, make such budgets challenging to reconstruct (Heckmann et al., 2008; Parsons, 2011). Over the years, various attempts have been made to bridge this gap by linking budget calculations with connectivity concepts, leading to hybrid approaches such as sediment budget cells (Dolan et al., 1987), conceptual models (Shi et al., 2025), and cascade or network representations (Cossart & Fressard, 2017; Heckmann & Schwanghart, 2013).

More recently, integrated conceptual models have emerged that seek to bring together multiple system components of sediment systems: external drivers, structural conditions, functional processes, and feedback responses. For instance, the model proposed by Heckmann et al. (2018) incorporates not only geomorphic features such as slope and surface roughness, but also external forcings (e.g., precipitation, gravity), hydraulic behavior, and sediment delivery outcomes. Other frameworks have moved toward greater interdisciplinarity, combining ecological, hydrological, and geomorphological processes into a unified perspective (Ali et al., 2018; Poeppl et al., 2017; Keesstra, 2020; Batista et al., 2022; Dwivedi et al., 2025).

A growing body of work also emphasizes the importance of non-linear feedback and process-response interactions in sediment systems. For example, Bracken and Croke (2007) demonstrated that sediment transfer depends not only on physical attributes but also on factors such as hillslope

position, runoff generation, and rainfall variability. Fryirs (2013) similarly pointed out the regulatory role of sediment sinks in modulating delivery and retention within catchments.

Building on long-standing geomorphic theory, some studies have renewed attention to paraglacial adjustments (i.e., Church & Ryder, 1972), legacy sediment storage, and delayed reactivation as fundamental dimensions of catchment behavior (Ballantyne, 2002). Sediments stored for decades, or even centuries, may be remobilized under specific hydroclimatic or ecological conditions (Cossart et al., 2013). In cold regions, these remobilizations are often episodic and threshold-driven, triggered by permafrost degradation, wildfire, or extreme runoff events. Capturing these legacy-driven sediment transfers requires a connectivity perspective, integrating spatial patterns with temporal dynamics.

1.1.1.2 Cold-Region Constraints and the Need for Tailored Frameworks

Cold-region river systems present a set of unique environmental constraints that fundamentally shape how sediment connectivity operates. Seasonal ice cover, snowmelt-driven hydrology, freeze–thaw weathering, and the legacy of glacial landscapes all play pivotal roles in modulating both structural and functional connectivity. These conditions often violate steady-state assumptions, introducing temporal variability and threshold effects that limit the applicability of standard models (Ettema & Daly, 2004; Beltaos & Burrell, 2021; Prowse, 2001; Vergara et al. 2024). Indeed, episodic and discrete events such as ice-jam or wood-jam breakups or thaw slumps drive sediment pulses that conventional models fail to capture due to their transient and threshold-sensitive nature. Moreover, the combined influence of cryospheric processes, ecological disturbances, and geomorphic memory creates a connectivity landscape that is fragmented in space and discontinuous in time. Feedback among these factors often results in sediment pathways that are unstable, hysteretic, and highly context-dependent. While recent efforts have acknowledged this complexity, most frameworks continue to generalize environmental drivers, neglecting the cold-specific processes that govern sediment behavior in northern rivers (Chassiot et al., 2020 ; Blåfield et al., 2024).

This disconnect highlights the need for tailored models that move beyond generalized assumptions. In cold-region systems, it is not enough to map structural features or simulate average conditions. What is required is a holistic, adaptive framework that accounts for delayed mobilization, episodic transfer events, and climate-sensitive feedback. Such a model also embraces uncertainty, recognizing that sediment dynamics in these landscapes are shaped as much by legacy effects and threshold exceedances as by current forcings.

The next section reviews methodological approaches commonly used to assess sediment connectivity and evaluates how well they meet the specific challenges posed by cold fluvial environments.

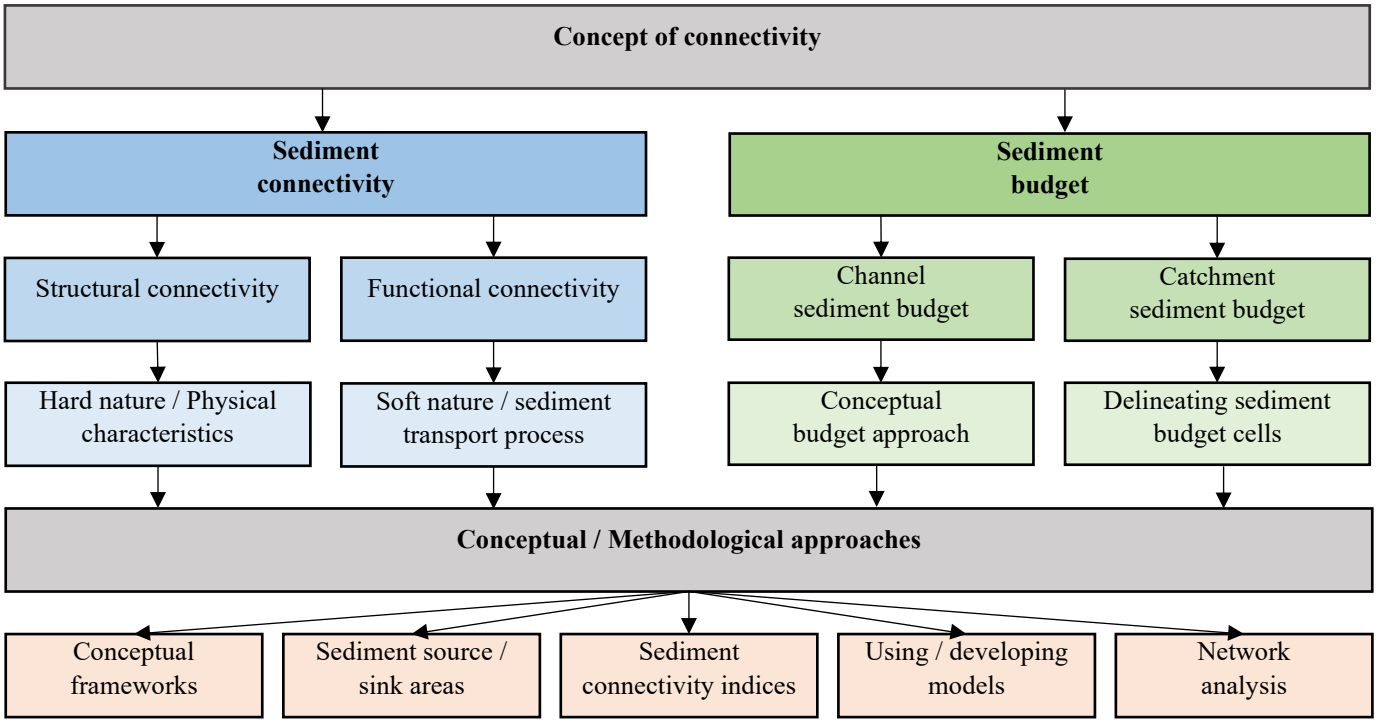

Figure 1.1 Conceptual structure of sediment connectivity and sediment budget approaches in fluvial systems. The diagram highlights the distinction between structural and functional connectivity and the integration of sediment budgeting perspectives at the channel and catchment scales. It also illustrates the link between conceptual foundations and methodological tools used to assess sediment dynamics.

1.2. Methodological Approaches to Sediment Connectivity

Over the past two decades, a diverse array of methods has been developed to assess sediment connectivity in fluvial systems (see Table 1.1). These approaches vary widely in terms of conceptual foundations, data requirements, spatial and temporal resolution, and adaptability to different landscape contexts. Drawing from recent literature (e.g., García-Ruiz et al., 2017; Poeppl et al., 2017; Heckmann et al., 2018; Najafi et al., 2021; Tangi et al., 2022; Cho et al. 2023), five major categories of methodological approaches were identified: conceptual frameworks, morphological budgeting, sediment connectivity indices, numerical models, and network-based analyses.

Table 1.1 Overview of Models and Tools for Sediment Connectivity Assessment and Mapping.

Author	Input parameters	Simulation process	Output parameters	Type
1. SedInConnect				
Crema & Cavalli, 2018	• DEM • Target feature • Sink feature • Weighting factor • Normalization procedure	• Based on open-source stand-alone software	• Raster of the index of connectivity (IC) • Upslope/downslope component	Modeling Mapping
2. Sediment-Connectivity and Surface Roughness (Python scripts)				
Cavalli & Marchi, 2008 Cavalli et al., 2013 Crema & Cavalli, 2018 Crema et al., 2020	• DTM • Desired moving window extent • Pit-filled DTM • Cell size • Weighting factor • Target shapefile	• Cavalli_roughness.py • SedInConnect_target.py	• Raster of the surface roughness • Raster of the roughness-derived weighting factor • Raster of the IC in respect to the desired target	Modeling Mapping
3. Connectivity Index (ArcGIS toolbox)				
Cavalli et al., 2013	• Working directory info • DTM • Cell size • Weighting factor raster	• Connectivity index • Connectivity index (targets) • Surface roughness	• Connectivity Index map	Modeling Mapping
4. CASCADE				
Tangi et al., 2019	• Slope [m/m] • Length [m] • Area of the basin (Ad) [Km2] • Discharge (Q) [m3/s] • Active channel width [m] • D16, D50, D84 [m] • Manning's roughness (n)	Network extraction: • Minimum Drainage Area • Network Segmentation CASCADE framework: • Transport formula • Hydraulic parameter computation • Dam implementation • External sediment sources • Erosion limit process	• Extracted the river network • Identified the river network reaches • Defined reach features • Estimated the sediment fluxes • Total transported sediment • Summary of transported/deposited sediment	Modeling Mapping
5. Framework for Analyzing Coastal Sediment Transport Pathways				
Pearson et al., 2020	• DTM • Geomorphic cells • Known sources and sinks of sediment • Field measurement data	• Graph theory • Delft3D model • Morphostatic (fixed bed) modeling approach • Structural vs functional connectivity analysis • Eulerian measurements	• Spatial map of sediment mass • Link density • Asymmetry • Modularity • Connectivity between nodes • Strength • Centrality	Modeling Mapping
6. TopoToolbox				
Schwanghart et al., 2014 Schwanghart & Kuhn, 2010	• DEM	• Set of MATLAB functions	• Relief and flow pathway analysis from DEM • Derived flow-related terrain metrics • Stream network characterization standard • Terrain attribute extraction	Modeling Mapping
7. TOPKAPI				
Ciarapica &Todini, 2002 Liu & Todini, 2002 Liu et al., 2005	• DEM • Discharge data	• Water cycle components • Channel water routing • Sub-grid modeling scheme	• Sediment transport	Modeling
8. The Reservoir Conservation Model RESCON 2				

Efthymiou et al., 2017	• Mean annual water inflow • Hydrologic variability coefficient • Statistical distribution of annual water flows • Mean annual total sediment	• Stand-alone open-source software for sediment management in reservoirs	• Sediment management planning • Recommendations strategies for reducing sediment yield • Identification of trapped sediment removal needs • Adaptive structural and functional measures	Modeling
9. BASEMENT: a freeware simulation tool				
ETH Zurich, 2021	• Topography values • Hydrology values • Soil parameters	• Morphodynamics models	• Sediment transport • Bedload transport • Morphological flux • Total cell conveyance • Discharge	Modeling
10. Cytoscape.js				
Franz et al., 2016	• Various input data	• Open-source JavaScript-based graph library • Mutable graphs • Graph traversal	• Visualization software component • Predicted/ recommended Graph types	Modeling
11. Delft3D				
Deltares, 2018	• Tidal waves • Precipitation	• Two- and three-dimensional hydrodynamic model	• Water quality • Sediment transport • Morphology evaluation • Ecology evolution	Modeling
12. SIFT				
Pulley & Collins, 2018	• Tracer distributions • Sediment data	• Applying tracer data • R-based computational environment	• Sediment source fingerprinting • Sediment source apportionment	Modeling
13. Structural sediment connectivity (Graph theory)				
Cossart & Fressard., 2017	• Sediment input • Topographic distance	• Simulation of graph scenarios	• Sediment delivery	Modeling
14. SWAT				
US Department of Agriculture (USDA) Shekhar & Xiong, 2008	• Identified sources of Sink • DEM • Topography, Drainage network and Land cover • Soil • Climate • Land management	• Applied in scenario analysis to assess connectivity aspects	• Sediment outputs • Connectivity aspects in sediment migration modeling	Modeling
15. GRASS GIS				
GRASS Development Team, 2022	• DEM	• Upslope approach • Downslope approach	• Sediment delivery ratio (SDR)	Modeling Mapping
16. SedSim				
Wild et al., 2019	• Elevation target • Evaporation data • Environmental flow data • Density current venting • General sediment removal	• Simulation of a wide range of reservoir sediment management techniques • Flushing, Sluicing, Bypassing processes	• Simulated water and sediment flows in reservoirs and river channels • Sediment transport • Reservoir sediment trapping	Modeling
17. SAGA GIS				
Conrad et al., 2015	• DTM • Slope • Channel network • Surface roughness • Meteorological data	• Sediment sampling tools • Soil erosion modeling	• Sediment yield estimation • Mapping sediment flow • Sediment yield concentration • Sediment balance	Modeling Mapping

18. SCIMAP				
Reaney et al., 2011	• DEM	• ArcGIS Pro plugin • Pollution risk mapping tool	• Channel Sediment Risk • Source erosion risk • Surface flow index • Network index	Mapping
19. GDCS				
Wheaton et al., 2010	• DEM	• Analyzing riverscapes • Spatial raster-based change detection	• Topographic change detection in rivers • Detected changes between surveys • Sediment transport	Mapping
20. Flow-3D's Sediment Transport Model				
Flow Science Team, 2019	• Various required input data for simulation	• Three-dimensional flow components • Hydrodynamic model • Validation capability	• Sediment transport modeling • Evaluated scour and deposition • Simulated bedload and suspended sediment transport	
21. SBAS				
Rosati & Kraus, 2001	• DEM • Shape file	• Sediment Budget Analysis System • Sediment-budget equation	• Sediment budget calculation	Modeling Mapping
22. GenCade				
Frey et al., 2012	• Beach specification • Wave specification	• Inlet sediment transfer factor	• Inlet sediment transport • Longshore sediment transport • Regional sediment transport • Breaking wave angles	Modeling
23. Telecoupling Toolbox				
Tonini & Liu, 2017	• Various input data • DEM	• Geospatial software tools	• Sediment delivery ratio	Modeling Mapping
24. EXZECO				
Pons et al., 2010	• DEM	• Extraction of flow zones • Extraction of flow concentration zones • Calculation of thalwegs	• Recognized Floodable area • Calculated Runoff risk area • Flood risk mapping	Modeling Mapping
25. RUSLE				
Renard et al., 1997	• Physically meaningful input values	• Erosion prediction packages	• Estimated soil erosion rates • Sediment transport • Sediment yield	Modeling
26. PERESA-L				
Borselli et al., 2011	• DEM • Various input data	• PESERA model procedures	• Sediment yield contribution due to shallow landslide • Degree of degradation by landslide assessment.	Modeling
27. D-CASCADE				
Tangi et al., 2022	• Slope • Length (L) • Discharge (Q) • Active channel width • Grain size distribution (GSD) • Manning's n • Sediment deposit data	• Sediment connectivity model • Sediment mobilization, erosion, and deposition components	• Sediment delivery and transport • Total sediment volume variation • Forecasted future sediment transport trajectories	Modeling
28. SEDD				
Ferro & Porto, 2000	• Different expressions of the erosivity	• Rainfall erosivity factor	• Basin sediment yields	Modeling

	• Topographic factors	• Sediment Delivery Ratio of morphological unit • Based on RUSLE	• Likelihood of eroded soils reaching the rivers	
29. RSEDD				
Chen & Thomas, 2020	• Topographic factors • Erosivity data	• Based on SEDD	• Sediment transport to river channels	Modeling
30. SeRFE				
Gilbert & Wilcox, 2020	• Geospatial data • Limited field data • Drainage network shapefile	• Pre-processing tools • Various sub-models	• Sediment recruitment modeling • Sediment transport	Modeling
31. CAST				
Tan et al., 2021	• DEM • Various input data	• Hydrological connectivity • Ecological indicator • Geostatistical analysis	• Quantified hydrological connectivity of floodplains	Modeling
32. InVEST				
Hamel et al., 2015	• Rasters of climate, soil, topography, land use and land cover	• Absolute prediction processes • Spatial variability in sediment export • Biophysical model	• Spatially explicit assessment of the sediment retention service • Map and quantify sediment delivery • Average annual sediment delivery and retention per sub-catchment • Maps representing the per-pixel contribution to sediment yield	Modeling Mapping
33. Hydrosedimentological Connectivity				
Zanandrea et al., 2021	• DTM • Cell size • Weighting factor raster • IPS raster • Input of the runoff raster • Working directory	• ArcGIS-based open-source software	• Index of hydrosedimentological connectivity (IHC) map	Modeling Mapping

1.2.1 Conceptual Frameworks

Conceptual models provide simplified frameworks to interpret sediment transfer across landscapes, especially where empirical observations are scarce or during early stages of a research project (Bracken et al., 2015; Owens, 2005; Poeppl et al., 2017). They aim to illustrate how external drivers (such as climate or LULC), structural elements (like topography and vegetation), and disturbance regimes interact to shape sediment pathways within a catchment. They are particularly effective for hypothesis generation, guiding fieldwork, and integrating knowledge across disciplines such as geomorphology, hydrology, and ecology (Corenblit et al., 2007; Ali et al., 2018). For instance, Fryirs (2013) highlighted the importance of identifying and mapping sediment sinks, while Heckmann et al. (2018) developed a more comprehensive model that incorporates external forcings, structural metrics (e.g., slope, drainage density), and functional processes (e.g., runoff, sediment delivery).

Despite these strengths, conceptual frameworks have limitations. Their qualitative nature makes it difficult to calibrate or validate without complementary data. Their predictive capacity is often modest, especially in systems where sediment behavior is governed by threshold effects or extreme events. In cold-region environments, for example, processes like snowmelt pulses, permafrost

thaw, or ice-jam breakups demand finer temporal resolution and a better integration of seasonal and cryospheric variables, elements that most existing models address only superficially.

In summary, conceptual frameworks remain invaluable tool for structuring research and navigating system complexity. However, to fully represent sediment dynamics in cold rivers, they must be complemented by empirical data and/or numerical modeling approaches.

1.2.2 Morphological Budgeting Approaches

Morphological sediment budgeting provides a direct means to assess sediment flux by quantifying changes in topography over time. This technique typically involves comparing surface elevation data from aerial photographs, LiDAR, UAV-based surveys, or bathymetric scans across two or more time points to detect zones of erosion and deposition (Lane et al., 1996; Wheaton et al., 2010). By measuring volumetric changes, researchers can estimate net sediment gains or losses within defined geomorphic units such as channel reaches, gravel bars, or floodplains.

This approach offers valuable insights into functional sediment dynamics, allowing for identifying active pathways and depositional sinks. It is particularly effective in landscapes undergoing rapid or disturbance-driven change. In cold-region systems, for example, morphological budgets have been used to detect sediment redistribution linked with permafrost thaw (Kokelj et al., 2009), spring ice-jam flooding (Beltaos & Burrell, 2021), and post-wildfire erosion (Rathburn et al., 2018). In addition, several studies have shown the utility of this method for evaluating restoration outcomes (Hodge et al., 2009), diagnosing sediment continuity, or validating hydrological models (Tangi et al., 2022; Dwivedi et al., 2025). Recent advances in remote sensing and Structure-from-Motion (SfM) photogrammetry have enhanced its spatial resolution and affordability (Williams et al., 2011; Westoby et al., 2012; Li et al. 2024).

However, the method comes with notable limitations. The accuracy of volumetric estimates depends heavily on the resolution and quality of the input datasets, as well as on the precise co-registration of repeat surveys (Wheaton et al., 2010; Williams et al., 2011). In areas with dense vegetation, turbid water, or seasonal snow cover, elevation differencing can introduce artifacts or obscure subtle topographic change. Another challenge lies in the temporal granularity of monitoring. In cold environments, sediment transfer may occur during brief, but intense pulses followed by extended periods of inactivity (press). Standard interannual or decadal comparisons may fail to detect these short-lived but geomorphically significant events. As Toone et al. (2014) argue, integrating event-based monitoring and high-frequency data acquisition is key to capturing such dynamics. Indeed, morphological budgets do not always reflect latent sediment fluxes, materials that are mobilized but remain in temporary storage, suspended in flow, or trapped beneath ice or vegetation. For this reason, they are best interpreted as snapshots of net geomorphic change rather than full accounts of sediment transport. Despite these constraints, morphological budgeting remains a robust and versatile tool for studying sediment dynamics in cold regions, especially when combined with hydrological data, connectivity indices, or conceptual models to triangulate findings.

1.2.3 Sediment Connectivity Indices

Sediment connectivity indices provide a relatively accessible and reproducible means of estimating the potential for sediment to move from source areas to downstream sinks. They usually rely on spatial metrics such as slope, contributing area, flow path length, surface roughness, or vegetation cover (Borselli et al., 2008; Cavalli et al., 2013; Gay et al., 2016). The most widely used formulation, the Index of Connectivity (IC), combines upslope sediment supply potential with downslope transfer efficiency to produce a pixel-based estimate of sediment linkage (Shi et al. 2025). These indices have proven useful for catchment-scale assessments, erosion risk mapping, and prioritization of landscape interventions. Their main appeal lies in their ease of implementation: once a high-resolution DEM is available, IC maps can be generated using open-source or GIS-based workflows, even in data-scarce regions (Keesstra et al., 2018; Cossart et al., 2018; Zhao et al., 2025). They also enable comparative analysis across land uses, slopes, and management scenarios.

Despite their widespread use, however, sediment connectivity indices present notable limitations (Hooke and Souza, 2021). First, these indices primarily reflect structural connectivity, based on terrain features, rather than actual sediment flux. As a result, they may overestimate connectivity in frozen or snow-covered landscapes, where steep slopes do not translate into active sediment transport (Najafi et al., 2021; Cossart & Fressard, 2017). Second, most indices assume steady-state conditions and fail to incorporate seasonal variability or transient processes. For example, an area with high IC values in summer may remain disconnected much of the year due to frozen ground or a hydrologic barrier. Likewise, post-disturbance changes like vegetation loss after wildfire, drought, clear-cutting or sediment infill from ice-jam floods can shift connectivity patterns in ways that static models fail to capture (García-Ruiz et al., 2017). To address these shortcomings, some researchers have developed modified or hybrid indices that integrate topographic data with hydrological or ecological variables (Asadi et al., 2023; Poeppl et al., 2017). For instance, incorporating snowmelt timing, intermittent flow, or cryospheric thresholds can significantly improve model performance in cold-climate settings. Overall, while connectivity indices serve as valuable screening tools, their effectiveness in cold environments depends on careful calibration, contextual interpretation, and integration with field data or dynamic modeling.

1.2.4 Numerical Models and Model Refinement

Numerical and process-based models offer a more formalized and quantitative approach to simulating sediment connectivity. Unlike morphological or index-based methods, these models use physical equations or empirical rules to simulate hydrological processes, sediment transport, and boundary conditions over time (Czuba & Foufoula-Georgiou, 2014; Hairsine & Rose, 1992a, 1992b; Wohl et al., 2017). These tools are particularly powerful for exploring hypothetical scenarios, forecasting sediment dynamics under changing conditions, or estimating fluxes in poorly instrumented regions. Models such as CAESAR-Lisflood, SEDNET, and Watershed Modeling System have been widely applied to simulate sediment budgets, routing, and channel evolution at various scales. Their ability to incorporate rainfall, runoff, slope, soil characteristics, and LULC

makes them especially attractive for predictive watershed management (Brasington & Richards, 2007; Baartman et al., 2013).

However, their implementation in cold regions is constrained by limited process-specific data and the lack of cryospheric-adapted parameterizations (Prowse, 2001; Kokelj et al., 2009). Indeed, many were developed for temperate or semi-arid environments. As Fryirs (2013) noted, sediment systems are highly sensitive to local-scale variations in morphology and boundary conditions, often oversimplified in large-scale simulations. Additionally, many models struggle to incorporate nonlinear feedback and threshold-driven disturbances, while these episodic events can dramatically alter sediment pathways, either amplifying or disrupting connectivity, in ways that defy equilibrium assumptions. Toone et al. (2014) and Rathburn et al. (2018) emphasized that capturing these dynamics requires integrating disturbance modules and legacy effects into sediment models.

Recent advances are beginning to fill this gap. Some researchers are coupling hydrological and sediment models with snowmelt or permafrost modules to better represent seasonal transitions and subsurface flows (Heckmann et al., 2018; Najafi et al., 2021). Others are experimenting with agent-based or probabilistic approaches to account for uncertainty and capture the stochastic behavior of sediment systems (Poeppl et al., 2017; Cossart et al., 2018).

In summary, numerical models hold considerable promise for advancing sediment connectivity research in cold environments, especially when paired with high-resolution data and grounded in a robust conceptual framework. But realizing this potential requires models explicitly tailored to the climatic, geomorphic, and ecological conditions of northern catchments.

1.2.5 Network and Graph-Based Approaches

Network and graph-based approaches represent a growing methodological frontier in sediment connectivity analysis. These models conceptualize river catchments as spatially structured networks, where nodes (e.g., sediment sources, confluences, sinks) are connected by links that represent sediment transfer pathways. Drawing on graph theory and geomorphometric principles, such methods allow researchers to explore topological properties of sediment systems, including pathway redundancy, centrality, or resistance to fragmentation (Heckmann & Schwanghart, 2013; Fryirs, 2013; Buter et al. 2022).

One of the major strengths of this approach is its ability to characterize the structure of connectivity rather than simply measuring the magnitude of fluxes. Representing the landscape as a graph enables the identification of critical nodes (e.g., sediment bottlenecks or hubs), assessment of how disturbances affect system cohesion, and simulation of sediment propagation through the network under different scenarios (Cossart & Fressard, 2017). This is particularly valuable in cold-region settings, where strong spatial discontinuities often occur related to fragmented landscapes. Graph-based methods can also be integrated with terrain metrics (e.g., the Index of Connectivity), morphological analyses, or hydrological models to enrich connectivity assessments. For example, Heckmann et al. (2018) developed a multi-layered framework that merges

topography, process domains, and external drivers into a unified network structure, offering a more holistic lens on sediment dynamics.

However, these approaches remain largely conceptual or exploratory. Many rely on simplified assumptions about link strength, transfer efficiency, or process thresholds; parameters that are often difficult to calibrate or validate, especially in northern remote environments. Additionally, most graph representations are static and may fail to capture the temporal dynamics that are so critical in cold climates (Beltaos & Burrell, 2021; Najafi et al., 2021). Recent work has begun addressing these limitations by introducing dynamic graphs or time-weighted connectivity matrices that evolve with season or disturbance regimes (García-Ruiz et al., 2017; Poeppl et al., 2017). Others have proposed coupling graph metrics with field-based indicators of sediment availability and flux to calibrate better network attributes (Cavalli et al., 2013; Gay et al., 2016).

Overall, network and graph-based methods offer a promising and flexible framework for analyzing the structure, vulnerability, and resilience of sediment transfer systems. Their potential for cross-scale integration and multi-source data fusion makes them particularly appealing in cold-region applications, provided their assumptions are carefully aligned with environmental realities and supported by empirical validation.

1.2.6 Synthesis

The variety of methodological approaches available for assessing sediment connectivity offers complementary strengths, yet each presents essential limitations (see Table 1.1), in the context of cold river systems.

Conceptual frameworks remain essential for generating process-based hypotheses and for organizing interdisciplinary knowledge. However, without empirical calibration, their explanatory power often proves insufficient in predictive or operational settings. Morphological budgeting enables detailed reconstructions of erosion and deposition (van Rooijen & Lotsari, 2024). Still, its reliability depends on the resolution and alignment of spatial data, the capacity to detect short-lived events, and the ability to translate volumetric change into actual sediment mass flux.

Sediment connectivity indices are valued for their efficiency and broad spatial coverage, offering rapid diagnostics across entire catchments. Yet, they tend to oversimplify the threshold-sensitive and highly dynamic nature of sediment transfer (e.g., seasonal disconnections, abrupt sediment pulses). Numerical and process-based models provide strong theoretical underpinning and mechanistic insight, but their usefulness is often constrained by high data demands, complex calibration procedures, and a limited representation of cryospheric processes. Network and graph-based approaches offer a powerful lens to analyse landscape structure, system resilience, and emergent connectivity patterns. However, they tend to abstract away transport mechanics, and their performance depends on the accurate segmentation of landscape units, a task that remains challenging in heterogeneous or transitional terrains.

Together, these tools offer complementary perspectives, but their effective use requires adaptation to the episodic, seasonally constrained, and disturbance-driven nature of sediment dynamics in cold-region rivers.

1.3. Towards a Holistic Conceptual Model of Sediment Connectivity in Cold-Region Rivers

Building on the limitations identified in previous sections, we propose a new conceptual model that better reflects the complexities of sediment connectivity in cold rivers. Rather than focusing on a single driver, method, or process domain, the model is designed to integrate multiple layers of influence (e.g., physical, climatic, structural, and ecological) while remaining sensitive to system dynamics, seasonal transitions, and legacy effects. The objective is to complement existing frameworks with a more adaptable structure for research and management.

1.3.1 Rationale for a Holistic Model

Current methodological approaches to sediment connectivity in cold rivers often emphasize structure or process isolation. Structural metrics provide broad spatial coverage but frequently overlook feedback and storage dynamics (Cavalli et al., 2013; Cossart et al., 2018; Fryirs, 2013), while process-based and network approaches struggle with delayed system responses, thresholds, or memory effects, which are key features in cryospheric and disturbance-prone systems (Poeppl et al., 2017; Fryirs & Brierley, 2016;Poeppl et al., 2020).

To address these gaps, we propose a four-layered conceptual model that brings together: i) external drivers (e.g., climate, disturbance); ii) structural controls (e.g., slope, vegetation); iii) functional processes (e.g., sediment transfer, storage); and iv) feedback mechanisms. This architecture captures how sediment connectivity unfolds through interactions across space and time, offering a flexible tool suited to the complexity of cold-region rivers.

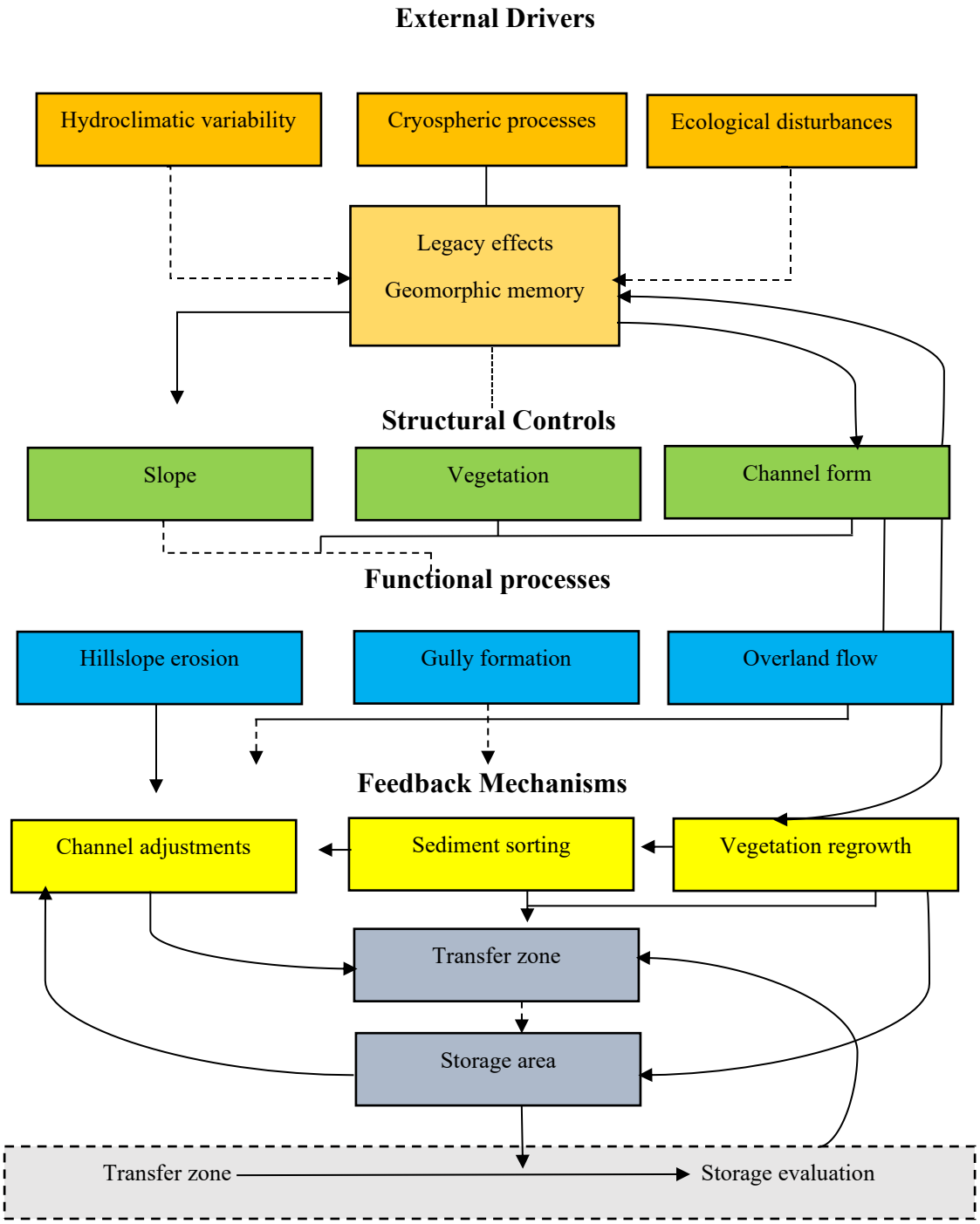

Figure 1.2. The conceptual model of sediment connectivity pathways in cold region rivers illustrates the sequence from source to transfer zones and storage areas. Environmental drivers influencing each stage are grouped by type, including hydroclimatic variability, cryospheric processes, ecological and anthropogenic disturbances, and the geomorphic legacy effects.

This first layer defines the external conditions that shape the potential for sediment connectivity within a catchment (Figure. 1.2). It encompasses climatic drivers (precipitation regimes, snowpack dynamics, temperature variability, freeze–thaw cycles), geologic and geomorphic contexts (glacial legacy features, basin relief, soil characteristics), and anthropogenic influences (LULC changes, river engineering, forestry practices). Cryospheric features such as permafrost and seasonal snow/ice are key modulators of sediment availability and mobilization potential.

The second layer refers to landscape attributes such as slope characteristics (composition, form, gradient…), vegetation, and channel form that influence sediment transfer potential (Figure. 1.2). These attributes structure the pathways available for sediment routing and may enhance or limit connectivity depending on terrain complexity. Though often treated as static, structural controls can shift over time in response to disturbances or ecological change.

The third layer addresses the processes responsible for sediment movement (Figure. 1.2; i.e., mobilization mechanisms and transport modes). These include hillslope erosion, gully formation, overland flow, channel transport, and floodplain exchange. Functional connectivity depends not only on the presence of pathways, but also on sediment availability, transport capacity, and hydrological triggers. As we mentioned earlier, in cold regions, these processes are highly variable in time and space, governed by seasonal transitions and disturbance events. They are also sensitive to cryospheric controls (e.g., ice jams, snowmelt timing, permafrost degradation).

The final layer captures the feedback loops that regulate sediment connectivity across spatial and temporal scales (Figure. 1.2). Key components include channel adjustments, sediment sorting, vegetation regrowth, and the formation or breaching of temporary storage zones (e.g., bars, dams, floodplains). Feedback can reinforce or disrupt connectivity depending on disturbance intensity and recovery trajectories (reaction and relaxation time, for example, Owens et al. 2010). In cryospheric systems, feedback often operates with time lags, amplifying or dampening sediment responses well after the triggering event. Integrating these dynamics is essential for understanding sediment fluxes and future system trajectories.

1.3.2. Synthesis of the Four-Layered Framework

The four interconnected dimensions of the framework (external drivers, structural controls, functional processes, and feedback mechanisms) combine across scales to shape sediment connectivity in cold-region rivers.

External conditions such as climatic variability, cryospheric processes, and ecological disturbances establish the broader environmental context and disturbance regime. Structural attributes, including slope, surface roughness, and drainage configuration, define the spatial configuration and potential pathways linking sediment sources to sinks (Borselli et al., 2008; Cavalli et al., 2013; Fryirs, 2013). This potential connectivity is only activated through functional processes, actual sediment fluxes driven by hydrology, climatic thresholds, and disturbance events (Czuba & Foufoula-Georgiou, 2015; Bracken et al., 2015; Cossart & Fressard, 2017).

In cold environments, these transfers are often abrupt and episodic, associated with snowmelt pulses, ice-jam floods, thaw-induced mass failures, or debris flows (Beltaos & Prowse, 2009; Kokelj et al., 2009; Lininger & Wohl, 2019; Zhang et al., 2023). Such events frequently exceed structural expectations, generating sudden shifts in connectivity. Feedback mechanisms further rework sediment pathways over longer timescales, leading to legacy effects, nonlinear responses, and delayed recovery trajectories. These include processes such as channel reconfiguration, storage redistribution, floodplain adjustments, and ecological succession (Moody & Martin, 2009;Corenblit et al., 2007; Wohl et al., 2017; Owens, 2020; Corenblit et al., 2024; Prugnes et al., 2025). By integrating these four dimensions, the model offers a dynamic and realistic account of sediment connectivity in cold-region rivers, addressing the limitations of conventional approaches that tend to isolate structural, functional, or environmental components.

1.3.3. Dynamic Interactions and Feedback across Layers

The four layers of the conceptual model are deeply interconnected across space and time, generating evolving patterns of sediment connectivity. A change in one layer can propagate across the system, altering sediment pathways in sometimes unexpected ways. For example, intensified snowmelt due to climate warming may trigger thaw slumps or modify runoff patterns, reshaping structural configurations and reactivating legacy sediment storages. Episodic events like debris flows or ice-jam floods can rapidly transform floodplains and influence the system's response to future disturbances or sediment input. Over time, feedback mechanisms such as hysteresis, threshold sensitivity, and delayed recovery further modulate sediment dynamics. These nonlinear responses reflect the memory and path dependency of fluvial systems, particularly under the influence of cryospheric and ecological processes.

While existing conceptual models have significantly advanced our understanding of sediment connectivity, most were designed for warm-temperate systems and do not fully account for the unique characteristics of cold-region rivers (Bracken et al., 2015). The framework proposed here introduces several key innovations tailored to cold environments: i) explicit integration of cryospheric controls across all layers; ii) incorporation of geomorphic memory and delayed responses; iii) recognition of ecological disturbances (e.g., beaver, wildfire, large woody debris) as core structuring processes in cumulative evolving manner.

1.4. Operational Implications for Research, Management, and Restoration

The conceptual model presented here offers a theoretical contribution and a practical structure for applied geomorphology (Table 1.2). Its layered organization lends itself to various uses, from scientific research to watershed planning and restoration. In research, the model encourages integrated, multiscale investigations of sediment dynamics. It supports the identification of key monitoring zones (e.g., sediment sources, transfer bottlenecks, legacy stores) and guides the interpretation of landscape changes following cold-region events (Rathburn et al., 2018; Kokelj et al., 2009; Owens, 2020).

Table 1.2. Potential applications of the conceptual framework for sediment modeling, risk assessment and restoration in cold-region fluvial systems

Scenario-based sediment modeling	
Thresholds	• Identify critical conditions under which sediment connectivity may abruptly shift (e.g., thaw slumps, debris flows) *(Beltaos & Prowse, 2009; Zhang et al., 2023).*
Cascading effects	• Simulate how disturbances propagate through sediment fluxes, floodplain dynamics, or channel morphology over time *(Owens, 2020).*
Resilience & hysteresis	• Assess non-linear and delayed responses of sediment pathways under different climate or land-use scenarios *(Moody & Martin, 2009).*
Model calibration	• Enhance the design and tuning of physically based, network-based, or hybrid sediment models suited to cold-region dynamics *(Cossart & Fressard, 2017; Cislaghi & Bischetti, 2019).*
Risk assessment and hazard management	
Sediment vulnerabilities	• Diagnose weak or sensitive source–sink linkages at risk from cryospheric, climatic, or anthropogenic disturbances *(Fryirs, 2013; Heckmann et al., 2018).*
Sensitive zones	• Prioritize monitoring in areas prone to disconnection, blockage, or hazard generation (e.g., post-ice-jam aggradation) *(Beltaos & Burrell, 2021).*
Early warning	• Support the development of alert systems by focusing on feedback-prone areas and dynamic thresholds *(Schmidt & Morche, 2006).*
Restoration planning and ecosystem management	
Reconnection strategies	• Identify priority locations for improving or disrupting sediment connectivity in restoration planning *(Fryirs, 2013).*
Adaptative design	• Guide interventions that consider system feedback and resilience, avoiding overly linear assumptions *(Moody & Martin, 2009; Poeppl et al., 2017; Prugnes et al., 2024).*
Ecological integration	• Incorporate riparian habitat recovery and sediment supply to wetlands into sediment management, especially in boreal environments *(Bracken et al., 2015; Owens, 2020; Corenblit et al., 2024).*

For management and restoration, it provides a decision-support tool to assess where interventions will be most effective given the structure and function of connectivity layers (Prugnes et al., 2024). For example, remediating structural barriers may be ineffective if functional transfer is already constrained by sediment starvation or altered hydrology. Similarly, reconnecting floodplains requires accounting for feedback and delayed sediment responses (Wohl et al., 2017; Fryirs, 2013). In planning contexts, particularly under changing climatic and freeze-thaw regimes, the framework aligns with scenario-based modeling and adaptive strategies. It helps anticipate future sediment trajectories by integrating crysospheric controls, system memory, and disturbance-driven variability (Moody & Martin, 2009). Ultimately, the model bridges conceptual insights and applied needs, offering a coherent platform for diagnosing sediment system behavior and guiding intervention strategies.

1.4.1 Implementation Limits and Future Refinements

Despite its versatility, the framework faces a few practical considerations. The first is the availability of suitable data, especially in remote or northern watersheds with sparse monitoring. Assessing functional and feedback layers requires time-series data, post-event surveys, or high-resolution topographic and sedimentary datasets (Toone et al., 2014; Wheaton et al., 2010; Williams et al., 2011).

In addition, operationalizing the model remains methodologically demanding. Existing tools (e.g., connectivity indices, sediment budgets, UAV-based surveys, etc.) each capture a portion of the system's behavior. Bridging these gaps will require hybrid approaches that combine terrain analysis, modeling, and field validation (Cavalli et al., 2013; Poeppl et al., 2017; Najafi et al., 2021). The model is not prescriptive and must be adapted to local conditions, including differences in permafrost extent, hydrological regimes, and disturbance histories. Its usefulness depends on iterative refinement grounded in expert knowledge.

Future improvements should enhance its ability to represent cryospheric feedback, eco-geomorphic couplings, and landscape memory. Further empirical testing across cold-region settings will be crucial to assess its diagnostic value and predictive potential. The framework should be seen as a living tool, adaptive, evolving, and grounded in both scientific rigor and applied relevance.

1.5. Environmental Drivers Shaping Sediment Connectivity in Cold-Region River Systems

Fluvial systems in cold climates are shaped by a distinct combination of environmental forces that operate across multiple scales. These forces produce irregular, non-linear sediment transfer dynamics driven by climate variability, cryospheric shifts, ecological disturbance, and human land use (Table 1.3).

Table 1.3. Main environmental drivers impacting sediment connectivity in cold temperate river systems

Cryospheric Processes	
Seasonal ice cover	• Regulates flow regimes, sediment scouring, and bed stabilization during winter (Beltaos and Burrell, 2021; Burrell et al., 2024).
Ice-jam Breakups	• Generate abrupt, high-magnitude sediment pulses through mechanical scour and sudden channel reconfigurations (Beltaos and Burrell, 2021; Kokelj et al., 2009).
Freeze-thaw cycles	• Induce surface destabilization, soil cracking, and sediment after major disturbances (Moody and Martin, 2009; van Rooijen & Lotsari, 2024).
Snowmelt floods	• Drive high-discharge events critical for sediment transport initiation, often following nonlinear thresholds in snowpack accumulation and melt timing (Prowse, 2001; Chassiot et al., 2020).
Permafrost degradation	• Mobilizes stored sediments through thaw slumps, retrogressive thaw failures, and thermokarst development, dramatically reshaping sediment fluxes and river morphology (Kokelj et al., 2009; Mancini & Lane, 2020; Gautier et al., 2021; Tananaev & Lotsari, 2022; Douglas et al., 2023).
Ecological Disturbances	
Wildfires	• Reduce vegetation cover, enhance surface runoff, and increase sediment detachment rates, often leading to post-fire sediment pulses (Wohl et al., 2017).
Beaver and dam dynamics	• Modifies channel and floodplain structures by damming, creating localized sediment retention zones but also promoting dynamic shifts upon dam failure (Hood and Bayley, 2008; Wohl, 2013; Jones et al., 2021).

Large herbivore grazing	• Alters vegetation density, soil compaction, and runoff patterns, potentially enhancing localized sediment production (Butler and Malanson, 2005).
Riparian vegetation dynamics	• Stabilize banks and modulate sediment interception, influencing both structural and functional connectivity over seasonal to decadal timescales (Corenblit et al., 2007).
Anthropogenic Pressures	
River engineering	• Channelization, levee construction, and damming alter flow regimes, sediment supply, and longitudinal connectivity (Petts, 1984).
Roads and forestry	• Create new sediment sources and reroute runoff pathways, enhancing erosion and localized sediment connectivity (Rathburn et al., 2018).
Urban development	• Increase impervious surfaces, accelerating runoff and sediment flushing into river systems (Fryirs, 2013).
Climate change interactions	• Amplify cryospheric degradation, altering sediment transport regimes beyond natural historical variability (Beltaos and Prowse, 2009; Gautier et al., 2021).

Cryospheric influences (seasonal ice cover, freeze–thaw cycles, and permafrost degradation) govern sediment availability, mobilization thresholds, and delivery timing. Such drivers often produce abrupt sediment pulses and delayed responses, as observed during ice-jam breakups or thaw-induced slope failures (Prowse, 2001; Kokelj et al., 2009; Mancini & Lane, 2020; Beltaos & Burrell, 2021; Tananaev & Lotsari, 2022; Douglas et al., 2023; Burrell et al., 2024). Ecological disturbances, such as wildfire, beaver activity, or large herbivores grazing and trampling, alter both structural and functional connectivity by reshaping vegetation cover and flow paths (Corenblit et al., 2007; Wohl, 2013). Riparian vegetation plays a long-term role in stabilizing banks and guiding channel evolution (Corenblit et al., 2024). Human pressures, including infrastructure, forestry, and hydrological alterations, add further complexity by modifying flow regimes and amplifying or dampening natural drivers (Fryirs, 2013; Rathburn et al., 2018). These drivers rarely act in isolation. Their effects are filtered by the landscape's history, past events that have modified morphology, storage zones, and sediment fluxes over decades.

1.5.1 Geomorphic Memory and Legacy Effects

Beyond immediate drivers, cold-region sediment dynamics are profoundly shaped by geomorphic memory, the lasting imprint of past disturbances on contemporary sediment behavior (Prugnes et al., 2025). Floods, thaw slumps, wildfire, and glacial legacies all contribute to the formation of dormant or reworked sediment stores that may remain inactive for years before reactivation (Kokelj et al., 2009; Wohl et al., 2017).

For instance, sediments deposited during major floods may persist in floodplains for decades (press) before being remobilized by a high-magnitude event (pulse) (Moody & Martin, 2009). Post-fire vegetation loss or hydrophobic soils can alter runoff and erosion patterns long after visible recovery (Rathburn et al., 2018). These legacy effects suggest that present-day transfers cannot be fully understood without considering historical conditions. In essence, cold-region rivers retain a form of « latent connectivity », a potential for sediment movement conditioned by past thresholds, modified pathways, and delayed system recovery (Bracken et al., 2015; Moody & Martin, 2009). Integrating this dimension into sediment connectivity assessment enhances predictive insight, especially in cold regions where disturbance cascades and recovery are highly non-linear. It also

underscores the importance of long-term monitoring and modeling approaches that go beyond static or short-term sediment budgets.

1.6. Knowledge Gaps and Future Research Directions

Despite recent progress, significant gaps remain in our understanding of sediment connectivity in cold-region river systems. These limitations undermine the reliability of predictive tools and reduce the effectiveness of sediment management in the face of rapid environmental change. We have identified four major categories of research gaps: empirical, methodological, conceptual, and strategic (Table 1.4).

Table 1.4. Knowledge gaps in sediment connectivity research in cold-region fluvial systems.

Category and Issues	Description	Barrier/Constraint
Empirical Gaps		
Seasonal variability	• Lack of data on sediment mobilization during winter, under ice, or snowmelt (Prowse, 2001; Beltaos and Burrell, 2021; Li et al., 2024).	• Logistical difficulty of winter fieldwork
Cryospheric processes	• Poorly documented effects of frazil ice, ice jams, and thaw-related mass wasting (Kokelj et al., 2009; Lininger and Wohl, 2019).	• Episodic and hard-to-instrument events
Legacy reactivation	• No long-term monitoring of stored sediment reactivation post-disturbance (Moody and Martin, 2009).	• Lack of sustained field programs
Methodological Gaps		
Static indices	• DEM-based metrics miss seasonal, cryospheric, and ecological dynamics (Borselli et al., 2008; Najafi et al., 2021).	• Tools adapted to temperate systems
Budget limitations	• Difficulty linking short-term changes to sediment storage–release cycles (Wheaton et al., 2010).	• Disconnection between metrics and process
Model calibration	• Lack of cold-specific parameters in numerical or network models (Heckmann et al., 2018; Cossart and Fressard, 2017).	• Calibration datasets not regionally adapted
Theoretical Gaps		
Geomorphic memory	• Frameworks insufficiently integrate delayed, threshold-based responses (Fryirs and Brierley, 2016; Wohl et al., 2022).	• Lack of temporal modeling integration
Compound disturbances	• Feedback from fire-flood-thaw cascades is rarely addressed jointly (Wohl et al., 2017; Cossart et al., 2013).	• Fragmented disciplinary approaches
Strategic research direction		
Monitoring infrastructure	• Few cold-region basins are instrumented for long-term sediment tracking (Owens, 2020; Toone et al., 2014).	• Funding and maintenance challenges
Cross-scalar modeling	• Models are needed to bridge hillslope, reach, and catchment scales under cold dynamics.	• Model resolution and data mismatch
Policy relevance	• Few frameworks link sediment connectivity to river governance and planning.	• Weak integration of science and policy

Empirical limitations stem from a lack of field-based data, particularly during winter and transitional periods. Processes such as ice-jam dynamics, thaw-triggered mass movements, and

post-event remobilization are poorly documented. Longitudinal, multi-seasonal datasets are especially needed to calibrate models under cryospheric influence (Li et al., 2024).

Methodological challenges include the mismatch between available tools, most developed for temperate climates, and the dynamic, threshold-sensitive, and episodic nature of sediment transfer in cold environments. Existing models often lack the ability to represent seasonal feedback or transient connectivity. Addressing this will require new indices and hybrid models that explicitly integrate cryospheric processes and short-term variability.

Conceptual gaps relate to the underrepresentation of system memory, hysteresis, and delayed recovery. These properties are essential for understanding lagged sediment responses and compound effects driven by repeated disturbances (i.e., wildfire-thaw-flood-drought interactions).

Strategically, the field needs a coordinated research agenda that includes: i) establishing instrumented long-term monitoring sites in representative cold-region basins; ii) designing models tailored to cryosphere-ecology interactions; iii) explicitly integrating sediment–ecosystem linkages into connectivity assessment tools; and iv) promoting scenario-based modeling approaches that capture legacy effects and cold-climate-specific variability. Filling these gaps will improve our ability to understand and manage sediment systems in rapidly changing northern landscapes, and to align science with the needs of adaptative, evidence-based river management.

1.7. Conclusion

Understanding sediment connectivity in cold river systems requires moving beyond models developed for temperate or arid landscapes. These northern environments are governed by a complex interplay of cryospheric dynamics, ecological disturbances, human interventions, and geomorphic memory. Their sediment regimes are shaped by thresholds, delays, and feedback that challenge linear or equilibrium-based assumptions. In response, this paper proposed a holistic conceptual model built around four interrelated layers: external drivers, structural attributes, functional processes, and feedback mechanisms. This structure integrates key cold-region dynamics such as freeze-thaw cycles, ecological disturbances, and delayed sediment responses into a unified perspective tailored for northern rivers.

The framework is designed to support both theoretical exploration and applied management. It helps guide scenario-based modeling, risk assessment, and restoration planning under shifting climatic and hydrological regimes. Yet, significant challenges remain, including the lack of empirical data during critical freeze-thaw transitions, the underrepresentation of geomorphic memory in predictive tools, and the need for connectivity metrics adapted to episodic, feedback-rich systems.

Moving forward, advancing sediment connectivity science in cold environments will require long-term monitoring, refined models, and stronger integration of ecological and cryospheric processes. Embracing the complexities is essential for capturing the actual behavior of northern sediment systems and shaping more resilient, adaptative river management in the face of accelerating environmental change.

CHAPTER 2

A novel statistical model for flood prediction in the Eel River watershed, New Brunswick, Canada

Ali Faghfouri[*a], Achraf Hentati[b,c], Guillaume Fortin[d], Daniel Germain[a,e]

[a]*Institute of Environmental Sciences, Université du Québec à Montréal, Québec, Canada.*

https://ca.linkedin.com/in/ali-faghfouri

https://orcid.org/0000-0001-6418-5436

[b]*Département de Génie Civil, Université de Moncton, Moncton, NB E1A 3E9, Canada*

[c]*Higher Institute of Water Sciences and Technologies of Gabes, University of Gabes, Zrig 6072, Tunisia*

https://ca.linkedin.com/in/achraf-hentati-phd-p-eng-40771914?trk=public_profile_browsemap

[d]*Department of History and Geography, Université de Moncton, New Brunswick, Canada.*

https://ca.linkedin.com/in/guillaume-fortin-94134b197/en

[e]*Department of Geography, Université du Québec à Montréal, Québec, Canada.*

https://ca.linkedin.com/in/daniel-germain-66022445

E-mails: faghfouri.ali@courrier.uqam.ca ; achraf.hentati@umoncton.ca;

guillaume.fortin@umoncton.ca ; germain.daniel@uqam.ca

[*]Corresponding author: Institute of Environmental Sciences, Université du Québec à Montréal, C.P. 8888, succursale Centre-ville, Montréal, Québec, Canada H3C 3P8

This paper was published in Water Science. (Faghfouri, A., Hentati, A., Fortin, G., & Germain, D. (2023). A novel statistical model for flood prediction in the Eel River watershed, New Brunswick, Canada. *Water Science*, 37(1), 251–268. https://doi.org/10.1080/23570008.2023.2243693)

Résumé :
Une forte corrélation entre les effets du changement climatique et l'augmentation de la fréquence ainsi que de l'ampleur des inondations a été rapportée au Canada. Par conséquent, il est essentiel d'examiner les effets des futurs scénarios de changement climatique sur les conditions d'inondation. L'objectif principal de cette recherche est de mieux comprendre les effets destructeurs des crues dans des conditions climatiques historiques et futures pour un petit bassin versant (bassin de la rivière Eel) au Nouveau-Brunswick (NB), dans l'Est du Canada. Un modèle pratique a été développé à l'aide d'un Réseau de Neurones Artificiels (RNA) modifié dans MATLAB par les auteurs de cette étude. L'architecture et la structure des données du RNA sont caractérisées par une rétropropagation utilisant la méthode de Levenberg-Marquardt. Les précipitations quotidiennes totales observées, les températures maximales et minimales quotidiennes de l'air, les débits journaliers pour la période 1967-1983, ainsi que les températures maximales et minimales mensuelles simulées et les précipitations mensuelles totales pour la période 1996-2099 issues du CanESM2, le modèle canadien du système terrestre de deuxième génération (CGCM), ont été utilisés comme données d'entrée du modèle. Les trajectoires représentatives des concentrations (RCP 4.5 et 8.5), en tant que scénarios de changement climatique appropriés, ont été retenues conformément aux recommandations du Groupe d'experts intergouvernemental sur l'évolution du climat (GIEC) pour les études d'inondation. Les valeurs quotidiennes de température, de précipitations et de débit ont été converties en valeurs mensuelles moyennes pour améliorer la précision des prédictions. De plus, deux séries de débits observés ont été préparées en utilisant le débit moyen mensuel (Qavg) et le débit journalier maximum (Qd) comme cibles du modèle. Pour une analyse plus précise, les périodes 1996-2012 (historique) et 2022-2038, 2039-2055, 2056-2072, 2073-2089 et 2083-2099 (futures) ont été considérées, chacune d'une durée de 16 ans. Les résultats du RNA ont permis de prédire les débits journaliers maximums (Qd) et moyens (Qavg) sous l'impact des scénarios climatiques. Dans le cadre du modèle développé, une Analyse de Fréquence des Crues (AFC) a été réalisée en utilisant les lois de valeurs extrêmes généralisées (GEV) et lognormale à trois paramètres (LN3) basées sur les débits prédits et observés. Les performances de l'AFC et du RNA ont été évaluées respectivement par les tests d'Anderson-Darling (AD) et du Khi carré (CS), ainsi que par le coefficient de corrélation (R) et l'erreur quadratique moyenne (MSE). En conclusion, les trois périodes critiques présentant les valeurs les plus élevées de débits prédits sont 2022-2038, 2056-2072 et 2073-2089 pour le scénario RCP 4.5, et 2039-2055, 2073-2089 et 2083-2099 pour le scénario RCP 8.5. De plus, selon l'AFC, les valeurs de récurrence des crues pour une période de retour de 100 ans augmenteront fortement durant les périodes critiques 2056-2072 (RCP 4.5) et 2039-2055 (RCP 8.5). Les résultats indiquent que le bassin de la rivière Eel sera confronté à des inondations sévères, avec une augmentation d'environ 50 % du débit moyen, en particulier au cours des périodes critiques. Enfin, la fréquence des crues présente une tendance croissante due aux effets du changement climatique durant ces périodes.

Mots-clés : RNA, prévision des crues, changement climatique, CGCM, Nouveau-Brunswick

Abstract:

A strong correlation between the effect of climate change and the increase in flooding frequency and magnitude has been reported in Canada. Consequently, there is a crucial need to examine the effects of future climate change scenarios on flooding conditions. The main objective of this research is to better understand the destructive effects of flood events under historical and future climate change conditions for a small watershed (Eel River watershed) in New Brunswick (NB), Eastern Canada. A practical model had been developed using the modified Artificial Neural Network (ANN) in MATLAB by the authors of this study. The architecture and data structure of ANN is characterized by a back propagation with the Levenberg-Marquardt method. The observed daily total precipitation, daily maximum and minimum air temperatures, daily discharge for the period 1967 to 1983, the simulated monthly maximum and minimum air temperatures, and monthly total precipitation for the period of 1996-2099 from the CanESM2, the second-generation Canadian Earth System Model (CGCM), were used as input of the model. The Representative Concentration Pathway (RCP 4.5 and 8.5), as suitable climate change scenarios, were selected based on the Intergovernmental Panel on Climate Change (IPCC) recommendations for flood studies. Daily values of temperatures, precipitations, and discharges were converted to monthly mean values for better prediction of the output results. In addition, two series of observed discharges were prepared using mean monthly (Qavg) and daily maximum discharges (Qd) as the Target of the model. For more accurate analysis, the time frames of 1996-2012 (for the historical) and 2022-2038, 2039-2055, 2056-2072, 2073-2089, and 2083-2099 (for the future) were considered with a duration of 16 years for each time frame. The output results of ANN were predicted daily maximum (Qd) and mean (Qavg) discharges under the impact of climate change scenarios. As a part of the developed model, Flood Frequency Analysis (FFA) was undertaken using the generalized extreme value (GEV) and the three-parameter lognormal (LN3) distributions based on the predicted and observed discharges. The performance of FFA and ANN were demonstrated using the Anderson-Darling (AD), the Chi-square (CS) tests and coefficient of correlation (R) and mean squared error (MSE) respectively. In conclusion, the three most critical time frames with the highest values of predicted discharges were 2022-2038, 2056-2072, and 2073-2089 for RCP4.5 and 2039-2055, 2073-2089, and 2083-2099 for RCP8.5. Also, based on the FFA the magnitudes of flood recurrence for the future time period of 100 years will dramatically increase according to the most critical time frames of 2056-2072 and 2039-2055 for RCP 4.5 and 8.5 respectively. Findings indicated that the Eel River watershed will encounter severe floods, and about a 50% increase in mean discharge, especially for the critical time frames. Finally, flood occurrences show increasing trends due to climate change effects in the most critical time frames.

Keywords: ANN; Flood prediction; Climate change; CGCM; New Brunswick

2.1 Introduction:

Floods in the context of global change can cause some major problems in relation to environmental disturbances such as urbanization, agriculture, deforestation, and so on (Alifu et al., 2022; Arnell and Gosling, 2016; Kundzewicz et al., 2013). Flooding has always been a pervasive natural hazard in Canada due to many rivers, lakes, bodies of water, climatic conditions, and the presence of communities in floodplains (Burn and Whitfield, 2016; Public Safety Canada, 2013). In addition, major disastrous floods that occurred in some Canadian provinces such as British Columbia, Newfoundland, and Nova Scotia in 2021 show the importance of this phenomenon. Indeed, according to the Canadian Disaster Database of the Public Safety Canada, more than 300 flood disasters have been recorded for the period 1902 to 2014, showing, on the one hand, the recurrence of the meteorological and hydrological triggering conditions and, on the other hand, the exposure and vulnerability of the population. In eastern Canada, the configuration of the river system and the climatic conditions - cold winter with significant snow cover - create favourable conditions for flooding related to snowmelt, in addition to the ice-jam formation (Rokaya et al., 2018; Gerard and Davar, 1995). Disaster statistics emerged to show flood occurrences are becoming more common in the context of NB, with medium-scale events increasing fastest due to severe changes in weather patterns and climate. For example, the springs of 2017 to 2019 were especially disastrous and costly because of the seriousness of the floods (Lin et al., 2019; Brogan et al., 2020; Henry et al., 2020). There are different reasons for the occurrence of floods in NB. In this province, inland flooding can occur with rapid snowmelt and heavy rainfall (Burrell et al., 2015) in addition to the water buildup behind an ice jam. In NB, due to some warm periods in wintertime, favourable to moderate ice-jam problems, flooding has dangerous effects due to the rapid melt of snow (Baronetti et al., 2019). In other months of the year, abundant rainfall during primary storms can cause flooding, especially in smaller rivers. Moreover, coastal flooding can be triggered by storm surges or high tides (Lindenschmidt et al., 2018; Mallet et al., 2018). Furthermore, the land near an area of delta or brackish water can be at a certain risk of flooding due to high water levels caused by high marine tides, storm surges and river flows that can act separately or in combination (Buttle et al., 2016).

Climate change can induce local variability in the amount, duration, frequency, and distribution of precipitations which causes a change in flooding regimes (Gaur et al., 2018; Mladjic et al., 2011). In the summertime, warming of the Atlantic Ocean related to global warming impacts the Atlantic provinces such as NB by producing more hurricanes or stronger ones. Hurricanes eventually diminish in intensity as they make landfall and become post-tropical storms that bring intense rainfall and damaging winds causing major flooding to the southern part of the province of NB. Also, due to the complex system of storm-flooding, prediction and tracking of these events might become more difficult (Collins et al., 2014). Climate change could also alter the hydrologic cycle and its components (physical parameters) so this study will be helpful to improve the knowledge of how flood patterns could be affected by climate change in NB for the future time frame. Coastal flooding is expected to increase in many parts of the province (e.g., the Eel River watershed) because of rising sea levels. Environmental changes need to be integrated not only at local sea levels but also into the global sea-level rise and local land uplift or subsidence. Local sea level is predicted to rise and increase flooding, in most parts of the Atlantic, and Pacific coasts of Canada and the Beaufort coast in the Arctic, where the land is subsiding or slowly uplifting. The loss of

sea ice in Atlantic Canada and the Arctic further increases the risk of damage to coastal infrastructures and ecosystems due to the larger storm surges and waves (Bush and Lemmen, 2019; McGrath et al., 2015) and the absence of an ice foot on the coast. This issue must be considered for analysing floods in NB because most of the large rivers (e.g. the Eel River) that end their course in the Atlantic Ocean or the Gulf of St. Lawrence are tidally influenced.

It is crucial to consider flooding problems including frequency and magnitude in NB with selecting an important watershed (in terms of water supply, biodiversity, agriculture, recreation, and sustainable development) such as the Eel River watershed that has the various mentioned involved parameters of flood occurrences within NB in connection to the newer version of the Canadian climate change model (4th generation) and atmospheric conditions to fill the gaps in previous studies. Previous studies mainly focused on the older version of the climate change model, the 3rd generation or the Coupled Global Climate Model (CGCM3), with a limited selection of scenarios to investigate flood issues (El-Jabi et al., 2013, 2016). The aim of this research is to understand the effects of climate change on the Eel River watershed, one typical small watershed with all the critical parameters that are important for flood studies in the province, using the modified ANN which linked the Flood Frequency Analysis (FFA) for the historical data and the future climate projection of the 4th generation of CGCM3 which is equal to the second generation Canadian Earth System Model (CanEsm2) using two Representative Concentration Pathways scenarios (RCP 8.5 and 4.5) for the future time frame 2022-2099.

2.2 Selected study area characteristics:

The Eel River watershed was selected as a study area due to the vulnerability of this important watershed towards various flood occurrences in NB based on Figure 1.1 The Eel River watershed is located in the range of Appalachian Mountain and is part of the Gulf of St. Lawrence drainage basin. The Eel River watershed is approximately 220 km^2 and 24 km long. The drainage area of the Eel River station near Eel River Crossing is equal to 88.6 km^2. Furthermore, the percentage of lakes and swamps in this watershed is 68 %. The Eel River itself is a main watercourse in the watershed with a length of around 135 km from its headwaters to its confluence with the Restigouche River and empties into the “Chaleur” Bay. The watershed can be considered rural, with a population of about 1953 (Statistic Canada, 2017), mainly concentrated in the Eel River crossing area near the mouth of the river. The Eel River crossing village has an area of 22.79 km^2 and is built on a plain bordered by the Appalachians except to the east, where the “Chaleur” Bay extends. Mount Dalhousie to the north, 160 meters high, is the highest point closest to the village. In addition, the Eel River crossing area is considered a Designated Watershed Protected Area (DWPR) by the Government of New Brunswick as a portion of the local population obtains their drinking water from this section of the river. Maritime Climate, with characteristics of high precipitation level and humidity, affects the Eel River watershed which brings mild summers and relatively mild winters. According to Koppen's climate classification (1930), the whole province of NB is defined as a humid continental climate (Dfb). However, according to Fortin and Dubreuil (2020), who produced a map of the different types of climates at the province scale, the study area is of East Coast type. For this climate type, the average temperature of the coldest month (January) is 0°C, while the average temperature of the hottest month (July) is 10.1°C, based on the reference

period of 1981 to 2010. This climate type's average annual precipitation is 1114 mm. The study area receives nearly 30% of its yearly precipitation as snow, and snow accumulation on the ground peaks at about 60.5 cm in February (Baronetti et al., 2019). Generally, during the melt period in March and April, the risk of flooding is most significant in the province.

The geology of the Eel River watershed which is formed in the southwestern Miramichi terrane of NB includes a calc-alkaline suite of volcanic rocks that are interlayered with intervals of polylith fragmental rocks in addition to the sedimentary rocks and are overlain by a thick sedimentary sequence (McClenaghan et al., 2006).

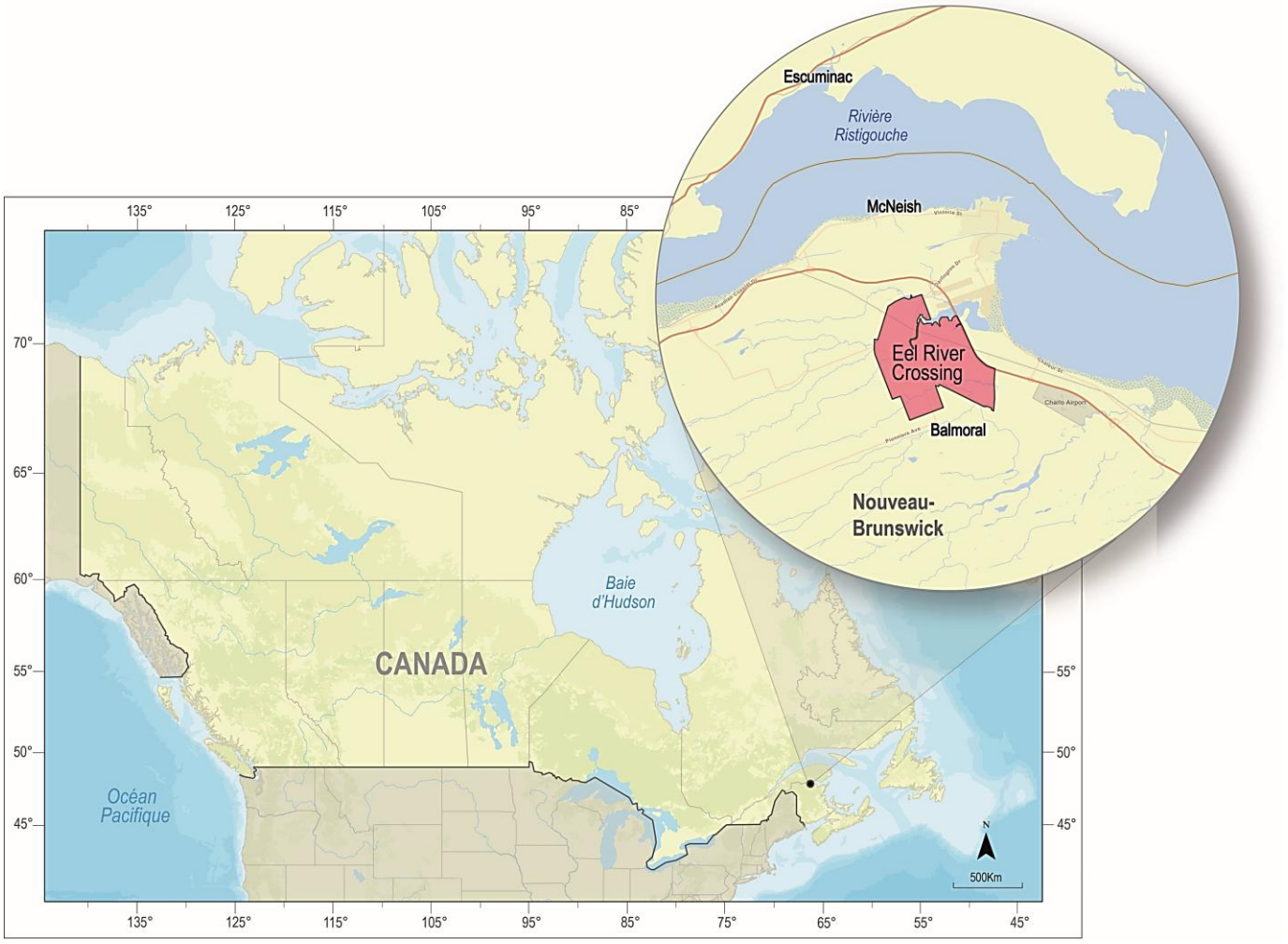

Figure 2.1. Case study area.

The Eel River watershed land use is divided into 89% forest, 6% cropland, and 5% urban development. Most of the territory has forests, old farmland, and wetlands and the altitude in the Eel River crossing village does not exceed twenty meters. It is unlikely that this insignificant land use and land cover has a major impact on the hydrological response of the watershed (Statistic

Canada, 2023; Laplante and Simard, 2013). Figure 2.2 shows the most recent land use map of the Eel River watershed.

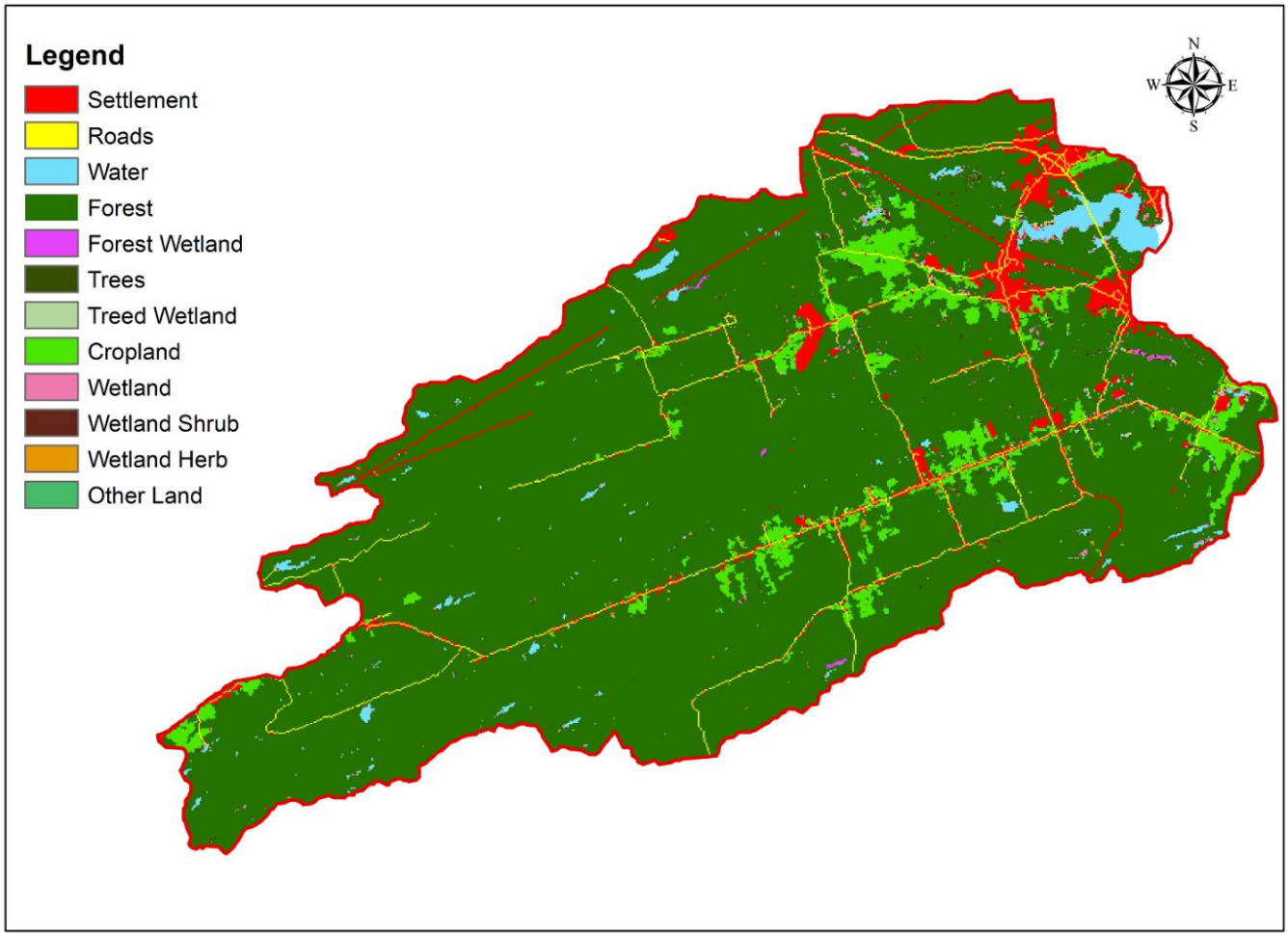

Figure 2.2 The most recent land use map of the Eel River watershed.

2.3 Materials and methods:

2.3.1 Data preparation:

Total precipitation and daily maximum and minimum air temperatures for the recorded period 1967 to 1983 as the observed data from Charlo A station in Eel River Watershed were obtained from Environment Canada's National Climate Data Archive, daily observed discharge (Qobs, m^3/s) data from 01BJ004 hydrological station was obtained as an observed data from Environment Canada's National Water Data Archive. Simulated monthly maximum and minimum air temperatures and total precipitation for the whole period of 1996-2099, in which 1996 to 2021 was defined as historical data and 2022 to 2099 defined as future data, were obtained from Canadian Centre for Climate Modelling and Analysis (CCCma) for simulated CanESM2/ RCP4.5 and 8.5 scenarios climate change model. The main reason for choosing RCP4.5 and 8.5 is that based on the IPCC report, RCP4.5 and 8.5 are described as intermediate and high emission scenarios that are appropriate for evaluating the future effects of climate change on flood events. In RCP4.5, the

emissions peak will occur around 2040, then they will decline. Moreover, RCP 4.5 needs carbon dioxide (CO_2) emissions to start decreasing by 2045 to reach approximately half of the levels of 2050 by 2100. RCP4.5 is more likely than not to result in a global temperature rise between 2 °C, and 3 °C, by 2100 with a mean sea level rise 35% higher than that of RCP 2.6. Many animal and plant species will be unable to adjust to the effects of RCP4.5 and higher RCPs in the near future (Thomson et al., 2011). RCP8.5 is regarded as the highest baseline emissions among RCPs and by the year 2100, this scenario predicts a 4.5 to 6 °C temperature increase (Riahi et al., 2011).

The developed database for analysis was checked in terms of data quality to find out if there is any missing data within a time series or not. There is no missing data reported within an entire database. It is important to note that daily values of temperatures, and precipitation, are converted to monthly mean values. In addition, two series of observed discharges were prepared using mean monthly (Qavg) and daily maximum discharges (Qd) to obtain better results. The daily maximum discharge is the highest selected value of the discharge for each month. For the analysis, the time frames of 1996-2012 (for the historical) and 2022-2038, 2039-2055, 2056-2072, 2073-2089, and 2083-2099 (for the future) were considered with a duration of 16 years for each time frame. The reason for choosing 16 years interval for each time frame is to cover the whole observed discharge data for the analysis.

It is recommended to use downscaled climate change data due to the scale accuracy reasons for ANN simulations. The aim of using downscaling climate models is to fill the gap between the effects of global and local by layering local-level data over larger-scale climate models. The downscaled models are mainly related to small areas, down to 25 km^2, and have higher resolution than that represented by global climate model simulations (Diffenbaugh and Ashfaq., 2010). The process of downscaling was done using Delta-change approach (Keller et al., 2022; Camici et al., 2014; Hay et al., 2000). Changes in mean climate are applied as follows as a simple modification in downscaling approach:

$$Tnew = Tobs + Tdelta \quad (1)$$

$$p_{new} = p_{obs} * p_{Fact} \quad (2)$$

Tdelta is the difference between the climate change model's (CGM) simulated mean temperature (projected in the future) and the historical mean temperature. *Pfact* is the ratio of the CGM simulated mean precipitation in the future time relative to the historical mean precipitation.

2.3.2 Model structure:

A novel model for the prediction of Qd and Qavg under historical and climate change conditions using ANN with consideration of FFA was proposed. Figure 2.3 represents schematically the structure of the model which was developed and utilized in this study. There are three major stages in this model, namely: I) single station FFA; II) ANN simulation for prediction of discharges based on observed and climate change data and; III) finally FFA based on predicted Qd and Qavg which was obtained from ANN simulations.

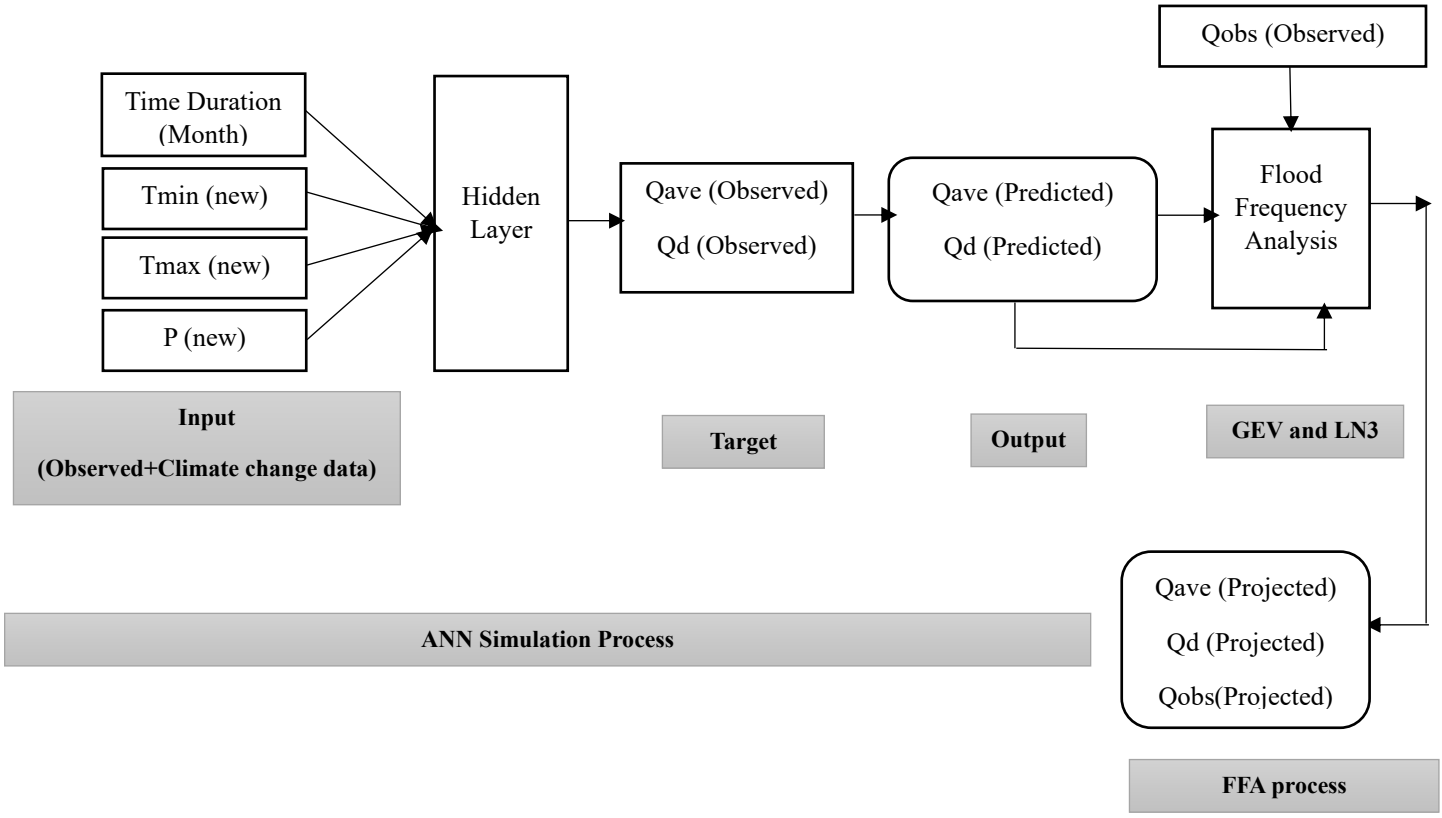

Figure 2.3. Flowchart of the developed model.

In Figure 2.1, Tmin (new), Tmax (new), and P (new) are modified monthly minimum, and maximum temperatures, and precipitation, respectively. The simulation process was done using ANN for data prediction. The observed (Qobs) and predicted discharges (Qd and Qavg) were evaluated using the generalized extreme value (GEV) and three-parameter lognormal (LN3) as common approaches in FFA (Saf, 2009).

The foundation of the ANN used in this research is characterized by a learning algorithm that is backpropagation with the Levenberg-Marquardt method. Seventy percent (70%) of the data was used as training data, and thirty percent (30%) of the data was used as testing data. A hidden layer of 8 to 12 neurons was utilized. Figure 2.4 shows the structure of ANN used in this study.

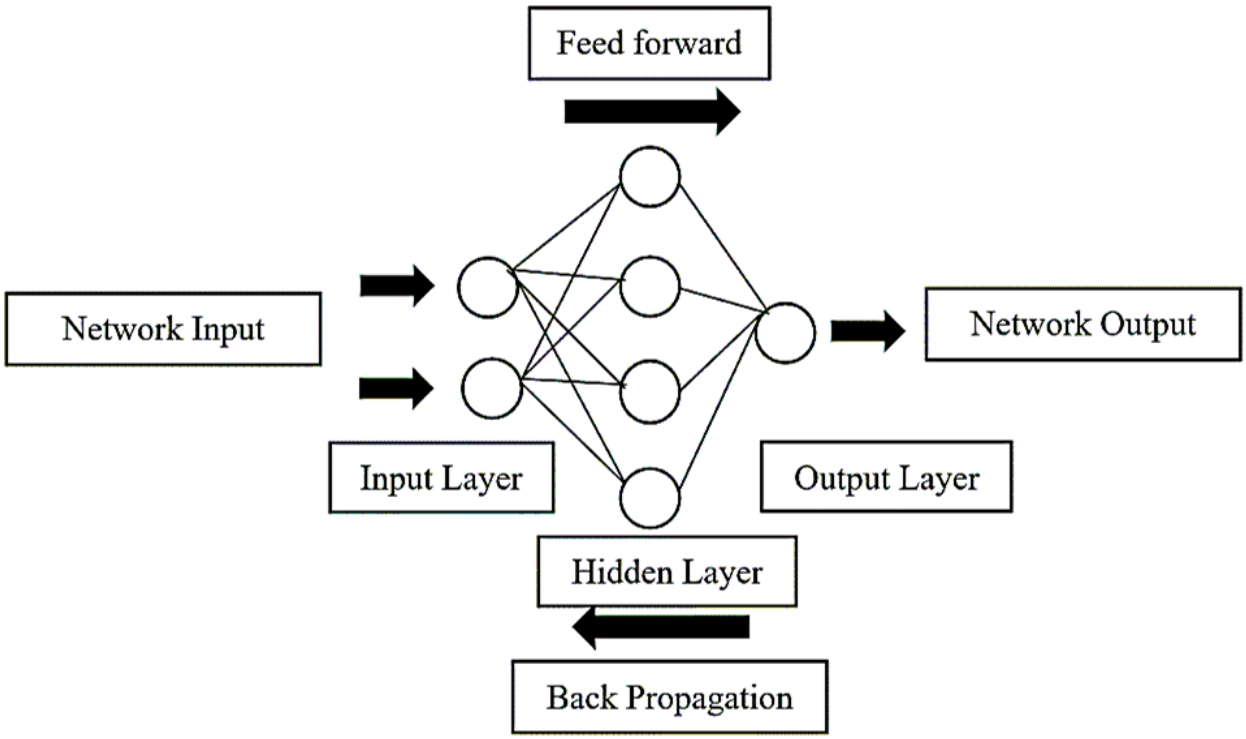

Figure 2.4. Structure of ANN used in this research.

2.3.3 Probability distributions:

There are numerous probability distributions (PD) used in hydrological sciences. Many different studies were carried out to understand which PD represents the best fitting for FFA. A number of PDs were proposed such as Gumbel, Normal, Lognormal, GEV, Weibull, LN3, and Gamma (Pearson type 3) in the FFA (Khosravi et al., 2012; Ndetei et al., 2007). For selecting an appropriate flood frequency model, several important steps should be undertaken such as an in-depth analysis of historical data, investigation of the flood magnitude using the event-descriptive variable, assessment of the acceptability among the 'distribution type' and the 'flood sample' to conduct a selection process. Finding the best fit probability and the calculation of its parameter were proposed as a crucial step (Bobee et al., 1993; Serinaldi et al., 2018). In this research, a comparison of two commonly acceptable PDs was conducted. GEV and LN3 were adopted due to their high performance and accuracy in the analysis of the statistical characteristics of the observed and predicted flood data of the Eel River watershed.

2.3.4 L-Moments Method:

The L-Moments method, previously developed based on mathematical statistics, improves the calculation process in frequency analysis studies (Stedinger and Lu, 1995). This approach, which was developed by Hosking (1990), has been widely used by hydrologists in flood-related studies. Hosking and Wallis (1997) concluded that L-moments were an alternative system of explaining the shapes of PDs. The L-moments are based on the probability-weighted moments (PWMs) of Greenwood et al.'s (1979) study. The L-Moments method has more accuracy compared to older frequency methods. Hosking (1990) indicated that the advantage of L-moment ratios in comparison

to product-moment ratios (PMR) is that the former is stronger in the presence of extreme values and does not have sample size-related bounds. In addition, L-moments and L-moment ratios are more efficient than PWMs because they are more representative measures of distribution scale and shape (Hosking, 1994).

GEV and LN3 were regarded as highly accepted and accurate PDs for FFA of various regions in Canada (Zhang et al., 2020; Faulkner et al., 2016). The reasons for choosing LN3 over other mentioned methods in NB are the feasibility of the LN3 for expressing severe flood events for gauging sites, and its accurate performance for evaluation of flood events (Aucoin et al., 2011; Environment Canada and New Brunswick Department of Municipal Affairs and Environment, 1987). GEV with consideration of its theoretical properties is a suitable distribution for describing flood events. Moreover, according to the theory of extreme value that explains annual daily discharge maxima as a part of extreme events distribution, GEV can accurately link up a probability concerning a distribution (Coles, 2001). In addition, GEV is the best-fitted PD for the evaluation of extreme hydrological events in Canada based on Zhang et al., 2020 research which acquired 227 Hydrometric Basin Network (RHBN) stations, the sub-set of Canadian hydrometric gauging stations, for the estimation of parameters using linear moments. Furthermore, LN3 and GEV distributions were far better choices among other approaches for flood forecasting and the best distributions for regional FFA for the selected study areas in Canada (Yue and Wang, 2004).

2.3.4.1-Generalized extreme value distribution (GEV): Based on Robson and Reed (1999), the GEV distribution has the following cumulative density function (CDF):

$$F(x) = exp\{-[1-\frac{k(x-\mu)^{1/k}}{\alpha}]\}\ k \neq 0 \quad (3)$$

$$F(x) = exp[-\exp(-\frac{x-\mu}{\alpha})] \quad k = 0 \quad (4)$$

Where μ, α, and k are the location, scale, and shape parameters, respectively. For $k > 0$ ($k < 0$) the variable x is upper (lower) bounded to $\mu + {\alpha}/{k}$. For $k > 0$ the variable x is unbounded.

2.3.4.2 Three parameters lognormal (LN3):

For a random variable *x*, if *y=ln(x-a)* has a normal distribution then *x* will have a lognormal distribution whose probability density function (PDF) can be developed as (Singh, 1998):

$$F(x) = \frac{1}{(x-a)c\sqrt{2\pi}} exp[\frac{-[\ln(x-a)-b]^2}{2c^2}] \quad (5)$$

where *a* is a positive quantity defined as a lower boundary, and *b* and c^2 are the form and scale parameters of the distribution. It occurs that *b* and c^2 are respectively equal to the mean ($\bar{y}$) and variance s_y^2 of *ln(x-a)*. Thus, the LN3 distribution has three parameters: *a*, *b*, and *c*. *(x-a)* represent a shifted variable. The standardized variable *u* is obtained in the usual order:

$$u = \frac{ln(x-a)-b}{c} \quad (6)$$

The CDF of the LN3 distribution can be rewritten as:

$$F(x) = \int_a^x \frac{1}{(x-a)c\sqrt{2\pi}} exp[\frac{-[\ln(x-a)-b]^2}{2c^2}\ dx \quad (7)$$

It is not possible to describe the LN3 distribution in terms of *x* using the *F* as a function because of the integral nature of the above equation.

2.3.5 FFA statistical tests:

2.3.5.1 Goodness-of-fit (GOF) tests

The goodness-of-fit (GOF) tests are commonly used to test that the observed data follow a particular distribution as a calibration process. The Anderson–Darling (AD) and Chi-square (CS) tests were selected for the statistical analysis of FFA. These tests are often used in FFA and have shown good performance in the case of small sample sizes and heavy-tailed distributions (Farooq et al., 2018; Laio, 2004; Önöz and Bayazit, 1995).

The AD test consists of the lists of critical values for GOF statistics which were calculated for various significance levels (alpha), as well as the acceptance of the null hypothesis for each of the level values. The AD statistic measures how well the data follows a particular distribution. For a specified data set and distribution, the better the distribution fits the data, the smaller this statistic will be. AD may also be considered as a "relative" measure of the GOF between different distributions (Predicted vs Observed data) for FFA.

The statistic test (A^2) for AD is defined as:

$$A^2 = -n - S \quad (8)$$

$$\text{Where } S = \sum_{i=1}^{n} \frac{(2i-1)}{n}\left[logF(yi) + log\left(1 - F(y_{n+1-i})\right)\right] \quad (9)$$

In equation 9, *n* is sample size and $F(y_i)$ represents the CDF of the specified distribution.

A CS test, also written as the $\chi 2$ test, is a statistical hypothesis test that is valid to perform when the statistic test is Chi-squared distributed under the null hypothesis. In general, smaller p-values are desirable according to this test. The smaller the p-value, the more certainty there is that the null hypothesis can be rejected. A very small p-value would indicate with a great deal of significance that the data distribution testing does not follow a standard normal distribution (null hypothesis).

The statistic test (x^2) for CS is defined as:

$$x^2 = \sum_{i=1}^{k} \frac{(o_i - E_i)}{Ei} \quad (10)$$

$$\text{Where } E_i = n\left(F(u) - F(y_l)\right) \quad (11)$$

In above equation, n is sample size and *F* is CDF with two variations for upper limit ($F(u)$) and lower limit ($F(y_l)$) for the class *i*.

2.4 Results:

The results of this study are presented in three phases: I) Single FFA without consideration of climate change effects; II) ANN simulation based on historical/ future climate data and; III) FFA using calculated Qd and Qavg derived from phase II.

The results of the single FFA based on the comparison of GEV and LN3 distributions with observed data which is derived from the 01BJ004 hydrological station is according to Figure 2.5.

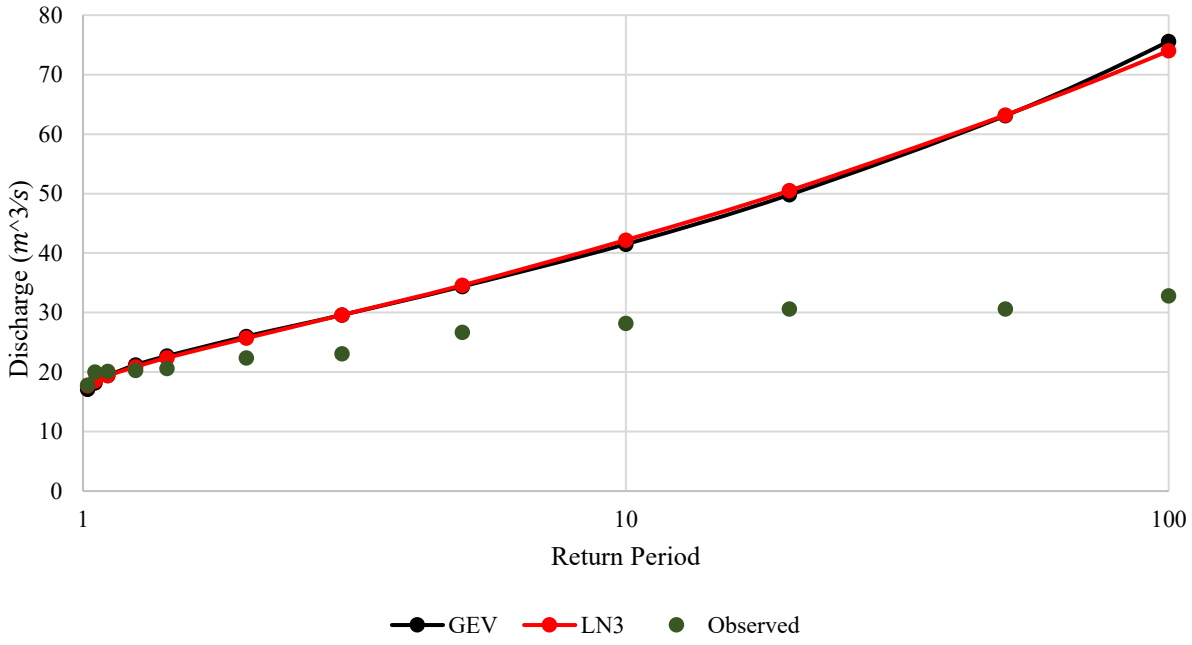

Figure 2.5. Single flood frequency analysis (FFA) using observed data (Qobs).

The ANN model simulated (Qd) and (Qavg) for 2022 to 2099 with selected time frames of 2022-2038, 2039-2055, 2056-2072, 2073-2089, and 2083-2099 compared to Qobs values while using modified input data (precipitation and temperatures). The three most critical time frames in terms of discharge's magnitude were selected for RCP4.5 (2022-2038, 2056-2072, 2073-2089) and RCP8.5 (2039-2055, 2073-2089, 2088-2099). Figure 2.6 presents the result of the simulated Qa and Qavg compared to Qobs for mentioned time frames. This figure shows the designed ANN model has the acceptable performance and the predicted data can accurately adapt to the behavior of observed data.

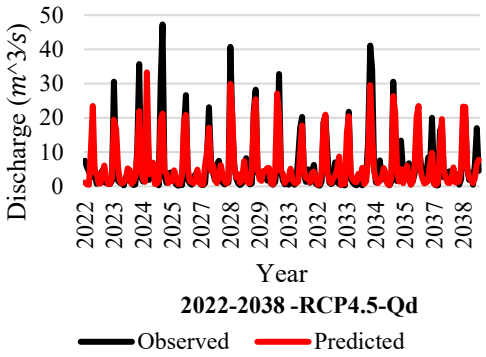
Discharge (m^3/s)
50
40
30
20
10
0
2022 2023 2024 2025 2027 2028 2029 2033 2032 2033 2034 2035 2037 2038
Year
2022-2038 -RCP4.5-Qd
Observed
Predicted

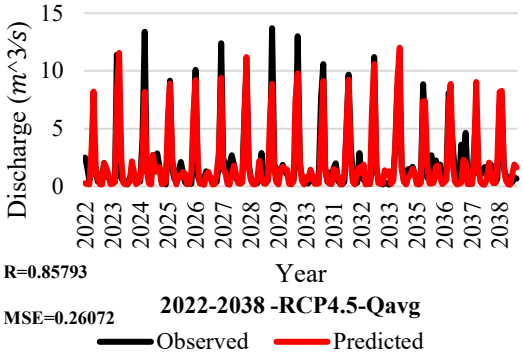
Discharge (m^3/s)
15
10
5
0
2022 2023 2024 2025 2026 2027 2028 2029 2033 2031 2032 2033 2035 2036 2037 2038
R=0.85793
Year
MSE=0.26072
2022-2038 -RCP4.5-Qavg
Observed
Predicted

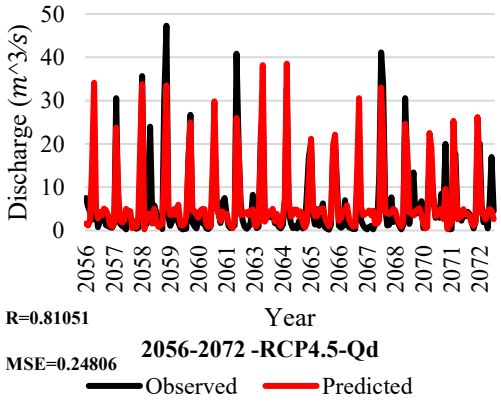
Discharge (m^3/s)
50
40
30
20
10
0
2056 2057 2058 2059 2060 2061 2063 2064 2065 2066 2067 2068 2070 2071 2072
R=0.81051
Year
MSE=0.24806
2056-2072 -RCP4.5-Qd
Observed
Predicted

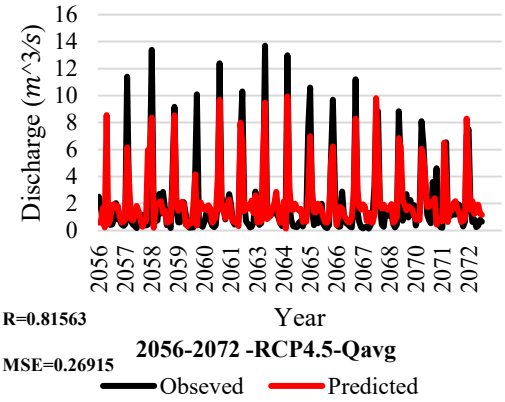
Discharge (m^3/s)
16
14
12
10
8
6
4
2
0
2056 2057 2058 2059 2060 2061 2063 2064 2065 2066 2067 2068 2070 2071 2072
R=0.81563
Year
MSE=0.26915
2056-2072 -RCP4.5-Qavg
Obseved
Predicted

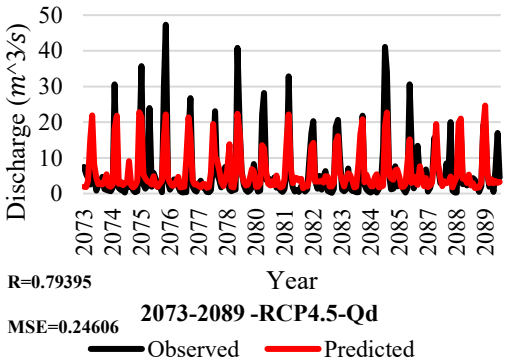
Discharge (m^3/s)
50
40
30
20
10
0
2073 2074 2075 2076 2077 2078 2080 2081 2082 2083 2084 2085 2087 2088 2089
R=0.79395
Year
MSE=0.24606
2073-2089 -RCP4.5-Qd
Observed
Predicted

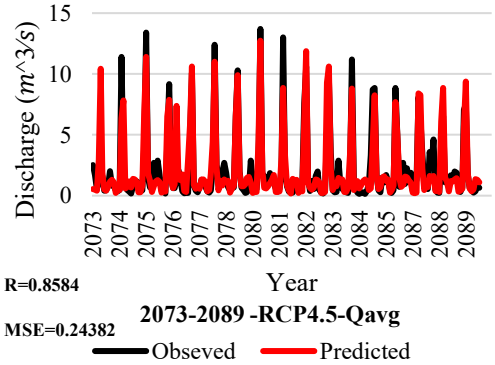
Discharge (m^3/s)
15
10
5
0
2073 2074 2075 2076 2077 2078 2080 2081 2082 2083 2084 2085 2087 2088 2089
R=0.8584
Year
MSE=0.24382
2073-2089 -RCP4.5-Qavg
Obseved
Predicted

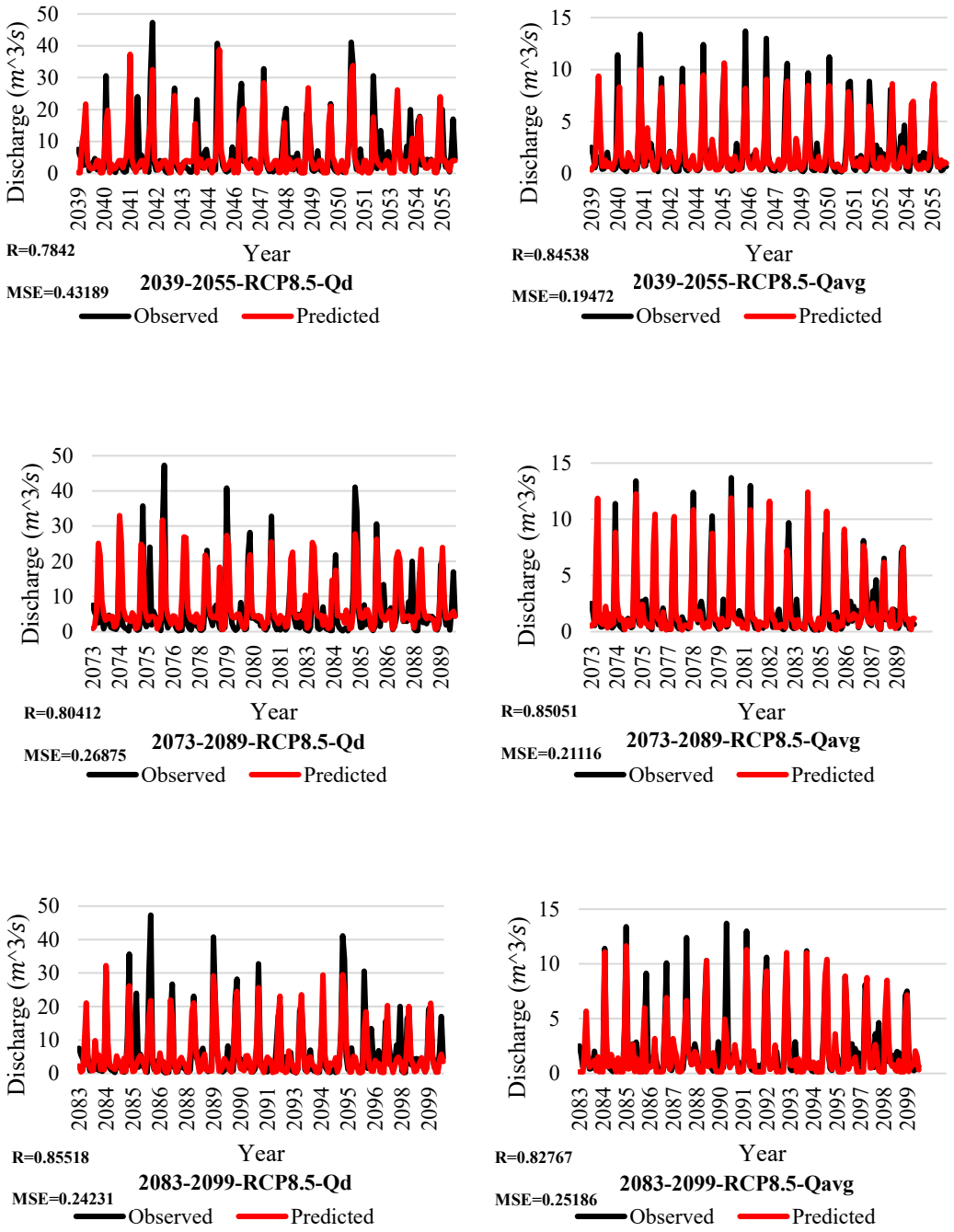

Figure 2.6. Comparison of observed and ANN predicted (Qd and Qavg) discharges based on the RCP4.5 and RCP8.5 for the critical time frames.

The ANN model simulated Qd and Qavg for the duration of 2022 to 2099 while using modified input data (precipitation and temperatures). Figure 2.7 introduces the results for the predicted Qd and Qavg for the RCP4.5 and 8.5 scenarios.

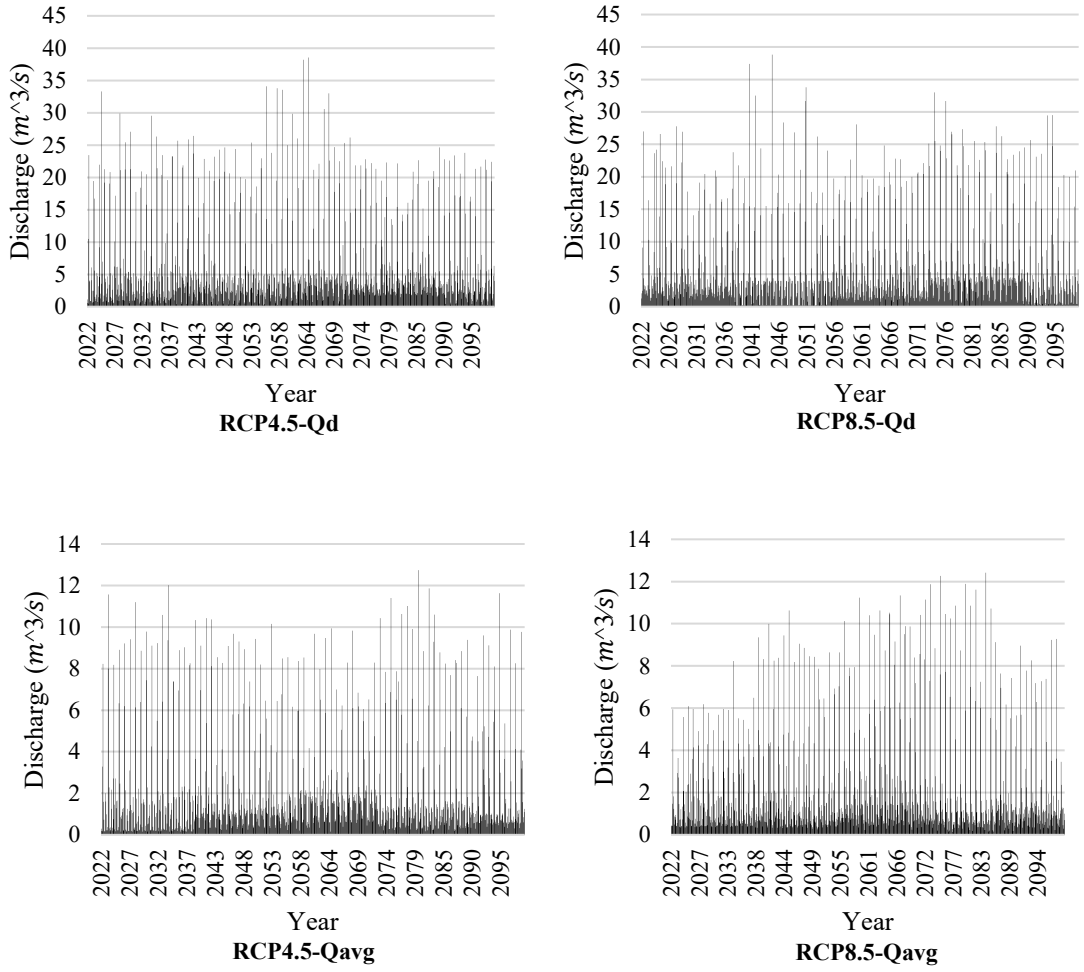

Figure 2.7. The total predicted discharges (Qd and Qavg) under the effects of RCP4.5 and 8.5 scenarios for the period of 2022-2099.

The results of FFA using GEV and LN3 for the most critical time frames based on the ANN-simulated Qd and Qavg, are illustrated in Figure 2.8.

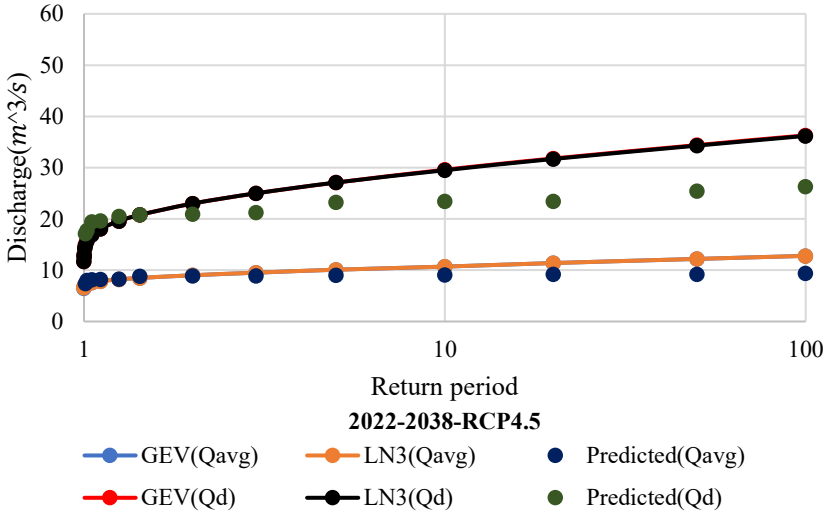
60
50
40
30
20
10
0
Discharge(m^3/s)
1
10
100
Return period
2022-2038-RCP4.5
GEV(Qavg)
LN3(Qavg)
Predicted(Qavg)
GEV(Qd)
LN3(Qd)
Predicted(Qd)

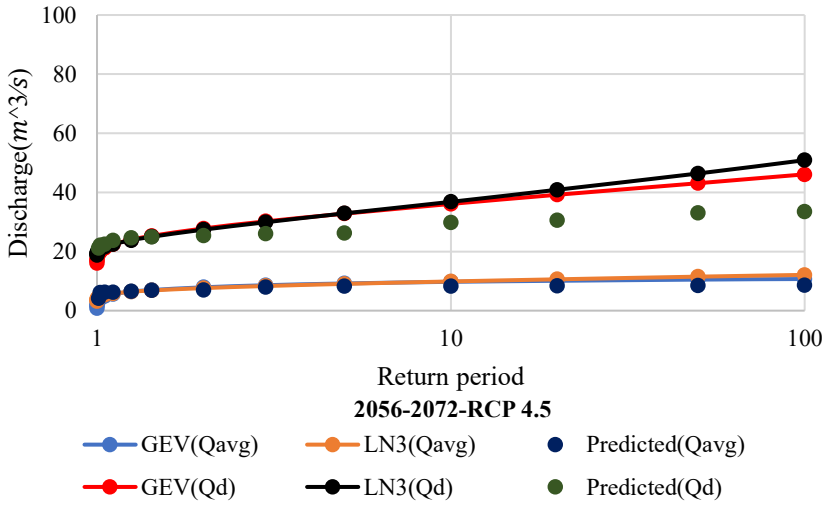
100
80
60
40
20
0
Discharge(m^3/s)
1
10
100
Return period
2056-2072-RCP 4.5
GEV(Qavg)
LN3(Qavg)
Predicted(Qavg)
GEV(Qd)
LN3(Qd)
Predicted(Qd)

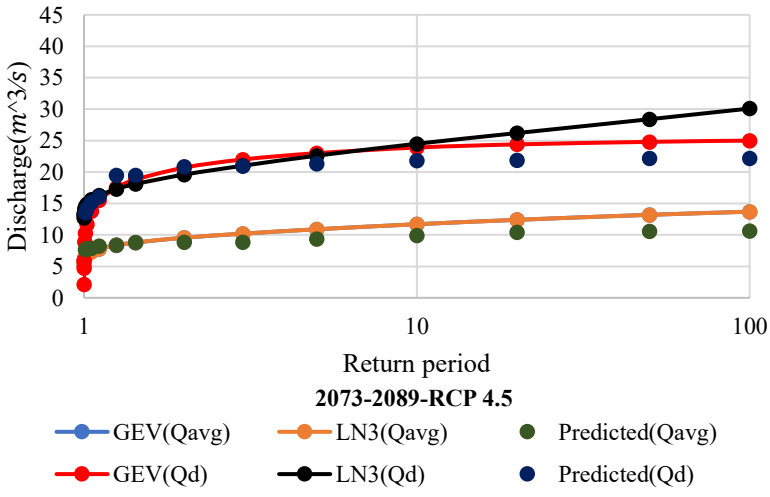
45
40
35
30
25
20
15
10
5
0
Discharge(m^3/s)
1
10
100
Return period
2073-2089-RCP 4.5
GEV(Qavg)
LN3(Qavg)
Predicted(Qavg)
GEV(Qd)
LN3(Qd)
Predicted(Qd)

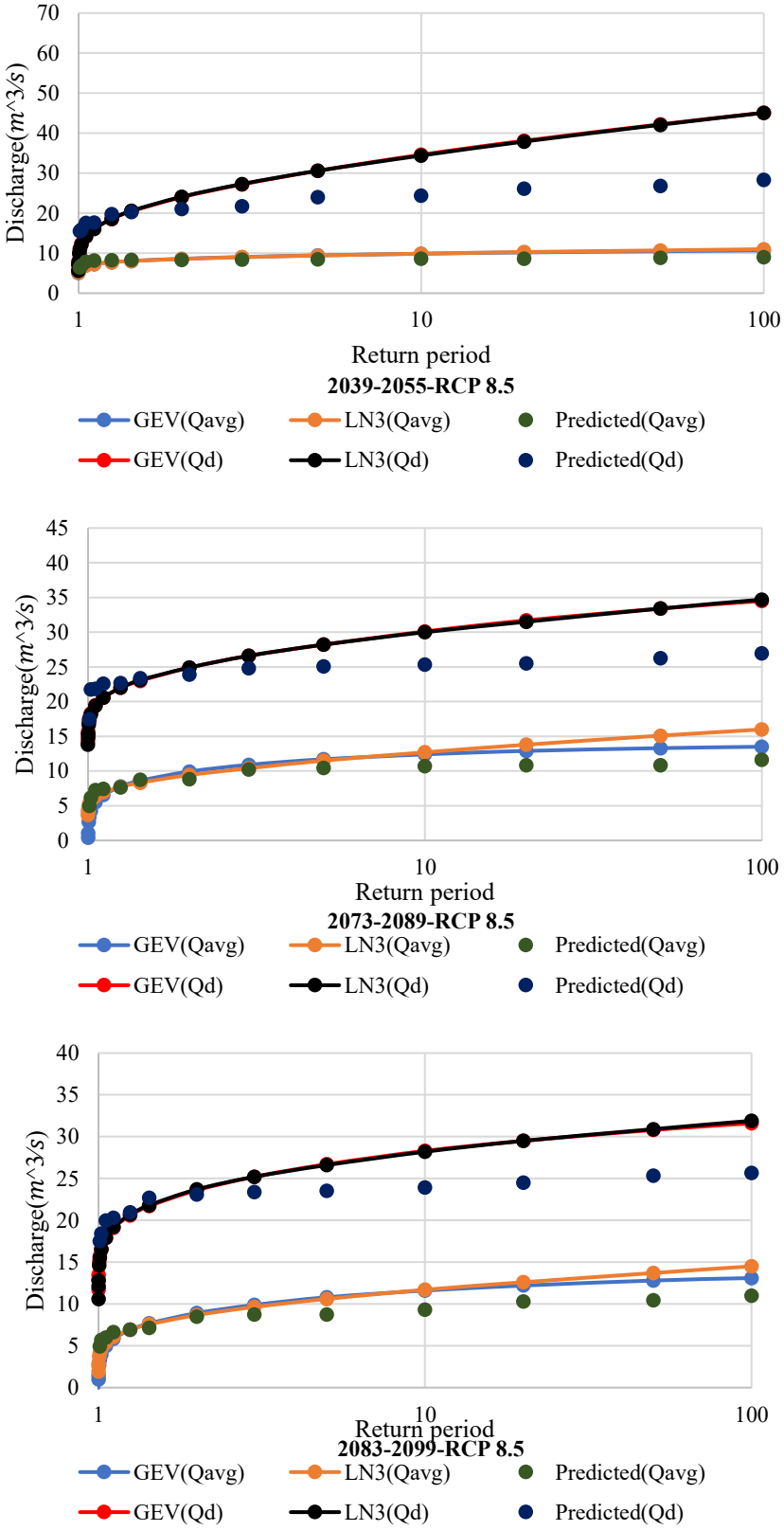

Figure 2.8. Future FFA based on the predicted discharges (Qd and Qavg) under the effects of RCP4.5 and 8.5 scenarios for the critical time frames.

Statistical results of ANN simulations for the most critical time frames according to the coefficient of correlation (R) and mean squared error (MSE) are presented in Figures 2.9 for RCP4.5 and 8.5 respectively. All values of R and MSE for the 'testing', 'training', 'validation', and 'total' stages were proposed. The closer the R-value to 1 the better the correlation. For MSE, the closer values to zero mean better performance of the model.

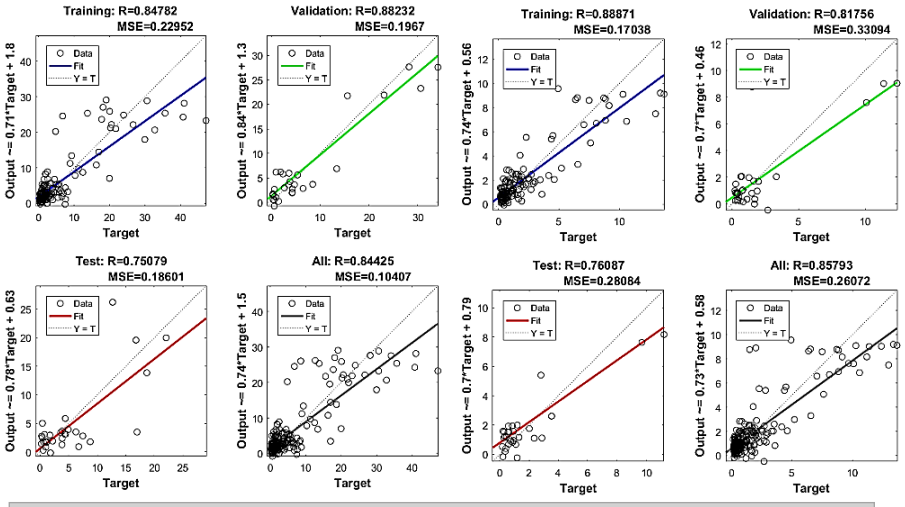

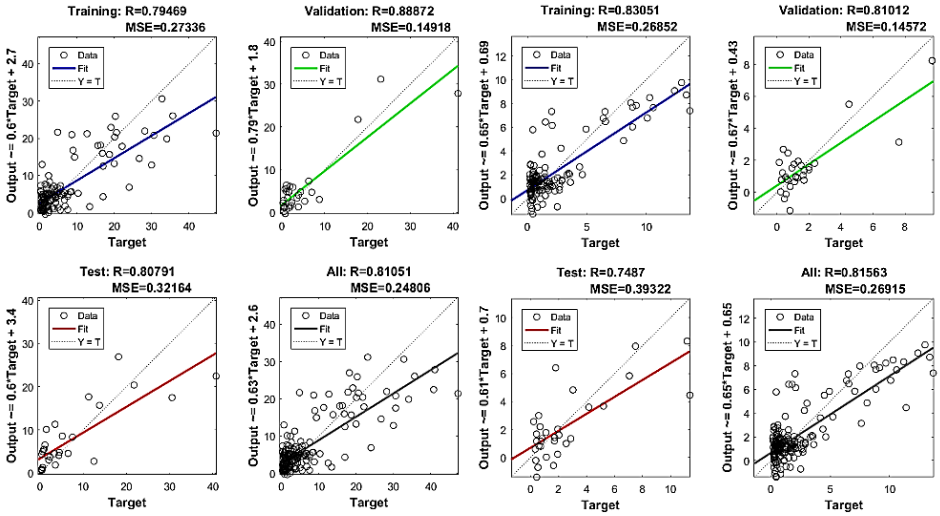

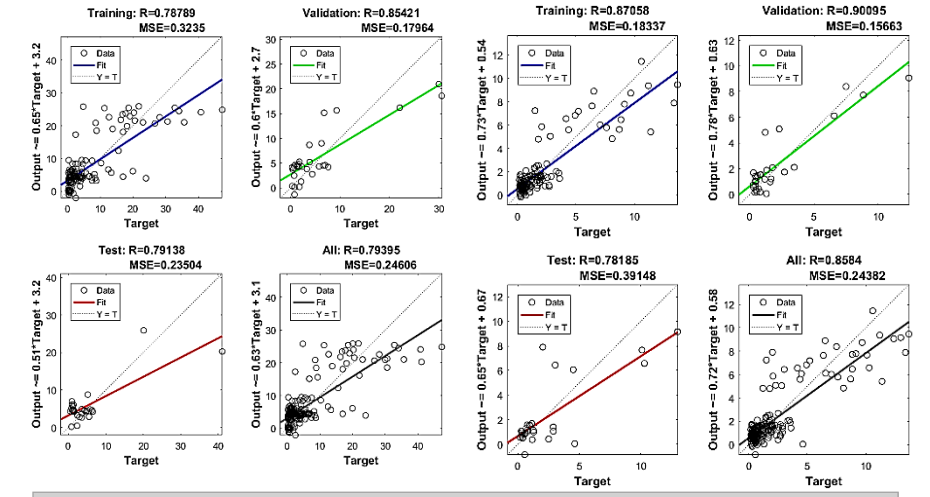

(Qd) 2073-2089-RCP4.5 (Qavg)

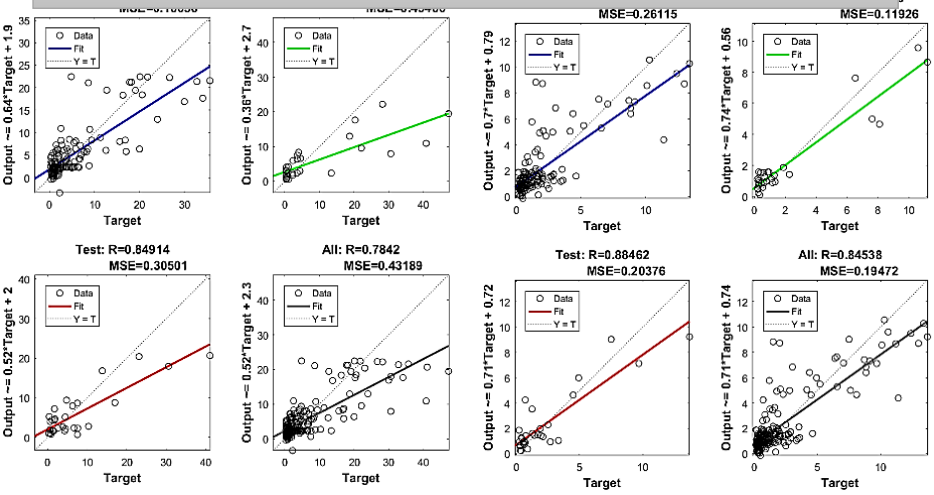

(Qd) 2039-2055-RCP8.5 (Qavg)

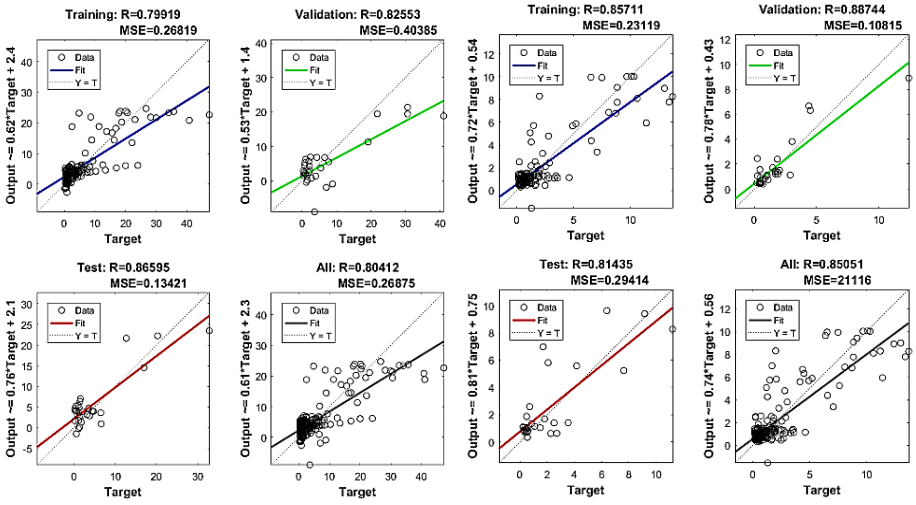

(Qd) 2073-2089-RCP8.5 (Qavg)

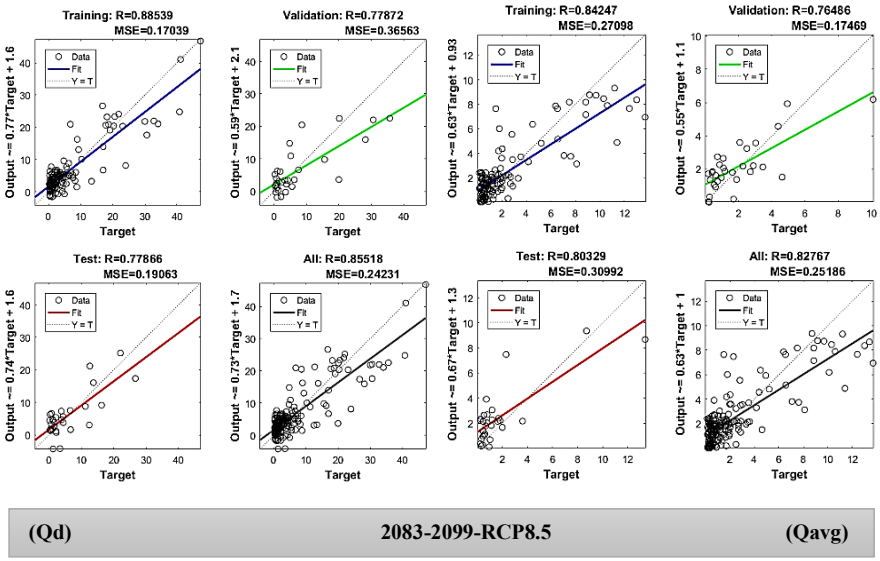

Figure 2.9. Statistical results of ANN simulations for the predicted discharges (Qd and Qavg) based on the RCP4.5 and RCP8.5 for the critical time frames.

The statistical results of the AD for single and the future FFA are presented in Tables 2.1 and 2.2:

Table 2.1 AD results for GEV distribution.

Name	Statistics
Single FFA	$A^2 = 0.64467$
2022-2038-4.5-Daily	$A^2 = 0.2458$
2056-2072-4.5-Daily	$A^2 = 0.41285$
2073-2089-4.5-Daily	$A^2 = 0.55827$
2022-2038-8.5-Daily	$A^2 = 0.44686$
2056-2072-8.5-Daily	$A^2 = 0.27379$
2073-2089-8.5-Daily	$A^2 = 0.36612$
2039-2055-4.5-Monthly	$A^2 = 0.4458$
2073-2089-4.5-Monthly	$A^2 = 0.38496$
2083-2099-4.5-Monthly	$A^2 = 0.37233$
2039-2055-8.5-Monthly	$A^2 = 0.44686$
2073-2089-8.5-Monthly	$A^2 = 0.60433$
2083-2099-8.5-Monthly	$A^2 = 0.5554$

Table 2.2. AD results for LN3 distribution.

Name	Statistics
Single FFA	$A^2 = 0.81673$
2022-2038-4.5-Daily	$A^2 = 0.18814$
2056-2072-4.5-Daily	$A^2 = 0.21285$
2073-2089-4.5-Daily	$A^2 = 0.35827$
2022-2038-8.5-Daily	$A^2 = 0.4047$
2056-2072-8.5-Daily	$A^2 = 0.26445$
2073-2089-8.5-Daily	$A^2 = 0.28819$
2039-2055-4.5-Monthly	$A^2 = 0.2458$
2073-2089-4.5-Monthly	$A^2 = 0.37249$
2083-2099-4.5-Monthly	$A^2 = 0.36041$
2039-2055-8.5-Monthly	$A^2 = 0.42063$
2073-2089-8.5-Monthly	$A^2 = 0.30433$
2083-2099-8.5-Monthly	$A^2 = 0.1554$

The statistical results of the CS for single and the future FFA are presented in Tables 2.3 and 2.4:

Table 2.3 CS results for GEV distribution.

Name	Statistics	P-value
Single FFA	$X^2 = = 5.75$	0.0464
2022-2038-4.5-Daily	$X^2 = 3.12$	0.0543
2056-2072-4.5-Daily	$X^2 = 2.41$	0.0594
2073-2089-4.5-Daily	$X^2 = 8.06$	0.0178
2022-2038-8.5-Daily	$X^2 = 1.71$	0.0562
2056-2072-8.5-Daily	$X^2 = 3.54$	0.0504

2073-2089-8.5-Daily	$X^2 = 2.89$	0.0594
2039-2055-4.5-Monthly	$X^2 = 2.41$	0.0573
2073-2089-4.5-Monthly	$X^2 = 4.53$	0.0512
2083-2099-4.5-Monthly	$X^2 = 3.82$	0.0578
2039-2055-8.5-Monthly	$X^2 = 5.96$	0.0565
2073-2089-8.5-Monthly	$X^2 = 5.65$	0.0530
2083-2099-8.5-Monthly	$X^2 = 1.71$	0.0562

Table 2.4 CS results for LN3 distribution.

Name	Statistics	P-value
Single FFA	$X^2 = 2.75$	0.0528
2022-2038-4.5-Daily	$X^2 = 4.12$	0.0504
2056-2072-4.5-Daily	$X^2 = 3.45$	0.0394
2073-2089-4.5-Daily	$X^2 = 14.41$	0.0007
2022-2038-8.5-Daily	$X^2 = 3.82$	0.0578
2056-2072-8.5-Daily	$X^2 = 4.71$	0.0562
2073-2089-8.5-Daily	$X^2 = 5.82$	0.0578
2039-2055-4.5-Monthly	$X^2 = 3.71$	0.0562
2073-2089-4.5-Monthly	$X^2 = 5.53$	0.0539
2083-2099-4.5-Monthly	$X^2 = 4.41$	0.0594
2039-2055-8.5-Monthly	$X^2 = 6.64$	0.0530
2073-2089-8.5-Monthly	$X^2 = 6.24$	0.0330
2083-2099-8.5-Monthly	$X^2 = 3.82$	0.0278

2.5 Discussion:

The results of the study were obtained in three definitive phases. First, the results of a single FFA for the 01BJ004 hydrological station in the Eel River watershed using GEV and LN3 approaches were obtained. The aim of utilizing a single FFA is to predict the discharge for the future time (100 years) without consideration of climate change effects. Based on Figure 2.5, and Tables 2.1 to 2.4, it is observed that GEV is a better fitting method for the prediction of discharge due to the smaller values of A^2 and P-value based on the AD and CS tests respectively.

For the prediction of Qd and Qavg using ANN with modified input data under the influence of RCP4.5 and 8.5 scenarios, the future period 2022 -2099 was considered. For obtaining better results, the future period was divided into 5 intervals of 2022-2038, 2039-2055, 2056-2072, 2073-2089, and 2083-2099. The reason for choosing 16 years of duration for each interval is the better adaptability and comparison with available Qobs. Based on the obtained results from the simulation process, the three most critical time frames with the highest values of predicted discharges were selected for RCP4.5 (2022-2038, 2056-2072, 2073-2089) and RCP8.5 (2039-2055, 2073-2089, 2083-2099). It is concluded that the developed novel model can accurately predict Qd and Qavg for RCP4.5 and 8.5 based on the comparison of predicted versus observed data and the acceptable statistical results in Figure 2.6. It is worth mentioning that ANN results based on Figure 2.6 miss the highest peaks in some years and there is a shift in time in some instances due to the preprogrammed selection of training data by the model, the complexity in the architecture design of ANN, and the importance of hyperparameters in the design phase of ANN, such as learning rate and regularization strength. Moreover, according to Figure 2.9, it is observed that R and MSE have acceptable values, the more the R and MSE values are respectively closer to 1 and 0 the better the performance of the model, for the ('training', 'validation', 'test', and 'total') sections. This derived fact shows that the developed model is working very well for the prediction of future Qd and Qavg by means of the accurate correlation between predicted and observed data.

The predicted Qd and Qavg with consideration of the RCP4.5 and 8.5 scenarios using ANN for the entire future period including the most critical time frames represented in Figure 2.7. The model simulation results show the higher values of Qd in comparison to Qavg for the two scenarios. The main reason for the differences between the two series of predicted discharges is a selection of observed discharge data for the Target section of the ANN model. The observed Qd has higher values in comparison to the observed Qavg. The predicted Qd has the highest values between 2054 to 2068 for RCP4.5 while the highest values for RCP8.5 were predicted between 2041 to 2051. For the predicted Qavg, the highest values occurred between 2023 to 2035 and 2078 to 2099 for RCP4.5 while RCP8.5 has the highest values between 2039 to 2055 and 2065 to 2084.

FFA based on the predicted Qd and Qavg, which was obtained by ANN simulation, was done using the GEV and LN3 approaches according to Figure 2.8. This figure compared the output data of FFA based on the predicted Qd and Qavg in two series (RCP 4.5 and 8.5) for the most critical time frames. According to this figure, the highest projected discharges were recorded in two critical time frames of 2056-2072 and 2039-2055 for RCP 4.5 and 8.5 respectively. Furthermore, the FFA based on the Qd has higher values of projected discharges in comparison to the FFA according to the Qavg due to the higher values of the predicted Qd for each critical time frame. Moreover, for

critical time frames of 2056-2072 and 2073-2089 based on the Qd of RCP4.5, LN3 has a better performance in comparison to GEV. On the other hand, for the critical time frames of 2073-2089 and 2083-2099, according to the Qavg of RCP8.5, LN3 has better performance compared to GEV.

LN3 is a better fitting approach for the future FFA related to the critical time frames of 2056-2072 and 2073-2089 for the predicted Qd of RCP4.5 and 2073-2089 and 2083-2099 for the predicted Qavg of RCP8.5 based on the statistical results from Table 2.1 to 2.4 which were derived according to the CS and AD tests. For the mentioned time frames, P-values LN3 are less than GEV according to Tables 2.1 and 2.2 of the CS test, and statistics (A^2) LN3 are less than GEV based on Tables 2.3 and 2.4 of the AD test, so it shows that LN3 is a better fitting approach than GEV. For other time frames, the statistical results were in acceptable ranges of fitting (P-values$\leq$ 0.05 of the CS test and equal statistics of the AD test), and no significant differences were observed between the performance of GEV and LN3.

2.6 Conclusion:

Climate change will undoubtedly alter flood problems in the Eel River watershed according to the obtained results from Figures 2.5 to 2.8. The success of industries (e.g., agriculture, forestry, recreational fisheries, and others) intrinsically linked to the climate conditions, are making NB watersheds such as the Eel River watershed particularly vulnerable to flooding occurrences. Other factors, such as changes in land cover and land use, are also likely to modify flows in the watershed. Shuster et al. (2005) mentioned that the land used development strongly correlates with the population growth proportion. This tends to increase the ratio of the impervious catchment surfaces, translating into faster surface runoff and, therefore, faster and more intense peak flooding. Such conditions would then be conducive to flooding. However, recent data for the region indicate a decrease (-5.6% by Statistic Canada, 2023) in population between 2016 and 2021, and very few developments occur during the same period in the Eel River watershed. Although development remains a possibility, nothing currently suggests this scenario. Recently, de Souza Cruz (2021) carried out a study to simulate flooding by considering changes in future climate (RCP 4.5 and RCP8.5) in combination with changes in land use in a Riverview neighborhood located southeast of the NB. Based on this research, it is concluded that the most significant change (76% increase in flood discharge) would occur in the case of intensive development (clearcutting of an urban woodlot) and the RCP8.5 scenario over a 2100 horizon. It should be noted that, according to the results of this study, climate change plays a less significant role. In contrast, land surface modification plays a much more critical role in modifying the hydrological regime and as an explanatory source of simulated future flooding. In the case of the Eel River watershed, the expected changes will be mainly caused by climate, as little development is expected in this devitalized region (Laplante and Simard, 2013).

The ANN model was effective in predicting the different flow components (Figures 2.6, and 2.7) using historical and future climate data. In addition, according to the statistical analysis (Figure 2.9), all the simulation steps were done accurately, and the output results had acceptable precision (Figure 2.6). According to the obtained results from the ANN simulation process, the three most critical time frames with the highest values of predicted discharges were 2022-2038, 2056-2072, and 2073-2089 for RCP4.5 and 2039-2055, 2073-2089, and 2083-2099 for RCP8.5. Moreover, it

is concluded that based on the FFA the magnitudes of flood recurrence for the future time period of 100 years will dramatically increase based on the most critical time frames. The most significant increase will occur in 2056-2072 and 2039-2055 for RCP 4.5 and 8.5 respectively (Figure 2.8), which means floods with bigger discharge magnitudes will hit the Eel River watershed due to the climate change effects.

The reliability of the results is so crucial for decision-makers and government sectors. In this regard, these results (Predicted discharge from ANN and projected discharges from the single and FFA) appear very significant for decision-makers and government in order to cope with the potentially disastrous effects of climate change on flood magnitudes, especially during the critical time frames in the Eel River watershed. The analyses showed that the Eel River watershed will be impacted by severe floods by comparison of projected verse predicted discharges with about a 50% increase in Qd and Qavg for each critical time frame based on Figure 2.8. The upward trend of increase in discharges is one of the indications of climate change effects on future flood occurrence in this watershed.

Understanding the nature and potential consequences of climate change at a regional scale in an ungauged context, remains a challenge. So, future studies are needed to take into consideration the ungauged contexts under climate change issues to produce regional equations that suit the NB context. In addition, land use and land cover changes might also affect flooding, but it is difficult at this time to extrapolate future development or any exogenous disturbances in this watershed. Moreover, the main limitation of using ANN is the fixed number of input layers within an architecture of the model that causes taking fixed input and output for any operation. So, for many pattern recognition tasks, this is a limiting constraint. In order to improve the performance of the ANN model in terms of the detection of the highest peaks for all years and satisfy the issue of shifting in time, firstly it is recommended to increase the diversity selection of the samples in the training dataset, especially those that represent extreme events and variations in the highest peaks, to give the ANN a better basis for learning and generalization. Secondly, to capture the complexity of the forecast more accurately, the model architecture can be modified. This can involve investigating various network topologies, deepening the network, or adding extra layers or nodes to help the model learn more complex patterns. Thirdly, by modifying parameters like learning rate, regularization strength, or batch size within a model architecture, the ability of the ANN model to effectively capture the highest peaks can be increased.

Declaration of interest statement

The authors declare no conflict of interest.

Data availability statement.

The database used in this study is available upon reasonable request by the corresponding author.

CHAPTER 3

Seven Decades of River Change: Sediment Dynamics in the Diable River, Quebec

Ali Faghfouri 1, Daniel Germain*,2 and Guillaume Fortin 3

[1] Institute of Environmental Sciences, University of Quebec at Montreal, Montreal, Canada; faghfouri.ali@courrier.uqam.ca

[2] Department of Geography, University of Quebec at Montreal, Montreal, Canada; germain.daniel@uqam.ca https://orcid.org/0000-0003-4757-3124

[3] Department of History and Geography, University of Moncton, New Brunswick, Canada; guillaume.fortin@umoncton.ca

* Correspondence: germain.daniel@uqam.ca

This paper is published in Geosciences. (https://www.mdpi.com/journal/geosciences) Faghfouri, A.; Germain, D.; Fortin, G. Seven Decades of River Change: Sediment Dynamics in the Diable River, Quebec. Geosciences 2025, 15, 388. https://doi.org/10.3390/geosciences15100388

Résumé

Cette étude reconstruit sept décennies (1949-2019) de changements morphodynamiques et de dynamiques sédimentaires de la rivière du Diable (Québec, Canada) à partir de neuf séries de photographies aériennes, d'un Modèle Numérique d'Élévation LiDAR à haute résolution (2021) et d'analyses granulométriques. Les objectifs étaient de documenter l'évolution fluviale à long terme, de quantifier l'érosion et la déposition, et d'évaluer la connectivité sédimentaire entre les falaises sableuses érodées et les zones de dépôt. L'analyse en planimétrie et les bilans sédimentaires dérivés des modèles de différences (DoD) révèlent une trajectoire oscillatoire, caractérisée par des phases alternées d'exportation sédimentaire et de stabilisation temporaire, plutôt qu'une simple tendance de dégradation ou d'aggradation. L'intervalle le plus dynamique (1980–2001) a été marqué par une migration généralisée des méandres et le plus grand export net (-142,5 m^3/km/an), tandis que la période 2001-2007 a montré un stockage net (+70,8 m^3/km/an) et une reprise géomorphologique à court terme. Les crues récentes (2017, 2019 ; périodes de retour de 20 à 50 ans) ont induit des pertes sédimentaires localisées mais persistantes, soulignant le rôle structurant des événements extrêmes. Les résultats granulométriques indiquent une connectivité partielle : les fractions grossières tendent à rester dans des formes de dépôt locales, tandis que les sédiments fins sont préférentiellement exportés vers l'aval. Ces résultats mettent en évidence la valeur géomorphologique des pièges sédimentaires temporaires (barres, plages) et soulignent la nécessité de stratégies de gestion adaptative des rivières intégrant les bilans sédimentaires et les savoirs locaux dans la gouvernance des plaines inondables.

Mots-clés : géomorphologie fluviale, bilan sédimentaire, connectivité sédimentaire, rivières tempérées froides

Abstract:

This study reconstructs seven decades (1949-2019) of morphodynamic changes and sediment dynamics in the Diable River (Québec, Canada) using nine series of aerial photographs, a high-resolution LiDAR Digital Elevation Model (2021), and grain-size analysis. The objectives were to document long-term river evolution, quantify erosion and deposition, and evaluate sediment connectivity between eroding sandy bluffs and depositional zones. Planform analysis and sediment budgets derived from DEMs of Difference (DoD) reveal an oscillatory trajectory characterized by alternating phases of sediment export and temporary stabilization, rather than a simple trend of degradation or aggradation. The most dynamic interval (1980–2001) was marqued by widespread meander migration and the largest net export (-142.5 m^3/km/year), whereas the 2001-2007 showed net storage (+70.8 m^3/km/year) and short-term geomorphic recovery. More recent floods (2017, 2019; 20–50-year return periods) induced localized but persistent sediment loss, underlining the structuring role of extreme events. Grain-size results indicate partial connectivity: coarse fractions tend to remain in local depositional features, while finer sediments are preferentially exported downstream. These findings emphasize the geomorphic value of temporary sediment sinks (bars, beaches) and highlight the need for adaptative river management strategies that integrate sediment budgets and local knowledge into floodplain governance.

Keywords: Fluvial geomorphology; Sediment budget; Sediment connectivity; Cold temperate rivers

3.1. Introduction

Rivers are dynamic systems that evolve continuously through the interplay of natural forces and human activities (Wang et al., 2020; Cienciala 2021). Their morphology responds to various drivers, including climatic shifts, sediment dynamics, hydrological fluctuations, and engineered alterations to flow regimes, all of which influence channel geometry and fluvial structure (Li et al., 2022; Haron et al., 2022). Gaining insight into these transformations is essential for anticipating flood behavior, assessing geomorphic stability, and informing restoration strategies aimed at ecological and social resilience (Gautam et al., 2022; Wohl, 2018; An et al., 2022).

A central concept in this regard is the internal functioning of river systems, which refers to the balance between sediment inputs, outputs, and storage that determines their morphodynamic behavior. A sediment budget provides a quantitative framework to analyze this internal functioning (Reid and Dunne, 2016; Slaymaker 2003), measuring how sediments are mobilized, routed, and retained across spatial and temporal scales (Clifton et al., 2022). Sediment budgets also serve as a diagnostic tool for evaluating morphodynamic responses to both climatic variability and anthropogenic pressure (Piqué et al., 2017; Parsons, 2012). Inputs generally include upstream fluxes, lateral erosion, and hillslope processes; outputs correspond to sediment export to downstream sections or depositional basins; and storage encompasses materials retained within channels, bars, floodplains, and other sediment sinks.

Over the past two decades, innovations in spatial technologies have greatly improved reconstructions of riverine change. Archival maps, aerial photographs, and satellite imagery combined with GIS allow detailed analyses of channel evolution, including bank erosion, channel migration, and planform adjustment (Saleem et al., 2020; Mukherjee et al., 2017; Ety and Rashid, 2020). These methods contribute directly to risk assessments and inform floodplain planning by highlighting patterns of geomorphic instability (Paul and Bhattacharji, 2022). In parallel, high-resolution techniques such as Unmanned Aerial Vehicle (UAV)-based photogrammetry (Borrelli et al., 2019), Light Detection and Ranging (LiDAR)-derived Digital Elevation Models (DEMs) (De Rose and Basher, 2011; Notebaert et al., 2009), and specialized toolkits like RivMAP (Schwenk et al., 2017) and Digital Shoreline Analysis System (DSAS) (Akay et al., 2022) have expanded the capacity to quantify volumetric change, model surface dynamics, and project future adjustments (Koohafkan and Gibson, 2018; Church 2010).

Building on these methodological advancements, this study focuses on the Diable River in southern Québec, Canada, a cold-temperate, sandy-bed stream flowing through a mountainous, protected landscape. Its downstream reach, the only segment crossing agricultural land dominated by pasture and hay production, has been impacted by recent major floods (2017, 2019) yet has never been analyzed through a quantitative sediment budget, reinforcing its relevance as a representative case study. Long-term data on channel evolution remain limited in this system, underscoring the need for a 70-years perspective (1949–2019) combining historical aerial imagery and recent high-resolution LiDAR data (2021). Specifically, this research aims to: 1) reconstruct the river's morphodynamic history across seven decades; 2) quantify spatial patterns and volumes of erosion and deposition; and 3) evaluate sediment connectivity by linking sediment sources (sandy bluffs)

with depositional sinks (beaches), to derive geomorphic implications for adaptive river management.

3.2. Materials and Methods

3.2.1. Study Area Description

The Diable River flows through southern Quebec, Canada, in a region governed by a humid continental climate (Dfb) as defined by the Köppen classification (Peel et al., 2007). The Diable River follows a nivo-pluvial hydrological regime, typical of mid-elevation forested watersheds in southern Québec. Its average annual discharge is approximately 30 m^3/s, but the river experiences severe spring floods driven by rapid snowmelt. During these events, peak flows often exceed 150 m^3/s and can occasionally surpass 200 m^3/s. In contrast, low-flow periods occur in mid-winter (February), when precipitation is locked as snow, and again in late summer (August) due to high evapotranspiration and falling groundwater levels. Precipitation is distributed evenly across the seasons, averaging around 1201 mm annually, while the mean annual temperature hovers near +4.4 °C. Geographically, the river traverses parts of the Lanaudière and Laurentides administrative regions (Figure 3.1), beginning its course at Lac du Diable, a 2.5 km-long lake situated within the territory of Lac-Legendre, in the Matawinie Regional County Municipality. From this headwater, the Diable River flows for about 82 km through varied terrain before joining the Rouge River, draining a catchment of approximately 1,163 km^2 (Figure 3.1).

A significant portion of the river's length runs through Mont-Tremblant National Park. This mountainous protected area encompasses more than 400 lakes, a dense network of tributaries, and six major river systems. In its upper stretches, the Diable meanders through predominantly forested landscapes, where visible signs of channel erosion remain scarce. This stability continues through the central portion of the watershed, including the nearby village sector, where the riverbanks still retain much of their natural structure and show limited evidence of human disturbance.

Conditions change markedly in the lower section of the river, especially just upstream of its confluence with the Rouge River. Here, signs of fluvial erosion and active sediment deposition become more pronounced, reflecting increased lateral channel migration. This downstream segment stands out as the only portion of the Diable watershed that passes through agricultural land, contrasting sharply with the otherwise forest-dominated basin (Figure 3.1). Land use in this corridor is dominated by pasture and hay production, making it distinct from the largely forested upstream and park sections. A diagnostic evaluation conducted more than a decade ago documented erosion-related concerns in this agricultural reach (Gallerand et al., 2015), although it did not provide a quantitative assessment of morphodynamic processes. The specific study area analyzed in this project corresponds to this downstream corridor, a roughly 12 km-long meandering reach identified as the most dynamic portion of the Diable watershed in terms of lateral channel mobility and sediment redistribution (Gallerand et al., 2015). Hydrological records further highlight the significance of recent flood events, with the 2017 flood corresponding to an estimated 20-year recurrence interval, and the 2019 flood approaching a 50-year event. These benchmarks provide valuable reference points for interpreting the morphodynamic changes documented over the 70-year analysis period. However, long-term hydrological data remain scarce for the Diable River. Existing records from nearby rivers are difficult to transpose reliability because of differences in

watershed size, physiography, and regulation effects. For this reason, only the 2009–2025 period could be analyzed in detail, based on the newly established hydrometric station (040238; 46.1141° N, 74.6014° W) located immediately upstream of our study reach.

Understanding the river's geomorphological trajectory required a combination of complementary methods, drawing on historical imagery, quantitative sediment analysis, and high-resolution elevation data. Each component provided a distinct lens on channel changes and sediment dynamics.

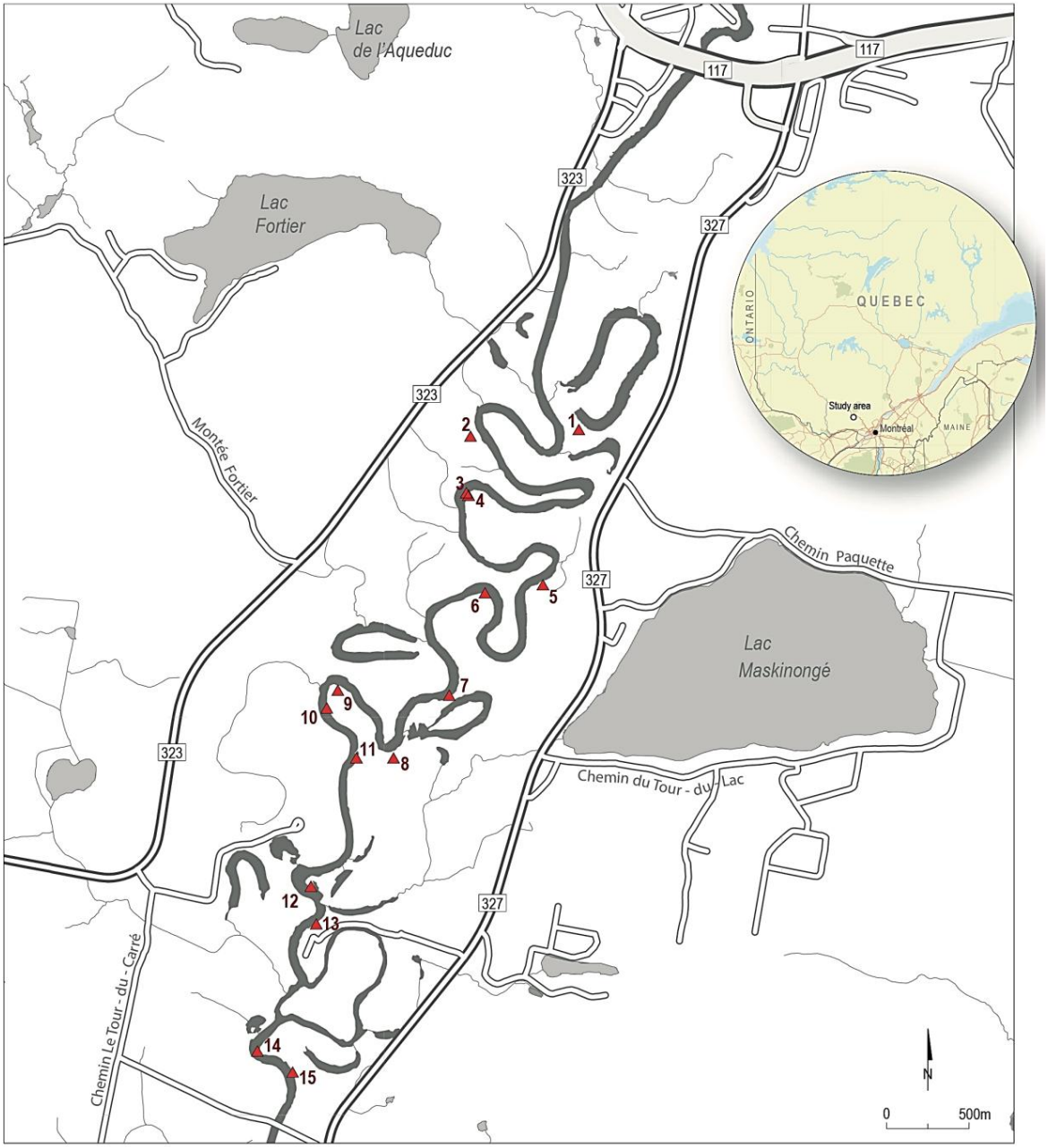

Figure 3.1. Location map of the study reach along the Diable River, south of Mount Tremblant (Laurentians, Québec, Canada). The mapped segment represents the agricultural corridor characterized by high lateral

mobility and active meander migration. Red triangles indicate 15 sampling sites used for grain-size analyses, corresponding to paired erosion sources (sandy bluffs) and depositional zones (beaches). The inset shows the position of the study area within the Province of Québec. The river flows from north to south, i.e., from the top to the bottom of the image.

3.2.2. Planform analysis of historical channel changes (2D)

To reconstruct the morphological evolution of the Diable River (1949–2019), we compiled nine series of aerial photographs from UQAM's physical archives and Geoindex database, complemented by a LiDAR DEM (2021, 1 m resolution) from the Ministry of Transportation of Quebec for orthorectification and validation (Table 3.1). Earlier images (1949–1980) were scanned for prints, whereas later ones (2001–2019) were available as digital files. All images were orthorectified in CATALYST and ArcGIS Pro, using ground control points (GCPs) from field surveys and high-resolution remote sensing. In periods with limited built structures, stable features such as bedrock outcrops, bridge abutments, and road intersections served as reference points. This georeferencing ensured high spatial accuracy for diachronic comparisons.

The orthorectification process followed three steps: (1) interior orientation using fiducial marks and camera calibration data; (2) exterior orientation refined through tie points and block adjustments; and (3) georeferencing, with GCPs and LiDAR-derived DEM to correct relied displacement and align images to real-world coordinates. This approach ensured high spatial accuracy, allowing robust diachronic comparisons of channel changes.

Using the orthorectified images, we digitized the channel outlines and extracted planform metrics across multiple time intervals. Key parameters such as average channel width measured at 100-m intervals, total channel length, and the sinuosity index (SI) were calculated to quantify planform changes over time. The SI, a metric describing the degree of meandering (Mueller, 1968), was calculated as:

$$SI = L/D \quad (1)$$

Where L is the channel length and D is the straight-line distance between endpoints. Here, L corresponds to the midline (talweg) distance of the channel, following the approach of Mueller (Mueller, 1968). SI values range from 1 (straight channel) to infinity, with higher values indicating greater sinuosity. The 2D analysis allowed us to detect lateral shifts in the river course and map zones of apparent erosion or deposition through time.

Table 3.1. Overview of historical aerial imagery and elevation data used in river morphodynamics analysis. The scale resolution ranged from 1:15,840 to 1:40,000 depending on the survey year.

Year	Scale	Color	Type	Number of photos
1949	1: 40,000	Black and white	Aerial	13
1964	1:15,840	Black and white	Aerial	27
1966	1: 40,000	Black and white	Aerial	15
1969	1:15,840	Black and white	Aerial	3

1980	1: 20,000	Black and white	Aerial	17
2001	1: 20,000	Black and white	Aerial	1
2007	1: 20,000	Black and white	Aerial	1
2014	1: 40,000	Black and white	Aerial	1
2019	1: 40,000	Black and white	Aerial	1
2021	1 :1	Color	LiDAR-derived DEM	High resolution LAZ dataset

3.2.3. Volumetric analysis and sediment budget calculation (3D)

To complement the planform analysis, we performed a volumetric assessment of erosion and deposition using Historical Structure from Motion (HSfM). Historical aerial photographs were processed with fiducial marks and calibration reports in CATALYST and ArcGIS Pro (Knuth et al., 2023), generating DEMs for each survey year. These DEMs were co-registered to the 2021 LiDAR DEM (1 m resolution) using the Nuth & Kääb (2011) method (Nuth and Kääb, 2011). Vertical uncertainties from LiDAR (±0.15 m Root Mean Square Error, RMSE) and orthorectification errors from historical imagery were propagated to define a minimum level of detection (LoD). Only elevation changes above this threshold were retained in the DEMs of Difference (DoDs). To avoid bias, disconnected oxbow was excluded from the analysis to prevent overestimation of sediment storage.

Surface differencing techniques (DEM of Difference, or DoD) (Capito et al., 2024) were applied across five key time intervals: 1949–1966, 1966–1980, 1980–2001, 2001–2007, and 2007–2019. For each period, elevation models were subtracted to generate raster surfaces highlighting areas of erosion (negative changes) and deposition (positive changes). These surfaces were mapped and converted into polygons corresponding to morphological change zones, from which volumes of sediment change were computed for each polygon using:

$$\Delta V = Va - Ve, \quad (2)$$

where *Va* is the accumulated sediment volume and *Ve* is the eroded volume. This calculation accounts for both vertical changes (bed incision or aggradation) and, indirectly, for lateral shifts when coupled with planform data (bank migration resulting from the mobility of the river's channel). In practice, however, because DEMs derived from historical aerial imagery represent Digital Surface Models (DSMs) including vegetation and lack bathymetric information, DoD outputs primarily capture floodplain and bank adjustments rather than submerged channel-bed dynamics.

The net sediment budget (ΔSB) was calculated as:

$$\Delta SB = \sum_{1=1}^{n} Va - \sum_{i=1}^{n} Ve \quad (3)$$

where *n* is the number of years in each interval.

Because the time intervals vary in length (ranging from 6 to 21 years), we reported results as: i) cumulative sediment volumes (in m^3), which indicate the total magnitude of geomorphic change; ii) annualized rates (in mm/year), which account for the differing duration of each interval; and iii) standardized rates per channel length (in m^3/km/year), providing a normalized metric for cross-period comparison of geomorphic activity. This 3D analysis is particularly relevant in the Diable River because several eroding banks consist of steep sandy bluffs, several meters high, that can release large quantities of sediment when destabilized.

3.2.4. Grain-size analysis

A total of 32 sediment samples were collected during field surveys from key erosion sources (e.g., steep sandy banks with freshly eroded faces) and depositional environments (e.g., point bars and beaches) along the Diable River. Samples were collected from the upper 0–20 cm of surface material, following standard protocols, to capture the most mobile sediment fraction of the bed and bank. Laboratory analyses were performed to determine grain-size distributions using the Folk and Ward (1957) method through dry-sieve analysis with a calibrated column of sieves (4 mm to 63 μm) ensuring reproducibility across samples. Statistical parameters, including mean, standard deviation, skewness, and kurtosis, were calculated, along with percentile-based indices (D90, D75, D25, D10) and their ratios (e.g., D90/D10, D75/D25). Percentile ratios were preferred over central tendency metrics (e.g., D50, D84) because they better capture contrasts in sorting and selective transport, which are particularly relevant in sandy systems with partial sediment connectivity. These data provide insights into grain-size selectivity and the transfer dynamics between upstream sources and downstream sinks.

3.3. Results

The Diable River has undergone substantial morphological transformations over the past seven decades. The results presented here reveal spatial and temporal variations in lateral mobility, sediment budgets, and elevation changes that reflect the river's complex adjustment processes.

3.3.1. River planform dynamics (2D analysis of mobility and geometry)

Over the past seven decades, the Diable River has experienced significant morphological changes, as reflected in variations in channel sinuosity and average width (Table 3.2). Across all years analyzed, the sinuosity index remained above 2.0 (mean SI of 2.32), confirming a consistently meandering planform with localized but recurrent phases of adjustment. Notably, 1969 recorded a sharp increase in both sinuosity and average width, suggesting a major erosional episode, while another peak in average channel width occurred in 2014, associated with one of the highest sinuosity values observed since 2001 (Table 3.2).

Despite differences in the length of observation intervals (6 to 21 years), the overall pattern points to a persistent geomorphic dynamism, even in the absence of significant land-use change in this downstream reach. The mean channel width across all years was 36.91 m, with considerable local variability. Spatial analysis of planform changes across the five intervals (1949–1966, 1966–1980, 1980–2001, 2001–2007, and 2007–2019) reveals a discontinuous and shifting distribution of

erosion and deposition zones along the river corridor (Figure 3.2), consistent with non-linear channel evolution.

Table 3.2. Sinuosity index (SI) and average channel width (W, in meters per 100 m reach) of the Diable River for selected years between 1949 and 2019. Scales of aerial photographs ranged from 1:15,840 to 1:40,000 depending on survey year (see Table 3.1).

Year	1949	1966	1969	1980	2001	2007	2014	2019
SI	2.18	2.10	2.31	2.06	2.25	2.45	2.38	2.41
W	35.04	32.57	43.66	33.99	37.17	35.30	43.85	37.83

The 1949–1966 period shows moderate activity, with typical meander migration and a spatial balance between erosion and deposition, reflecting relatively stable lateral dynamics (Figure 3.2a). The average channel width and sinuosity index are consistent with a well-developed meandering pattern. By contrast, 1966–1980 displays narrower widths and lower sinuosity indicating a temporary contraction of lateral mobility, with only minor localized changes (Figure 3.2b).

Between 1980–2001, lateral activity intensified sharply, with widespread cutbank erosion and point-bar accretion (Figure 3.2c). The average channel width increased to 37.2 m, and sinuosity rose to 2.25 (Table 3.2), marking the most dynamic interval of the record.

In 2001–2007, the channel appears more stable despite a high sinuosity (2.45). Width remained relatively high (35.3 m; Table 3.2), but the predominance of accumulation suggests localized deposition rather than active meander migration (Figure 3.2d).

The 2007–2019 interval is characterized by moderate adjustments, maximum widths in 2014 (43.85 m) before narrowing in 2019 (37.82 m) (Table 3.2). Sinuosity remained relatively stable throughout this period, fluctuating around 2.40 (2.45 in 2007, 2.38 in 2014, and 2.41 in 2019; Table 3.2). Spatial patterns also shift, with erosion becoming more prominent in the upper reaches, while sediment deposition dominates downstream (Figure 3.2e).

Overall, the spatial distribution of erosion and deposition along the Diable River reveals no clear upstream-downstream gradient over the seven-decade period. Instead, lateral adjustments are concentrated around actively migrating meanders, with the most intense planform activity during the 1980–2001 and more localized changes thereafter. While planform 2D analysis captures the timing and distribution of lateral mobility, it does not quantify vertical sediment storage or the net balance of erosion and deposition. These limitations motivate the complementary 3D DoD analysis presented in the next section.

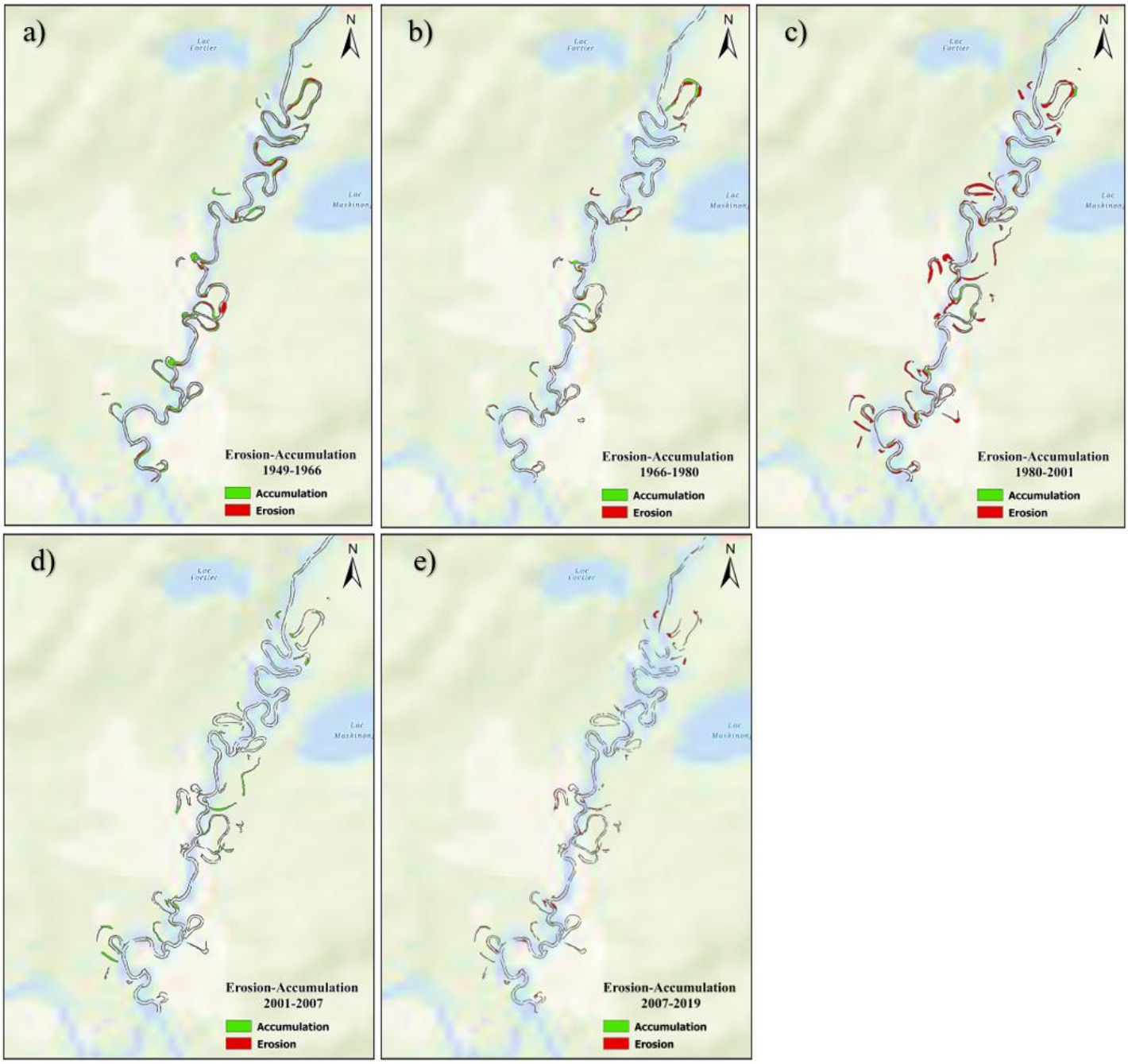

Figure 3.2. Spatial distribution of erosion (in red) and accumulation (in green) along the Diable River during five successive intervals: (a) 1949–1966; (b) 1966–1980; (c) 1980–2001; (d) 2001–2007; (e) 2007–2019. The maps highlight temporal variations in channel bank dynamics and spatial patterns of sediment mobilization and deposition.

Figure 3.2 illustrates these changes through a series of erosion-accumulation maps for each period, allowing visual comparison of spatial dynamics. While lateral changes are not always directly proportional to sediment volumes gained or lost (as shown in the following section 3.3.2), these patterns provide key insights into the morphological behavior, mobility, and sediment redistribution of the river system.

3.3.2. Sediment budgets and volumetric changes (3D LiDAR-based analysis)

We quantified volumetric sediment dynamics using LiDAR-derived DEMs and DoD analysis across five key intervals: 1949–1966, 1966–1980, 1980–2001, 2001–2007, and 2007–2019. The results (Figure 3.3; Table 3.3) highlight strong contrasts in erosion, deposition, and net sediment balance that are not always apparent from planform analysis and metrics alone. Figure 3.3a shows annual erosion and deposition volumes, while Figure 3.3b presents the net sediment balance, distinguishing between gross sediment fluxes and net outcomes.

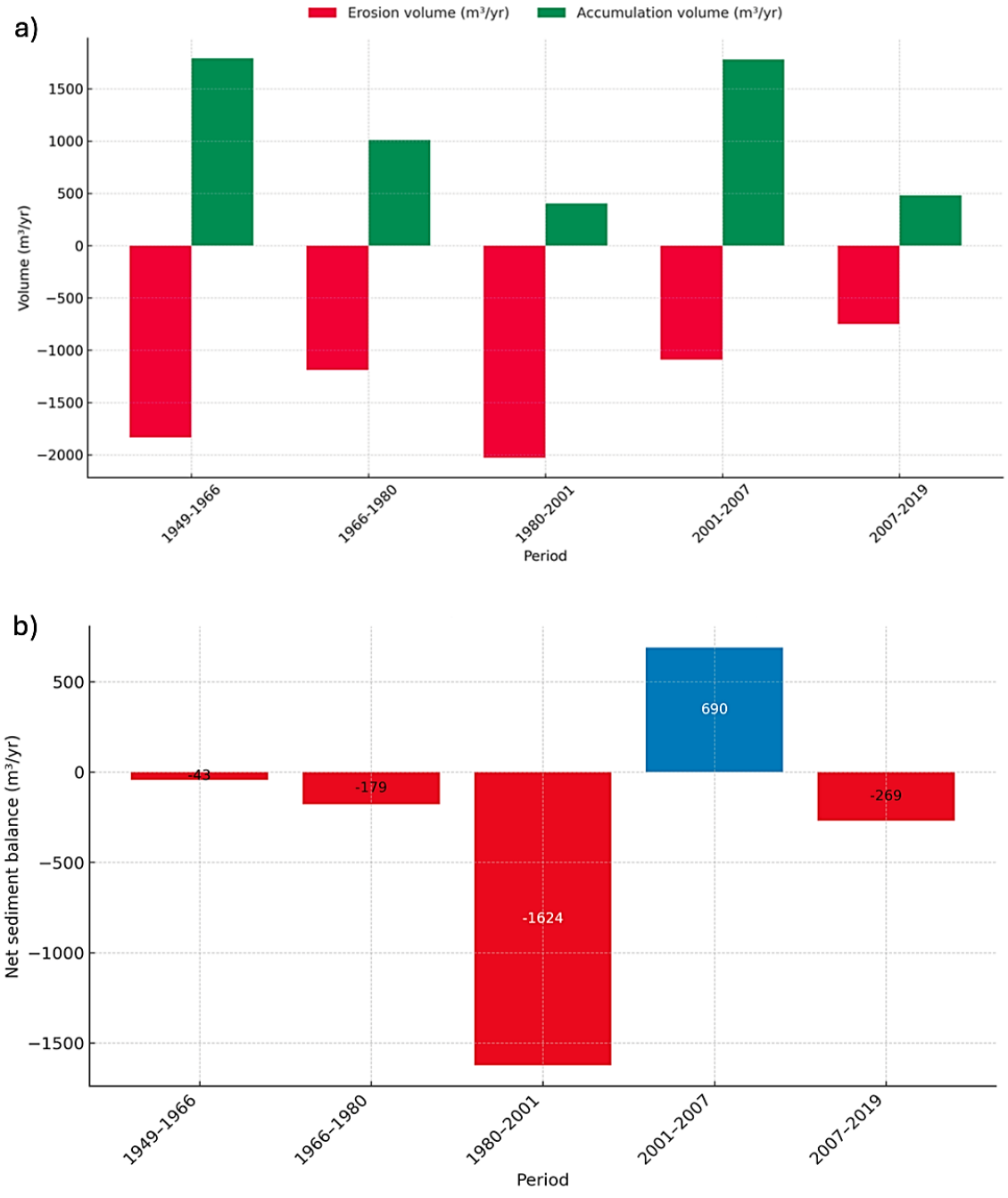

Figure 3.3. (a) Annual erosion (in red) and accumulation (in green) volumes (m^3/year) for the Diable River segment across the five analyzed periods (1949–2019). **(**b**)** Net sediment balance per year for the Diable River segment across the five periods (1949–2019). Negative values (in red) indicate a sediment deficit (net erosion), while the single positive value (in blue) during the 2001–2007 period reflects a net sediment surplus (deposition).

The 1949–1966 interval shows moderate sediment activity, with erosion (8.9 mm/year) and deposition (6.4 mm/year). The net sediment loss (~31,000 m^3; 124 m^3/km/year) indicates moderate lateral and vertical adjustments within an otherwise stable meandering system (Figure 3.3).

The 1966–1980 period displays relatively balanced dynamics; with erosion and accumulation rates of 10.5 mm/year and 9.9 mm/year, respectively. The net sediment loss (~16,666 m^3) translates to an erosion rate of 86.4 m^3/km/year. These values suggest steady geomorphic activity with limited lateral adjustments.

The 1980–2001 interval represents the most dynamic erosional phase in the record (Figure 3.3a). The vertical erosion rate reached 9.2 mm/year, and volumetric export was the highest (142.5 m^3/km/year), with a net sediment loss exceeding 42,500 m^3 (Figure 3.3b). Deposition rates declined sharply (4.6 mm/year), contributing to a pronounced sediment imbalance and a period of enhanced lateral migration and channel widening.

In 2001–2007, both erosion (17.2 mm/year) and deposition (10.6 mm/year) peaked, producing intense sediment turnover but only limited net loss (~6,544 m^3; 70.8 m^3/km/year) (Figure 3.3b; Table 3.3). Spatially, accumulation was concentrated downstream while erosion remained localized upstream, suggesting a short-lived phase of geomorphic recovery.

The 2007–2019 interval shows reduced but persistent sediment export loss (~8,990 m^3; 47.0 m^3/km/year) (Figure 3.3; Table 3.3), with erosion (6.0 mm/year) lower than deposition (8.6 mm/year). This reflects localized adjustments and a return to more moderate levels of channel activity.

Together, these results emphasize that volumetric analysis captures both extreme erosional phases (1980-2001) and transient recovery periods (2001-2007), demonstrating the added value of 3D DoD methods for understanding sediment dynamics beyond planform observations (Table 3.3).

Table 3.3. Annual volumetric and vertical rates of erosion and accumulation for the studied river segment (1949–2019). Values are standardized both per year and per kilometer of channel length to allow comparison across intervals.

Period	Duration	Erosion		Deposition	
	Years	$m^3\ yr^{-1}$	$mm\ yr^{-1}$	$m^3\ yr^{-1}$	$mm\ yr^{-1}$
1949-1966	17	-1835	8.9	1792	6.4
1966-1980	14	-1190	10.5	1011	9.9
1980-2001	21	-2027	9.2	402	4.6
2001-2007	6	-1090	17.2	1780	10.6
2007-2019	12	-749	6.0	480	8.6

3.3.3. Sediment connectivity between erosion and deposition zones

To evaluate sediment connectivity along the Diable River, we compared grain-size distributions between samples collected on steep sandy bluffs (erosion sources) and nearby depositional zones (beaches). Paired sampling at 15 locations along the river corridor provided a framework to assess downstream transfer based on particle-size characteristics and statistical parameters.

The analysis confirms that sediments are predominantly sandy, ranging from fine to very coarse sand. However, systematic differences emerged between bluff and beach materials. As shown in Figure 3.4a, bluffs are mainly composed of medium to coarse sand, while beaches tend to concentrate coarser fractions, particularly in the middle and downstream reaches. Sorting patterns (Figure 3.4b) reveal greater variability and poorer sorting in bluff samples, consistent with heterogeneous releases during bank collapse. In contrast, beach deposits are predominantly moderately well to well sorted, reflecting selective transport and hydrodynamic sorting.

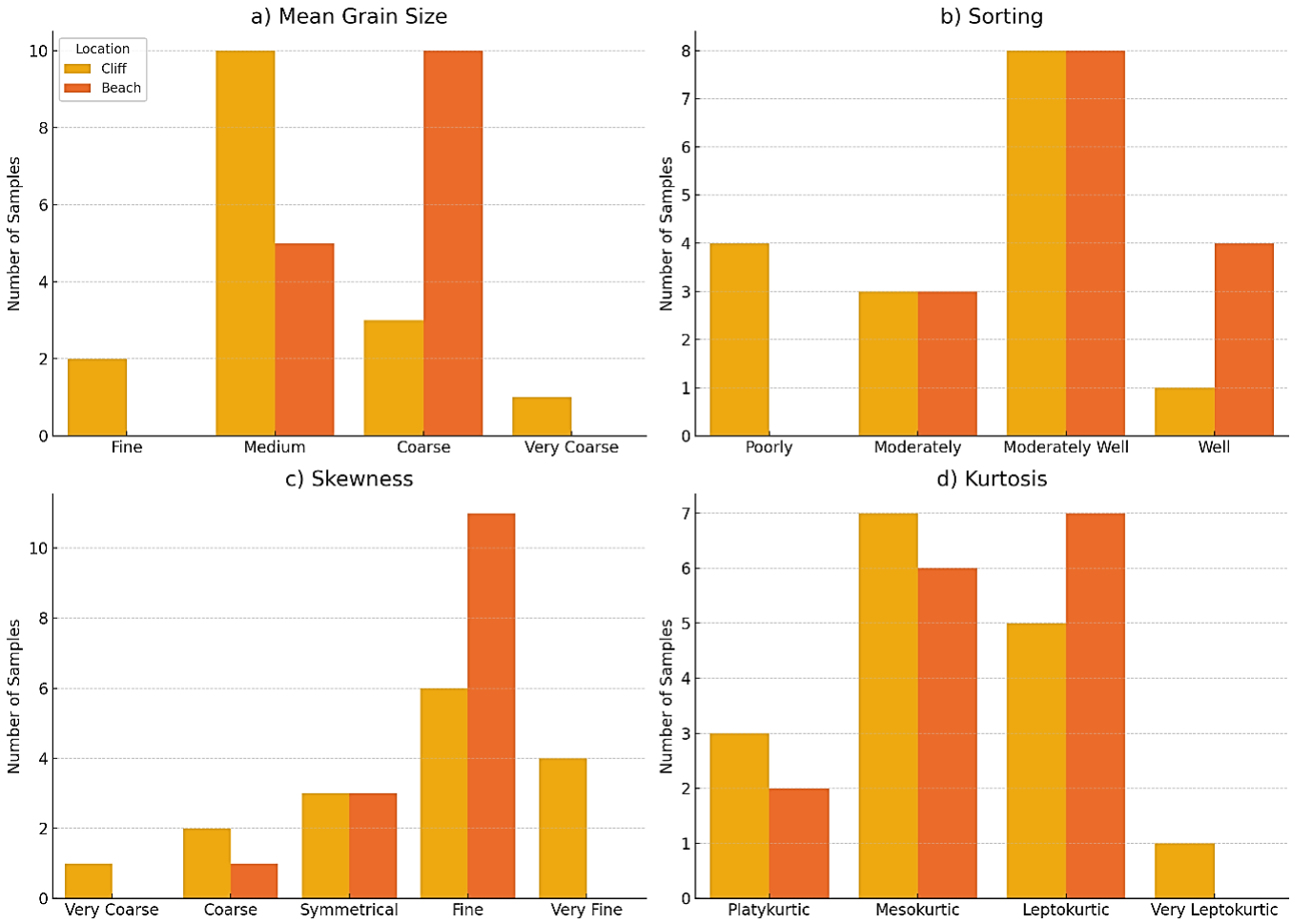

Figure 3.4. Grain-size characteristics of sediment samples from bluff and beach environments: (a) mean grain size, (b) sorting, (c) skewness, and (d) kurtosis. Bars indicate the number of samples within each category (sandy cliff/bluff: yellow; beach: orange).

While bluffs show higher variability across several parameters (Figure 3.4), no statistically significant differences were detected (all p-value > 0.16) (see Appendix A.3.1, Figure A.3.1). This reinforces the view that contrasts in sediment behavior emerge more clearly from paired analyses and grain-size ratios than from global statistical descriptors. Skewness and kurtosis further highlight sediment differentiation (Figure 3.4c, d): bluffs frequently show fine to very fine skewness (higher proportion of fines) and meso- to platykurtic distributions, whereas beaches show mainly fine skewness with narrower, leptokurtic distributions.

To further assess potential relationships among granulometric descriptors, bivariate comparisons were conducted across all samples, comparing combinations of mean grain size, sorting, skewness, and kurtosis (see Appendix A.3.2, Figure A.3.2). Table 3.4 summarizes descriptive statistics (mean, sorting, skewness, kurtosis) for all bluff and beach samples. Although no significant correlations were found among granulometric descriptors (all p-value > 0.16), these values provide a reference baseline for comparing source and sink material.

Table 3.4. Comparison of grain-size characteristics between cliff/bluff (erosion) and beach (deposition)samples along the Diable River. Sampling site locations are shown in Figure 3.1.

Sample	Mean	Sorting	Skewness	Kurtosis
1.1 Bluff	Coarse Sand	Moderately Sorted	Very Fine Skewed	Mesokurtic
1.2 Beach	Coarse Sand	Moderately Well Sorted	Coarse Skewed	Leptokurtic
2.1 Bluff top	Coarse Sand	Poorly Sorted	Symmetrical	Mesokurtic
2.2 Bluff	Medium Sand	Poorly Sorted	Coarse Skewed	Mesokurtic
2.3 Beach	Coarse Sand	Moderately Well Sorted	Fine Skewed	Leptokurtic
3.1 Bluff	Very Coarse Sand	Poorly Sorted	Fine Skewed	Mesokurtic
3.2 Beach	Coarse Sand	Moderately Well Sorted	Fine Skewed	Platykurtic
4.1 Bluff	Medium Sand	Moderately Well Sorted	Coarse Skewed	Mesokurtic
4.2 Beach	Coarse Sand	Moderately Well Sorted	Symmetrical	Leptokurtic
5.1 Bluff	Medium Sand	Moderately Well Sorted	Symmetrical	Platykurtic
5.2 Beach	Medium Sand	Well Sorted	Fine Skewed	Mesokurtic
6.1 Bluff	Medium Sand	Well Sorted	Fine Skewed	Leptokurtic
6.2 Beach	Medium Sand	Well Sorted	Fine Skewed	Leptokurtic
6.3 Old Meander	Fine Sand	Moderately Sorted	Coarse Skewed	Leptokurtic
7.1 Bluff	Medium Sand	Moderately Well Sorted	Very Fine Skewed	Leptokurtic
7.2 Beach	Coarse Sand	Moderately Well Sorted	Fine Skewed	Leptokurtic
8.1 Bluff	Medium Sand	Moderately Well Sorted	Very Fine Skewed	Mesokurtic
8.2 Beach	Coarse Sand	Moderately Well Sorted	Fine Skewed	Leptokurtic
9.1 Bluff	Medium Sand	Moderately Well Sorted	Fine Skewed	Leptokurtic
9.2 Beach	Coarse Sand	Moderately Sorted	Fine Skewed	Platykurtic
10.1 Bluff	Medium Sand	Moderately Sorted	Fine Skewed	Platykurtic
10.2 Beach	Medium Sand	Well Sorted	Fine Skewed	Mesokurtic
11.1 Bluff	Medium Sand	Moderately Well Sorted	Fine Skewed	Platykurtic
11.2 Beach	Coarse Sand	Well Sorted	Fine Skewed	Mesokurtic
12.1 Bluff	Coarse Sand	Moderately Well Sorted	Fine Skewed	Leptokurtic
12.2 Beach	Medium Sand	Moderately Sorted	Symmetrical	Mesokurtic
13.1 Bluff	Medium Sand	Moderately Well Sorted	Very Fine Skewed	Leptokurtic

13.2 Beach	Coarse Sand	Moderately Well Sorted	Fine Skewed	Mesokurtic
14.1 Bluff	Fine Sand	Poorly Sorted	Very Coarse Skewed	Very Leptokurtic
14.2 Beach	Medium Sand	Moderately Well Sorted	Symmetrical	Leptokurtic
15.1 Bluff	Fine Sand	Moderately Sorted	Symmetrical	Mesokurtic
15.2 Beach	Coarse Sand	Moderately Sorted	Fine Skewed	Mesokurtic

3.3.3.1. Grain-size ratios and implications for sorting and sediment transfer

Beyond qualitative classification, sediment connectivity was further assessed through granulometric ratios (D90/D10, D75/D25), which measure the spread between the coarsest and finest fractions, with higher values indicating a wider grain-size distribution and poorer sorting. In general, bluff samples exhibited higher D90/D10 and D75/D25 ratios than paired beach samples (Figure 3.5), confirming that eroded material is more heterogeneous. Conversely, lower D90/D10 and D75/D25 ratios in beach samples indicate better sorting, with most particles falling within a narrower size range (Figure 3.5).

A particularly informative result concerns the comparison of D90 values: in many cases, D90 was greater on beaches than on bluffs, indicating that coarser fractions are effectively transferred downstream and deposited in accumulation zones. Conversely, higher D10 values on bluffs suggest that finer particles are less likely to be deposit locally. This pattern supports the interpretation of partial but effective downstream connectivity, where coarse particles are selectively retained while finer material is preferentially exported further downstream.

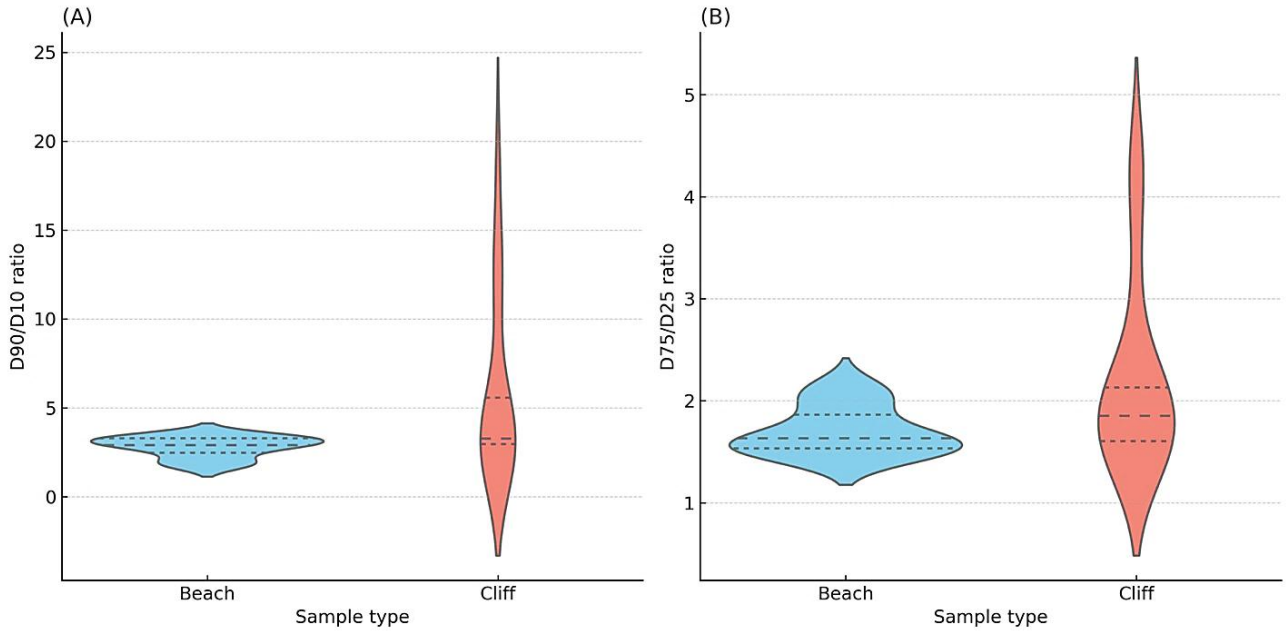

Figure 3.5. Violin plots comparing grain-size ratios for bluff (in red) and beach (in blue) samples: (a) D90/D10; (b) D75/D25. Each violin plot displays the full distribution of grain-size ratios for each sample type. The width of each violin plot represents the relative density of observations at different values. The central dashed line indicates the median, while the two horizontal dashed lines within the violin indicate the first and third quartiles.

These analyses reveal systematic though subtle differences between erosion sources and depositional environments, reinforcing the role of selective transport in shaping sediment connectivity along the Diable River. These findings are explored in greater detail in the Discussion section.

3.4. Discussion

The Diable River's geomorphic trajectory over the past seven decades reflects alternating phases of sediment export and storage, modulated by flood events and internal geomorphic thresholds. This discussion examines their spatial and temporal dynamics and highlights their relevance for sediment connectivity and adaptive management.

3.4.1. A dynamic fluvial system shaped by alternating phases of activity and stabilization

Over the past seven decades, the Diable River has exhibited a non-linear geomorphic evolution marked by alternating periods of relative stability and increased channel activity (Figure 3.6). The planform metrics (Section 3.3.1) show variations in sinuosity ranging from 2.06 to 2.45, and average channel width from 32.57 to 43.85 m, with peaks in 1969 and 2014. However, these metrics alone do not fully capture the river's dynamism. Volumetric analysis from LiDAR-based DoD (Section 3.3.2) provides a clearer picture of sediment fluxes and storage. This approach aligns with recent efforts to quantify riverbank erosion and sediment budgets using historical imagery and LiDAR data (Spiekermann et al., 2017), offering a robust basis for long-term river monitoring (Prugne et al., 2025). Similar methods have also been applied in cold-temperate rivers using sequential LiDAR and historical aerial photographs (De Rose and Basher, 2011; Spiekermann et al., 2017), demonstrating their reliability for quantifying erosion and sediment fluxes in sandy-bed rivers. Similar long-term approaches (e.g., Hajdukiewicz et al., 2019; Kiss et al., 2024; Chassiot et al., 2020) confirm that combining planform and volumetric perspectives is particularly effective for detecting hidden phases of geomorphic instability.

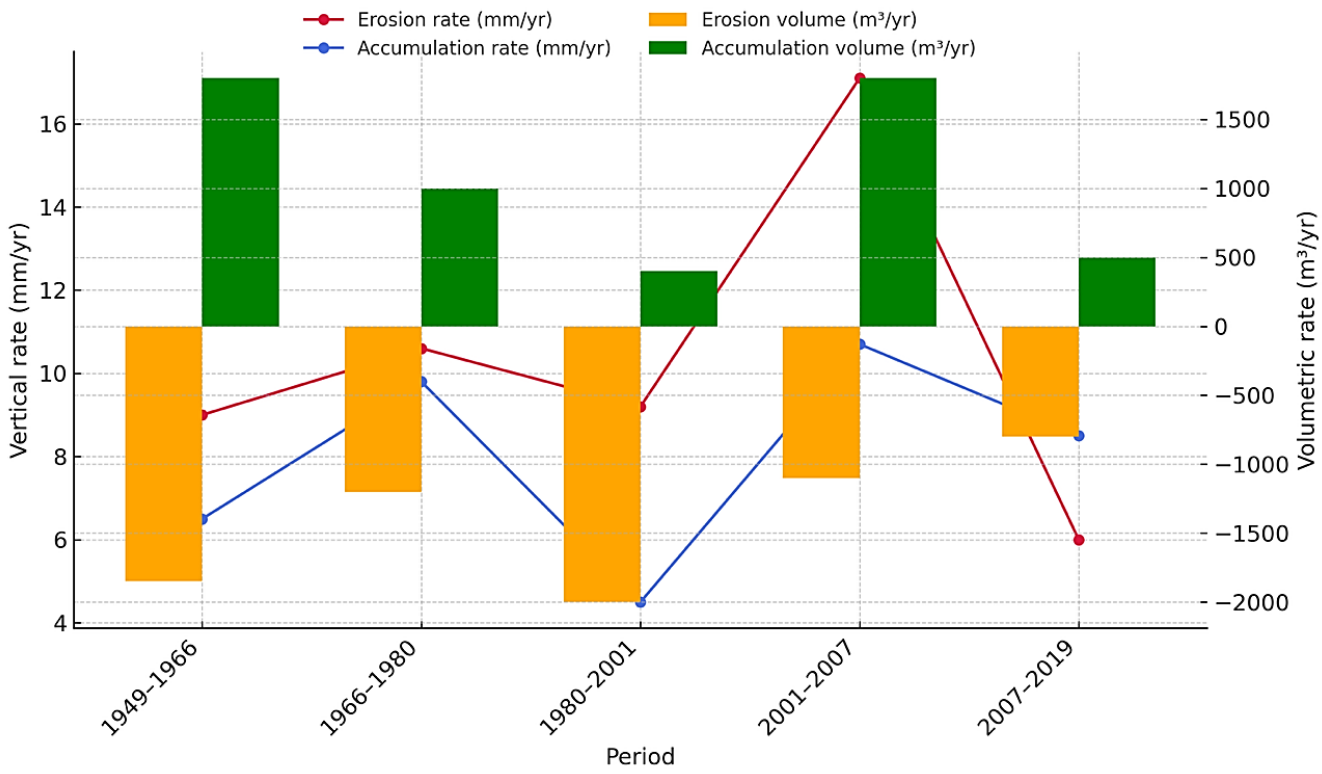

Figure 3.6. Combined vertical and volumetric sediment dynamics of the Diable River segment across the five periods analyzed (1949-2019). Line plots represent vertical erosion and accumulation rates (mm/year), while bars represent annual volumetric erosion and accumulation (m^3/year). Note that vertical rates indicate average elevation change, while volumetric rates reflect sediment mass transfer normalized by river length.

The 1980–2001 interval stands out as the most erosive phase, with a total sediment loss of -42,568 m^3 and the highest net sediment export rate (-142.5 m^3/km/year). This period reflects widespread lateral instability, high meander mobility, and cutbank erosion, consistent with intense planform adjustments.

In contrast, the 2001–2007 period recorded the highest vertical erosion rate (17.2 mm/year) together with substantial deposition (10.6 mm/year) (Figure 3.6). Despite these high turnover rates, the net sediment loss was modest (-6,544 m^3), and the standardized balance was positive (+70.8 m^3/km/year). This indicates a phase of intense sediment recycling and temporary geomorphic recovery.

Earlier periods (1949–1966 and 1966–1980) show relatively balanced erosion and deposition (8.9/6.4 mm/year and 10.5/9.9 mm/year, respectively), pointing to persistent but lower-magnitude geomorphic activity (Figure 3.6). Finally, the most recent period (2007-2019) was marked by lower vertical erosion (6.0 mm/year) but continued net sediment export (-47.0 m^3/km/year), suggesting localized adjustments following earlier disturbances.

These results highlight that the Diable River does not follow a linear trajectory of degradation or aggradation but oscillates between phases of disequilibrium and partial re-stabilization, shaped by both internal geomorphic thresholds and external hydrometeorological events. This oscillatory

behavior echoes broader conceptualizations of river trajectories, where alternating phases of instability and re-stabilization are seen as intrinsic to fluvial systems (Church, 2010; Wohl, 2018). Such alternating cycles of export and storage have also been observed in other temperate rivers (Piqué et al., 2017; Hajdukiewicz et al., 2019; Kiss et al., 2024), highlighting the broader relevance of this dynamic behavior.

3.4.2. Flood events as key drivers of sedimentary transitions

Flood events have played a pivotal role in shaping the sedimentary regime of the Diable River, acting as primary triggers for both erosion and deposition. Among the five historical intervals, the 1980–2001 period stands out with multiple high-magnitude floods (e.g., 1995, 1996, 1997), coinciding with the largest volumetric sediment loss (−42,568 m^3). Despite only moderate vertical erosion (9.2 mm/year), this prolonged erosive phase reflects the cumulative impact of successive high-energy events, which mobilized large sediment volumes through bluff failure and channel widening. The corresponding net export (-142.5 m^3/km/year) further illustrates the intensity and persistence of these flood-driven processes.

By contrast, the 2001–2007 illustrates a distinct post-flood recovery phase. This is the only interval with a net positive sediment budget (+70.8 m^3/km/year), marked by both high accumulation (10.6 mm/year) and the highest vertical erosion rate (17.2 mm/year). Deposition clustered in point bars and inner meanders, suggesting stabilization in lower-energy zones, potentially reinforced by reduced peak discharges and increasing riparian vegetation. The subsequent period (2007–2019) featured lower erosion (6.0 mm/year) and a moderate net export (−47.0 m^3/km/year).

Hydrograph data from station 040238 (2009–2025; Figure 3.7) provide direct evidence of the flood regime during this interval: the 2011 event reached ~160 m^3/s, while the 2017 and 2019 floods exceeded 200 m^3/s, with 2019 peaking above 230 m^3/s (approximately a 50-year recurrence interval). More recent events (2023–2024) generated moderate floods (150–190 m^3/s), highlighting ongoing but less extreme disturbances. These peaks appear to have induced localized erosion such as bank undercutting rather than broad planform migration, explaining the moderate sediment export observed in this period.

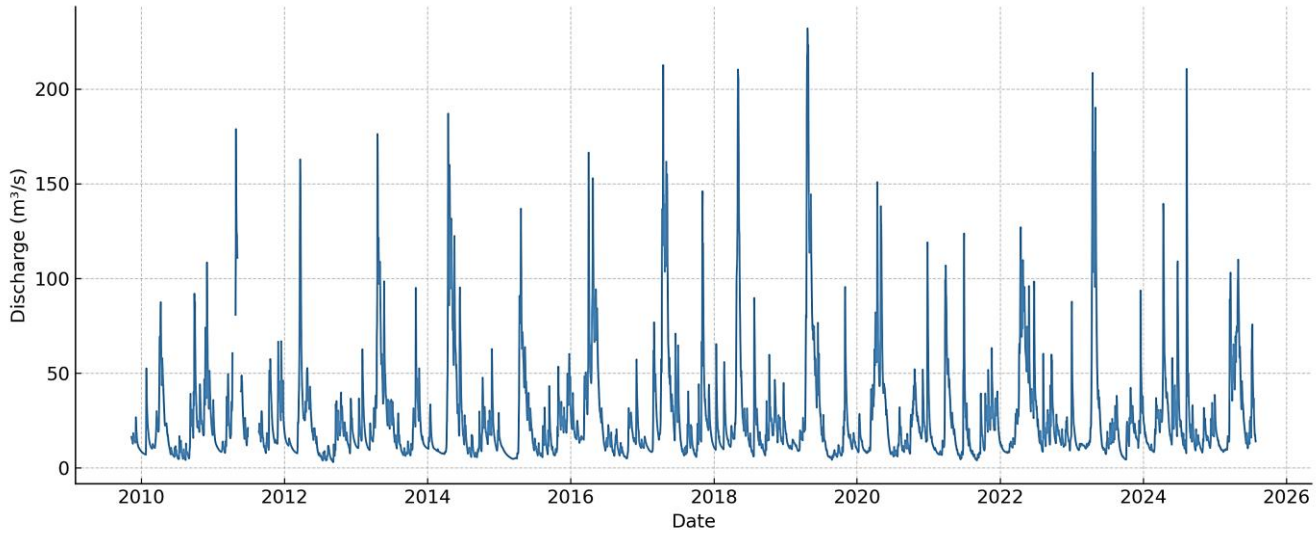

Figure 3.7. Hydrograph of the Diable River at hydrometric station 040238 (2009–2025), located immediately upstream of the study reach. The graph illustrates the interannual and seasonal variability of daily discharges, with spring flood peaks exceeding 200 m^3/s.

Overall, the comparison of flood-linked intervals highlights the varied geomorphic responses to hydrological forcing. Similar patterns of flood-driven sediment dynamics have been reported in temperate rivers worldwide (Wohl, 2018; Prugne et al., 2025), emphasizing the influence of extreme events on sediment budgets and channel morphology. The integration of recent discharge records confirms that the Diable River's sedimentary response is strongly conditioned by flood magnitude and frequency, with major floods (2017, 2019) acting as turning points in its morphodynamic trajectory, while intermediate floods (2011, 2023–2024) contributed to adjustments without major geomorphic reorganization. Comparable flood-driven sediment exports have also been observed in temperate and cryosphere-influenced rivers, where repeated high-magnitude events reset channel morphology (Zhang et al., 2023; Prugne et al., 2025).

Hydrograph data (Figure 3.7) provide additional insight into these dynamics. Between 2009 and 2016, peak annual discharges remained consistently below 200 m^3/s, but in five of the subsequent eight years (2017–2019 and 2023–2024), peaks exceeded this threshold, with maxima ranging from 208 to 232 m^3/s. This pattern may suggest emerging cycles or shifts in flood regime; however, the short observational record prevents robust conclusions. Nonetheless, the recurrence of extreme flows in recent years supports the interpretation that high-magnitude floods are increasingly structuring the river's morphodynamic trajectory.

3.4.3. Sediment connectivity and granulometric selectivity

The granulometric analysis of paired samples from sandy bluffs (erosion sources) and beaches (accumulation zones) provides key insights into sediment connectivity along the Diable River. Although no statistically significant differences were found when comparing global descriptors (e.g., mean, sorting, skewness, and kurtosis), grain-size ratios and spatial contrasts revealed consistent patterns: sediment transfer is selective rather than uniform.

Bluff samples, typically composed of moderately to poorly sorted medium to coarse sands, exhibited higher D90/D10 and D75/D25 ratios (Figure 3.5), indicating a broader grain-size distribution and a greater abundance of fines. These fine fractions reflect the unconsolidated nature of sand bluffs, which deliver heterogenous material through bank failure, slumping and significant biogenic activity locally (Germain et al., 2022, Figure 3.4). In contrast, beach deposits were generally better sorted and more enriched in coarse sand, especially in downstream reaches. This pattern suggests that coarse fractions are preferentially trapped locally, while finer particles are transported further downstream or remain in suspension, a behavior consistent with observations in other temperate rivers where fine sediment often bypass local storage and is redistributed downstream (Chassiot et al., 2020).

Such trends indicate a system with partial but functionally significant connectivity: upstream bluffs provide a wide grain-size spectrum, but only a subset (mainly coarse particles) is retained in local depositional settings. Finer particles largely bypass these zones, contributing to suspended loads and potential downstream siltation. Similar patterns of selective sediment transfer have been reported in other catchments (Clifton et al., 2022), reinforcing this interpretation. Additional evidence from agricultural and human-impacted basins also confirms that selective transport and partial connectivity dominate sediment routing (Clifton et al., 2022; Piqué et al., 2017). Hydraulic sorting, modulated by flow energy, bank roughness, and vegetation cover explains these differences. Well-sorted beach deposits reflect repeated reworking under moderate-energy conditions, while the heterogeneity of bluff material mirrors stochastic, gravity-driven erosion processes.

These grain-size evidences support the view of the Diable River as a partly coupled sediment system, where connectivity operates through selective transfers. This interpretation is supported by sediment budget reconstructions in European sandy rivers (Kiss et al., 2024), reviews of riverbank erosion in cold environments (Chassiot et al., 2020), and observations from other temperate systems (De Rose and Basher, 2011; Hajdukiewicz et al., 2019). It also aligns with recent frameworks conceptualizing connectivity as a gradient process rather than a binary state (Bracken et al., 2015; Shi et al., 2025). Standardized volumetric rates complement this interpretation by highlighting alternating phases of net sediment export and temporary storage.

3.4.4. Implications for river management and future geomorphic scenarios

The spatial and temporal variability of geomorphic processes in the Diable River underscores the need for adaptive, sediment-informed management strategies. Floodplain delineation, often treated as a neutral technical exercise, must be understood as a process with direct societal implications, shaping land use and local vulnerability (Gouvernement du Québec, 2025). This reinforces the importance of grounding management decisions in both geomorphic evidence and local knowledge of river dynamics.

The alternation between phases of intense erosion (1980–2001, 2007–2019) and temporary sediment recovery (2001–2007) highlights the importance of maintaining lateral accommodation space to absorb disturbances and facilitate natural recovery through deposition. Sediment sinks such as beaches act as temporary storage zones that buffer downstream sediment fluxes during floods. Protecting these features by limiting channelization or encroachment can enhance fluvial

corridor resilience. Similarly, post-flood aggradation zones should be recognized as natural sediment traps and integrated into restoration strategies.

Sediment transfer is also highly selective: coarser fractions settle locally, while finer particles are remobilized and exported downstream. Management must therefore address these contrasting behaviors, for instance, stabilizing fine-sediment sources (e.g., vegetated banks near bluffs) to reduce turbidity, while conserving coarse-sediment deposition zones to maintain geomorphic resilience.

From a governance perspective, effective management requires bridging top-down regulatory frameworks with situated local expertise, ensuring both technical robustness and social legitimacy (Haughton et al., 2015; McEwen and Jones, 2012). Looking ahead, climate change is likely to intensify hydrological extremes, exacerbating erosion and sediment fluxes. Proactive measures such as riparian reforestation, dynamic setback zones, and floodplain reconnection should therefore be prioritized (Prugne et al., 2024). Complementary evidence from cold-region rivers suggests that bioengineering and vegetation-based stabilization can also mitigate recurrent bluff erosion (Prugne et al., 2024). More broadly, sediment budgets provide a robust framework (Reid and Dunne, 2016) for guiding management strategies that align with the Diable River's geomorphic dynamics and support long-term ecological and social resilience (Brierley and Fryirs, 2022).

3.5. Conclusions

The Diable River's geomorphic evolution (1949–2019) reveals a system oscillating between phases of sediment export and temporary stabilization, rather than following a unidirectional trend of aggradation or degradation. Major erosional phases (e.g., 1980–2001) alternated with short-lived recovery periods (e.g., 2001–2007) and more localized adjustments in recent years, underscoring the non-linear nature of channel change.

Grain-size analyses confirm selective and partial sediment connectivity; coarse fractions are partly retained in local depositional zones, while finer sediments are preferentially exported downstream. This filtering effect illustrates the combined role of hydraulic energy and sediment properties in shaping river dynamics.

These findings stress the importance of sediment-informed management that preserves temporary storage features and maintains lateral space for adjustment. Rather than controlling fluvial dynamics, management should focus on the river's natural oscillatory behavior, using sediment budgets as a guiding framework. Anticipated increase in flood frequency and magnitude due to climate change (Zhang et al., 2023) make such approaches especially critical. In the Québec context (Valois et al., 2023), linking sediment continuity with flood mitigation offers a practical foundation for strengthening both geomorphic resilience and community safety.

Supplementary Materials: Please see Appendix A including Appendix A.3.1 and A.3.2.

Author Contributions: "Conceptualization, A.F. and D.G.; methodology, A.F. and D.G; software, A.F.; validation, A.F., D.G. and G.F.; formal analysis, A.F. and D.G; investigation, A.F., D.G, and

G.F; resources, D.G.; data curation, A.F.; writing—original draft preparation, A.F. and D.G; writing—review and editing, A.F., D.G, and G.F; visualization, A.F. and D.G; supervision, D.G. and G.F; project administration, D.G.; funding acquisition, D.G. All authors have read and agreed to the published version of the manuscript."

Funding: This research was funded by the Natural Sciences and Engineering Research Council of Canada, grant number RGPIN-2023-05504 to Daniel Germain.

Data Availability Statement: The data supporting the conclusions of this article will be made available by the authors on request. The historical aerial photographs can be obtained from Geoindex database: https://geoapp.bibl.ulaval.ca/login#. The LiDAR data can be acquired from Ministry of Transportation of Quebec database: https://www.donneesquebec.ca/recherche/dataset/produits-derives-de-base-du-lidar.

Acknowledgments: The authors would like to express their sincere gratitude to Professor Olivier Caron and undergraduate student Laurence Prud'homme from the Department of Geography at UQAM for their valuable consultations and recommendations during the preliminary stages of data preparation and selection. Special thanks are also extended to Sylvie Trudeau, Computer Technician at the Department of Geography, UQAM, for her assistance with administrative procedures and communications related to data acquisition from government agencies. We also thank Jean-François Milot, graduate student in the same department, for his support during the fieldwork process, and Mourad Djaballah for the improvement of Figure 3.1.

Conflicts of Interest: The authors declare no conflicts of interest.

Abbreviations

The following abbreviations are used in this manuscript:

DEM Digital Elevation Model

DoD DEMs of Difference

DSAS Digital Shoreline Analysis System

DSM Digital Surface Model

GCPs Ground Control Points

GIS Geographic Information System

HSFM Historical Structure from Motion

LiDAR Light Detection and Ranging

LoD Level of Detection

SI Sinuosity Index

UAV Unmanned Aerial Vehicle

CHAPTER 4

A Multi-Method Statistical Framework for Quantifying Fluvial Sediment Transport and Geomorphic Dynamics in a Cold-Region River System

Ali Faghfouri[1], Daniel Germain[2], Guillaume Fortin[3]

[1]*Institute of Environmental Sciences, Université du Québec à Montréal, Québec, Canada.*

https://orcid.org/0000-0001-6418-5436

faghfouri.ali@courrier.uqam.ca

[2]*Department of Geography, Université du Québec à Montréal, Québec, Canada.*

https://orcid.org/0000-0003-4757-3124

germain.daniel@uqam.ca

[3]*Department of History and Geography, Université de Moncton, New Brunswick, Canada.*

https://orcid.org/0000-0002-9583-9188

guillaume.fortin@umoncton.ca

The paper is under revision for Earth Surface Processes and Landforms.
(https://onlinelibrary.wiley.com/journal/10969837)

Résumé

Cette étude propose un cadre statistique complet et multi-méthodes pour quantifier la dynamique du transport sédimentaire et l'activité géomorphologique dans une section représentative de la rivière du Diable (Mont-Tremblant, Québec, Canada). En combinant les données granulométriques de 32 échantillons de falaises et de plages avec des mesures hydrauliques, nous avons évalué les taux de transport à l'aide de cinq approches de modélisation : la contrainte de cisaillement (SSA), la pente énergétique (ESA), la régression (RA), la méthode probabiliste (PA) et la mobilité égale (EMA). Des équations sans dimension de charriage ont été appliquées à la fois aux tailles de grains moyennes et spécifiques aux échantillons. Les résultats indiquent que les échantillons de falaises produisent systématiquement des taux de transport plus élevés que ceux des plages, en particulier pour la fraction grossière (Φ_{90}), soulignant l'influence de la pente, de la granulométrie et des conditions hydrauliques locales. La variabilité temporelle a été évaluée à l'aide de l'analyse de la puissance du cours d'eau et des courbes de durée d'écoulement (FDC), identifiant des périodes d'activité géomorphologique accrue lors de la fonte nivale printanière et des crues épisodiques, notamment en 2011 et 2017-2019. Les schémas spatiaux de risque d'érosion ont été cartographiés à l'aide de l'Indice de Transport Sédimentaire (STI) et de l'Indice de Puissance du Cours d'eau (SPI), dérivés de modèles numériques de terrain à haute résolution. Les zones de STI et SPI élevés correspondent étroitement aux points chauds prédits par les modèles, démontrant un lien étroit entre l'énergie hydraulique, la topographie et la disponibilité des sédiments. Nos résultats suggèrent que les falaises agissent comme des sources sédimentaires à fort potentiel de transport, tandis que les plages jouent un rôle de zones de remaniement, en particulier lors d'événements à haute énergie affectant les matériaux grossiers. Ce cadre intégratif constitue une approche robuste et transférable pour identifier les points chauds géomorphologiques dans les systèmes fluviaux de petite à moyenne taille soumis à une variabilité hydrologique saisonnière.

Mots-clés : géomorphologie fluviale, modélisation du transport sédimentaire, analyse granulométrique, équations sans dimension du charriage, Indice de Transport Sédimentaire (STI), Indice de Puissance du Cours d'eau (SPI), courbe de durée d'écoulement (FDC), dynamiques hydro-sédimentaires

Abstract

This study proposes a comprehensive multi-method statistical framework to quantify sediment transport dynamics and geomorphic activity in a representative section of the Diable River (Mont-Tremblant, Quebec, Canada). By combining grain-size data from 32 cliff and beach samples with hydraulic measurements, we assessed transport rates using five modeling approaches: Shear Stress (SSA), Energy Slope (ESA), Regression-based (RA), Probabilistic (PA), and Equal Mobility (EMA). Dimensionless bedload equations were applied to both mean and sample-specific grain sizes. Results indicate that cliff samples consistently yield higher transport rates than beach samples, particularly for coarser grain fraction (Φ_{90}), highlighting the influence of slope, grain size, and local hydraulic conditions. Temporal variability was assessed using stream power analysis and flow duration curves (FDCs), identifying periods of heightened geomorphic activity during spring snowmelt and episodic floods, notably in 2011 and 2017-2019. Spatial patterns of erosion risk were mapped using the Sediment Transport Index (STI) and Stream Power Index (SPI), derived from high-resolution digital elevation models. Zones of high STI and SPI closely match model-predicted hotspots, demonstrating a close coupling between hydraulic energy, topography, and sediment availability. Our findings suggest that cliffs act as sediment sources with high transport potential, while beaches function as reworking zones, particularly during high-energy events for coarser materials. This integrative framework provides a robust and transferable approach to identify geomorphic hotspots in small to medium-sized fluvial systems subject to seasonal hydrological variability.

Keywords: Fluvial geomorphology, Sediment transport modeling, Grain size analysis, Dimensionless bedload equations, Sediment Transport Index (STI), Stream Power Index (SPI), Flow duration curve (FDC), Hydro-sedimentary dynamics

4.1. Introduction

River systems are dynamic environments where geomorphic processes such as erosion, sediment transport, and channel adjustment are governed by complex interactions between hydraulic forces and sediment properties. Accurately characterizing these processes is essential for anticipating fluvial responses to climatic variability, extreme flood events, and human-induced changes in land use and hydrology (Nerantzaki et al., 2015; Hirschberg et al., 2021). While many studies have emphasized the variability of sediment transport mechanisms and the importance of local controls, especially grain-size heterogeneity, quantifying sediment flux across diverse fluvial settings remains challenging due to spatial heterogeneity in geomorphic context and temporal fluctuations in flow regimes (Kumar et al. 2024; Le Minor et al. 2022).

Statistical modeling offers powerful tools to address these challenges by integrating physical observations with empirical relationships to estimate sediment mobility and geomorphic dynamics. Deterministic models, particularly those based on shear stress (SSA) and energy slope (ESA) formulations, define physically meaningful thresholds for sediment entrainment (e.g., Shields, 1936; Meyer-Peter & Müller, 1948). These remain foundational due to their mechanistic clarity and widespread use in laboratory and field applications (Hidayati et al., 2023; Wang et al., 2023), although their application in natural rivers is often limited by calibration uncertainties.

Regression-based approaches, linear, nonlinear, or log-transformed, offer simplicity and ease of calibration against field data. They establish empirical relationships between sediment transport rates and hydraulic parameters such as discharge, slope, and grain size (Ampomah et al., 2020a,b; Harun et al., 2021; Grauso et al., 2021). Classic formulations by Yalin (1963), Engelund & Hansen (1967), Ashida & Michiue (1972), Engelund-Fredsøe (1976) rely on statistically derived coefficients and exponents to predict bedload transport.

Probabilistic models conceptualize sediment movement as a stochastic process governed by turbulence and grain interactions (Einstein, 1942; Einstein, 1950; Parker, 1979). These are especially suitable for event-driven systems with episodic sediment pulses (Furbish et al., 2012; Monsalve et al., 2016; Shojaeezadeh et al., 2018).

Recently, machine learning (ML) and deep learning (DL) models have emerged as data-driven alternatives capable of capturing nonlinear sediment dynamics from large datasets (Heng and Suetsugi, 2013; Allawi et al., 2023; Latif et al., 2023). However, their use in cold-region rivers is limited by high data demands and low interpretability (Javadi et al., 2022). Hybrid models that combine deterministic, probabilistic, and machine learning components show increasing promise in capturing spatio-temporal sediment complexity (Ehteram et al., 2021; Zounemat-Kermani et al., 2020).

Despite this growing diversity of tools, few studies have compared or combined multiple modeling paradigms within a single, instrumented cold-region fluvial system. Most research tends to apply only one model family or focus on isolated time periods, limiting our understanding of sediment dynamics where erosion, deposition and transport co-occur.

To address this gap, we develop a multi-method statistical framework to model sediment transport and geomorphic activity in a flood-prone, meandering reach of the Diable River (Mont-Tremblant, Québec, Canada). Our objectives are to: 1) quantify how grain size and hydraulic conditions influence sediment transport using a suite of dimensionless bedload equations; 2) contrast spatial patterns between cliff (erosional) and beach (depositional) environments; and 3) identify the timing and intensity of geomorphic activity using stream power analysis, flow duration curves (FDCs), and spatial indices (STI, SPI).

We hypothesize that cliff segments function primarily as sediment sources with high potential but limited reworking, while beaches act as reworking zones that mobilize and redistribute sediments downstream, particularly during high-energy events.

4.2. Study Area and Sediment Characteristics

The Diable River is a mid-sized river system located in the Lanaudière and Laurentides regions of Quebec, Canada (Figure 4.1a). It originates from Lac du Diable, a 2.5 km-long lake in the Lac-Legendre territory of the Matawinie Regional County Municipality and flows southward for 82 km through Mont-Tremblant National Park. This protected watershed encompasses more than 400 lakes, numerous tributaries, and six major river corridors.

The region experiences a humid continental climate (Dfb, Köppen classification), with cold winters, warm summers, and precipitation distributed throughout the year. The Diable River exhibits a nivo-pluvial hydrological regime, typical of mid-elevation forested basins in southern Quebec. Its average annual discharge is approximately 30 m^3/s, but peak flows during the spring snowmelt frequently exceed 150 m^3/s and can occasionally surpass 200 m^3/s. Low-flow conditions occur in mid-winter (February), when precipitation is stored as snow, and again in late summer (August), owing to high evapotranspiration and declining groundwater levels. The average annual temperature is 3.5 °C, and the average annual precipitation is 1,130 mm at the Saint-Donat weather station for the period 1981–2010. Nearly 25% of the precipitation falls as snow (279.6 mm), mostly from November to April. Availability of observations recorded by weather stations in the study area is complicated because the St-Jovite station has several missing precipitation data (for the 1991–2020 period). However, two other weather stations are located within a radius of less than 50 km of the watershed boundaries (Arundel and Saint-Donat), but the normals cover the period from 1981 to 2010. However, it is important to have this data to better understand the climatic context that influenced the amount of water contributed by rain or snowmelt. We therefore also used MSWX data to supplement data from nearby stations. Multi-Source Weather (MSWX) is a high-resolution operational weather product (updated every 3 hours, with a grid resolution of 0.1°, or approximately 11.1 km in our study area), with bias correction applied (Beck et al., 2022). We thus obtained the variable values for grids within the watershed for the years in which significant geomorphological activity was observed (winters of 2010–2011, 2016–2017, 2017–2018, 2018–2019, and 2022–2023). The selected study reach (Figure 4.1b) is in a meandering section characterized by alternating cliff (erosional) and beach (depositional) environments, making it ideally suited for paired sampling. The river exhibits high sinuosity and pronounces lateral migration, shaped by a transition zone between resistant bedrock and unconsolidated glaciofluvial

deposits. This geologic setting fosters morphological complexity and promotes local instabilities such as bank undercutting and episodic sediment redistribution.

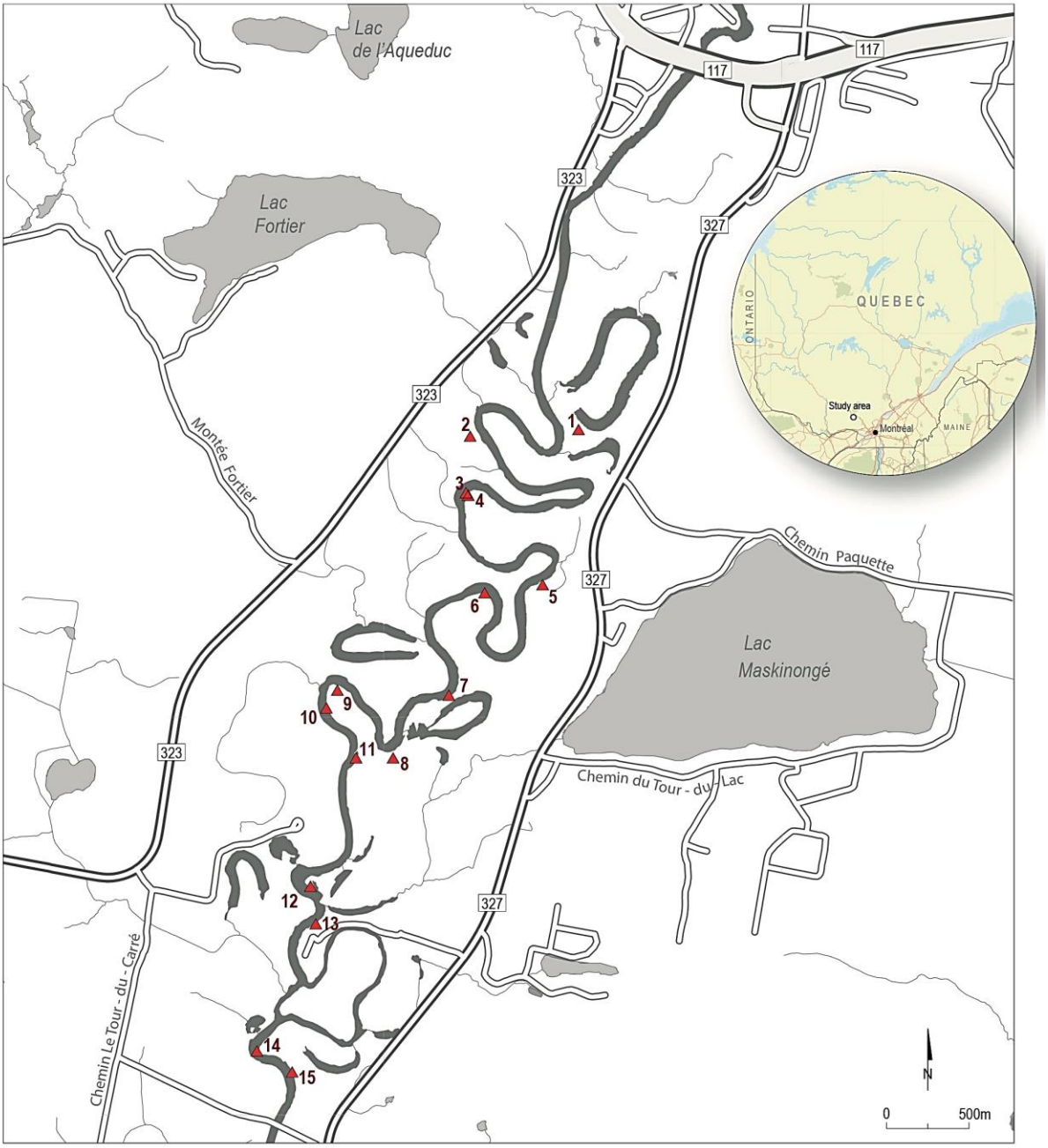

Figure 4.1. Location and geomorphic setting of the Diable River watershed (Quebec, Canada). The red dots show the placement of sample locations.

A total of 32 samples were collected along this reach, from paired cliff and beach locations, allowing direct comparison of contrasting geomorphic context. Grain size distributions were analyzed using the Folk and Ward (1957) method, yielding parameters including mean grain size, sorting, skewness, and kurtosis (Please see Appendix B.4.1). These descriptors provide insight into depositional processes and sediment transport dynamics.

The riverbed is predominantly sandy, ranging from fine to very coarse sand, and exhibits moderate to well sorting. Cliff samples typically display a downstream fining trend, with coarser grains upstream and finer sediments becoming more dominant downstream. Beach samples show greater variability, with coarse sands appearing at both ends of the reach and medium sands more prevalent in the mid-section. Sorting is consistently better in beach samples, which range from moderately well to well sorted, whereas cliff samples ate generally poorly or moderately sorted, indicative of limited reworking and episodic input. Skewness patterns diverge across environments: cliff samples tend to be symmetrical or very finely skewed, while beach samples display a broader range from fine to coarse skewness. This divergence suggests selective entrainment and hydraulic sorting within depositional zones.

To further quantify sediment texture and sorting, percentile-based metrics (d_{10}, d_{25}, d_{50}, d_{75}, d_{90}) were computed from cumulative grain-size distributions. Sorting indices such as d_{90}/d_{10} and d_{75}/d_{25} where derived to characterize grain-size dispersion (Figure 4.2). Higher d_{90} values in beach samples confirm the local accumulation of coarser particles, likely derived from nearby cliffs. In contrast, higher d_{50} values in cliff samples suggest retention of finer sediments, though these may be mobilized during high flows. Sorting rations (d_{90}/d_{10} and d_{75}/d_{25}) are higher in cliff samples, indicating greater textural heterogeneity, possibly resulting from mass wasting or undercutting processes. In comparison, beach samples display lower ratios, consistent with sustained hydraulic reworking.

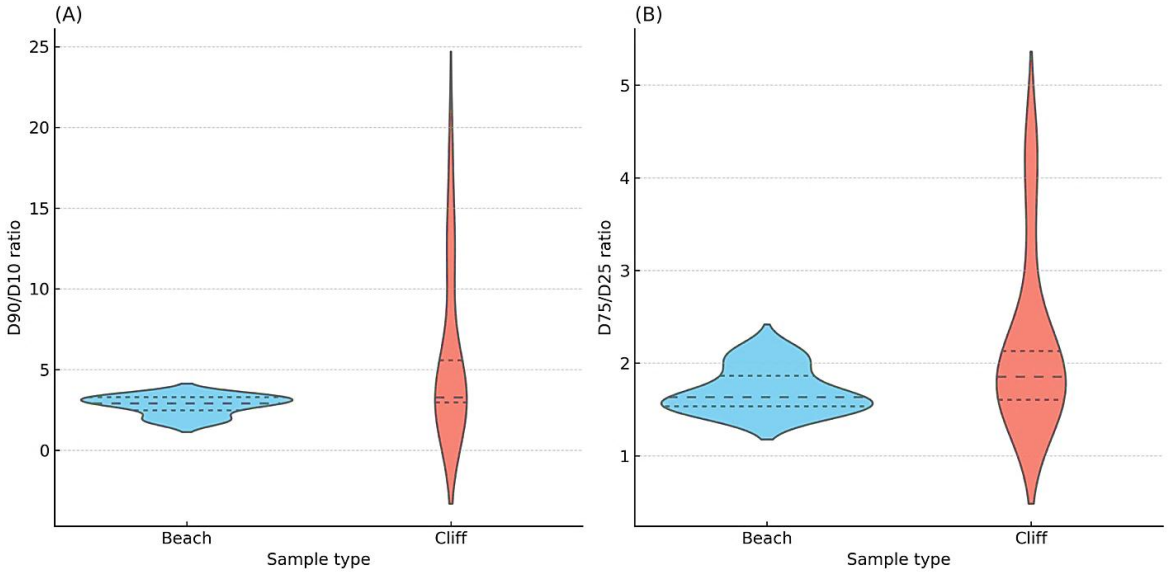

Figure 4.2. Violin plots of grain-size ratios d_{90}/d_{10} (a) and d_{75}/d_{25} (b) for cliff and beach samples. Each violin plot displays the full distribution of grain-size ratios for each sample type. The width of each violin plot represents the relative density of observations at different values. The central dashed line indicates the median, while the two horizontal dashed lines within the violin indicate the first and third quartiles.

In summary, the granulometric analysis underscore a clear functional differentiation: cliffs serve as sediment sources characterized by poorly sorted, heterogeneous deposits, while beaches act as

zones of active reworking and sorting particularly during high-energy events that mobilize coarser fractions.

4.3. Methodology

4.3.1. Bedload transport modeling framework

To estimate bedload transport rates, we implemented five distinct modeling paradigms commonly used in fluvial geomorphology: Shear Stress Approach (SSA), Energy Slope Approach (ESA), Probabilistic Approach (PA), Regression-based Approach (RA), and Equal Mobility Approach (EMA) (Hosseiny et al., 2023; Ancey, 2020a, b).

Each models links hydraulic and sedimentological parameters to estimate bedload transport under open-channel flow conditions. The framework integrates site-specific grain-size distributions and hydraulic variables (discharge, slope, flow depth, and sediment density) obtained from field surveys and hydrological records. Transport rates are expressed in dimensionless form (Φ), allowing for cross-model comparisons. The initiation of sediment motion is defined by the exceedance of a critical bed shear stress (τc), typically determined using the Shields criterion (θc) (Shields, 1936; Ancey, 2020a, b).

4.3.1.1. Initial parameters and base equations

Table 4.1 summarizes the core hydraulic and sedimentological parameters used in all five modeling approaches. These include variables such as shear stress (τ), Shields stress (θ), shear velocity (u), and unit discharge (q).

Table 4.1. Computed hydraulic and sediment parameters (excerpt)

Parameter	Equation	Value	Units	Description
Shear stress	$\tau = \rho g h S$	6.87	Pa	Shear stress exerted by the flow on the channel bed surface
Critical shear stress	$\tau_c = \varphi \rho_s g d50$	0.59	Pa	Minimum shear stress required to initiate sediment motion
Shields parameter	$\theta = \frac{\tau}{(\gamma_s - \gamma)d}$	0.88	---	Dimensionless parameter expressing the ratio of applied shear to resisting gravitational force on a particle
Shields critical	$\theta_c = \frac{\tau_c}{(\gamma_s - \gamma)d}$	0.075	---	Threshold Shields value above which sediment transport begins
Shear velocity	$u_* = \sqrt{\frac{\tau}{\rho}}$	0.083	m s^{-1}	Friction velocity representing flow turbulence near the bed
Critical shear velocity	$u_{*cr} = \sqrt{\frac{\tau_{cr}}{\rho}}$	0.024	m s^{-1}	Minimum friction velocity needed to initiate sediment motion

Table 4.2 presents definitions and representative values for key physical parameters derived from field measurements and laboratory analyses. These values, grain size (d_{50}), sediment and water density, slope, Manning's roughness coefficient, and cross-sectional geometry are representative of sandy-bed rivers in cold regions. Together, Tables 4.1 and 4.2 form a standardized input dataset for all models, ensuring internal consistency across formulations.

Table 4.2. Definitions and values of hydraulic and sediment parameters used in bedload modeling

No.	Variable	Symbol	Value	Units	Description
1	Density of water	ρ	1000	kg m^{-3}	Standard freshwater density
2	Density of sediment	ρ_s	2650	kg m^{-3}	Quartz-based sediment
3	Gravitational acceleration	g	9.81	m s^{-2}	Constant
4	Flow depth	h	5	m	Computed from A / B
5	Cross-sectional area	A	200	m	Field-measured
6	Top width of river	B	40	m	Field-measured
7	Flow velocity	v	1.16	m s^{-1}	From Q / A
8	Maximum discharge	Q	232	m^3 s^{-1}	From discharge records
9	Channel slope	S	0.00014	---	Derives via Manning's equation
10	Hydraulic radius	R	4	m	R = A / P
11	Wetted perimeter	P	50	m	Fieldwork observations
12	Median grain size	d_{50}	0.0004845	m	Grain size analysis
13	Manning's roughness Coefficient	n	0.025	---	Sandy-bed rivers
14	Specific weight of water	γ	9810	N m^{-3}	$\gamma = \rho g$
15	Specific weight of sediment	γ_s	25996.5	N m^{-3}	$\gamma_s = \rho_s g$
16	Specific gravity of sediment	Gs	2.65	---	$Gs = \rho_s / \rho$
17	Unit discharge	q	5.8	m^2 s^{-1}	$q = Q / B$
18	Empirical coefficient	φ	0.047	---	For sandy rivers (Shields-related)

4.3.1.2. Shear Stress Approach (SSA)

The SSA directly relates bedload transport to the excess bed shear stress (Hidayati et al., 2023). Sediment transport occurs when the applied shear stress (τ) exceeds the critical threshold (τc), defined by the Shield parameter ($\theta > \theta c$). Originating from Shields (1936), this approach is widely applied in experimental and natural settings (Wang et al., 2023).

Although conceptually simple, SSA models differ in how they define transport thresholds and the functional dependence on excess. We tested ten classical SSA equations (Table 4.3), including those by Wilson (1966), Fernandez-Luque & van Beek (1976), Graf & Suszka (1987), and Wong & Parker (2006a, b). These equations encompass a range of empirical and theoretical formulations and allow assessment of model sensitivity under consistent hydraulic conditions.

Table 4.3. The shear stress approach equations

No.	Reference	Equation
1	Wilson (1966)	$\Phi = 12(\theta - \theta_c)^{3/2}$
2	Fernandez-Luque & van Beck (1976)	$\Phi = 5.7(\theta - \theta_c)^{3/2}$
3	Graf & Suszka (1987)	$\Phi = \begin{cases} 10.4\theta^{1.5}\left(1 - \frac{0.045}{\theta}\right)^{2.5} & \theta < 0.068 \\ 10.4\theta^{2.5} & \theta \geq 0.068 \end{cases}$
4	Ashmore (1988)	$\Phi = 3.11(\theta - 0.045)^{1.37}$
5	Wiberg & Smith (1989)	$\Phi = \alpha_s(\theta - \theta_c)^{3/2}$ $\alpha_s = 9.64(\theta^{0.166})$
6	Soulsby (1997)	$\Phi = 5.1(\theta - \theta_c)^{3/2}$
7	Graf (1998)	$\Phi = 8(\theta - \theta_c)^{3/2}$
8	Ribberink (1998)	$\Phi = 11(\theta - \theta_c)^{1.65}$
9	Wong & Parker (2006a)	$\Phi = 4.93(\theta - 0.047)^{1.6}$
10	Wong & Parker (2006b)	$\Phi = 3.97(\theta - 0.0495)^{3/2}$

4.3.1.3. Energy Slope Approach (ESA)

ESA uses the energy gradient of flow (rather than shear stress) as the main driver of sediment transport. It assumes that only surplus energy, beyond that needed to overcome resistance, contributes to particle motion (Schneider et al. 2016; Huang et al. 2010). We applied the widely used Meyer-Peter & Müller (MPM) equation (1948) to compute the dimensionless transport rate (Φ). Originally derived from flume studies, the MPM model remains relevant for estimating sediment fluxes in natural systems.

$$\Phi = \begin{cases} 8(\theta - \theta_c)^{\frac{3}{2}} & \theta \geq \theta_c \\ 0 & \theta < \theta_c \end{cases} \quad (1$$

4.3.1.4. Probabilistic Approach (PA)

The PA treats sediment transport as a stochastic process shaped by turbulent fluctuations, grain interactions, and bed surface heterogeneity. Rather than relying on a deterministic threshold, PA models estimate the probability of particle entrainment under variable flow conditions (Einstein, 1950; Furbish et al., 2012).

We applied two classical formulations: Einstein's transport function (1950; Equation 2) and Parker's nonlinear adaptation (1979; Equation 3), both of which yield dimensionless transport rates

(Φ). These models are particularly suited to systems like the Diable River, where flashy flows, coarse grains, and intermittent supply challenge deterministic modeling (Armanini et al., 2015).

Einstein (1950): (2

$$\Phi = \begin{cases} \dfrac{\text{Kexp}\left(-\dfrac{0.391}{\theta}\right)}{0.465}\theta < 0.182 \\ 40K\theta^3 \qquad\qquad \theta \geq 0.182 \end{cases}$$

Where $K = \sqrt{\dfrac{2{,}36}{3}\dfrac{d^3}{3}} - \sqrt{\dfrac{36}{d^3}}$

Parker (1979): (3

$$\Phi = 11.20\frac{(\theta-0.03)^{4.5}}{\theta^3}$$

4.3.1.5. Regression-Based Approach (RA)

RA models use empirical relationships derived from flume or field datasets to relate Φ to hydraulic and sediment variables (e.g., slope, velocity, d_{50}). Such models are especially useful where transport behavior is too nonlinear or site-specific for mechanistic predictions (Sinnakaudan et al., 2006).

We applied 12 regression-based equations, including seminal works by Yalin (1963), Engelund & Hansen (1967), Ashida & Michiue (1972), and Engelund & Fredsoe (1976), along with more recent formulations for sand- and gravel-bed rivers, such as Van Rijn (1993), Nino & Garcia (1994), Julien (1995, 2002), Madsen (1991), Nelson (1988), Abraham & Gao (2006), and Camenen et al. (2006).

Table 4.4. Regression-based equations for predicting dimensionless bedload transport rates

No.	Reference	Equation
1	Yalin (1963)	$\Phi = 0.635r\sqrt{\theta}\left[1 - \dfrac{1}{\sigma r}\ln(1+\sigma r)\right]$ $r = \dfrac{\theta}{\theta_c} - 1 \qquad \sigma = 2.45\dfrac{\sqrt{\theta_c}}{s.4}$
2	Engelund & Hansen (1967)	$\Phi = 0.05\left(\dfrac{u}{u_*}\right)^2 \theta^{5/2}$
3	Ashida & Michiue (1972)	$\Phi = 17(\theta - \theta_c)\left[(\theta)^{1/2} - (\theta_c)^{1/2}\right]$
4	Engelund-Fredsoe (1976)	$\Phi = 18.74(\theta - \theta_c)\left[(\theta)^{1/2} - 0.7(\theta_c)^{1/2}\right]$
5	Nelson (1988)	$\Phi = 12\theta^{1/2}(\theta - \theta_C)$
6	Madsen (1991)	$\Phi = \left(\theta^{1/2} - 0.7\theta_c^{1/2}\right)(\theta - \theta_c)$
7	Van Rijn (1993)	$\Phi = \dfrac{0.053}{d_*^{0.3}}\left(\dfrac{\theta}{\theta_c} - 1\right)^{2.1}$
8	Nino & Garcia (1994)	$\Phi = \dfrac{12}{\mu_d}\left(\theta^{1/2} - 0.7\theta_c^{1/2}\right)(\theta - \theta_c),\ \mu_d = 0.23$

9	Julien (1995)	$\Phi = \begin{cases} 2.15e^{-0.391/\theta} & \theta < 0.18 \\ 40\theta^3 & 0.18 \le \theta \le 0.52 \\ 15\theta^{1.5} & \theta > 0.52 \end{cases}$
10	Julien (2002)	$\Phi = \frac{18\sqrt{g}d^{3/2}\theta^2}{\sqrt{g(s-1)d^3}}$
11	Abrahams & Gao (2006)	$\Phi = \theta^{1.5}\left(1 - \frac{\theta_c}{\theta}\right)^{3.4}\frac{u}{u_*}$
12	Camenen et al. (2006)	$\Phi_b = 12\theta^{0.5}\exp\left(-4.5\frac{\theta_c}{\theta}\right)$

4.3.1.6. Equal Mobility Approach (EMA)

EMA assumes that, beyond a certain energy threshold, all sediment fractions become equally mobile. This allows transport to be modeled using a representative grain size (typically d_{50}) rather than the full distribution (Marion et al. 2003). This simplification is valuable in systems with moderately sorted sediments and episodic high flows.

We implemented the Wilcock (2001) formulation (Equation 4), which incorporates a modified Shields parameter to account for relative mobility. EMA was initially developed for sand-gravel rivers and validated in several settings (Wilcock & Crowe, 2003; Gaeuman et al., 2009). It is well suited for the Diable River, where sediment is predominantly sandy, moderately sorted, and mobilized during spring floods.

$$\Phi = \frac{q_b}{\sqrt{\left(\rho s/\rho - 1\right) d^3}}$$

Where,

$$q_b = \frac{W_s^* u_*^3 \rho_s}{(s-1)g} \qquad W_s^* = 11.2\left(1 - 0.846\theta_{50}^{-\frac{1}{2}}\right)^{4.5} \tag{4}$$

$$\theta = \frac{u_*^2}{(s-1)gd}, \theta_{50} = \frac{\theta}{\theta_c}$$

4.3.2. Timing of Geomorphic Activity

Temporal variations in geomorphic activity were assessed using stream power analysis, a widely accepted proxy for the energy available to entrain sediment and reshape the riverbed. Stream power per unit width (ω) is calculated as:

$$\omega = \rho_w \cdot g \cdot q \cdot S \tag{5}$$

where ρ_w is water density (kg m^{-3}), g is gravitational acceleration (m s^{-2}), q is unit discharge (m^2 s^{-1}), and S is channel slope.

Unit discharge q(t) is estimated as:

$$q\,(t) = \frac{Q\,(t)}{B} \tag{6}$$

where Q(t) is the daily river discharge ($m^3 s^{-1}$) and B is channel width (40 m, based on field data).

To identify periods of active sediment transport, we computed a critical stream power threshold (ω_c), derived from the hydraulic and sediment properties listed in Tables 4.1 and 4.2:

$$\omega_{\text{critical}} = \tau_c \cdot U_{\text{critical}} \quad (7$$

$$U_{\text{critical}} = \sqrt{\frac{\tau_c}{\rho_w}} \quad (8$$

where $U_{critical}$ is the critical shear velocity. Based on site-specific parameters, $\omega_{critical}$ was calculated as 0.0144 and $U_{critical}$ as 0.0243.

Periods when $\omega(t) > \omega_c$ were interpreted as indicative of significant geomorphic activity, including sediment mobilization, bank erosion, and bed reworking (Magilligan et al., 2015; Yochum et al., 2017). These periods generally coincide with snowmelt events or intense rainfall.

4.3.3. Sediment Transport Index (STI)

The STI is a topographic metric that identifies areas with high erosion and transport potential by combining upslope contributing area and local slope (Asadi et al. 2025). It is calculated as:

$$STI = \left(\frac{As}{22.13}\right)^{0.6} \times \left(\frac{\sin\theta}{0.0896}\right)^{1.5} \quad (9$$

where A_s is the upslope contributing area per unit width (m^2), and θ is the slope angle (in degrees).

Higher STI values are associated with locations where steep slopes and converging flow enhance sediment transport, such as along undercut banks, rills, or unstable hillslopes. In this study, STI was computed from a high-resolution digital elevation model (DEM) using standard GIS-based hydrological modeling tools.

STI maps were generated for the entire study area to highlight spatial contrast in erosion risk and sediment delivery potential, with particular attention to the contrast between cliff and beach zones. These maps provide spatially explicit estimates of morphodynamic potential and contribute to identifying geomorphic hotspots.

4.3.4. Stream Power Index (SPI)

The SPI, also referred to as Sediment Power Index in some literature, estimates the erosive potential of concentrated surface runoff by combining slope and upstream drainage area (Abu El-Magd et al. 2021). It is computed as:

$$SPI = \left[\ln(As + 0.001) \times \left(\frac{\beta}{100} + 0.001\right)\right] \quad (10$$

where As is the upslope contributing area (m^2), and β is the slope in percent. The small constant (0.001) avoids undefined values in flat terrain.

Higher SPI values indicate zones where steep gradients and concentrated runoff combine to increase hydraulic energy, typically corresponding to incised channels, steep headwaters, or bank

erosion sites. SPI was calculated using the same DEM and GIS workflow as STI, allowing for comparative analysis.

The resulting SPI maps provide a hydro-geomorphic interpretation of energy concentration along drainage pathways. When integrated with STI, ω(t), and sediment grain-size data, SPI enhances the spatial diagnosis of fluvial processes.

4.3.5. Flow Duration Curve (FDC)

The FDC are used to represent the temporal distribution of discharge and to identify flow magnitude associated with different recurrence probabilities. FDCs plot the discharge (Q) against the percentage of time it is equaled or exceeded, offering insights to flow variability, magnitude, and persistence (Ghotbi et al., 2020).

We applied a log-normal distribution model to describe the FDC, well-suited for snowmelt-driven rivers like the Diable (Ma et al., 2024). The model assumes that the natural logarithm of discharge follows a normal distribution:

$$f(x) = \frac{1}{x\sqrt{2\pi}\sigma} exp\left[-\frac{1}{2\sigma^2}(ln\, x - \mu)^2\right] \quad x > 0 \qquad (11$$

where x is the discharge, μ is the logarithmic mean and σ is the logarithmic standard deviation (scale parameter).

FDCs were generated using daily discharge records from 2009 to 2023. Specific percentiles (Q_{10}, Q_{50}, Q_{90}) were extracted to classify extreme, median, and low-flow conditions. The values were then compared with the stream power threshold ω_c to evaluate the frequency and duration of flows capable of initiating geomorphic activity. This integrative approach enables the temporal classification of years by their geomorphic effectiveness, providing essential context for interpreting model outputs and understanding sediment dynamics in relation to hydroclimatic regimes.

4.4. Results

4.4.1. Bedload estimates derived from mean d_{50} grain size

Using the modeling approaches described in Section 4.3.1, dimensionless bedload transport rates (Φ) were computed using the mean grain size (d_{50}). The outputs were compared across model families and individual formulations (Figure 4.3).

Results show considerable variation among models, with Φ values ranging from near 1 to over 30. The overall mean value (Φ = 7.09), indicated by the red dashed line in Figure 4.3, serves as a benchmark. Most models fall between (Φ) 3 and 10, but several outliers exceed this range.

Shear stress-based models (blue), such as Wilson (1966), Graf & Suszka (1998), Wiberg & Smith (1989), and Ribberink (1998) produce values close to the mean, indicating relatively stable and coherent predictions grounded in physically based thresholds. These models are particularly appropriate for sandy-bed rivers like the Diable River.

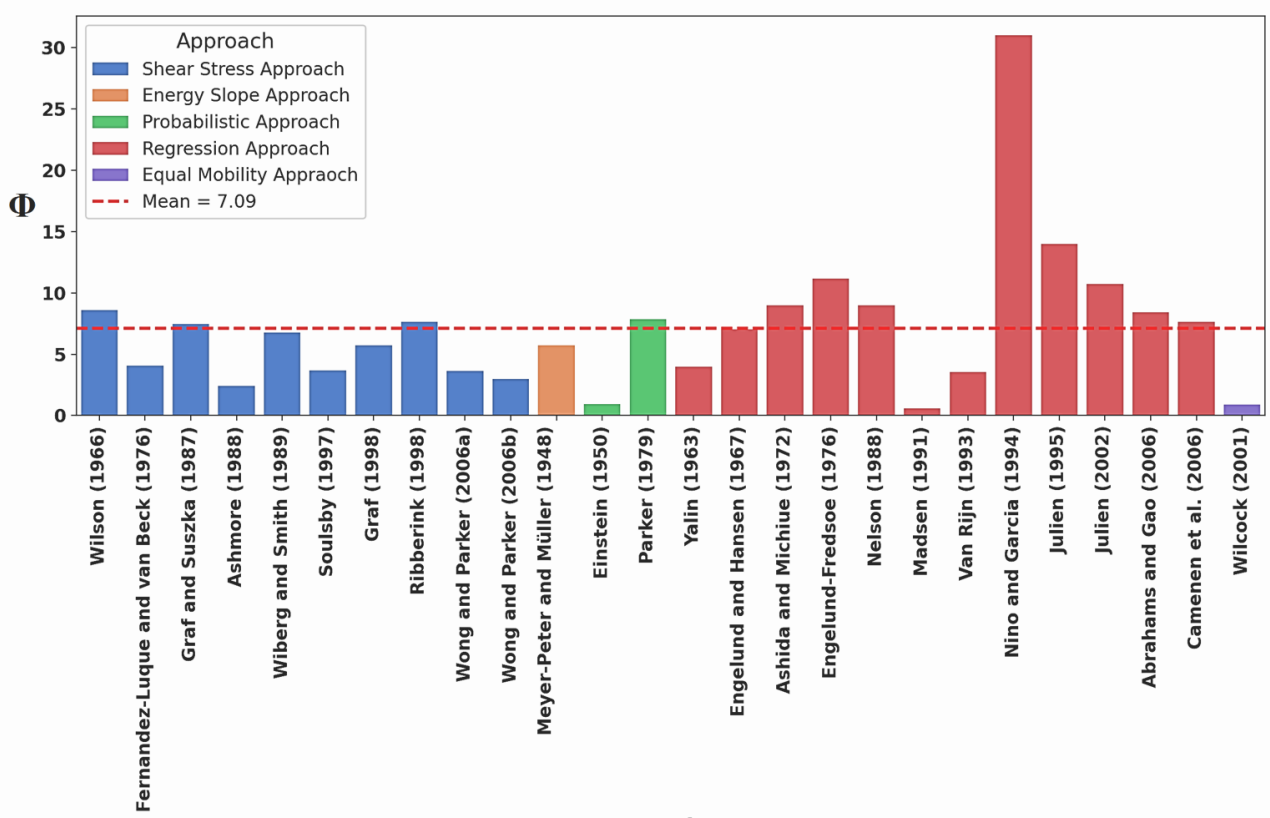

Figure 4.3. Comparison of dimensionless bedload transport rates (Φ) predicted by a range of equations grouped by modeling approach. The red dashed line indicates the overall mean (Φ = 7.09). Color coding reflects the theoretical basis of each model. Y-axis: Dimensionless bedload transport rates (Φ).

Regression-based models (red) display the widest dispersion. Notably, the Nino & Garcia (1994) formulation yields an outlier result (~30), likely due to overprediction in coarse, mixed-grain conditions. Conversely, the formulations of Camenen et al. (2006), Engelund & Hansen

(1967), and Abrahams & Gao (2006) fall nearer to the mean and align better with expected transport dynamics.

Probabilistic models (green), such as Einstein (1950), tend to predict lower transport rates, reflecting their sensitivity to flow intermittency. Parker (1979) provides a result closer to the mean, suggesting better accommodation of coarse-bed conditions.

The energy slope model (orange) of Meyer-Peter & Müller (1948) yields intermediate Φ values close to the mean, validating its application to high-energy systems, despite its laboratory origins.

The equal mobility model (purple) by Wilcock (2001) predicts the lowest Φ values overall, likely due to conservative entrainment assumptions in systems with moderately sorted sediments.

Overall, the results highlight the influence of model structure on transport estimates: regression-based models tend to overpredict, while physically based formulations, particularly those based on shear stress or energy slope yield more consistent values for cold-region rivers.

4.4.2. Sample-specific bedload estimates computed with multiple grain-size approaches

4.4.2.1. Shear Stress Approach (SSA)

Figure 4.4 presents the dimensionless transport rates (Φ) calculated using six shear stress-based equations applied to 32 sediment samples from both cliff and beach environments. Each model was used with three grain-size percentiles (d_{10}, d_{50}, and d_{90}) to capture the influence of fine, medium, and coarse fractions on transport estimates.

Although all SSA formulations share the foundational assumption that sediment transport scales with excess shear stress, they differ in the functional form and thresholds used, resulting in variability in Φ prediction. For instance, models such as Wilson (1966) and Graf (1998) applied to Φ_{90} in cliff samples yield considerably higher transport estimates compared to those applied to Φ_{10} and Φ_{50} in beach samples. Despite these differences, several consistent trends emerge:

- Φ_{90} values (coarse fraction) are systematically the highest across all models, particularly for cliff samples. This reflects the combined effect of steeper local slopes, coarser grain sizes, and elevated hydraulic energy, all of which promote high excess shear stress and enhanced mobilization.
- Beach samples consistently exhibit higher Φ values than cliff samples for Φ_{10} and Φ_{50}, suggesting that finer and moderately sized particles are more easily mobilized in depositional zones. This pattern likely results from repeated hydraulic reworking and sorting of available sediments during medium- to high-flow events.
- The contrast between cliff and beach sites is most pronounced for Φ_{90}, indicating a strong spatial control on the mobilization of coarser materials. This trend is less evident for finer fractions, where hydraulic thresholds for motion are more uniformly exceeded.
- The variability among SSA models also depends on the grain-size class. Coarser fractions tend to amplify differences in transport estimates, while finer fractions yield more consistent values across equations.

Overall, SSA reinforce the nonlinear relationship between grain size and transport potential. While finer fractions respond more uniformly to flow conditions, coarse grains are selectively mobilized under localized shear stress surges, especially at cliff sites where geomorphic thresholds are more frequently exceeded. The SSA framework, despite differences among formulations, effectively captures this spatial and granulometric structuring of bedload dynamics in the Diable River.

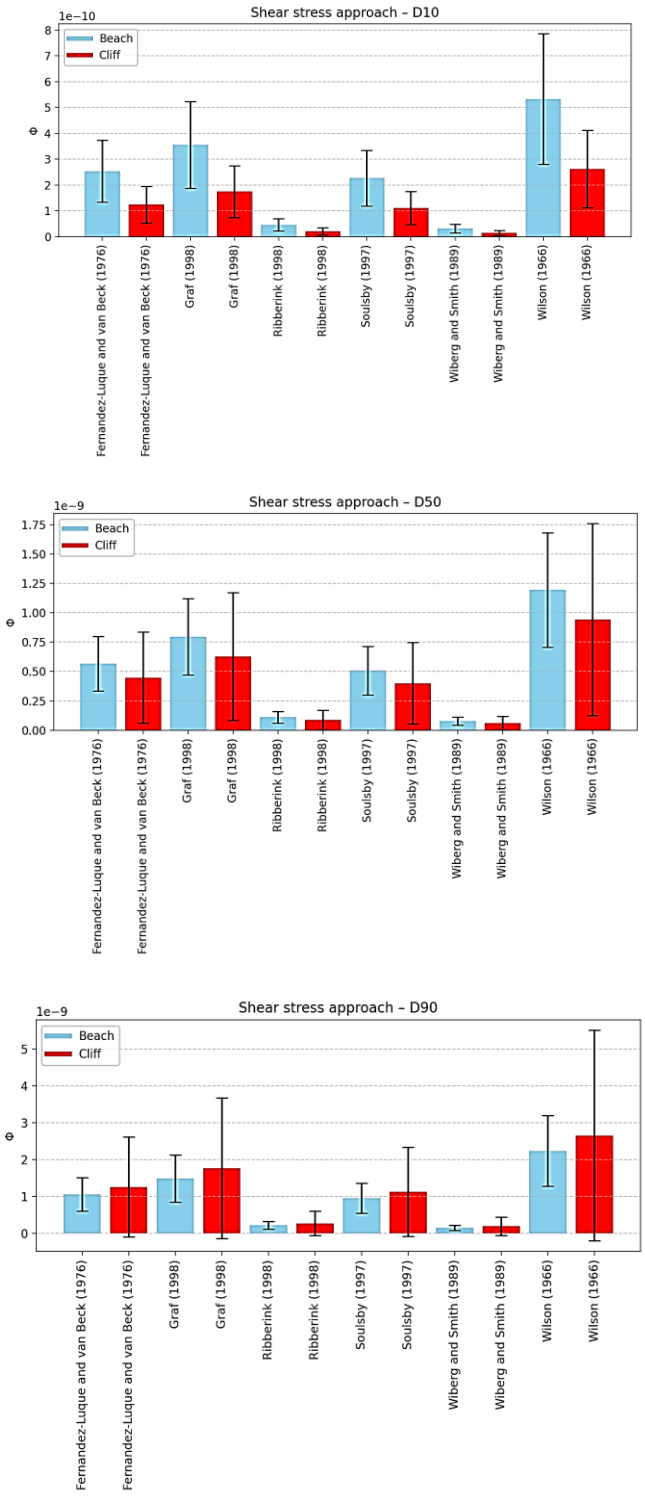

Figure 4.4. Bar chart showing the predicted dimensionless bedload transport rates (Φ) using six shear stress-based equations for two sedimentary site types (Cliff and Beach) and three grain-size percentiles (d_{10}, d_{50}, d_{90}). Each group of six bars represents one grain-size percentile, with Cliff sites shown in red and Beach sites in blue. Values represent the mean ± standard deviation calculated from the sampled sites along the studied river reach.

4.4.2.2. Energy Slope Approach (ESA)

Figure 4.5 presents the dimensionless bedload transport rates (Φ) estimated using the ESA, based on the Meyer-Peter & Müller (1948) equation. As expected, the ESA yields systematically lower Φ values than the SSA for all grain-size classes and sample types. This is largely due to the conservative nature of the MPM model, which was originally calibrated in flume experiments using uniform coarse sediments. Nevertheless, despite the lower magnitudes, several patterns observed in the SSA results are reproduced here with consistency:

- Φ_{90} values (coarse fraction) continue to produce the highest transport rates overall, particularly in cliff samples. This suggests that coarser particles located in steep, erosional environments experience the highest mobilization potential when flow energy exceeds the critical threshold.
- Beach samples exhibit higher Φ values than cliff samples for Φ_{10} and Φ_{50}, reinforcing the idea that finer to intermediate grain sizes are more easily entrained in depositional environments where sediment is actively reworked by repeated flow events.
- The magnitude of transport rate differences between sample types is lower than in SSA results. This may be attributed to the more uniform energy input assumed by the ESA and the absence of explicit shear stress thresholds sensitive to localized turbulence and slope variation.
- The variability within and between sample types is smaller in ESA than in SSA. For example, the standard deviation for Φ_{90} values is narrower in beach samples, suggesting that in ESA, the influence of site-specific conditions is somewhat dampened compared to more physically detailed models.

In summary, while the ESA tends to underestimate absolute transport rates, particularly for coarse material, it reproduces the same grain-size-dependent trends seen in SSA: i) transport increases with grain size; ii) cliffs dominate at Φ_{90}, and; iii) beaches show higher transport at Φ_{10} and Φ_{50}. The reduced variability in ESA results may reflect the influence of uniform energy assumptions and simplified sediment response mechanics inherent in the model. Nevertheless, these findings confirm the role of local slope and grain-size effects in driving sediment mobility, even when modeled through a conservative energy-based framework.

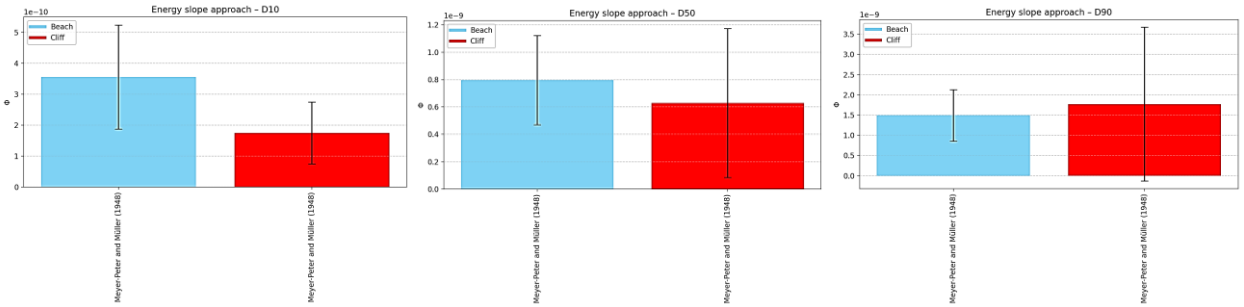

Figure 4.5. Bar chart showing the predicted bedload transport rates (Φ) for the Energy Slope Approach (Meyer-Peter & Müller, 1948), grouped by grain-size percentiles (d_{10}, d_{50}, d_{90}) and site type (Cliff vs. Beach). Error bars represent ±1 standard deviation across the sampled sites.

4.4.2.3. Regression Approach (RA)

Figure 4.6 presents the dimensionless bedload transport rates (Φ) calculated using five regression-based equations. This family of models relies on empirical relationships derived from flume or field datasets, offering a complementary perspective to physically based approaches.

As expected, the RA yields the widest range of Φ values, both in terms of absolute magnitude and variability across samples and grain sizes. This dispersion reflects the diversity of datasets and hydraulic conditions under which the original regressions were calibrated:

- Φ_{90} values are again the highest in most models, particularly in cliff samples. Notably, the formulation by Nino & Garcia (1994) produces the most extreme transport rates, with Φ values often exceeding 25–30 for cliff-derived coarse sediments. This suggests that the Nino & Garcia model may be overly sensitive to slope or grain coarseness in cold-region contexts, potentially overestimating transport rates under these conditions.
- The formulations by Yalin (1963), Camenen et al. (2006), and Abrahams & Gao (2006) yield more moderate and internally consistent results. These models predict Φ values closer to the multi-model mean, especially for d_{50} and d_{10} in beach samples. Their behavior appears more stable across grain-size classes and sample types, indicating a better fit for the Diable River context.
- Beach samples display systematically higher transport values for Φ_{10} and Φ_{50}, while cliff samples dominate in Φ_{90}, aligning with the trends observed in SSA and ESA. This pattern emphasizes that, even within a purely empirical framework, the geomorphic functional contrast between cliffs and beaches remains evident.
- Intra-model variability is particularly notable for Φ_{90}, where small differences in slope or grain size lead to large discrepancies in predicted transport. This reflects the high sensitivity of RA models to their input parameters, and the tendency for certain formulations to amplify coarse-grained effects in steep settings.

Despite these disparities, the RA results broadly confirm key spatial and granulometric patterns: coarser fractions (d_{90}) in cliff samples drive the highest transport estimates, while finer and moderately sorted sediments (d_{10} and d_{50}) in beach settings yield more consistent and moderate Φ values. However, the exaggerated responses in some models (e.g., Nino & Garcia, 1994) underscore the importance of contextual model selection. Regressions derived from warm, gravel-bed rivers may not be directly transferable to cold-region systems with predominantly sandy substrates, like the Diable River.

Ultimately, RA models provide useful comparative benchmarks, but they must be interpreted with caution. Their high variability, combined with their empirical origins, limits their standalone predictive utility. Nonetheless, when integrated with the more physically grounded SSA and ESA approaches, they help to triangulate consistent trends in sediment transport dynamics across environments and grain-size classes.

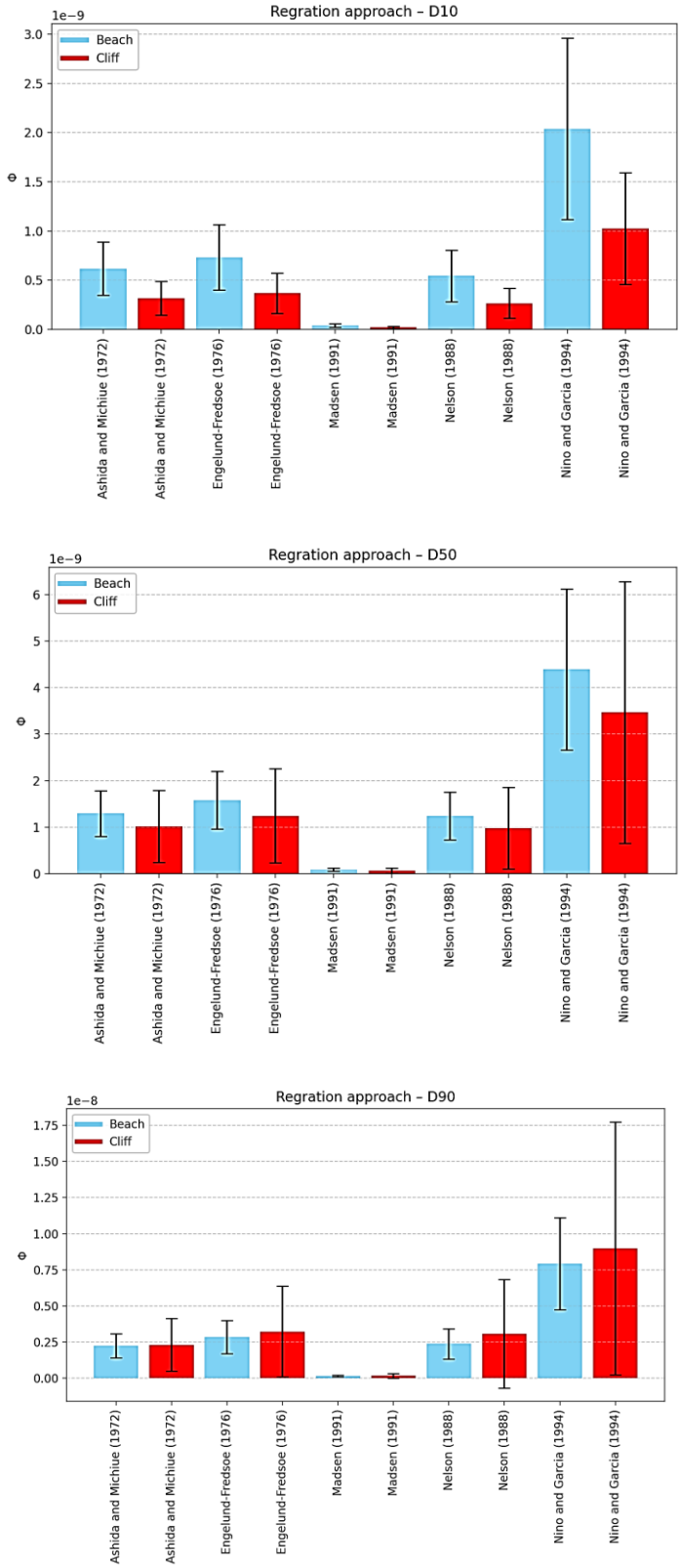

Figure 4.6. Predicted dimensionless bedload transport rate (Φ) for five regression-based equations across three grain-size percentiles (Φ_{10}, Φ_{50}, Φ_{90}), differentiated by site type (Cliff vs. Beach). Each pair of bars

compares Cliff (red) and Beach (light blue) values for a given grain-size percentile and transport equation. Values represent the mean ± standard deviation calculated from the sampled sites along the studied river reach.

4.4.3. Temporal analysis of geomorphic activities

To investigate the temporal variability of geomorphic activity in the Diable River, daily discharge data from 2009 to 2023 were used to compute stream power per unit width (ω). The time series of ω(t) was then compared to the critical stream power threshold ($\omega_{critical}$ = 0.0144), calculated based on site-specific hydraulic and sediment parameters (see Section 4.3.2).

Figure 4.7 presents the annual evolution of ω(t) and highlights the frequency and magnitude of exceedance over $\omega_{critical}$. Several years stand out as geomorphically active, particularly 2011, 2017 to 2019, and 2023 during which ω(t) frequently exceeded 5.0, indicating high-energy conditions capable of mobilizing coarse sediments and driving substantial morphological changes. The most significant geomorphological activity recorded during these years occurred during the snowmelt period (March-May). Indeed, most precipitation in southern Quebec falls as snow until March and April (Buttle et al., 2016). According to a study by Brooks et al. (2001), 65% of floods in Canada between 1900 and 1998 were caused by snowmelt. St-Laurent et al. (2009) obtained similar results for the period from 1865 to 2005, during which 59% of major floods in the Saint-François River watershed occurred between March and May.

We analyzed total monthly precipitation for December through May using data from three stations of the national network (ECCC, 2026): St-Jovite (46°04'49.860" N, 74°33'20.730" W, 234.40 m), Saint-Donat (46°19'00.000" N, 74°12'00.000" W, 388.60 m) and Arundel (45°57'00.000" N, 74°37'00.000" W, 191.40 m), all located near the study watershed. Moreover, we use reanalysis precipitation data from MSWX (Multi-Source Weather; see Beck et al., 2022 for more details) for the same period to get a better picture of conditions within the watershed, because even though the stations are located less than 50 km from the watershed's boundaries, they remain outside of it. Ultimately, the difference between the observed values and those from the reanalyses is small (less than 5%). Our results show that every April (2011, 2017, 2018, 2019 and 2023) has exceeded the normals (1981-2010) for nearby stations. Furthermore, the total cumulative precipitation for the period from December to May (2011, 2017, 2018, 2019, and 2023) exceeds the normals in all years except 2017–2018, where the observed amount is close to the normals observed at nearby stations.

On the other hand, 2009 and 2020-2022 show limited exceedance of $\omega_{critical}$ corresponding to weaker snowmelt or shorter melt durations. This variability underscores the dominant hydroclimatic control on sediment transport processes in cold-region fluvial systems. To identify the most and least effective geomorphic moments, Figures 8 and 9 isolate the three highest and three lowest $\omega_{(t)} - \omega_{critical}$ values per year (See Appendix B, Supplementary Tables B.4.1 and B.4.2 for more details about the three most and least significant periods of geomorphic activities and their interpretations). These snapshots capture both the peak disturbance events and stable hydrological phases.

- The most geomorphically active days occurred primarily in April-May, with maximum $\omega_{(t)} - \omega_{critical}$ values reaching 7.9 (2019), 7.2 (2023), 7.1 (2017), 6.1 (2011), and 5.3 (2018). These events represent the upper tail of the stream-power distribution and likely correspond to bank destabilization, channel incision, and coarse sediment transport.
- The least active periods, with $\omega(t)$ barely exceeding $\omega_{critical}$ (e.g., 0.12-0.25), occur in late summer (August) and mid-winter (February), reflecting low discharge and minimal geomorphic activity during phases of snow accumulation or high evapotranspiration.
- The frequency of geomorphically effective flows varies markedly among years: 2017–2019 registered >25 days/year with $\omega(t)$ >1.0, whereas 2021-2022 recorded few or none. This temporal clustering of high-magnitude flows suggests multi-year pulses of enhanced sediment transport alternating with periods of quiescence.

Overall, the analysis reveals that geomorphic work is both seasonal and episodic. The main drivers are snowmelt-induced floods, occasionally reinforced by rain-on-snow events, producing strong interannual variations in both magnitude and frequency. These findings validate the use of stream-power exceedance as a proxy for geomorphic effectiveness, providing a robust temporal framework for interpreting sediment-transport estimates and morphological evolution in subsequent sections.

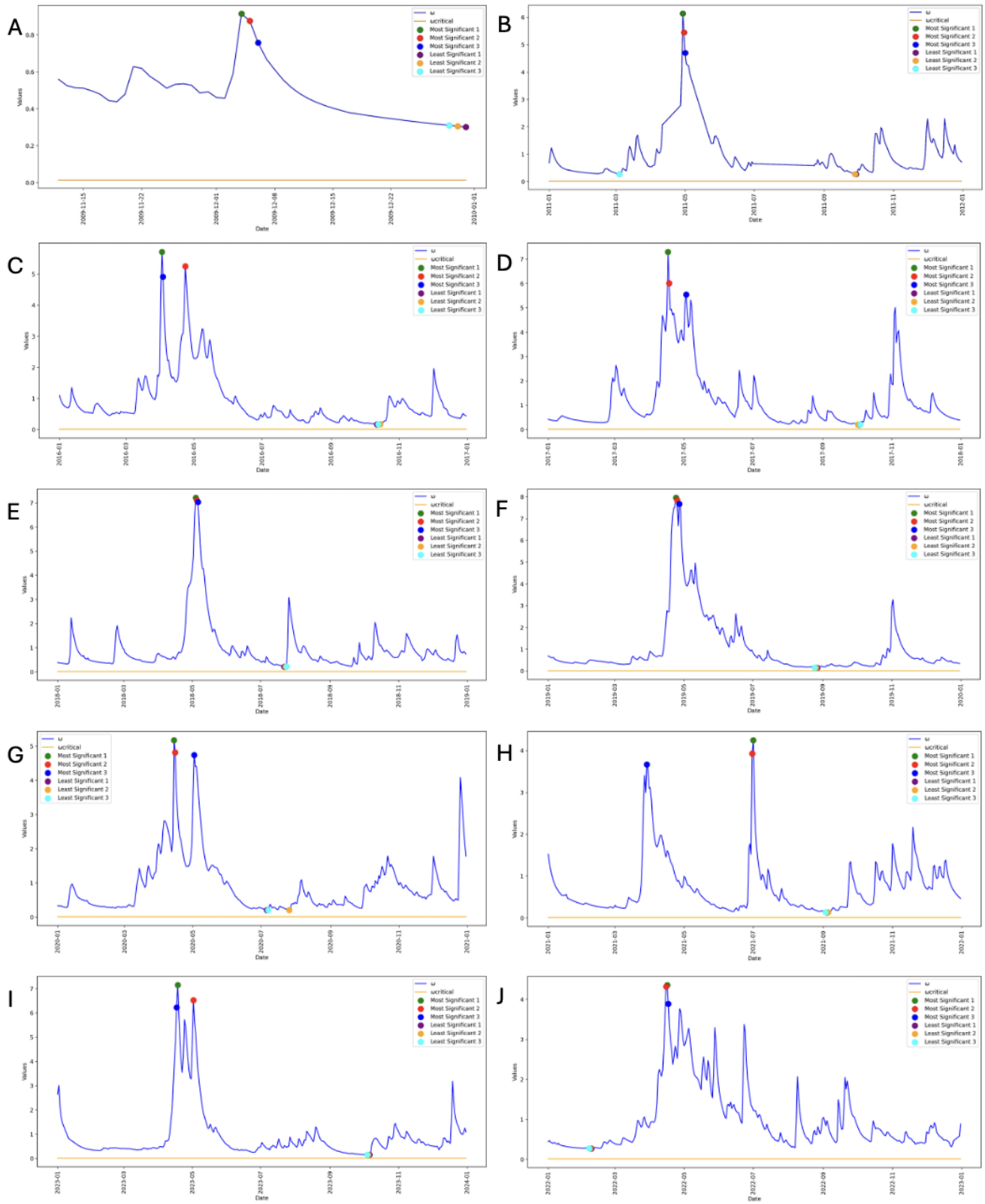

Figure 4.7. Timing of geomorphic activity for each year: a) 2009; b) 2011; c) 2016; d) 2017; e) 2018; f) 2019; g) 2020; h) 2021; i) 2023; and j) 2022.

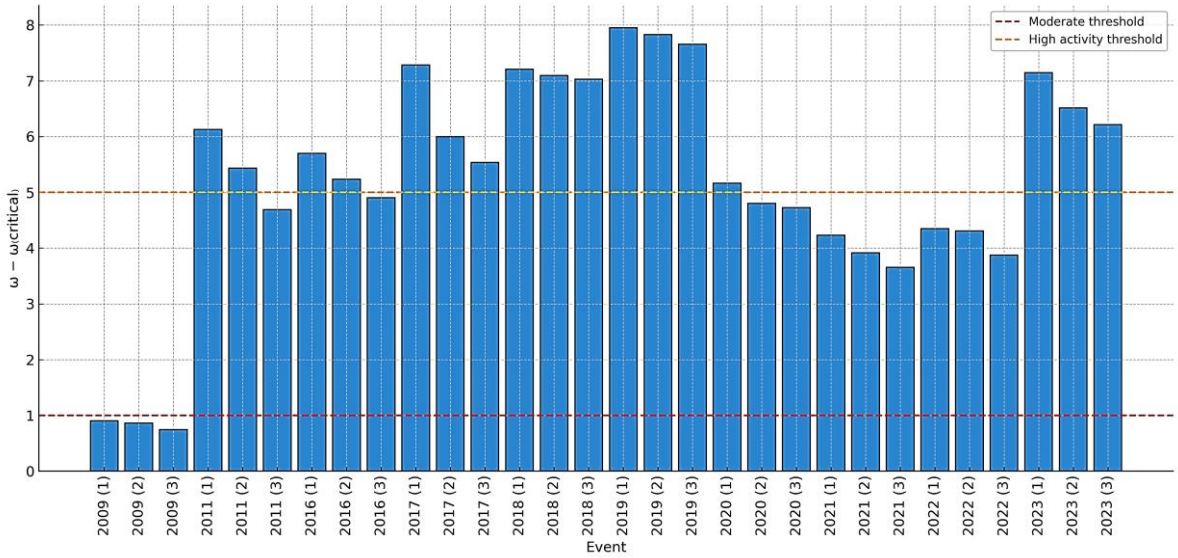

Figure 4.8. The three most significant periods for each year

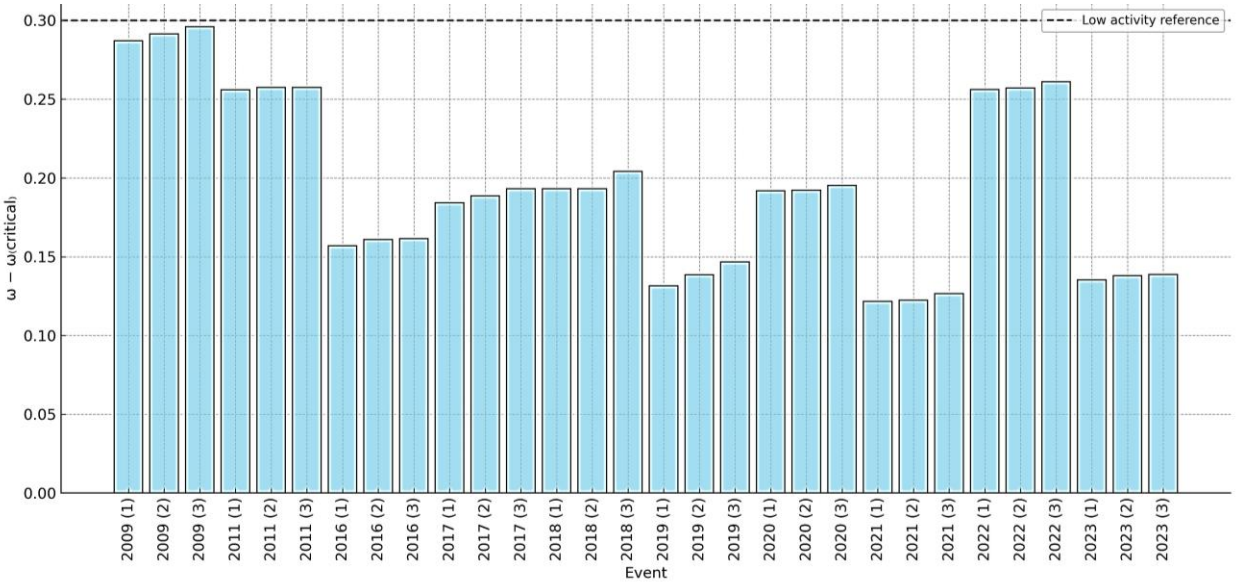

Figure 4.9. The three least significant geomorphic periods for each year

4.4.4. Sediment Transport Index (STI)

The Sediment Transport Index (STI) was used to estimate the spatial distribution of erosion and transport potential across the study area. Computed from high-resolution 1 m DEM using the ArcGIS Spatial Analyst toolbox, STI integrates local slope and upslope contributing area (A_s) to quantify the topographic potential for sediment detachment and downslope transfer. The analysis was conducted for the entire fluvial corridor and surrounding catchment, encompassing both cliff and beach environments.

STI values were visualized using a continuous color gradient ranging from purple (low values) to yellow (high values), allowing the identification of spatial contrasts and areas with high transport potential (Figure 4.10). Rather than discrete classification, this approach illustrates continuous spectrum of detachment and transport potential, low values associated with minimal slope and small contributing area, to high values concentrated in steep terrains with focused surface runoff. The resulting map reveals a strong spatial organization of STI values across geomorphic settings, reflecting the contrast between sediment source and depositional environments:

- Cliff environments display significantly higher STI values, with concentrations of high and very high values in steep zones directly connected to the river. These sectors are often characterized by shallow colluvium and steep slopes that concentrate surface runoff. The combination of topographic gradient and hydrological convergence promotes high sediment detachment potential, especially during intense spring melt events or high-intensity rainfall events.
- Beach environments, by contrast, exhibit lower STI values. Their gentle slopes and depositional nature reduce erosion potential, even though these zones are frequently reworked by fluvial processes. Despite the regular remobilization of surface sediments during high-flow events, the contributing area and slope remain low, reducing the gravitational component of sediment transport and STI values overall.
- A few localized hotspots of elevated STI were detected outside the main channel, including gullies and small tributary catchments with step headwaters. These features may act as episodic sediment sources during extreme runoff events, although their contribution is more spatially limited and temporally intermittent.

The STI results are consistent with previous findings based on modeled transport rates (Sections 4.4.2.1–4.4.2.3). Areas with high STI values correspond to sites where transport thresholds (e.g., Φ_{90}) are most frequently exceeded, especially in cliff environments. In contrast, the lower STI values observed in beach zones reinforce their role as sediment sinks or reworking areas, rather than primary sources. Overall, STI provides a robust spatial indicator of sediment source potential along the Diable River corridor. It reinforces the geomorphic asymmetry between cliff and beach sites and offers a useful diagnostic for identifying areas where sediment production is most likely to occur under high-flow conditions. At a larger scale, linear features with elevated STI, potentially corresponding to roads, trails, or deforested corridors, suggest anthropogenic influences on sediment dynamics. Such features may serve as sediment sources or conduits during heavy rainfall events, posing risks for infrastructure stability and increasing downstream sediment loads.

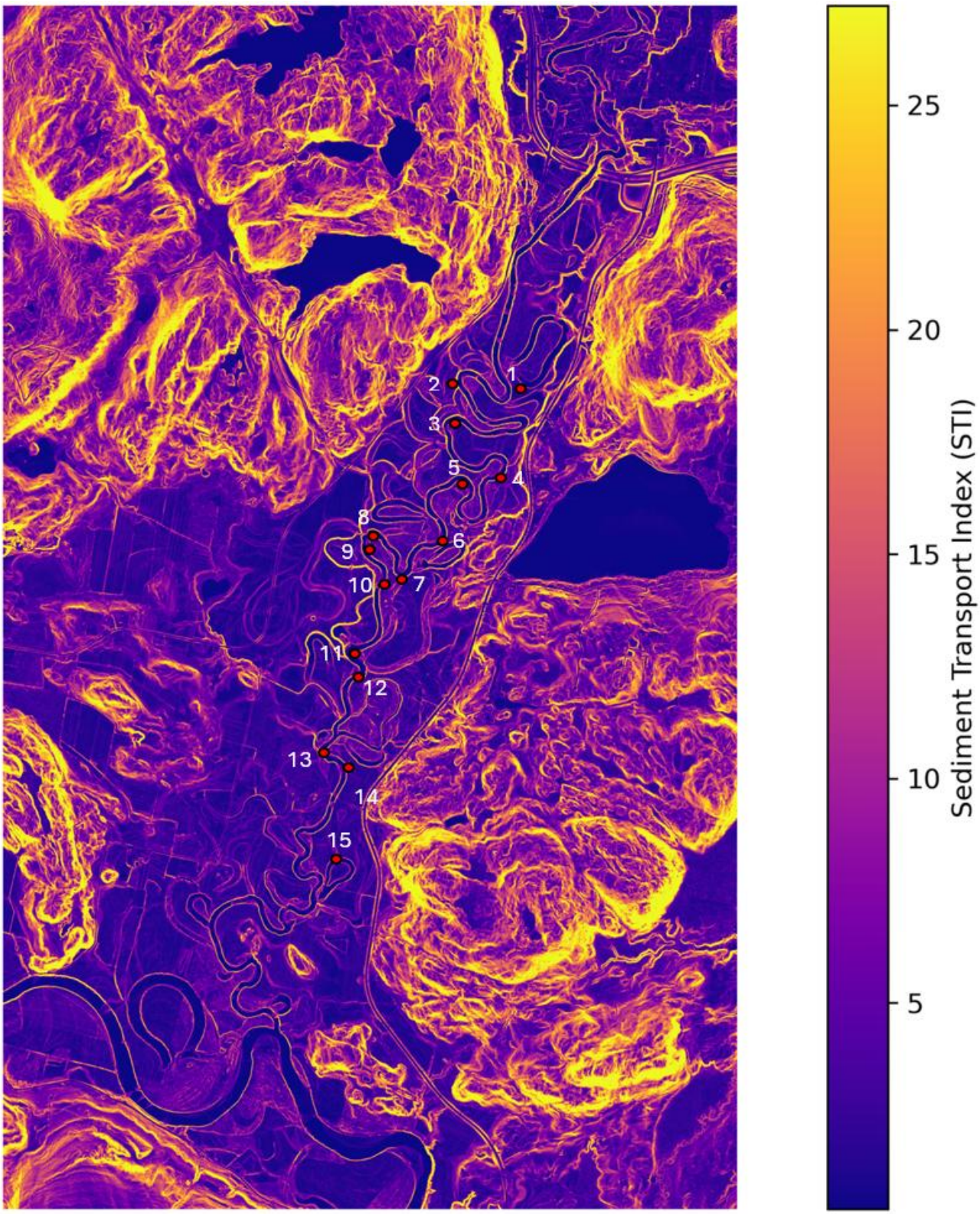

Figure 4.10. Sediment Transport Index (STI) map derived from topographic parameters. The points show the location of collected samples.

4.4.5. Stream Power Index (SPI)

The Stream Power Index (SPI) was calculated to evaluate spatial patterns of potential stream energy throughout the Diable River corridor. Derived from a 1 m resolution DEM using the formula SPI = A_s x tan (β), this index combines local slope (β) and upstream contributing area (A_s) to estimate the erosive force exerted by concentrated overland or channelized flow. The analysis was performed using the ArcGIS Spatial toolbox and covers the same spatial extent as the STI analysis.

SPI values were visualized using a continuous color gradient from dark blue (low values) to yellow (high values), emphasizing spatial variability in stream energy across the catchment (Figure 4.11a). Unlike the sediment transport index (STI), which captures hillslope-scale processes, SPI reflects channelized flow energy, making it particularly relevant for identifying zones of fluvial erosion, incision, and bank destabilization. The results indicate a strong spatial differentiation between geomorphic units:

- Cliff environments exhibit elevated SPI values, especially along steep channel margins and headwater incisions. These areas combine high local slopes with focused flow accumulation, resulting in high potential stream power. This pattern is consistent with observed erosion features such as channel scouring and bluff retreat.
- Beach environments, in contrast, show lower SPI values due to gentle slopes and reduced contributing area. These sectors correspond to lower-energy depositional zones where lateral accretion and sediment storage dominate over incision or vertical erosion.
- Some secondary high-SPI zones are also present in tributary channels and confluences with steep longitudinal gradients. These locations may act as local energy hotspots, contributing episodically to sediment input during high-flow events.

The spatial distribution of SPI reinforces the findings from SSA, STI, and critical transport thresholds, confirming that energy availability is a key driver of geomorphic activity in the Diable River system. High SPI values frequently overlap with zones where Φ_{90} values and stream power (ω) exceedance are most prominent, indicating strong alignment between topographic energy metrics and modeled sediment transport capacity. This pattern is particularly evident in the detailed view (Figure 4.11b), which shows that SPI values are concentrated along the inner bends and thalweg of the meandering main channel. The red zones, marking peak stream power, typically correspond to tight meander curves and segments with steep hydraulic gradients. These local maxima highlight areas with increased potential for bank erosion and channel adjustment, underscoring the spatial heterogeneity of fluvial energy distribution in the Diable River corridor.

Taken together, the SPI results provide an additional layer of spatial interpretation, highlighting the link between drainage structure, slope configuration, and fluvial energy concentration. This complements the sediment-focused STI by emphasizing the role of hydrological connectivity and gravitational forcing in shaping erosion-prone landscapes.

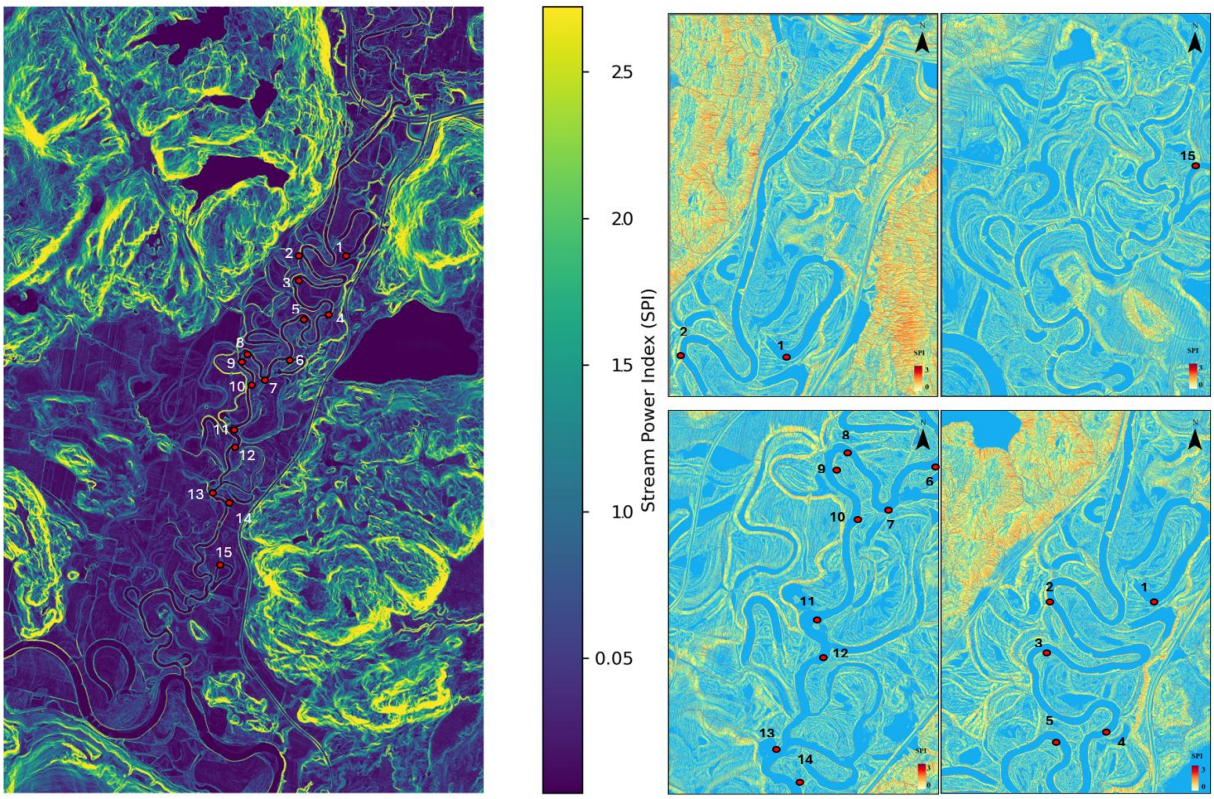

Figure 4.11. Stream Power Index (SPI) map derived from slope and contributing drainage area (a) and close-up view of SPI distribution in a selected river section (b). The points show the location of collected samples.

4.4.6. Flow Duration Curve (FDC):

Flow Duration Curves (FDCs) were constructed for each hydrological year from 2009 to 2023 to assess interannual variability in discharge regimes and to identify years characterized by geomorphically effective flows. FDCs were based on daily discharge values and plotted using a logarithmic scale to enhance contrast in the upper tail of the distribution (Figure 4.12).

The results highlight substantial variability in the magnitude and frequency of high flows across the study period. Years such as 2011, 2017, 2018, 2019, and 2023 stand out with elevated curves in the upper percentiles ($Q_{0.01}$ to $Q_{0.1}$), indicating frequent and sustained high-flow conditions. These years correspond to those identified in Section 4.4.3 as having the greatest exceedance of the critical stream power threshold ($\omega > \omega_{(c)}$), reinforcing the link between discharge regime and geomorphic activity.

Conversely, 2009, 2016, 2021, and 2022 exhibit flatter curves with lower Q-values across all percentiles, reflecting drier conditions and reduced runoff. These years coincide with limited exceedance of $\omega_{(c)}$ and a marked reduction in sediment transport potential. The intermediate years (e.g., 2010, 2013, 2015) show more balanced curves, with moderate but less frequent high flows.

The steepness and curvature of the FDCs also reflect variations in hydroclimatic drivers. Steeper curves suggest flashier regimes, often resulting from intense melt pulses or rain-on-snow events,

while flatter curves indicate more prolonged, stable flow regimes. This distinction has important implications for sediment transport: flashy years can produce short but powerful mobilization events, whereas sustained high flows may support longer periods of sediment entrainment and channel adjustment.

Overall, the FDC analysis confirms that the temporal distribution and recurrence of high flows is a critical control on geomorphic activity in the Diable River. When combined with the ω-exceedance data (Section 4.4.3) and transport estimates (Sections 4.4.2–4.4.5), these curves provide a robust hydrological context for interpreting spatial and sedimentological patterns across the river corridor.

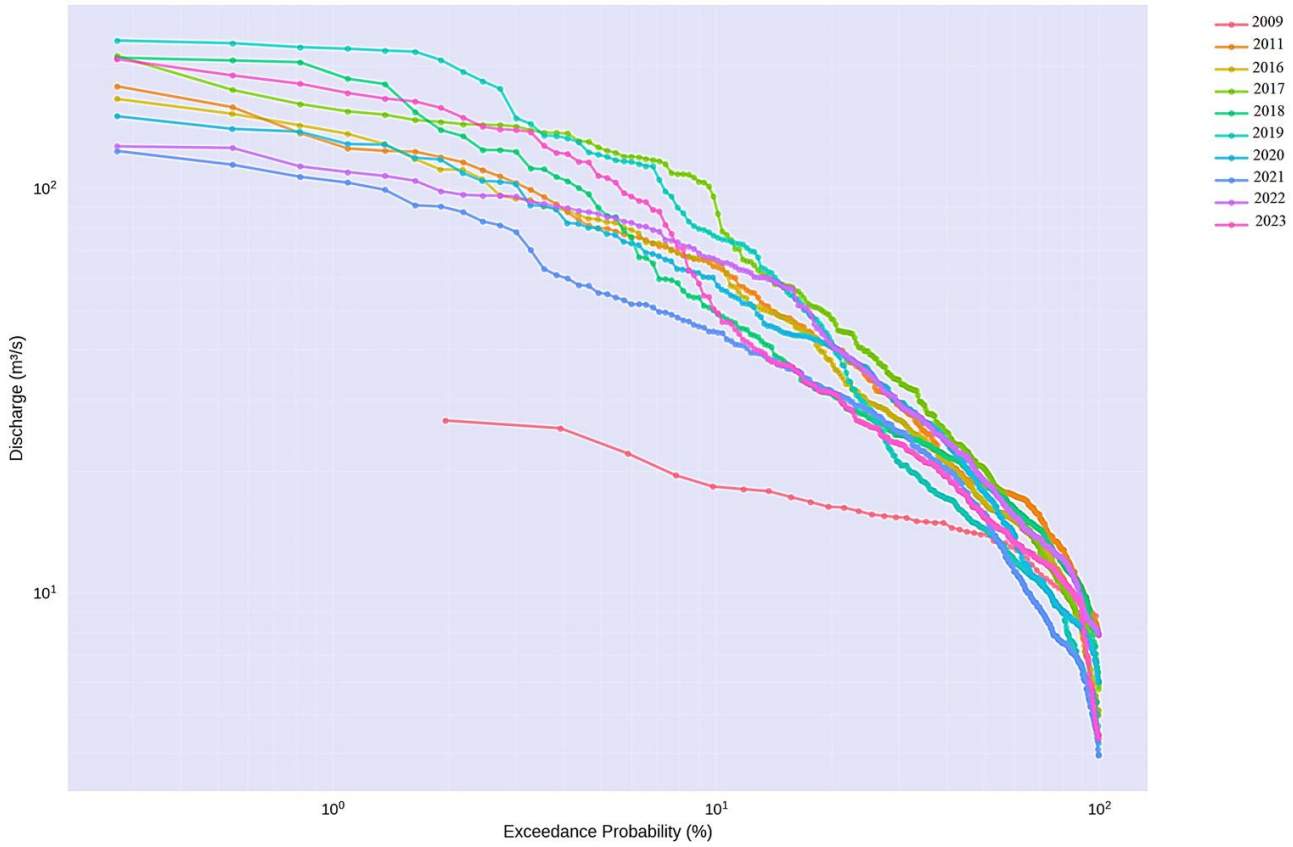

Figure 4.12. Flow Duration Curves (FDC) for ten hydrological years, showing the relationship between exceedance probability (%) and discharge ($m^3\ s^{-1}$) on logarithmic axes.

4.5. Discussion

4.5.1 Comparative Insights Across Modeling Approaches

This study demonstrates the value of a multi-method statistical framework for identifying and quantifying sediment transport dynamics in cold-region fluvial systems. Each approach implemented in this study; SSA, ESA, RA, and geomorphic indices (STI and SPI), offers a complementary perspective on sediment behavior across temporal and spatial dimensions.

The SSA method, based on signal decomposition of modeled transport capacity, effectively captures recurrent seasonal signals and anomalies across the 15-year period. However, it remains a statistical abstraction and cannot fully account for physical thresholds or geomorphic responses. ESA addresses this limitation by explicitly calculating the exceedance of critical stream power ($\omega > \omega c$) and transport capacity thresholds ($\Phi > \Phi_c$), thereby grounding the analysis in physically meaningful thresholds. ESA results offer a more direct interpretation of geomorphic activity, especially in identifying high-transport years and their frequency within each season.

The transport-discharge rating analysis (e.g., Parker, 1979; Meyer-Peter Müller, 1948) provides an additional layer of empirical validation. By examining the statistical relationship between discharge and transport capacity at the monthly scale, it highlights the nonlinear behavior of sediment transport and accounts for site-specific conditions, such as hysteresis and flow variability. While more sensitive to outliers and calibration artifacts, RA reinforces trends observed in SSA and ESA, particularly in confirming the strong interannual variability of transport potential.

The integration of topographic indices (STI and SPI) complements the time series analyses by introducing spatial structure into the framework. These indices allow for a spatial differentiation of sediment sources and energy hotspots along the fluvial corridor. Although they are static representations and do not capture temporal dynamics, their convergence with the temporal models, especially in high-transport years, adds a spatial dimension that is crucial for geomorphic interpretation at a larger scale.

A series of converging insights emerged across all three modeling approaches. Cliff environments consistently displayed higher dimensionless bedload transport rates (Φ) than beach sites, particularly when calculated using d_{90}, reflecting their steeper slopes, higher localized stream power, and coarser sediment textures. Among the percentile-based metrics, Φ_{90} systematically yielded the highest transport values, emphasizing the nonlinear nature of sediment flux once larger particles are entrained. While absolute values varied between equations, the relative spatial patterns of transport intensity and grain-size sensitivity remained consistent, underscoring the robustness of the multi-approach design and enhancing confidence in the framework.

Overall, this integrative approach enables a cross-validation of results and enhances the robustness of the findings. By combining statistical, empirical, and physically-based metrics, the framework allows for a more comprehensive understanding of sediment transport processes than any single method alone. It is particularly well-suited to systems where episodic and seasonal processes dominate, and where spatial variability in energy and sediment availability is a critical control. This methodological plurality is essential not only for scientific understanding but also for informing river management, hazard assessment, and restoration planning in cold-region environments.

4.5.2 Temporal and Hydrological Controls on Geomorphic Activity

The results presented in Sections 4.4.2 and 4.4.3 highlight the importance of intra- and interannual variability in sediment transport dynamics. At the seasonal scale, most sediment transport occurs during spring, particularly in April and May. This pattern, consistently identified across SSA, ESA, and flow duration curve analyses (FDCs), reflects the dominance of snowmelt-induced high flows (Zhang et al., 2021; Shin et al., 2023) in generating geomorphically effective discharge events in the Diable River. These early spring peaks are not only associated with the highest modeled

transport values but also with the most frequent exceedance of critical thresholds for both stream power (ω) and transport capacity (Φ).

The temporal patterns also reveal significant interannual variability. Years such as 2011, 2017, 2018, 2019, and 2023 stand out for their elevated transport indices and sustained exceedance of ω_c. These same years show high values for Φ_{90}, indicating not just more frequent transport events, but also the mobilization of coarser fractions (Zhang et al., 2021). The convergence of high ω and Φ values during these years provides strong evidence of increased sediment supply, transport competence, and geomorphic work. These findings are further supported by flow duration curves, which highlight the persistence of high flows during these key years.

By contrast, years like 2009, 2016, 2021, and 2022 are characterized by lower transport values, reduced ω-exceedance, and flatter FDCs. These years reflect hydrological regimes that are less favorable to sediment mobilization, either due to lower total discharge or more subdued melt pulses. The variability in sediment transport between active and inactive years reflects the strong control exerted by seasonal hydrology, particularly snowpack conditions, melt timing, and precipitation inputs (Zhang et al., 2023).

These results reinforce the episodic nature of sediment transport in cold-region fluvial systems, where the bulk of geomorphic work is concentrated in a limited number of high-flow periods. The identification of geomorphically effective years is essential for understanding sediment budgets, modeling channel evolution, and anticipating the impact of future hydrological changes (Hirschberg et al., 2021; van Hamel et al., 2025). In this context, the use of multiple transport thresholds (Φ_{10}, Φ_{50}, Φ_{90}) offers valuable insights into the range of sediment sizes mobilized and the magnitude of events required to entrain coarser particles. This multi-threshold approach allows for a more nuanced interpretation of transport competence and helps bridge the gap between process-based models and field-based observations.

4.5.3 Spatial Signature and Geomorphic Potential

In addition to temporal variability, this study reveals marked spatial contrasts in sediment transport potential and geomorphic activity along the Diable River corridor. The combined results of the transport indices (STI, SPI), as well as the modeled transport rates, consistently show higher values in cliff environments compared to beach settings, highlighting a fundamental asymmetry in morphodynamic functioning.

Cliffs exhibit steep slopes, concentrated drainage areas, and elevated SPI values, all of which enhance local stream power and sediment detachment potential. These zones are frequently identified as sediment source areas, particularly during high-flow periods. The convergence of high STI, SPI, and Φ values in these areas suggests intense erosion, slope-channel coupling, and high sediment yield, especially for coarse particles. Moreover, their upstream and convex positions along the longitudinal profile reinforce their role as dominant sediment contributors to the fluvial system.

Conversely, beaches show lower STI and SPI values, indicating reduced slope gradients, dispersed flow paths, and limited energy for sediment transport. These areas function more as transient sediment sinks, where fine particles are deposited or reworked during moderate to high flow conditions. Despite episodic remobilization, especially during spring floods, beach environments exhibit overall lower transport competence, and their contribution to downstream sediment fluxes appears to be secondary compared to that of the cliffs.

This spatial differentiation illustrates a form of morphodynamic asymmetry (Czuba et al., 2017; Czuba, 2018), where sediment sources and storage zones are not evenly distributed but are organized according to topographic and hydrological controls. Such asymmetry has important implications for sediment connectivity (Wainwright et al., 2011; Bracken et al., 2015), as the spatial decoupling of erosion and deposition zones may lead to discontinuities in transport and delayed sediment transfer (Cho et al., 2023; Turley and Hassan, 2023). It also affects river evolution over time, with cliffs driving vertical and lateral adjustment, while beaches tend to stabilize or buffer channel morphology.

The spatial structure revealed in this study is consistent with the broader conceptual understanding of sediment cascades in small, steep watersheds (Fryirs, 2013; Macurová et al., 2024). It underscores the need for spatially explicit approaches to sediment budgeting and risk assessment (Lu et al., 2004). Identifying persistent source zones such as unstable cliffs can help target monitoring efforts, inform mitigation strategies, and anticipate areas of geomorphic sensitivity under changing hydrological regimes.

4.6. Conclusion

This study proposes a multi-method statistical framework to quantify fluvial sediment transport and geomorphic dynamics in a cold-region river system. By combining the Shear Stress Approach (SSA), Energy Slope Approach (ESA), Regression Approach (RA), spatial indices of stream power (SPI) and sediment transport (STI), and flow duration curves (FDCs), the proposed framework provides a comprehensive view of sediment behavior across temporal and spatial scales.

The results reveal strong interannual variability in sediment transport, with a limited number of hydrologically active years (e.g., 2011, 2017–2019, 2023) accounting for the bulk of geomorphic activity. Spring floods, primarily driven by snowmelt, emerge as the dominant driver of sediment mobilization, especially when discharge exceeds critical thresholds of stream power and transport capacity. These patterns are corroborated by stream power metrics and flow duration curves, highlighting the importance of both magnitude and persistence of high flows in controlling sediment dynamics.

Spatially, the framework reveals clear contrasts between geomorphic settings. Cliffs consistently display higher transport potential and energy concentration, acting as primary sediment sources. In contrast, beach environments show lower energy levels and function predominantly as transient storage or reworking zones. This morphodynamic asymmetry underlines the role of topographic structure and drainage configuration in shaping sediment pathways.

By integrating complementary methods (mechanistic, empirical, and topographic) the framework enables a nuanced understanding of sediment transfer processes in cold-region rivers. It supports the identification of transport-efficient periods, source–sink dynamics, and the role of seasonal hydrology in modulating geomorphic work. This integrated approach is particularly useful in data-scarce environments, where combining multiple lines of evidence enhances interpretative robustness.

Future research should aim to improve the temporal resolution of modeled sediment transport, incorporate vegetation and land cover dynamics, and validate model outputs through field-based observations. Extending this framework to other cold-region systems will further test its applicability and contribute to a more refined understanding of sediment connectivity in diverse geomorphic contexts.

CHAPTER 5

Trends and historical patterns of meteorological droughts in New Brunswick, Canada, using PDSI and SEDI indices

Ali Faghfouri[a]*, Guillaume Fortin[b], Albin Ullmann[c], Florian Raymond[d], Charlotte Poirier[e], Vincent Dubreuil[f], and Daniel Germain[g]

[a]*Institute of Environmental Sciences, Université du Québec à Montréal, Québec, Canada.*

https://orcid.org/0000-0001-6418-5436

faghfouri.ali@courrier.uqam.ca

[b]*Department of History and Geography, Université de Moncton, New Brunswick, Canada.*

https://orcid.org/0000-0002-9583-9188

guillaume.fortin@umoncton.ca

[c]*Centre de Recherches de Climatologie, UMR 6282 Biogéosciences, CNRS / Université Bourgogne Franche-Comté, Dijon, France.*

https://orcid.org/0000-0002-0259-0636

albin.ullmann@u-bourgogne.fr

[d]*LADYSS, UMR 7533 / Université Vincennes- Saint-Denis Paris 8, France.*

https://orcid.org/0000-0002-4090-3082

florian.raymond02@univ-paris8.fr

[e]*Master in Environmental Studies, Université de Moncton, New Brunswick, Canada.*

poirierc94@gmail.com

[f]*CNRS, UMR6554 LETG, Université Rennes 2, Place du Recteur H. Le Moal, 35043 Rennes Cedex, France.*

https://orcid.org/0000-0001-8383-805X

vincent.dubreuil@univ-rennes2.fr

[g]*Department of Geography, Université du Québec à Montréal, Québec, Canada.*

https://orcid.org/0000-0003-4757-3124

germain.daniel@uqam.ca

* Corresponding author

Institute of Environmental Sciences, Université du Québec à Montréal, C.P. 8888, succursale Centre-ville, Montréal, Québec, Canada H3C 3P8

This paper was published in Theoretical and Applied Climatology. (Faghfouri, A., Fortin, G., Ullmann, A. et al. Trends and historical patterns of meteorological droughts in New Brunswick, Canada, using PDSI and SEDI indices. Theor Appl Climatol 156, 257 (2025). https://doi.org/10.1007/s00704-025-05467-2)

Résumé

Les sécheresses sont de plus en plus reconnues comme un enjeu mondial majeur, avec des impacts sévères observés dans les provinces des Prairies canadiennes. Bien que moins fréquentes dans l'Est du Canada, des déficits prolongés de précipitation, notamment durant l'été, peuvent conduire à des conditions de sécheresse sévères. Cette étude examine les causes et conséquences des sécheresses au Nouveau-Brunswick (NB) en employant deux indices de sécheresse : l'Indice de Sévérité des Sécheresses de Palmer (PDSI) et l'Indice Standardisé du Déficit d'Évapotranspiration (SEDI) — calculés pour dix stations météorologiques du NB sur la période 1971–2020. Le jeu de données CANGRD des anomalies maillées de température et de précipitations au Canada (1979–2014) a également été utilisé pour étudier la variabilité spatio-temporelle des sécheresses et sa concordance avec les observations stationnelles. Des analyses statistiques, dont le test de Mann–Kendall et l'estimateur de pente de Sen, ont été appliquées pour évaluer les tendances des indices de sécheresse à l'échelle annuelle et saisonnière en utilisant à la fois les données stationnelles et maillées. Les résultats ont permis d'identifier les régions les plus vulnérables au NB et ont révélé une importante variabilité spatiale et temporelle de la sévérité des sécheresses sur la période 1971–2020. Les analyses de tendance ont en outre mis en évidence l'intensification d'événements de sécheresse extrême certaines années. Les zones côtières du sud du NB se révèlent particulièrement susceptibles aux conditions de sécheresse sévère comparativement aux régions intérieures, ce qui concorde avec la diminution observée de la fréquence des jours de pluie et des quantités de précipitation quotidiennes dans ces secteurs. Ces résultats soulignent la nécessité de stratégies ciblées d'atténuation de la sécheresse, en particulier pour les zones côtières du NB, afin de répondre à la vulnérabilité croissante face aux événements extrêmes.

Mots-clés : conditions de sécheresse, indices de sécheresse, analyse de tendance, Indice de Sévérité des Sécheresses de Palmer (PDSI), Indice Standardisé du Déficit d'Évapotranspiration (SEDI)

Abstract:

Droughts are increasingly recognized as a significant global challenge, with severe impacts observed in Canada's Prairie provinces. While less frequent in Eastern Canada, prolonged precipitation deficits, particularly during summer, can lead to severe drought conditions. This study investigates the causes and consequences of droughts in New Brunswick (NB) by employing two drought indices: the Palmer Drought Severity Index (PDSI) and Standardized Evapotranspiration Deficit Index (SEDI)– at ten weather stations across NB from 1971 to 2020. Additionally, the Canadian Gridded Temperature and Precipitation Anomalies (CANGRD) dataset (1979-2014) was utilized to examine spatial and temporal drought variability and its alignment with station-based observations. Statistical analyses, including the Mann-Kendall test and Sen's slope estimator, were applied to assess trends in drought indices on annual and seasonal timescales using both station and gridded data. The results identified the most drought-vulnerable regions in NB and revealed significant spatial and temporal variability in drought severity over the 1971-2020 period. Trend analyses further highlighted the intensification of extreme drought events during specific years. Coastal areas in southern NB were found to be particularly susceptible to severe drought conditions compared to inland regions, consistent with observed declines in both the frequency of rainy days and daily precipitation amounts in these areas. These findings underscore the need for targeted drought mitigation strategies particularly in NB's coastal zones, to address the region's increasing vulnerability to extreme drought events.

Keywords: Drought conditions, Drought indices, Trend analysis, Palmer Drought Severity Index (PDSI), Standardized Evapotranspiration Deficit Index (SEDI)

5.1. Introduction:

Drought, a stochastic natural hazard, is defined by precipitation scarcity with severe and repetitive durations. Droughts can be detrimental to hydrology, agriculture, forests, and communities. The characteristics of droughts are unique from other natural hazards and were observed as variations in severity and duration with multiple dynamic dimensions (Lamy and Dubreuil 2013; Dubreuil 2005; Dubreuil 1997). The recognition of droughts is complex due to their subjective and pervasive nature (Zargar et al. 2011). The fundamental reasons contributing to droughts include inadequate precipitation, low soil humidity, and high temperatures, which can cause deprivation of stored water resources and damage agricultural sectors (Bullock et al. 2018; Cook et al. 2018; Kennedy et al. 2017).

Meteorological, hydrological, and agricultural droughts have been recognized as the three main physical drought types to which ecological and socioeconomic droughts can be added. However, the classification of droughts in these categories is challenging, as they may exhibit characteristics belonging to multiple categories (Vicente-Serrano et al. 2022). In addition, there is a direct link between these types of droughts. A deficiency of precipitation (or moisture supply) over some period (e.g., weeks to months) and within a particular area can cause meteorological drought, subsequently impacting the soil moisture, groundwater, and surface waters. A shortage of water in water bodies such as lakes, rivers, and streams can then lead to a hydrological drought (Zargar et al. 2011; Kumanlioglu 2020; Ding et al. 2021; Huang et al. 2021; Mtilatila et al. 2020; Abbas et al. 2021). When a water deficit persists and causes damage or loss of crops, it is referred to as agricultural drought (Huang et al. 2021; Wu et al. 2021). A lack of soil moisture impacts ecosystems, a phenomenon called ecological drought (Zang et al. 2020). Additionally, a water shortage that disrupts the balance of supply and demand for various human activities is known as a socioeconomic drought (Wang et al. 2023). Beyond categorization by type, droughts are further classified based on their severity, duration, and spatial distribution. Moreover, other key factors, such as frequency, magnitude, predictability, and rate of onset, contribute to a deeper understanding of the nature of drought (Salas 1993).

Droughts have been a widespread phenomenon across various regions of Canada. Between 1950 and 2002, an increase in drought occurrences was observed across most parts of the country, as determined through Palmer Drought Severity Index (PDSI) analysis (Bonsal et al. 2011). Asong et al. (2018) analyzed historical droughts nationwide using the Standardized Precipitation Evapotranspiration Index (SPEI) across multiple temporal scales from 1950 to 2013. Their findings, supported by the Mann–Kendall test and other statistical approaches, identified the Canadian Prairies and northern central Canada as primary centers of drought evaluation. Dryer conditions were observed in southern Canada, while northern regions experienced wetter conditions during the same period. Multi-year dry episodes intermittently affected the Canadian Prairies, notably in 1890, 1910, 1930, 1950, 1960, 1980, and 1999 to 2005 (Bonsal and Regier 2007; Chipanshi et al. 2006). Future projections suggest that drought intensity and duration will increase, driven by prevailing climate conditions and their intrinsic characteristics (Bonsal et al. 2020).

Western Canada has endured prolonged droughts throughout the last century. The interior valleys of British Columbia, due to their topography and precipitation deficits, were particularly susceptible (Bonsal et al. 2004). The Canadian Prairie provinces, including Saskatchewan and Alberta, experienced dramatic drought impacts in specific years (Mousavi et al. 2023; Wheaton et al. 2008). For instance, the drought of 2001 led to significant reductions in crop yields, as reflected by the Normalized Difference Vegetation Index (NDVI) (Wilson et al. 2002), and declining water levels in closed-basin lakes (Van Der Kamp et al. 2008). A severe drought in 2017 was attributed to below-average winter snowfall, a dry spring, and less than half the average precipitation during the agricultural season (Statistics Canada 2016; Government of Canada 2017). This drought highlighted the interconnected impacts of snow drought and other types of droughts, as described by Cowherd et al. (2023).

Droughts in central and eastern Canada have been less frequent and less severe compared to western regions (Bonsal et al. 2004; Bonsal et al. 2011). However, significant droughts were reported in Ontario and Quebec throughout the 20th century (Klaassen 2002b). Southern Ontario experienced major drought episodes between 1920 and 1999 and from 2001 to 2002 (Klaassen 2002a; Wheaton et al. 2008). Regional drought assessments in Ontario by Klaassen (2000b) explored connections between droughts and climate variability cycles, confirming severe regional droughts, particularly in the late 1990s.

In the Maritime provinces, including New Brunswick (NB), drought occurrences have been less frequent but are a significant concern due to the lower adaptability of the region (Nova Scotia Department of Agriculture and Fisheries 2001). A general decrease in measurable precipitation has also been documented, attributed to climate change and warming trends (Vincent and Mekis 2006). In southwestern Nova Scotia, moderate to severe drought occurred during the summer and fall of 2016. Although droughts are relatively rare in NB, their potential impacts on ecosystems, water resources (surface and groundwater), and human activities can be significant. These impacts include reduced access to drinking water, increased risk of forest fires, and stress on agriculture. Larocque et al. (2019) highlighted that groundwater resources in NB are under pressure from agriculture, urban development, and drinking water needs, particularly in densely populated areas of Eastern Canada. Furthermore, Drought remains an understudied hazard in NB despite its potential severity (Mallet et al. 2018). For example, the summer of 2020 underscored the province's vulnerability, particularly in coastal areas, where precipitation deficits significantly impacted water availability. In a recent study, Poirier et al. (2022) employed the Standardized Precipitation Index (SPI) and Standardized Precipitation Evapotranspiration Index (SPEI) to evaluate the frequency, duration, and intensity of droughts in NB. Their findings indicated a slight increase in drought occurrences but revealed significant spatial inconsistencies. Recognizing the need for a more precise understanding of historical droughts and their spatial and temporal evolution, this study proposes the use of complementary indices, specifically the Palmer Drought Severity Index (PDSI) and the Standardized Evapotranspiration Deficit Index (SEDI).

This research aims to provide a comprehensive analysis of droughts in NB over the past 50 years (1971-2020) by leveraging historical climate series from station-based and gridded datasets (e.g., CANGRD) and employing robust analytical methods, including selected drought indices and trend

analysis. This study's novelty lies in conducting the first systematic meteorological drought analysis for the entire province, using indices such as PDSI and SEDI. These indices, in combination with the climate datasets, provide critical insights into drought trends and identify regions most susceptible to severe droughts. The primary objectives are to quantify the frequency, duration, and intensity of historical drought events and identify the most vulnerable regions and periods within NB. Unlike previous studies that predominantly focused on the Canadian prairies, this investigation offers one of the first updated and systematic analyses of historical droughts in NB, covering the entire province. While earlier studies in NB (El-Jabi et al. 2013; Turkkan et al. 2011) concentrated on hydrological droughts and their return periods, they provided limited insights into spatial and temporal variability across the province.

While the self-calibrated PDSI (sc-PDSI) and similar indices have been used in other regions, their application in Canadian drought research remains limited. According to Yildirim et al. (2022), only two Canadian studies have employed sc-PDSI, underscoring its rarity in this context. Furthermore, despite its potential, SEDI is not mentioned in their study, it remains a marginal and little-used index in Canada. This study establishes a baseline for understanding the historical variability and spatial distribution of droughts in NB by applying these robust indices in a previously unexamined context. These findings provide a critical foundation for future research, including projections of drought variability under changing climate scenarios. Establishing historical variability is a necessary first step in advancing knowledge of regional drought dynamics and informing effective mitigation and adaptation strategies.

5.2. Study area:

This research on drought issues in NB, one of Canada's Maritime provinces, utilizes recorded historical data to observe the adverse consequences of drought occurrences from 1971 to 2020. Figure. 5.1 displays the map of NB, indicating all the meteorological stations utilized in this study. NB is the largest Canadian maritime province, alongside the state of Maine (USA), below the Gaspé Peninsula of Quebec province. Comprising eight major cities, namely Bathurst, Campbellton, Dieppe, Edmundston, the provincial capital of Fredericton, Miramichi, Moncton, and Saint John, NB spans a total area of 73,440 km² and is home to 775,610 inhabitants (Statistics Canada 2022). The primary land cover of NB, around 83%, is forested, with the dedication of the northern half to Appalachians (Government of New Brunswick 2022; Statistics Canada 2022). The climate of NB is categorized as humid continental, which means hot summers with snowy winters (see Fortin and Dubreuil 2020, for more details). Baronetti et al. (2019) described the snow conditions and distribution over the province. In general, milder winters are in the southern NB along the Northumberland Strait and Fundy Bay coastlines. Then, in the northwest, the most significant snowfall is found, lasting the longest. Finally, between these two zones, a transition zone is found where snowfalls are abundant, but rainfalls, which are more frequent in the southern portion, can also be received.

The rivers in NB drain into the Bay of Fundy (south) and the Gulf of St. Lawrence (east). The total annual runoff for the NB watershed is about 77.8 x 10^9 m^3. Maximum daily unit discharges and minimum daily unit discharges range from 0.19 to 1.42 and 0.02 $\times$ 10^{-3} to 2.1 $\times$ 10^{-3} $m^3 / s / km^2$, respectively. Furthermore, the mean annual precipitation varies from 1450 mm to 950 mm

for the southern coastline to the northwest, respectively. Snowfall alters from about 200 mm to 900 mm of water equivalent to the coast of the northeastern area (Burrell and Anderson 1991).

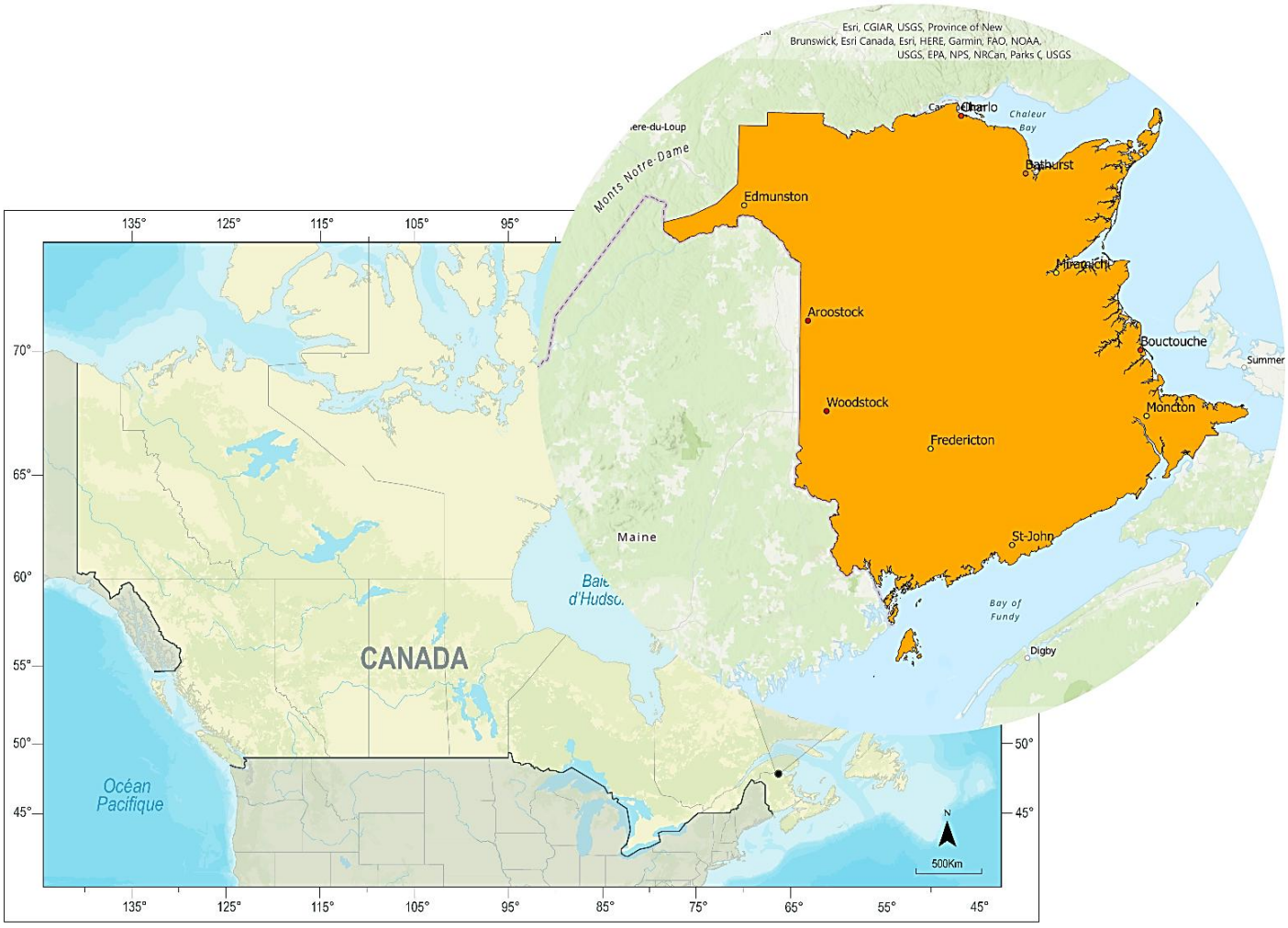

Figure. 5.1 The map of NB with all the meteorological stations.

5.3. Data collection and preparation processes:

Historical adjusted monthly maximum and minimum temperatures, along with monthly total precipitation, were obtained from Environment and Climate Change Canada's (2010) database. A selection of ten meteorological stations across the province was made based on data quality, availability, and geographic distribution (see Table 5.1). Although weather stations across the province provided the necessary data, a notable absence of stations in the central region resulted in limited representation for that area. To address data gaps, raw daily climate data from the Environment and Climate Change Canada (2011) were also utilized to supplement the adjusted monthly dataset. Most stations provided continuous data for the full study period (1971-2020), except the Woodstock station, which had data available from 1974 to 2020. Despite this, the

shortest period analyzed of 46 years exceeds the recommended minimum standard of 30 years for climate time series analysis (Wilks and Livezey 2013).

The inclusion of gridded weather data is critical for developing a comprehensive climate database, enabling the evaluation of long-term climatic patterns across the entire study area. Gridded datasets, such as the Canadian Gridded Temperature and Precipitation Anomalies (CANGRD), offer significant advantages by providing spatially continuous data covering regions without station-based observations. The CANGRD dataset comprises temperature and precipitation anomalies derived from interpolated, adjusted, and homogenized climate station data (AHCCD) dating back to 1948. The anomalies are calculated by subtracting baseline averages (using the 1961-1990 reference period) from monthly, seasonal, and annual mean daily maximum and minimum temperatures, as well as total precipitation values. Precipitation anomalies are normalized by expressing them as percentages relative to the mean reference period, resulting in normalized precipitation departures (Environment and Climate Change Canada 2018).

Table 5.1. The characteristics of meteorological stations across NB.

Station	Lat (deg)	Long (deg)	Duration (year)	Elevation (m)
Aroostook	46.71	-67.72	1971-2020	80
Bathurst	47.63	-65.74	1971-2020	58.8
Charlo	47.99	-66.33	1971-2020	42
Miramichi	47.01	-65.47	1971-2020	33
Moncton	46.11	-64.68	1971-2020	70.7
St John	45.32	-65.89	1971-2020	108.8
Woodstock	46.15	-67.54	1974-2020	154
Edmundston	47.42	-68.32	1971-2020	154.2
Fredericton	45.92	-66.61	1971-2020	35.08
Bouctouche	46.52	-64.72	1971-2020	10.7

After validating the conformity of the data, quality control (QC) procedures were implemented to detect possible breaks, eliminate outliers, and fill the gaps in the collected datasets (Poirier et al. 2023; Wang et al. 2010). According to the NB climate analysis conducted by Roy and Huard (2016), the data, despite some exemptions based on the percentage of missing values, were sufficient for conducting a comprehensive climate analysis throughout the study period. Notably, no breaks, outliers, or missing data were observed in the CANGRD dataset. For all ten meteorological stations, the percentage of missing data was calculated. While the rate of missing data is relatively low overall, data availability varied across stations and over time. Among the adjusted monthly datasets, five stations (Aroostook, Bathurst, Charlo, Woodstock, and Edmundston) had at least one year with an annual missing data rate exceeding 20%. Similarly, for raw daily datasets, four stations (Charlo, Miramichi, Saint John, and Bouctouche) experienced specific years with more than 20% missing data. To address these gaps, the ClimPact2 software

(Alexander and Herold 2016) was employed to detect aberrant data. Outliers were replaced by the average surrounding values. For corrected data, the mean historical values for the respective station were used to fill in missing temperature data (Environment and Climate Change Canada 2011). For precipitation data, the inverse distance weighting method, as described by Shepard (1968), was applied. This approach estimates precipitation at a location based on measurements from the surrounding stations, weighted by the inverse of their distances, offering greater accuracy than simpler methods such as the standard ratio or arithmetic mean (Singh and Singh, 1991).

Therefore, filling in missing data is crucial for all stations, especially in the case of raw daily data. Various data-filling methods were tested on the data series, and the Multiple Imputation Estimation Method (MIEM) offered the most realistic results. MIEM was applied to all datasets to fill in missing data using Markov Chain Monte Carlo (MCMC). The MCMC generates pseudorandom draws from multidimensional and unsolvable probability distributions via Markov chains (Schafer 1997), helping to reduce uncertainties and increase the robustness of an incomplete data series (Yozgatligil et al. 2013). Finally, the homogenization of the data series was validated using the RHtests package in R software, which is a practical method for homogenizing data without relying on a reference station. The RHtest package was applied for temperature data, while the Rhtest_dlyPrcp package was used for precipitation data. Once the raw daily data underwent quality control, monthly means were calculated, and the missing years from the series of adjusted monthly data were added to the end. Since the adjusted monthly data series also contained months without data, the inverse-variance weighted average method (IVW) was applied to raw monthly data from neighboring stations to fill in these missing values. Subsequently, the monthly series was revalidated using RHtests to ensure consistency. Notably, Bathurst's minimum temperature data series exhibited two breaks. After careful observation, no evidence justified these breaks, and smoothing was applied using Spencer's method (S.M.) at 15 points to obtain a homogenized data series. The flowchart of the data preparation process for a station-based dataset is shown in Figure. 5.2.

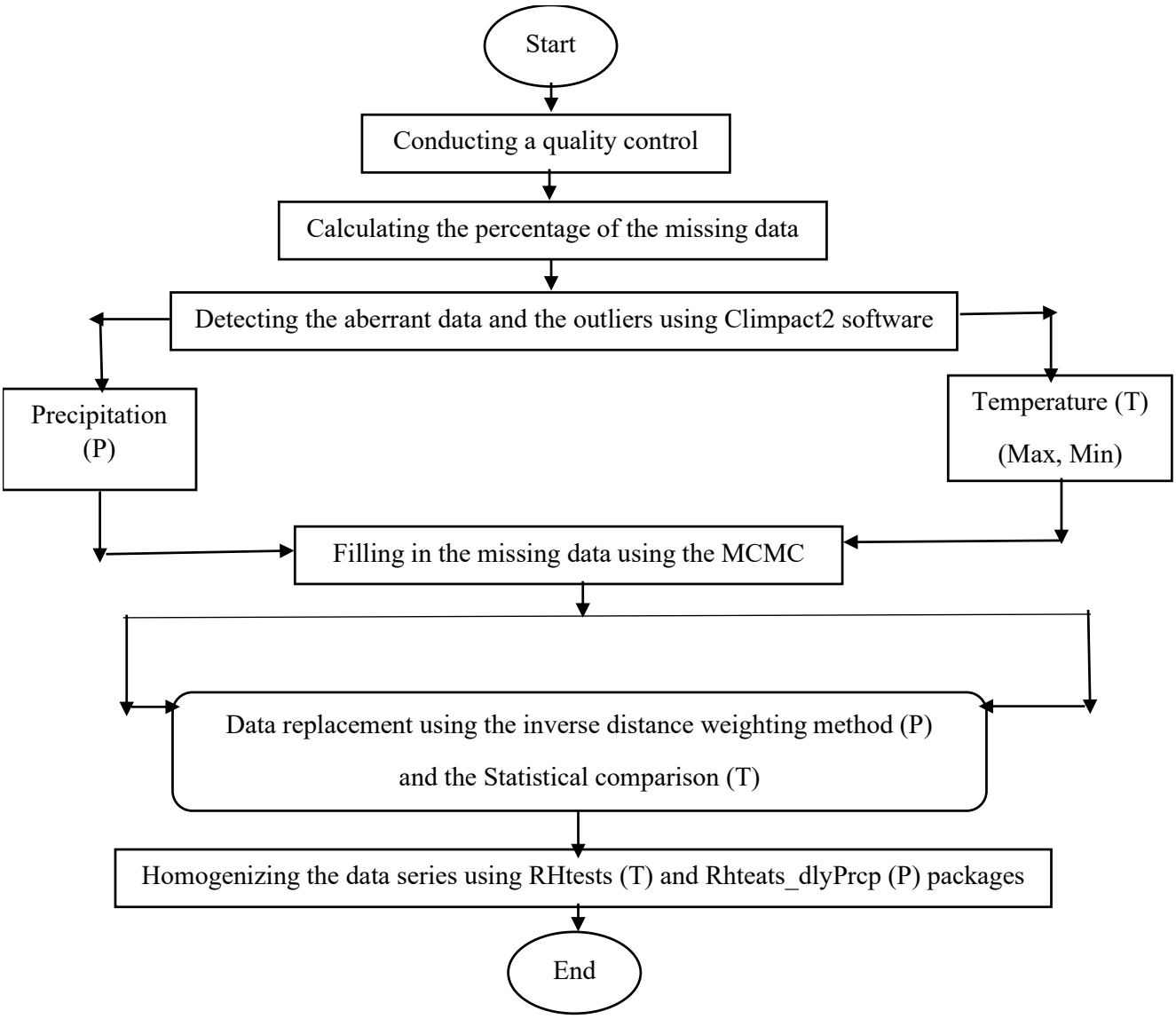

Figure. 5.2 Data processing flowchart for station-based dataset.

5.4. Drought indices:

The assimilation of data from multiple variables, such as evapotranspiration and precipitation, into a single numerical value allows drought indices to effectively differentiate between various levels of drought severity. By employing drought indices, researchers can identify and analyze delayed hydrological and agricultural impacts, such as reduced reservoir levels, soil moisture depletion, and climate dryness anomalies (Yihdego et al. 2019; Van der Schrier et al. 2011; Pellicone et al. 2019; Vessella and Schirone 2022). Developed through straightforward yet robust methodologies, drought indices serve as essential tools for detecting and evaluating drought conditions.

Droughts are influenced by critical variables, including precipitation deficits, streamflow reductions, and evapotranspiration rates. The indicators that define drought indices encompass a wide range of factors: hydrological variables, such as groundwater levels and streamflow; meteorological parameters, including precipitation and cloud cover; and water supply and demand aspects, such as reservoir storage. Additionally, indicators like potential evapotranspiration, soil properties, and vegetation cover play significant roles in broader applications (Tsakiris and Vangelis 2005). Together, these factors provide a comprehensive framework for assessing drought conditions and their impacts across different scales.

5.4.1. Drought indices selection:

The selection of drought indices is influenced by the study goals, data availability, study area, and prevailing climate conditions. While some drought indices are specifically tailored for applications or impacts, others are designed to capture a broader range of implications and applications (Zargar et al. 2011). Commonly used drought indices, such as SPI, SPEI, PDSI, and SEDI, rely on observational data from weather stations. These indices have been extensively applied in drought analysis by researchers across various contexts (Cerpa Reyes et al. 2022; Liu et al. 2021; Pyarali et al. 2022; Zhou et al. 2022; Soleimani-Motlagh et al. 2022). The PDSI, for instance, captures long-term moisture conditions, including evaporation, runoff, recharge, and soil infiltration, making it suitable for analyzing droughts over extended periods. In contrast, the SEDI is particularly effective for characterizing short, intense droughts driven by rapid evaporation (Ho et al. 2021).

In this study, parametric indices were selected over non-parametric ones due to their superior ability to account for extreme droughts, as highlighted by Palagiri and Pal (2024). Meteorological droughts in NB are relatively rare compared to those in the Canadian Prairies and generally follow a normal distribution. Parametric indices are advantageous because they are not constrained by the range of extreme observed values, allowing for more robust modelling of drought conditions over defined reference period. In contrast, non-parametric indices rely heavily on the range of observed data within the reference climatology, limiting their applicability when long-term data are unavailable or insufficient. Moreover, parametric indices are particularly effective in modelling the tails of distributions, which correspond to extreme values –critical for understanding the severity and intensity of droughts (Noguera et al., 2022, Beguería et al., 2014; Stagge et al., 2015; Vicente-Serrano and Beguería, 2016; Svensson et al., 2017).

The use of parametric tests further enhances the reliability of these indices. When the data satisfy assumptions of normality, linearity, and homogeneity of variance, parametric tests provide more powerful and accurate estimates than non-parametric tests. These tests are better at detecting true differences and patterns, leading to stronger conclusions. Non-parametric tests, such as the Mann-Whitney U test or the Kruskal-Wallis test, are appropriate for asymmetrical data distributions, such as highly skewed precipitation data influenced by extremely dry or wet years. However, this condition does not apply to the datasets used in this study, which satisfy parametric assumptions. After the preparation and validation of data, PDSI and SEDI were selected as the most appropriate drought indices based on the study's datasets, regional climate conditions, and specific characteristics. Each index was calculated based on annual and seasonal timeframes to effectively represent drought occurrences and their temporal variations.

5.4.2. Palmer Drought Severity Index (PDSI):

The PDSI, developed by Palmer in 1965, is a widely used meteorological drought index designed to quantify long-term drought conditions. It incorporates key variables such as local rainfall, temperature, and physical water balance model. The PDSI calculates relative dryness by integrating precipitation, temperature, and the locally available soil water content, making it a comprehensive tool for assessing drought severity. The index values range from -4 (extremely dry) to +4 (extremely wet), as outlined in Table 5.2. One of the main advantages of PDSI is its ability to detect the primary effects of global warming on drought conditions by accounting for changes in potential evapotranspiration. However, it is important to note that monthly PDSI values are not suitable for detecting droughts on time scales shorter than 12 months (Palmer 1965). For further details on the formulation of PDSI, refer to Appendix C.5.1.

Table 5.2. PDSI values and corresponding conditions.

PDSI Value	Condition
4.00 or more	Extremely wet
3.00 to 3.99	Very wet
2.00 to 2.99	Moderately wet
1.00 to 1.99	Slightly wet
0.50 to 0.99	Incipient wet spell
0.49 to −0.49	Near normal
−0.50 to −0.99	Incipient dry spell
−1.00 to −1.99	Mild drought
−2.00 to −2.99	Moderate drought
−3.00 to −3.99	Severe drought
−4.00 or less	Extreme drought

5.4.3. Self-calibrated Palmer Drought Severity Index (sc-PDSI):

Wells et al. (2004) introduced the self-calibrating PDSI (sc-PDSI) as an enhancement to the original PDSI, improving its comparability across diverse climate regimes. By replacing the empirical constants in the original equation with dynamically determined values, the sc-PDSI automatically calibrates its behavior for any given location. This feature allows the sc-PDSI to retain the core strengths of the PDSI while improving its accuracy by adjusting calibration constants to reflect the specific climatic conditions of individual stations. As a result, the sc-PDSI is better equipped to capture localized variations in drought patterns, facilitating precise inter-regional comparisons that reflect site-specific conditions. Its versatility, enhanced by the ability to estimate drought conditions at various time steps, makes it particularly suitable for applications across diverse climatic contexts.

Li and Cai (2024) employed the sc-PDSI as a standard drought index in their study of drought patterns in China, comparing its performance against several other indices. Their findings confirmed that the sc-PDSI provided more stable, accurate, and consistent results than its counterparts, making it a reliable tool for assessing drought in diverse subregions. While other indices, such as the SPEI, performed well in certain areas, the sc-PDSI's flexibility and adaptability reinforced its suitability for comparative analyses. Furthermore, Van der Schrier et al. (2013) demonstrated the potential of integrating seasonal snow dynamics into water balance models, a method that could further enhance drought assessments. However, this study focuses on meteorological droughts, where the sc-PDSI has proven its applicability, even in colder regions.

In this research, sc-PDSI was chosen over the original PDSI due to its self-calibrating nature and its enhanced accuracy, achieved by dynamically calculating constants based on historical climatic data. Specifically, the climatic characteristic (K) and duration factors (p =0.897 and q= 1/3), empirically derived in the original PDSI, were replaced with automatically calculated values tailored to the historical climate of the study area. While the sc-PDSI is a variant of the original PDSI distinguished by its self-calibrating capability, the general term "PDSI" is used throughout this study for simplicity, except when explicitly referring to the original version. For detailed information on the sc-PDSI calculation method, refer to Appendix C.5.2.

5.4.4. Standardized Evapotranspiration Deficit Index (SEDI):

The SEDI is derived from anomalies in evapotranspiration deficits (D), calculated using Potential Evapotranspiration (PET) and Actual Evapotranspiration (AET). These parameters represent the direct volume of water evaporated from soil and vegetation, making SEDI a robust indicator of ground-level drought conditions (Abyani et al. 2019). SEDI has been widely utilized for assessing hydrological and meteorological droughts (Vicente-Serrano et al. 2018; Kim and Rhee 2016) and monitoring agricultural droughts. Additionally, the relationship between snow cover area (SCA) and drought conditions has been extensively studied using SEDI. For example, Safari et al. (2024) demonstrated a strong correlation between SCA and SEDI in Iran. Their findings emphasized that SEDI effectively captures the combined effects of evaporation and atmospheric demand on snow cover, underlining its significance for monitoring and forecasting snow cover dynamics.

For the calculation of SEDI, a revised indirect approach was employed, incorporating methodologies and insights from previous studies (Zhang et al. 2019; Wu et al. 2021; Kim and Rhee 2016; Kim et al. 2019; Vicente-Serrano et al. 2018; Chattopadhyay and Hulme 1997; Alsafadi et al. 2022). The formulation of SEDI is detailed in Equation 1.

$$SEDI = \frac{D-DAVE}{DSTD} \quad (1)$$

In this equation, it is essential to highlight that for simplicity in the calculation procedure, the precipitation minus the PET component of the SPEI was substituted with the evapotranspiration deficit (D). Additionally, $DAVE$ and $DSTD$ represent the evapotranspiration deficit's multi-year mean and standard deviation, respectively. Table 5.3 summarizes the range of SEDI values and their corresponding drought severity classifications.

Table 5.3. SEDI values and corresponding conditions.

SEDI	Condition
2.0 or more	Extremely wet
1.5 to 1.99	Severely wet
1.0 to 1.49	Moderately wet
0.5 to 0.99	Mildly wet
-0.5 to 0.5	Normal
-0.99 to -0.5	Mild drought
-1.49 to -1.0	Moderate drought
-1.99 to -1.5	Severe drought
-2.0 or less	Extreme drought

5.5 Drought trend analysis:

5.5.1. Mann-Kendall test:

Mann-Kendall (MK) is a widely used nonparametric method for detecting trends in time series data, even when a seasonal component is present. This statistical test is designed to capture monotonic trends in climate, hydrological, and environmental data series without requiring assumptions about the data's normality. Initially proposed by Mann (1945), the test was further refined by Kendall (1975) and later enhanced by Hirsch et al. (1982, 1984) to account for seasonality. In the MK test, the null hypothesis (H0) assumes no trend in the time series, while the alternative hypothesis (Ha) suggests the presence of a monotonic trend, which can be positive, negative, or non-null. As a nonparametric test, the MK test is robust to outliers and does not assume a normal data distribution (Alemu and Dioha 2020). The test calculates Kendall's Tau (τ), a measure of the association between paired observations, based on the relative ranking of the data. This approach assumes independent and unbiased observations (Fan et al. 2020). For a detailed explanation of the MK test calculation procedure, refer to Appendix C.5.3.

In the seasonal MK test, seasonality is explicitly considered. For example, in monthly data with 12-month seasonality, the analysis evaluates trends within specific months across years (e.g., trends for January from one year to the next, and similarly for February, and so on). This method calculates Kendall's Tau (τ) identifying the direction and magnitude of upward or downward trends. An average of Kendall's Tau is then estimated for the entire series. The variance of statistics can be calculated assuming independence (e.g., January and February are independent) or dependent, which requires the computation of covariance (Zhang et al. 2016). Details of the seasonal MK test procedure are provided in Appendix C.5.4.

Kendall's correlation coefficient (τ_b) was later introduced as a nonparametric measure to assess the direction and strength of the association between two variables measured on at least an ordinal scale (Kendall 1938). This coefficient is particularly useful when the relationship between two

variables is monotonic. Unlike the original to utilize Kendall's Tau, *τb* accounts for tied ranks in the data (Agresti 2010). The coefficient ranges are from -1 (indicating a perfect negative association) to +1 indicating a perfect positive association), with 0 denoting no association. Appendix C.5.5 provides further details on the calculation of Kendall's correlation coefficient.

5.5.2. Sen's Slope estimator:

Sen's estimator is another widely used nonparametric method in drought studies for determining the magnitude of trends. This approach estimates the trend's slope using Sen's method, which requires a minimum of ten observations in the time series to ensure reliable results. The slope is calculated as the linear rate of change over time, while the intercepts are derived using Sen's procedure (Sen 1968). This robust method is advantageous in analyzing datasets with outliers or non-normally distributed data. For detailed calculations and methodology, refer to Appendix C.5.6.

5.6. Results:

5.6.1. PDSI values:

PDSI calculations were conducted for ten weather stations across NB, covering the historical timeframes from 1971 to 2020, except for Woodstock, which spanned from 1974 to 2020. The results for each station are illustrated in Figure 5.3.

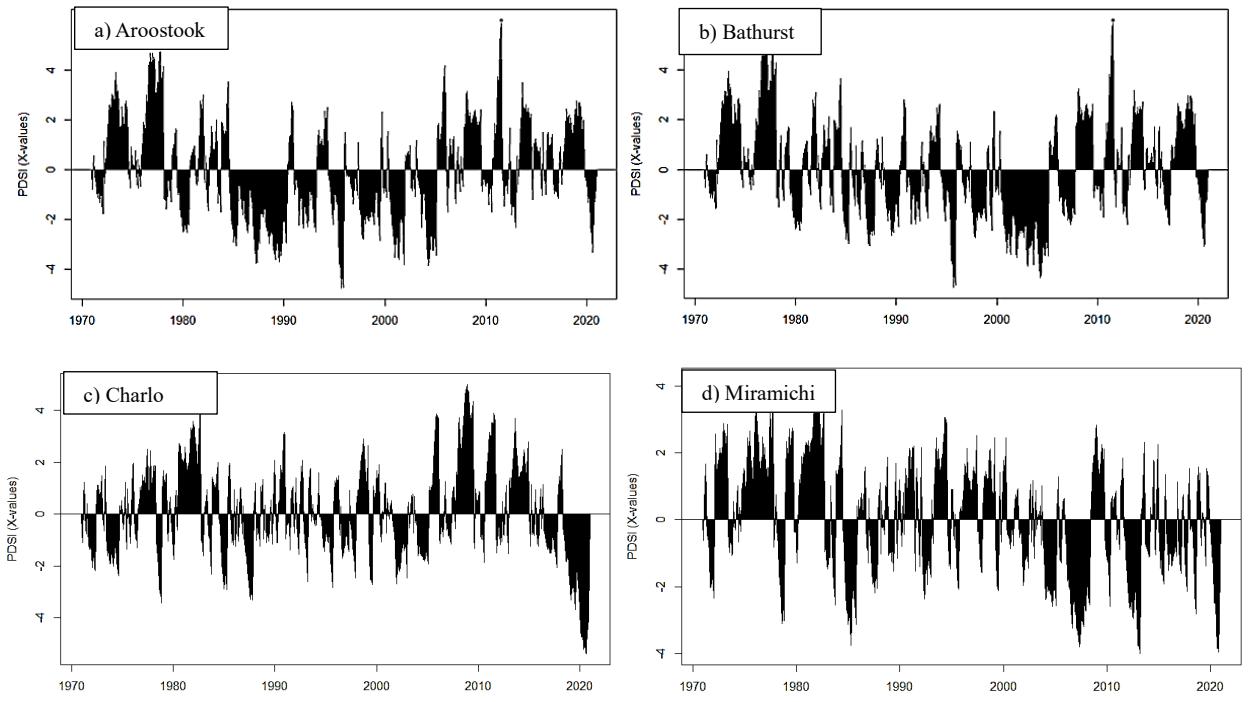

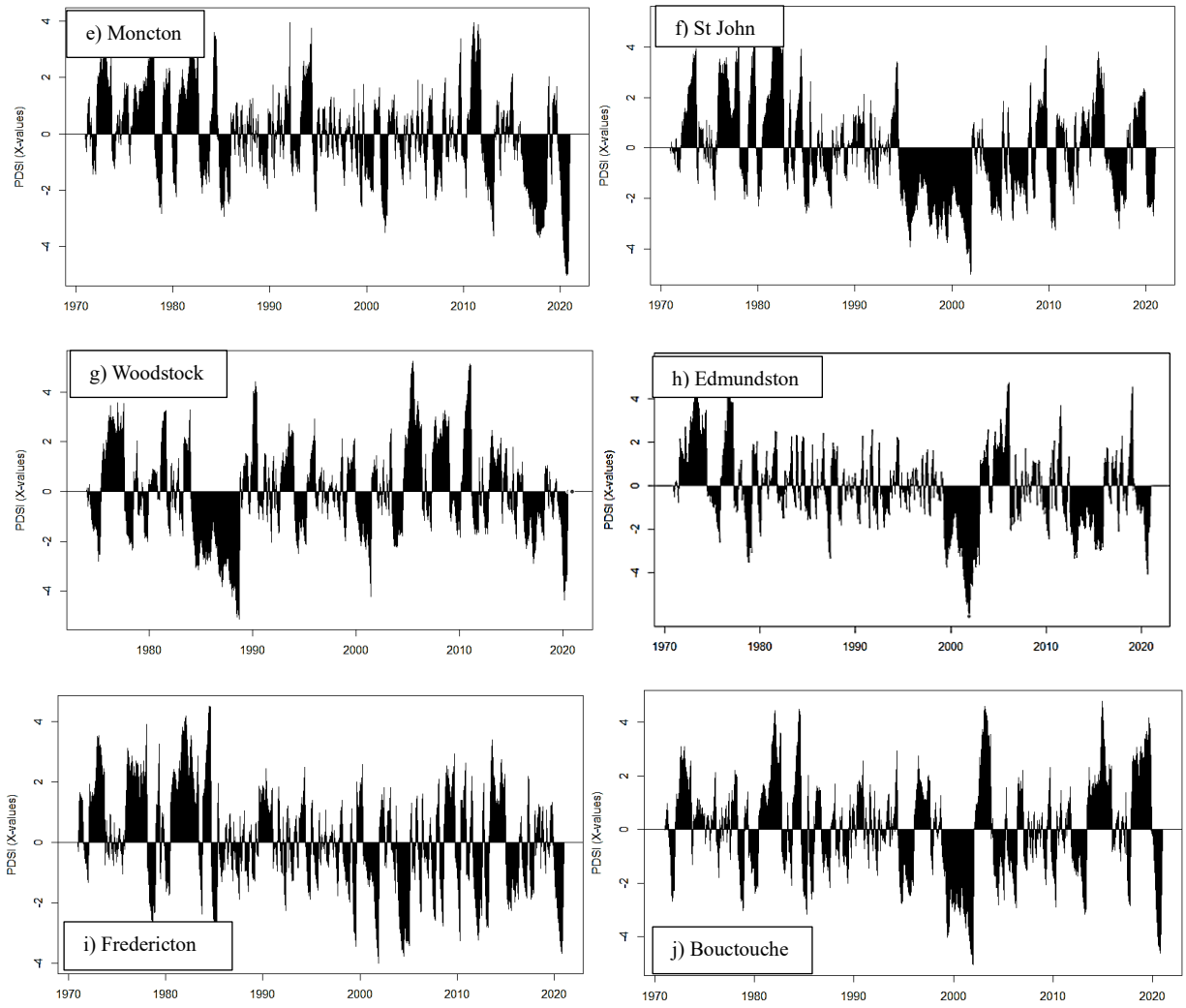

Figure. 5.3 PDSI values for each station across NB.

Based on Figure 5.3a-j, the annual PDSI values for each weather station were calculated and presented. PDSI values of +4 and higher indicate very wet conditions, while values of -4 and lower represent extreme drought conditions (refer to Table 5.2 for a detailed description of threshold values). Each sub-figure in Figure 5.3 provides PDSI values for every year within the study period, offering a comprehensive overview of historical drought conditions across NB. Additionally, the figure allows for a year-to-year comparison of drought severity across all stations. A notable observation is that all ten stations experienced moderate to extreme drought conditions at various points. Specifically, extreme droughts were recorded around 2000 in stations such as Aroostook, Bathurst, Bouctouche, Miramichi, Saint John, Woodstock, and Edmundston. In 2020, moderate to extreme drought conditions were observed in Fredericton, Bouctouche, Charlo, Moncton, Woodstock, and Edmundston. Furthermore, some stations, including Aroostook, Bathurst, Saint John, Edmundston, Moncton, and Woodstock, experienced consecutive years of moderate to severe droughts (PDSI values between -2 and -4 or lower) during specific periods: 1982-1990, 2000-2005,

1995-2002, 2000-2004, 1985-1989, and 2003-2007, respectively. During these periods, no wet conditions were recorded at these stations.

The PDSI results for CANGRD (Figure. 5.4) indicate that NB experienced moderate to extreme drought conditions between 1998 and 2003 and in 2010, with PDSI values falling below -4. Extreme drought conditions, characterized by PDSI values equal to -4, were also observed in 2006, 2009, and from 2012 to 2014.

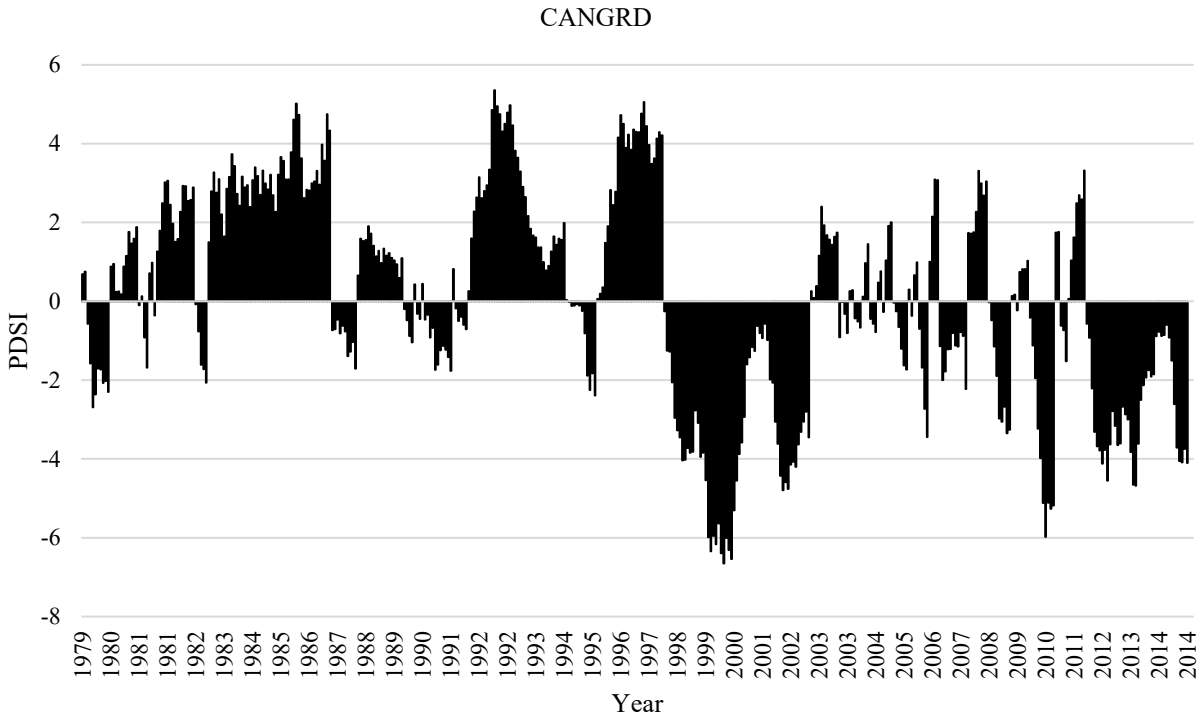

Figure. 5.4 PDSI values for CANGRD-(1979-2014).

5.6.2. SEDI values:

This section presents the calculated SEDI values, as detailed in Section 5.3.4, covering the period from 1971 to 2020 for all weather stations in NB, except for Woodstock, which spans 1974 to 2020. The results are illustrated in Figure 5.5a-j.

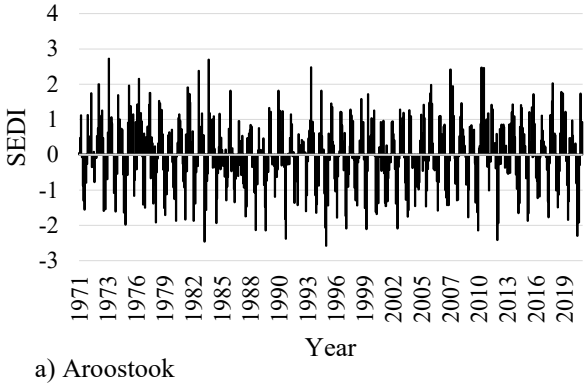

a) Aroostook

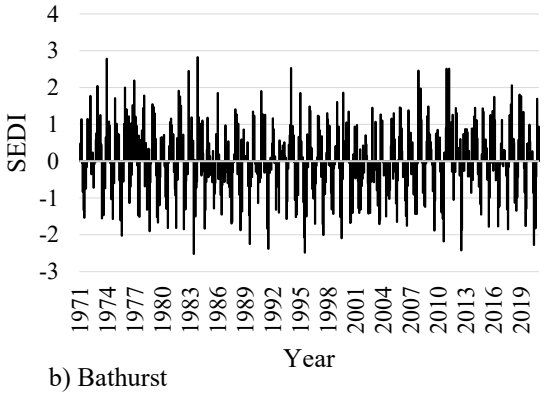

b) Bathurst

c) Charlo

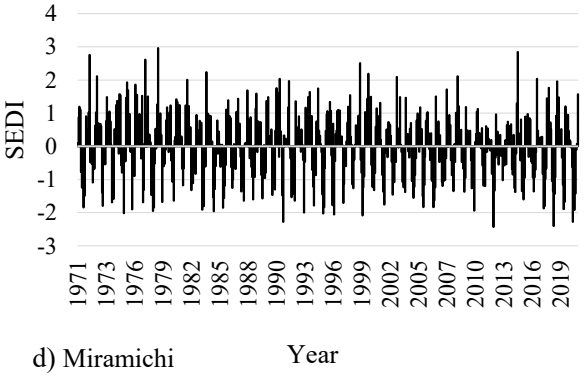

d) Miramichi

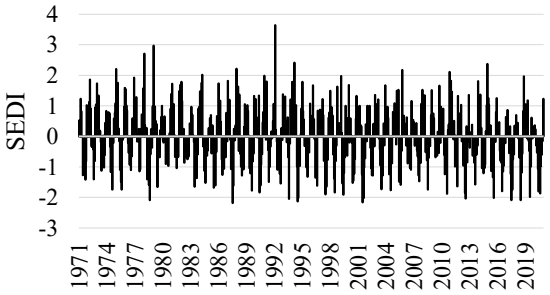

e) Moncton

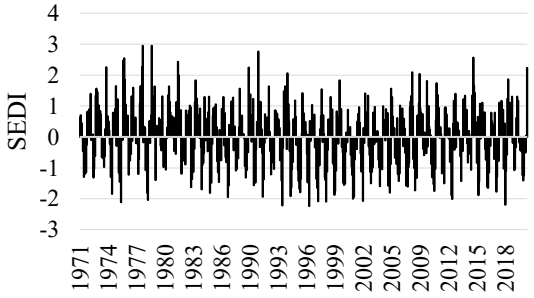

f) St John

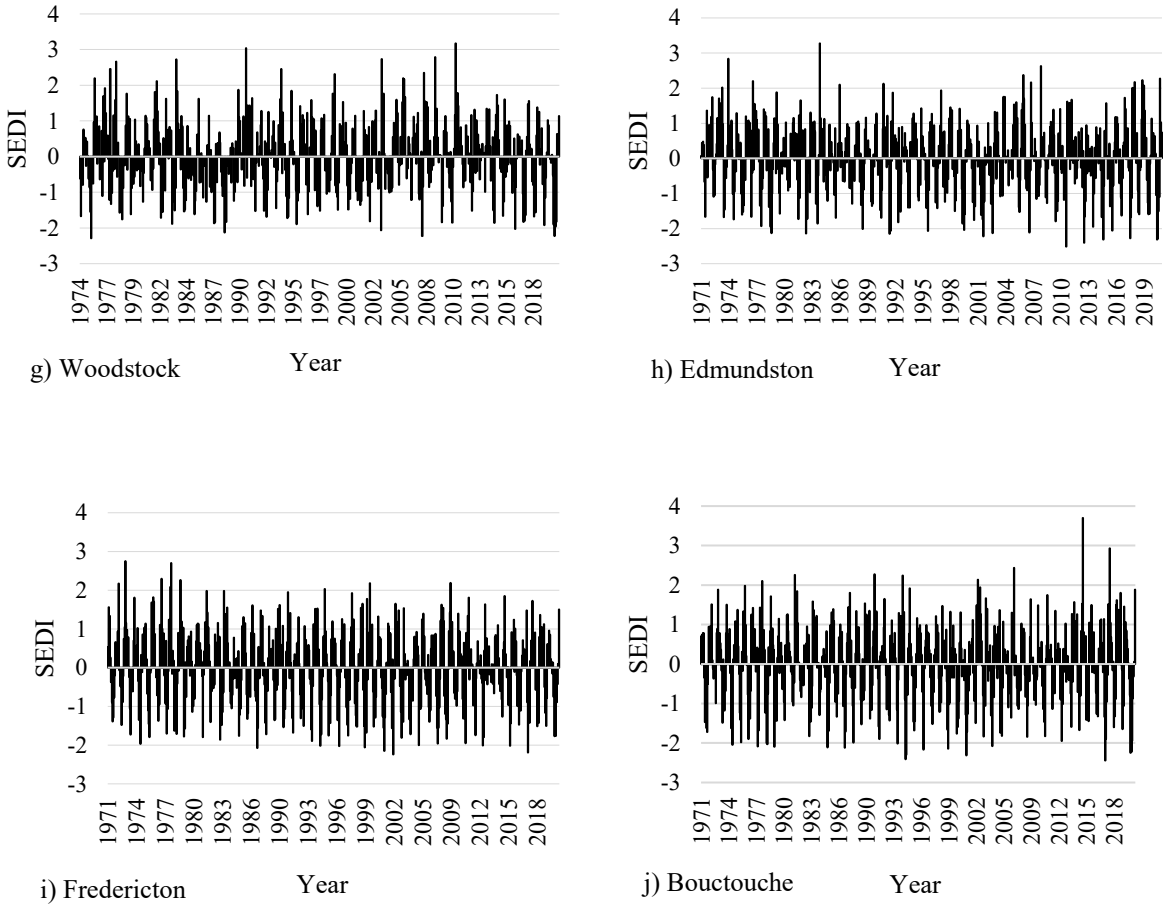

Figure. 5.5 SEDI values for each station across NB.

The SEDI values range from +2 and higher, indicating highly wet conditions, to -2 or lower, representing extreme drought conditions, Within the range of -2 to +2, the lower values correspond to more intense drought conditions (see Table 5.3 for a complete description and threshold values). The results depicted in Figure 5.5 reveal moderate to extreme drought conditions at all stations, with pronounced extreme drought conditions observed in stations such as Aroostook, Bathurst, Charlo, Miramichi, Saint John, Edmundston, and Bouctouche. These findings highlight the heightened vulnerability of these stations to drought impacts. A closer examination of Figure 5.5 shows that extreme droughts were more frequent across most stations between 1990 and 2020 compared to the earlier period from 1971 to 1989. This pattern suggests that NB has experienced more severe drought conditions in recent decades. The increased frequency and intensity of droughts may be attributed to the effects of climate warming, particularly rising temperatures, which accelerate the water cycle, enhance evapotranspiration, and reduce soil moisture availability.

The SEDI values calculated for the CANGRD dataset (Figure. 5.6) further confirm this pattern. Extreme drought conditions (SEDI values below -2) were observed in 1996 and 2003. Additionally, moderate drought periods were identified during 1981-1985, 1998-2000, 2008-2010, and 2011-2013.

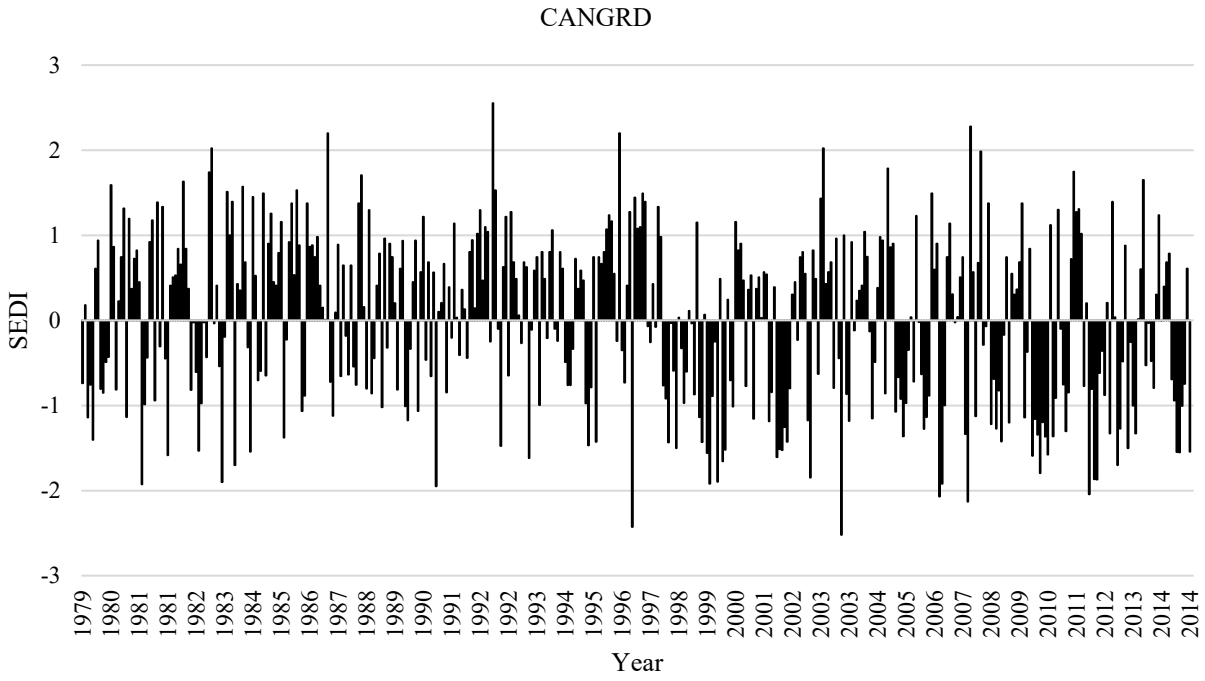

Figure. 5.6 SEDI values for CANGRD-(1979-2014).

5.6.3. Trend analysis:

5.6.3.1. Annual trend analysis

An annual trend analysis of PDSI was conducted using the Mann-Kendall test for each station from 1971 to 2020. The results, presented in Table 5.4, include the P-value, Sen's Slope, and Kendall's Tau. In this analysis, Kendall's Tau signifies the direction and significance of the observed trend, while Sen's slope provides a measure of the trend's magnitude. A P-value of less than 0.05 indicates a statistically significant trend, whereas a P-value equal to or greater than 0.05 suggests no discernible monotonic trend. Positive Kendall's Tau (τ) values signify increasing trends, while negative values indicate a decreasing trend.

Table 5.4. Mann-Kendall's annual trend analysis based on PDSI.

Station	Kendall's tau	P-value	Sen's slope
Aroostook	0.025	0.358	0.010
Bathurst	-0.064	0.020	-0.010
Charlo	-0.035	0.196	-0.003
Miramichi	-0.229	<0.0001	-0.039
Moncton	-0.227	<0.0001	-0.038
St John	-0.171	<0.0001	-0.032
Woodstock	0.015	0.586	0.008
Edmundston	-0.189	<0.0001	-0.032
Fredericton	-0.205	<0.0001	-0.033
Bouctouche	-0.028	0.302	-0.002

The results in Table 5.4 reveal decreasing trends in PDSI values at Bathurst, Miramichi, Moncton, Saint John, Edmundston, and Fredericton stations, as indicated by negative Kendall's Tau values. No significant trends were observed at the Aroostook, Charlo, Woodstock, and Bouctouche stations. Furthermore, the negative values of Sen's slope at stations with decreasing trends corroborate the magnitude of the decline.

Similarly, the Mann-Kendall test was applied to annual SEDI values for each station over the same period (1971-2020), except for Woodstock, which covered 1974-2020. Table 5.5 presents the corresponding P-value, Sen's Slope, and Kendall's Tau.

Table 5.5. Mann-Kendall's annual trend analysis based on SEDI.

Station	Kendall's tau	P-value	Sen's slope
Aroostock	0.008	0.760	0.003
Bathurst	-0.006	0.826	0.001
Charlo	-0.004	0.881	0.002
Miramichi	-0.060	0.028	-0.004
Moncton	-0.050	0.068	-0.003
St-John	-0.048	0.077	-0.003
Woodstock	0.014	0.620	0.004
Edmundston	-0.041	0.129	-0.003
Fredericton	-0.046	0.091	-0.003

Bouctouche	-0.025	0.355	-0.001

Based on the results in Table 5.5, a statistically significant decreasing trend in SEDI values was detected only at the Miramichi station, evidenced by a P-value below 0.05 and a negative Kendall's Tau value. For the remaining stations, P-values exceeding 0.05 indicated no significant annual trends in SEDI values over the analyzed period.

Historical annual trend analyses were also conducted on PDSI and SEDI values using the CANGRD dataset, with results detailed in Tables 5.6 and 5.7, respectively. Negative annual trends were observed for both PDSI and SEDI over the available timeframe (1979-2014), indicating a consistent decline in drought-related indices.

Table 5.6. Historical annual analysis-CANGRD-PDSI (12)- (1979-2014).

Series\Test	Kendall's tau	P-value	Sen's slope
PDSI12-CANGRD (1979-2014)	-0.279	< 0.0001	-0.113

Table 5.7. Historical annual analysis-CANGRD-SEDI (12)- (1979-2014).

Series\Test	Kendall's tau	P-value	Sen's slope
SEDII12-CANGRD (1979-2014)	-0.111	0.005	-0.020

5.6.3.2. Seasonal trend analysis

Seasonal trend analysis of PDSI values was conducted using the Mann-Kendall seasonal test. Monthly PDSI values from January 1971 to 2020 were examined, with the analysis for Woodstock covering the period 1974-2020. The analysis focused on identifying trends for each month across the study period, beginning with January and iterating through all subsequent months to provide a comprehensive assessment of seasonal drought analysis. Figure 5.7 illustrates the seasonal trend analysis results, where K, P, and S represent Kendall's Tau, P-value, and Sen's Slope, respectively.

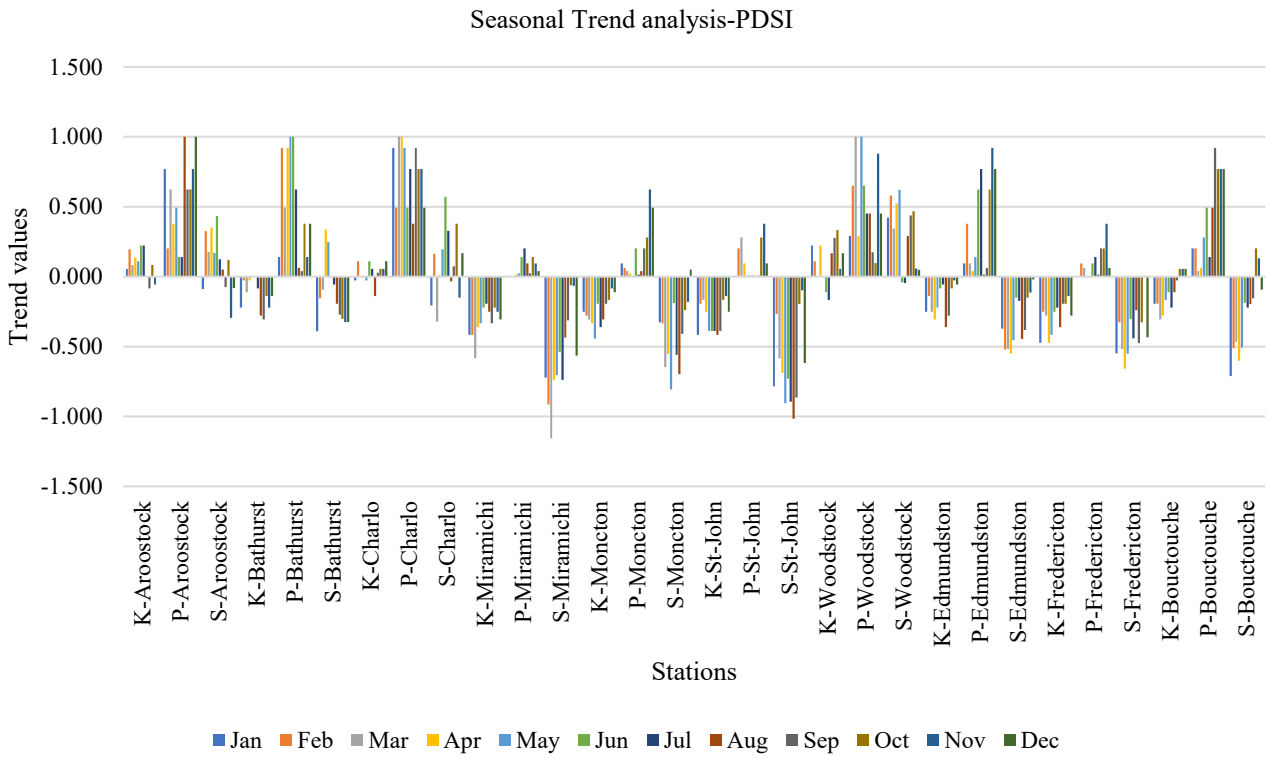

Figure. 5.7 Seasonal Mann-Kendall trend analysis based on PDSI.

Figure 5.7 reveals that no monthly trends were detected for the Aroostook, Charlo, and Woodstock stations, as indicated by P-values exceeding 0.05. In contrast, a decreasing trend was observed at Bathurst station for August and September, supported by a P-value below 0.05 and negative Kendall's Tau values. At the Miramichi station, decreasing trends were recorded from January through May and September through December. Similarly, Moncton station showed a decreasing trend for March through May and July through August. At the Saint John station, decreasing trends were detected from January to May and from September onwards. Edmundston station displayed decreasing trends in April and August. Additionally, at Fredericton and Bouctouche stations, decreasing trends were identified in January, March, April, May, and August.

Seasonal trend analysis for SEDI values was also conducted using the Mann-Kendall seasonal test. Monthly SEDI values from 1971 to 2020 (1974 to 2020 for Woodstock) were analyzed to identify trends for each month. This analysis aimed to determine trends from one January to the next, and similarly for other months. Figure 5.8 provides a comprehensive overview of the seasonal trend analysis for SEDI, with K, P, and S denoting Kendall's Tau, P-value, and Sen's Slope, respectively.

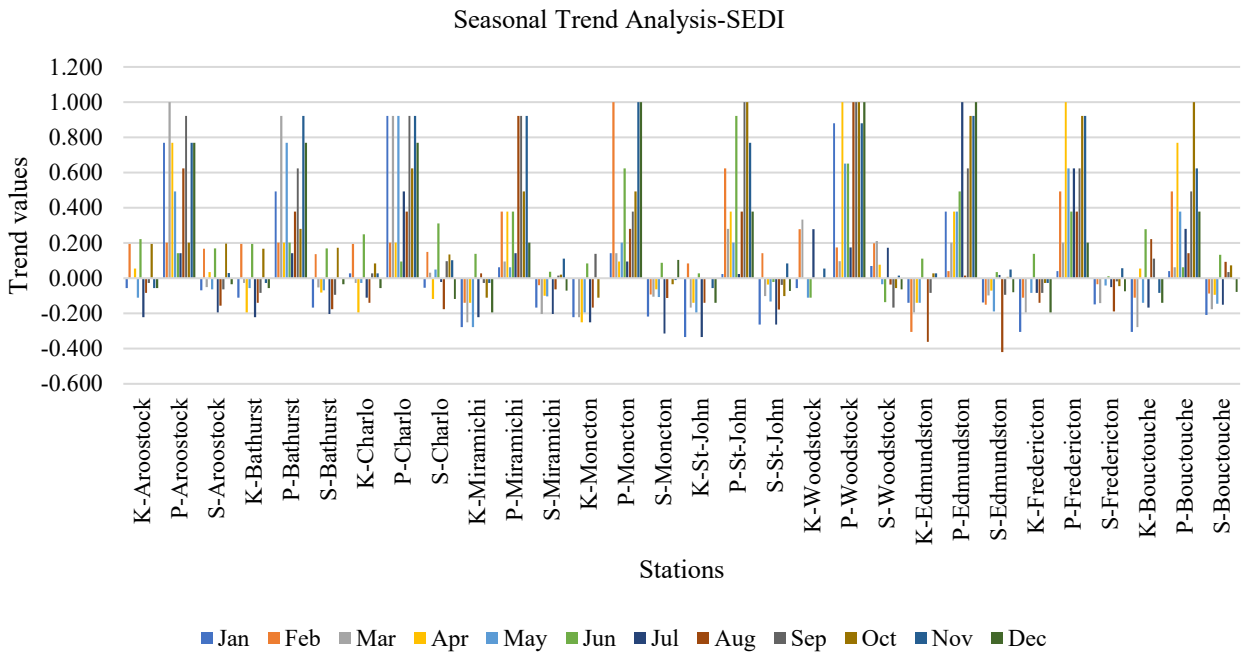

Figure. 5.8 Seasonal Mann-Kendall trend analysis based on SEDI

Based on Figure 5.8, no significant trends were detected for any month at the Aroostook, Bathurst, Charlo, Miramichi, Moncton, and Woodstock stations, as indicated by P-value greater than 0.05. However, a decreasing trend was observed at Saint John station for January and July, supported by a P-value below 0.05 and negative Kendall's Tau values. Similarly, decreasing trends were recorded at the Edmundston and Bouctouche stations for February and August. For the Fredericton station, a decreasing trend was observed only in January.

Historical seasonal trend analyses were also performed for PDSI and SEDI values using the CANGRD dataset. Over the analyzed timeframe, negative seasonal trends were observed for PDSI values across all months except February, as detailed in Table 5.8. However, no significant seasonal trends were recorded for SEDI values during the same period.

Table 5.8. Historical seasonal analysis-CANGRD-PDSI (12)- (1979-2014).

Series\Test	Kendall's tau	p-value	Sen's slope
PDSI12-CANGRD (1979-2014)-Jan	-0.286	0.015	-0.114
PDSI12-CANGRD (1979-2014)-Mar	-0.270	0.021	-0.096
PDSI12-CANGRD (1979-2014)-Apr	-0.286	0.015	-0.114
PDSI12-CANGRD (1979-2014)-May	-0.273	0.020	-0.110
PDSI12-CANGRD (1979-2014)-Jun	-0.267	0.023	-0.101
PDSI12-CANGRD (1979-2014)-Jul	-0.283	0.016	-0.112
PDSI12-CANGRD (1979-2014)-Aug	-0.286	0.015	-0.119
PDSI12-CANGRD (1979-2014)-Sep	-0.305	0.009	-0.126
PDSI12-CANGRD (1979-2014)-Oct	-0.324	0.006	-0.130
PDSI12-CANGRD (1979-2014)-Nov	-0.273	0.020	-0.107
PDSI12-CANGRD (1979-2014)-Dec	-0.343	0.003	-0.124

5.6.4. Drought vulnerability:

Drought vulnerability across NB was assessed using the calculated dry values of PDSI and SEDI. The Kendall's Tau values derived from the annual trend analysis served as indicators of drought intensity and frequency, facilitating the identification of regions most vulnerable to drought within the province. Table 5.9 presents the results of this vulnerability assessment, based on the absolute values of Kendall's Tau and their statistical significance. Regions with higher absolute Tau values, coupled with a P-value below 0.05, were identified as more vulnerable to frequent drought occurrences.

Table 5.9. The results of the NB vulnerability based on drought frequency.

Station/Gridded dataset	PDSI-Tau values	P-values	Trend	SEDI-Tau values	P-values	Trend
Bathurst	-0.064	<0.05	Yes	-0.006	>0.05	No
Miramichi	-0.229	<0.05	Yes	-0.060	<0.05	Yes
Moncton	-0.227	<0.05	No	-0.050	>0.05	No
St John	-0.171	<0.05	Yes	-0.048	>0.05	No
Edmundston	-0.189	<0.05	Yes	-0.041	>0.05	No
Fredericton	-0.205	<0.05	Yes	-0.046	>0.05	No
CANGRD	-0.279	< 0.0001	Yes	-0.111	<0.005	Yes

5.7. Discussion

The spatial and temporal variations of observed droughts using PDSI and SEDI can be attributed to multiple factors, including temperature, groundwater characteristics, precipitation, snowpack, and human activities. Among these, precipitation and temperature emerge as the most critical explanatory variables for meteorological droughts. Given that this study examines historical drought events between 1971 and 2020, it is important to consider the leading causes of drier-than-normal episodes during this period.

From a temporal perspective, Poirier et al. (2023) provided a comprehensive analysis of drought events in NB, utilizing data from the same ten weather stations as this study to calculate SPI and SPEI indices. Their research incorporated documentary sources, such as newspapers, to validate station observations, revealing slight differences between the two indices. Stations in southern NB have shown a slight increase in drought frequency since the 1970s, while northern stations have not exhibited statistically significant trends. However, more pronounced trends were observed when examining SPI and SPEI indices across 1-, 3-, 6-, and 12-month periods, particularly for the 6- and 12-month timescales, with an increasing tendency toward drought in several stations. Similarly, Mallet et al. (2018) investigated drought conditions in northeastern NB and found that approximately 70% of extreme events, including droughts, identified from weather observations were corroborated by newspaper accounts. Their study, which spanned 1950 and 2012, categorized droughts and wildfires together, reporting 20 drought-related events out of 282 extreme occurrences (7% of total events). While this research demonstrated that droughts are not a recent phenomenon in NB, it is also highlighted that historical droughts, as reported in newspapers, were primarily hydrological, agricultural, or socioeconomic, impacting human activities such as low surface water levels, dry wells, and crop losses.

From an intra-annual perspective, droughts in NB are most likely to occur during the summer months, whereas high flows typically occur in spring (due to snowmelt) and fall (with minimal interception and evapotranspiration) (Chouaib and Caissie 2021). Fall is also characterized by extratropical storms and heavy precipitation. Winter and spring are generally less conducive to droughts, as snow accumulation during winter recharges groundwater, and significant snowmelt during spring contributes to water availability. However, conditions such as reduced snowfall or early spring melt, as seen in Western Canada in 2015 (Szeto et al. 2016), can lead to drought episodes.

The choice of drought indices significantly influences the results, as different indices rely on varying input variables. SEDI was selected in this study for its ability to capture rapid and extreme drought conditions, commonly referred to as flash droughts (Clark et al. 2022; Li et al. 2020). Flash droughts are particularly relevant in NB's climate, where high temperatures during heat waves are concentrated in the summer months (June to September). However, there remains a lack of literature focused on this specific drought type in eastern Canada, highlighting the need for further research.

Understanding the causes and mechanisms behind drought occurrence over varying timeframes requires examining the central atmospheric systems responsible for conditions that do not bring precipitation. In general, weather systems that fail to deliver precipitation. While weather systems

associated with heavy rainfall are well-studied, there is limited research on the atmospheric conditions that contribute to drought in Eastern Canada. Bonsal and Shabbard (2008) emphasize the need for more detailed studies on the spatial and temporal relationships between atmospheric circulation variability and low-flow conditions in eastern and northern Canadian watersheds. A thorough analysis of the interplay between droughts and atmospheric circulation would provide valuable insights into the conditions favorable for drought occurrence in this region.

5.7.1. Impact of drought on groundwater

In NB, where over 75% of the population relies on groundwater for drinking water (Statistics Canada, 2010), the importance of this resource extends far beyond domestic use. Groundwater also supports agricultural, municipal, commercial, institutional, and industrial needs, underscoring its critical role in the province's sustainability. Consequently, understanding the potential impacts of global warming on groundwater availability is imperative. Groundwater serves as a vital resource for mitigating vulnerability and alleviating the adverse effects of drought, particularly hydrological droughts (Lin et al. 2021).

However, there is limited data on groundwater in NB and insufficient information regarding the impacts of climate change on groundwater dynamics (Larocque et al. 2019). The size and characteristics of aquifers play a crucial role in determining groundwater storage capacity and, by extension, the resilience of populations to drought events. Smaller, shallower aquifers are particularly vulnerable to drought and less capable of withstanding the effects of climate warming. The reduction in groundwater monitoring infrastructure exacerbates this vulnerability; in the early 2000s, the province's groundwater monitoring network was largely dismantled, leaving only a handful of operational wells. This significant reduction in data availability has limited the capacity for comprehensive groundwater assessment at the provincial level (Larocque et al. 2019).

5.7.2. Impact of drought on precipitation and snowpack

Ullmann (personal communication, 2024) analyzed the statistical distributions of daily rainfall in NB, and their evolution from 1970 to 2022. The results indicate that most rainy days fall within low to medium rainfall ranges, particularly in the western part of the province near the border with Maine. Over time, daily rainfall has been increasingly characterized by lower quantities, with values typically classified as average or heavy becoming less frequent. Although the number of rainy days has remained relatively stable between 1970 and 2022, the daily precipitation amount has shown a decreasing trend.

Snowfall and persistence during winter are critical factors influencing groundwater levels, water table recharge, and river flows in the region (Chouaib and Caissie 2021). However, episodes of warmer winter temperatures, reduced snow accumulation, and increased winter rainfall, are expected to alter these dynamics. These conditions could lead to higher river discharge and groundwater recharge during winter but reduced spring flooding and diminished spring groundwater recharge. The full extent of winter groundwater recharge dynamics under changing climate conditions remains insufficiently studied (Larocque et al. 2019). While the influence of warming temperatures on snow and hydrological processes is well documented, the sensitivity of evapotranspiration and its impact on vegetation is less understood (Cook et al. 2018).

Baronetti et al. (2019) examined the spatial and temporal distribution of snow cover in NB, identifying three main snow climate zones aligned along a northwest-southeast gradient. These zones are separated by a transitional region. The southernmost zone, characterized by the highest annual precipitation, exhibits weaker average snow depth and shorter snow cover duration, often lasting only a few weeks. In contrast, the northwest zone, with colder temperatures (approximately 4°C lower minimum temperatures) and lower annual precipitation (less than 100 mm), has a higher snow-to-rain ratio, resulting in deeper and longer-lasting snow cover. This persistent snow cover is critical in the hydrological budget by delaying snowmelt, ice breakup, groundwater recharge, and surface water flows. Consequently, the northwest zone experiences reduced the likelihood of late summer and early fall hydrological droughts. Water demand peaks during the warmest months (July-August), coinciding with high evaporation and evapotranspiration rates. For example, the severe drought that affected western Canada in 2015 was partly attributed to early snowmelt triggered by high late-winter temperatures (Szeto et al., 2016). Similarly, lower snow depths recorded in coastal and southern NB weather stations may partially explain the region's slightly higher drought frequency.

The form and intensity of precipitation, whether snow or rain, significantly influence drought conditions. Intense rainfall events promote surface runoff rather than infiltration and groundwater recharge, potentially exacerbating drought impacts (Larocque et al. 2019). Consequently, an intensification of rainfall events under a changing climate could further aggravate drought conditions.

5.7.3. Impact of drought on human activities

While the drought indices used in this study do not incorporate socioeconomic or demographic variables, these factors are critical dimensions of water resource management. Urbanized regions, characterized by dense populations and concentrated economic activities, place significant pressure on water demand and are particularly vulnerable to the impacts of drought. In New Brunswick, the southern region hosts the province's most significant urban centers - Saint John, Moncton, and Fredericton— with populations in 2022 estimated at 242,720, 179,836, and 153,061, respectively. Combined, the cities account for nearly 71% (575,617) of the provincial population (Statistics Canada 2022). Human activities can significantly exacerbate vulnerability to drought, particularly in the absence of effective water resource management practices. Traditional water resource management approaches have predominantly focused on environmental variables; however, the escalating impacts of the climate crisis necessitate the integration of the human component into drought risk mitigation and adaptation strategies. This study highlights those cities in highly drought-prone regions, such as Moncton, which also have large and growing populations, face heightened vulnerability to extreme droughts. Despite the evident risks, drought risk is not currently integrated into many such cities' climate change adaptation plans. Addressing this gap requires a paradigm shift in urban water resource management. For example, measures such as incorporating sustainable water use practices, enhancing urban infrastructure resilience, and fostering community awareness about water conservation can significantly reduce drought vulnerability. By embedding these strategies into climate adaptation frameworks, cities can better prepare for and mitigate the compounded risks of extreme drought events and population pressures.

5.8. Conclusion

This study conducted a comprehensive meteorological drought analysis for New Brunswick (NB) to evaluate drought events' severity, magnitude, and recurrence. Significant trends and regional vulnerabilities were identified using the Palmer Drought Severity Index (PDSI) and Standardized Evapotranspiration Deficit Index (SEDI), which were calculated from station-based and gridded datasets spanning 1971–2020.

The analysis revealed that all ten weather stations experienced moderate to extreme droughts, with increased frequency and intensity from 2000 to 2020, likely linked to global warming. Severe droughts were prevalent in Bathurst, Miramichi, Moncton, Saint John, Edmundston, and Fredericton. Trend analyses indicated annual and seasonal declines in PDSI values across multiple stations, with some stations showing no discernible trend. For SEDI, fewer stations exhibited significant trends, highlighting variability in drought metrics. Results from gridded data (CANGRD) corroborated station-based findings, further validating the methodology and outcomes.

Periods of pronounced drought were identified between 1998 and 2014, with extreme events in 1996, 2003, 2006, 2009, and 2012–2014. These findings underscore the increasing intensity and frequency of droughts in NB over recent decades. While uncertainties remain regarding future drought responses to climate change, projections indicate heightened risks of extreme precipitation and drought events compounded by population growth in vulnerable areas. Future research should explore satellite-based drought indices as a complementary validation tool and assess future drought variability using climate projections to refine regional adaptation strategies.

Acknowledgments

We thank the Government of New Brunswick and the Environmental Trust Fund of New Brunswick for supporting this research.

Statements and Declarations

Funding

This work was supported by the [Environmental Trust Fund of New Brunswick] under Grant [number 210294].

Competing Interests

The authors report there are no competing interests to declare.

Author contributions

All authors A.F., G.F., A.U., F.R., C.P., V.D., and D.G. contributed to the study conception, design and discussion. Material preparation, data collection, analysis, and supervision were performed by A.F., and G.F. The first draft of the manuscript was written by A.F. and all authors G.F., A.U., F.R., C.P., V.D., and D.G. commented on previous versions of the manuscript. All authors A.F., G.F., A.U., F.R., C.P., V.D., and D.G. read and approved the final manuscript.

Data availability

The datasets supporting this study's findings are available from the corresponding author Ali Faghfouri, upon reasonable request. In addition, raw data that was used in this study is available from the Environment and Climate Change Canada website: https://www.canada.ca/en/environment-climate-change.html

Conclusion Générale

Dans un contexte où les rivières en climat froid subissent une pression croissante liée aux changements climatiques et aux perturbations anthropiques, cette thèse a approfondi la compréhension de leurs dynamiques hydro-sédimentaires grâce à une approche intégrée combinant cadre conceptuel, analyses empiriques, reconstructions historiques et modélisation prédictive. L'ensemble des travaux, articulé autour de cinq chapitres rédigés sous forme d'articles scientifiques, explore chacun une dimension spécifique mais complémentaire des systèmes hydro-sédimentaires soumis aux contraintes saisonnières et aux changements globaux.

Elle apporte en particulier cinq contributions scientifiques majeures :

- La proposition d'un cadre conceptuel renouvelé de la connectivité sédimentaire adapté aux rivières en climat froid.
- Le développement d'un outil prédictif de crues basé sur les réseaux de neurones et intégrant le changement climatique.
- La reconstruction historique sur 70 ans de l'évolution morpho-sédimentaire de la rivière du Diable (Québec).
- La mise en place d'un cadre multi-modèles pour le transport sédimentaire, permettant d'identifiant les « hotspots » géomorphologiques.
- L'analyse spatiale et temporelle des régimes de sécheresse au Nouveau-Brunswick (1971–2020).

Ces cinq volets, en dialogue constant, relient concepts, données de terrain et outils de modélisation, et ouvrent de nouvelles perspectives pour mieux comprendre et anticiper les dynamiques hydro-sédimentaires en contexte de changements climatiques.

Le premier chapitre a proposé un cadre conceptuel renouvelé de la connectivité sédimentaire adapté aux rivières en climat froid. Ce modèle à quatre couches — facteurs externes (*drivers*), attributs structurels, processus fonctionnels et rétroactions — intègre explicitement des phénomènes caractéristiques des milieux froids, tels que les cycles gel–dégel, les crues nivales et les effets hérités des perturbations passées. À la différence des modèles issus de contextes tempérés, il met en avant l'importance des déclencheurs épisodiques (fonte rapide, ruptures d'embâcles, sécheresses) et des états saisonniers « on/off » dans l'activation des transferts sédimentaires. Il identifie également plusieurs lacunes, notamment la rareté des données hivernales, le manque d'indices dynamiques de connectivité et la sous-intégration des processus cryosphériques. Ce cadre fournit une base conceptuelle inédite pour relier structure, processus et dynamique fluviale dans les rivières tempérées froides.

Le deuxième chapitre a développé un outil de prévision des crues adapté au changement climatique dans le bassin de la rivière Eel, au Nouveau-Brunswick. Basé sur un réseau de neurones artificiels (ANN) entraîné à partir de séries historiques de précipitations, températures et débits, ce modèle a été calibré et validé sous les scénarios climatiques RCP 4.5 et 8.5. Les résultats montrent une excellente capacité de reproduction des débits journaliers et mensuels passés, et surtout une

forte intensification des crues futures. La crue centennale, par exemple, pourrait voir son débit moyen augmenter de près de 50 % d'ici le milieu du siècle, avec deux périodes critiques identifiées : 2056–2072 sous RCP4.5 et 2039–2055 sous RCP8.5. Ces résultats soulignent une accentuation claire du risque d'inondation dans un bassin déjà vulnérable et mettent en évidence la nécessité d'adapter les infrastructures et les plans de gestion.

Le troisième chapitre a réalisé une reconstruction historique sur 70 ans de l'évolution de la rivière du Diable au Québec, en combinant photographies aériennes, modèles numériques LiDAR et bilans sédimentaires volumétriques. L'analyse a révélé une alternance de phases d'exportation et de stockage, illustrant un comportement pulsé caractéristique des rivières froides. Entre 1980 et 2001, la rivière a connu une phase d'export net d'environ –142,5 m³/km/an, caractérisée par une forte migration des méandres et un recul marqué des berges. Cette dynamique a été suivie d'une phase de stockage entre 2001 et 2007, avec un gain net de +70,8 m³/km/an, associée à une stabilisation relative du tracé et à une aggradation de la plaine. Cette alternance export–récupération met en évidence le rôle déterminant des événements extrêmes et des rétroactions morphologiques dans la trajectoire des rivières tempérées froides. Elle confirme également que la connectivité sédimentaire est sélective : les sables grossiers ont tendance à être retenus localement, alors que les particules fines sont exportées hors du tronçon.

Le quatrième chapitre a établi un cadre multi-modèles de quantification du transport sédimentaire, appliqué au même tronçon de la rivière du Diable. Cinq approches complémentaires (*Shear Stress, Energy Slope, Probabilistic, Regression, Equal Mobility*) ont été mobilisées à partir de 32 échantillons granulométriques représentatifs (talus et plages). Les résultats montrent des écarts considérables selon la granulométrie et la morphologie : les échantillons prélevés sur les falaises sableuses abruptes (Φ90) produisent des taux de transport d'un à deux ordres de grandeur supérieurs à ceux des plages sableuses. Cette divergence met en évidence l'importance des conditions locales de pente et de tri sédimentaire dans le contrôle de la mobilité. L'intégration de ces modèles avec les indices de puissance spécifique et de transport (SPI, STI) a permis de produire des cartes de « hotspots » géomorphologiques, identifiant les secteurs les plus vulnérables aux crues printanières et aux événements extrêmes récents comme ceux de 2011, 2017–2019, et 2023. Ces cartes, validées par la convergence des approches, constituent un outil robuste pour cibler les zones à risque.

Enfin, le cinquième chapitre a évalué les régimes de sécheresse au Nouveau-Brunswick (1971–2020) à partir de deux indices complémentaires : le *Palmer Drought Severity Index* (PDSI) et le *Standardized Evapotranspiration Deficit Index* (SEDI). L'analyse statistique et spatiale, appuyée sur des données maillées et dix stations climatiques, a révélé une intensification des sécheresses, particulièrement dans le sud-est de la province. Cette région, traditionnellement humide, est apparue comme la plus vulnérable, avec une baisse notable du nombre de jours de pluie et des précipitations totales. Ces résultats confirment que le réchauffement climatique affecte non seulement les crues mais aussi les étiages, introduisant une double contrainte sur les réseaux fluviaux et accentuant leur vulnérabilité future.

Synthèse transversale

Pris dans leur ensemble, les cinq chapitres de cette thèse démontrent que les systèmes fluviaux en climat tempéré froid sont gouvernés par une combinaison complexe de contrôles saisonniers, de rétroactions internes et de pressions climatiques et anthropiques. La variabilité climatique (fonte nivale, sécheresses, précipitations extrêmes) en constitue le moteur principal, mais les réponses des rivières sont modulées par leur mémoire morphologique et par la sélectivité des connexions sédimentaires, qui déterminent quelles portions du réseau sont actives ou en dormance. Trois constats transversaux émergent :

1. La variabilité climatique comme moteur principal des dynamiques fluviales. Les résultats mettent en évidence que les crues nivales, les redoux hivernaux et les sécheresses estivales conditionnent directement la connectivité sédimentaire et l'évolution morphologique des chenaux. Les projections climatiques (Chapitre 2) suggèrent une intensification des crues au cours des prochaines décennies, tandis que l'analyse diachronique des sécheresses régionales (Chapitre 5) révèle une tendance nette à leur aggravation. La combinaison de ces dynamiques, crues plus violentes et sécheresses plus fréquentes, accentue les contrastes saisonniers et annonce une instabilité accrue des systèmes hydro-sédimentaires.

2. La connectivité comme clé de lecture des réponses fluviales. Au-delà du climat, la manière dont les sédiments circulent dans les réseaux fluviaux dépend de l'intermittence des connexions entre sources, voies et puits. Le cadre conceptuel développé (Chapitre 1) a montré que ces connexions sont modulées par les processus cryoclimatiques et par la mémoire géomorphologique accumulée dans le bassin. Cette perspective a trouvé confirmation dans l'étude empirique de la rivière du Diable (Chapitre 3), où une dynamique « pulsée » a été mise en évidence. Les phases d'exportation massive alternent avec des périodes de stockage, reflétant l'activation ou la désactivation temporaire des réseaux de connectivité. Ce constat souligne que la compréhension des trajectoires fluviales en climat froid passe par l'analyse des états successifs de (dé)connexion.

3. La valeur des approches intégrées et multi-modèles. Enfin, cette thèse démontre l'intérêt de mobiliser des méthodes complémentaires — reconstructions diachroniques, analyses granulométriques, formules de transport, réseaux de neurones artificiels, indices climatiques — pour croiser les échelles spatiales et temporelles. En combinant ces approches, il a été possible de réduire les incertitudes propres à chacune et de dégager une vision plus robuste des dynamiques fluviales. Les résultats convergent vers l'idée que seule une articulation étroite entre de cadres conceptuels, données empiriques et outils de modélisation permet d'anticiper la complexité des réponses fluviales dans les environnements froids.

En résumé, cette synthèse transversale montre que seule une approche intégrée, reliant processus saisonniers, trajectoires morphologiques à long terme et projections climatiques, permet d'appréhender la complexité et l'instabilité croissante des systèmes fluviaux en climat tempéré froid.

Contributions scientifiques

Les contributions de cette thèse à la géomorphologie fluviale et aux sciences de l'environnement se déclinent sur trois plans complémentaires : conceptuel, méthodologique et appliqué.

Sur le plan conceptuel, l'apport majeur réside dans la proposition d'un cadre intégré de la connectivité sédimentaire spécifiquement adapté aux rivières tempérées froides. Ce cadre réinterprète les modèles issus des contextes tempérés en y intégrant explicitement les processus cryoclimatiques, tels que les cycles gel–dégel, les crues de débâcle ou encore les sécheresses estivales. Il met en évidence la manière dont ces processus activent ou désactivent les voies de connectivité, et propose une lecture renouvelée des interactions entre structure paysagère, processus hydrologiques et rétroactions morphologiques. Ce faisant, il contribue à combler un vide théorique et ouvre la voie à une meilleure articulation entre recherche fondamentale et gestion opérationnelle des bassins versants en climat froid.

Sur le plan méthodologique, cette thèse innove à travers plusieurs approches complémentaires. Elle a d'abord développé un modèle de prévision des crues basé sur des réseaux de neurones artificiels, calibré à partir de données hydrologiques et climatiques historiques et projeté sous scénarios RCP. Elle a ensuite réalisé une reconstruction diachronique sur sept décennies des dynamiques morpho-sédimentaires de la rivière du Diable, combinant analyses planimétriques issues de photographies aériennes, modèles numériques LiDAR et bilans volumétriques. Par ailleurs, un cadre multi-modèles de transport sédimentaire a été établi, comparant cinq approches granulométriques et croisant ces résultats avec des indices morpho-hydrauliques. Enfin, l'application combinée d'indices climatiques (PDSI, SEDI) et de données maillées a permis de caractériser, à une échelle régionale, les régimes de sécheresse au Nouveau-Brunswick. Ensemble, ces méthodes offrent une boîte à outils diversifiée et robuste pour étudier les dynamiques fluviales en contexte froid.

Sur le plan appliqué, les résultats obtenus présentent un intérêt direct pour la gestion et l'adaptation. La thèse identifie notamment des « *hotspots* » géomorphologiques où les taux d'érosion et de transport sont les plus élevés, offrant ainsi un levier pour prioriser les actions de stabilisation ou de restauration. Elle met également en lumière les trajectoires contrastées de la rivière du Diable, marquées par des phases d'export sédimentaire suivies de périodes de stockage, offrant ainsi une lecture fine des trajectoires fluviales utiles pour l'aménagement du territoire. Enfin, elle propose des outils prospectifs, tels que le modèle ANN pour la prévision des crues et l'analyse régionale des sécheresses, directement transférables aux pratiques de gestion hydrologique et de planification en contexte de changement climatique.

En somme, la thèse dépasse la simple juxtaposition de cas d'étude pour proposer un cadre intégré et opérationnel. Elle contribue ainsi à renforcer à la fois la compréhension théorique, l'innovation méthodologique et l'applicabilité pratique de la recherche sur les rivières tempérées froides, dans un contexte de changements environnementaux rapides.

Limites et perspectives

Malgré ses apports, cette thèse comporte certaines limites qui ouvrent de riches perspectives de recherche.

La première limite tient à la spécificité géographique des études de cas. Les analyses empiriques se concentrent sur deux bassins versants de l'Est du Canada – la rivière Eel au Nouveau-Brunswick et la rivière du Diable au Québec – situés dans un contexte de climat continental humide et de terrains postglaciaires. Si le cadre conceptuel proposé a été conçu pour être généralisable, son application à d'autres environnements froids (bassins arctiques, alpins, périglaciaires) reste à tester. Une extension de ces travaux à des contextes variés (toundra arctique, Andes, Himalaya) permettrait de mieux évaluer la robustesse et la transférabilité des modèles développés.

Une deuxième limite concerne les contraintes liées aux données. Les mesures directes des processus hivernaux demeurent rares, en particulier durant les périodes de couverture nivale et de glace. Les dynamiques subglaciaires ou sous couvert de glace ont donc dû être en partie inférées à partir d'indicateurs indirects. De même, la reconstruction morphologique repose sur des séries de photographies aériennes disponibles à intervalles de plusieurs décennies, ce qui limite la capacité à saisir des événements ponctuels mais potentiellement déterminants, tels que des crues éclairs ou des glissements de terrain localisés. Le recours futur à des réseaux de capteurs automatisés, à la télédétection à haute fréquence et à des relevés LiDAR répétés pourrait pallier ces lacunes.

Sur le plan méthodologique, les modèles ANN et les approches multi-modèles de transport sédimentaire ont été calibrés pour des bassins spécifiques. Leur transposition à d'autres bassins non jaugés nécessitera des efforts de validation et d'adaptation, notamment en tenant compte des particularités géologiques et hydrologiques locales. Dans le même esprit, le cadre conceptuel de la connectivité gagnerait à être enrichi par l'intégration de dimensions écologiques et biologiques, par exemple en étudiant le rôle de la végétation riveraine, des espèces ingénieures comme le castor ou encore des rétroactions liées aux habitats aquatiques. Ces apports interdisciplinaires élargiraient la portée du modèle, en articulant plus directement processus géomorphologiques et dynamiques écosystémiques.

Enfin, cette thèse invite à développer des recherches prospectives davantage centrées sur les interactions entre aléas et processus. L'augmentation concomitante des sécheresses et des crues laisse présager des séquences d'aléas composés, où des périodes prolongées d'étiage peuvent fragiliser les berges et préparer le terrain à des épisodes érosifs majeurs lors du retour des crues. De telles dynamiques séquentielles exigent de dépasser l'analyse statique pour adopter des approches temporelles intégrées, par exemple via la modélisation de cycles sécheresse–crue et l'évaluation de leurs effets cumulés sur la connectivité et la morphologie. L'intégration de scénarios de changement climatique et d'occupation du sol, couplée à des approches bayésiennes ou probabilistes, apparaît essentielle pour mieux anticiper ces évolutions et accompagner la gestion adaptative des bassins versants en climat froid.

Retombées pour la gestion et l'aménagement

Au-delà de ses apports conceptuels et méthodologiques, cette thèse comporte plusieurs retombées concrètes pour la gestion des rivières en climat tempéré froid. Les résultats soulignent la nécessité d'approches intégrées tenant compte à la fois de la variabilité saisonnière et des changements climatiques dans la planification des bassins versants.

Premièrement, l'analyse de la connectivité sédimentaire (Chapitre 1) fournit un cadre conceptuel opérationnel permettant d'identifier les unités paysagères jouant un rôle de sources, de puits ou de zones tampons. Cette lecture multi-échelles peut orienter des stratégies de conservation, de restauration ou de gestion du risque, en ciblant les secteurs critiques qui régulent la connectivité.

Deuxièmement, le modèle prédictif de crues fondé sur les réseaux de neurones (Chapitre 2) constitue un outil prospectif directement transférable à la gestion des inondations. En intégrant les scénarios climatiques, il offre une base pour concevoir des infrastructures adaptées aux crues futures et pour renforcer les dispositifs d'alerte précoce.

Troisièmement, la reconstruction morpho-sédimentaire de la rivière du Diable (Chapitre 3) met en lumière l'importance des phases alternées d'exportation et de stockage des sédiments. Cette compréhension fine des trajectoires fluviales invite à préserver les plaines inondables et les espaces de liberté des cours d'eau, qui jouent un rôle d'effet tampon face aux crues et à l'érosion.

Quatrièmement, l'approche multi-modèles de transport sédimentaire (Chapitre 4) permet d'identifier des « *hotspots* » d'érosion et de dépôts. Ces résultats fournissent une base scientifique solide pour cibler les interventions de stabilisation ou de restauration, en hiérarchisant les secteurs prioritaires selon leur vulnérabilité.

Enfin, l'évaluation des régimes de sécheresse au Nouveau-Brunswick (Chapitre 5) attire l'attention sur la vulnérabilité croissante de certains territoires, en particulier les zones côtières. Ces résultats sont essentiels pour anticiper les tensions sur les ressources hydriques, ajuster les usages de l'eau et planifier des stratégies d'adaptation en contexte de sécheresses accrues.

En somme, l'ensemble de la thèse propose non seulement une meilleure compréhension scientifique des dynamiques fluviales en climat froid, mais aussi des outils et des grilles de lecture utiles aux gestionnaires, ingénieurs et décideurs. Ces retombées pratiques contribuent à renforcer la résilience des territoires face aux aléas hydrologiques et aux pressions climatiques. En définitive, cette thèse démontre que l'intégration de cadres conceptuels, d'analyses empiriques et de modélisation constitue une approche féconde pour comprendre les dynamiques fluviales en climat tempéré froid. Les résultats contribuent à enrichir la recherche fondamentale sur la connectivité sédimentaire et les extrêmes hydrologiques, tout en offrant des pistes concrètes d'application pour la gestion adaptative des bassins versants.

Appendices

Appendix A

Appendix A.3.1

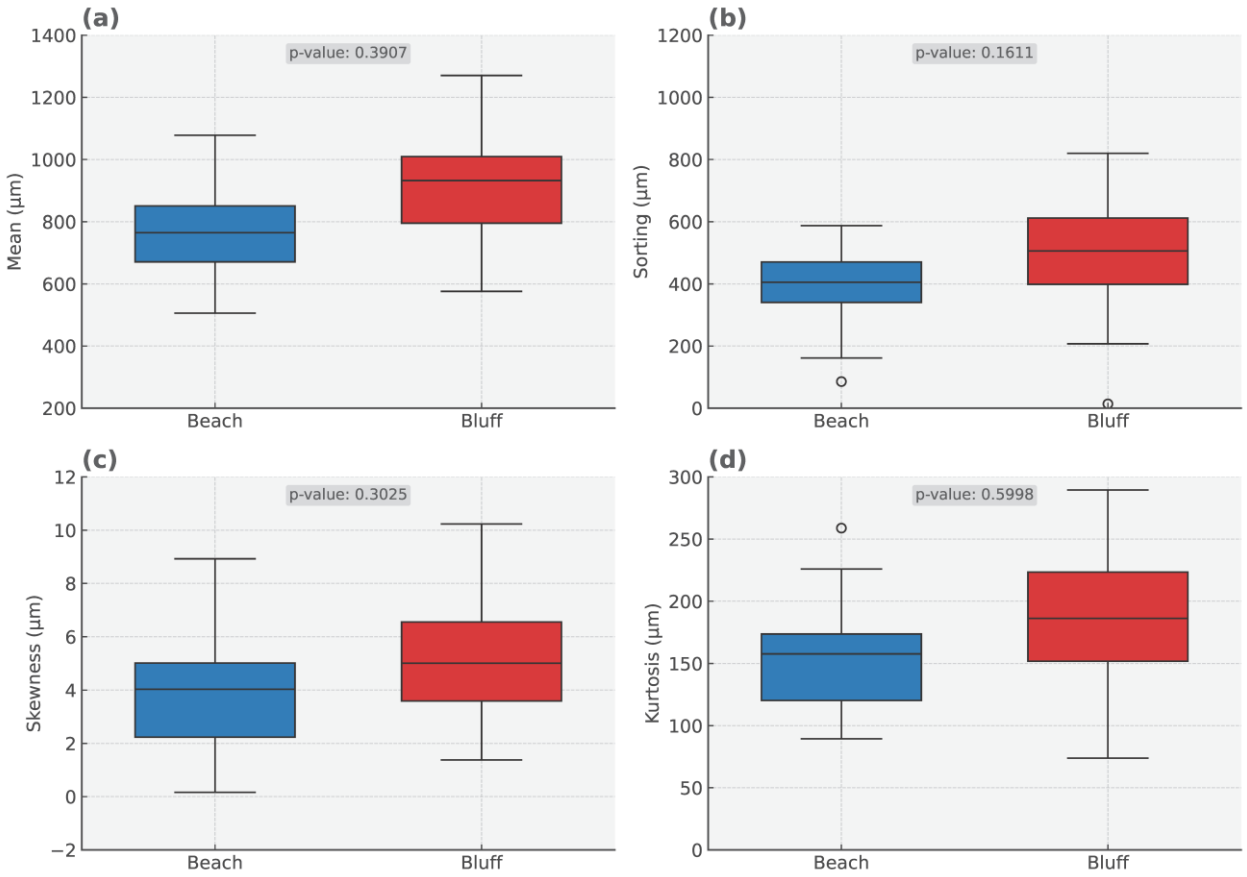

Figure A.3.1. Boxplots comparing grains size statistics between cliff/bluff and beach samples (a) Mean grain size, (b) Sorting; (c) Skewness, and (d) Kurtosis. Blue boxes represent beach, and red boxes represent cliff/bluff samples. Although beach sediments generally exhibit narrower distributions and lower variability, particularly in sorting and kurtosis, no statistically significant differences were observed between the two groups (all p-value >0.16). These results confirm the greater heterogeneity of cliff/bluff -derived sediments but also highlight limited discriminative power of individual grain-size parameters.

Appendix A.3.2

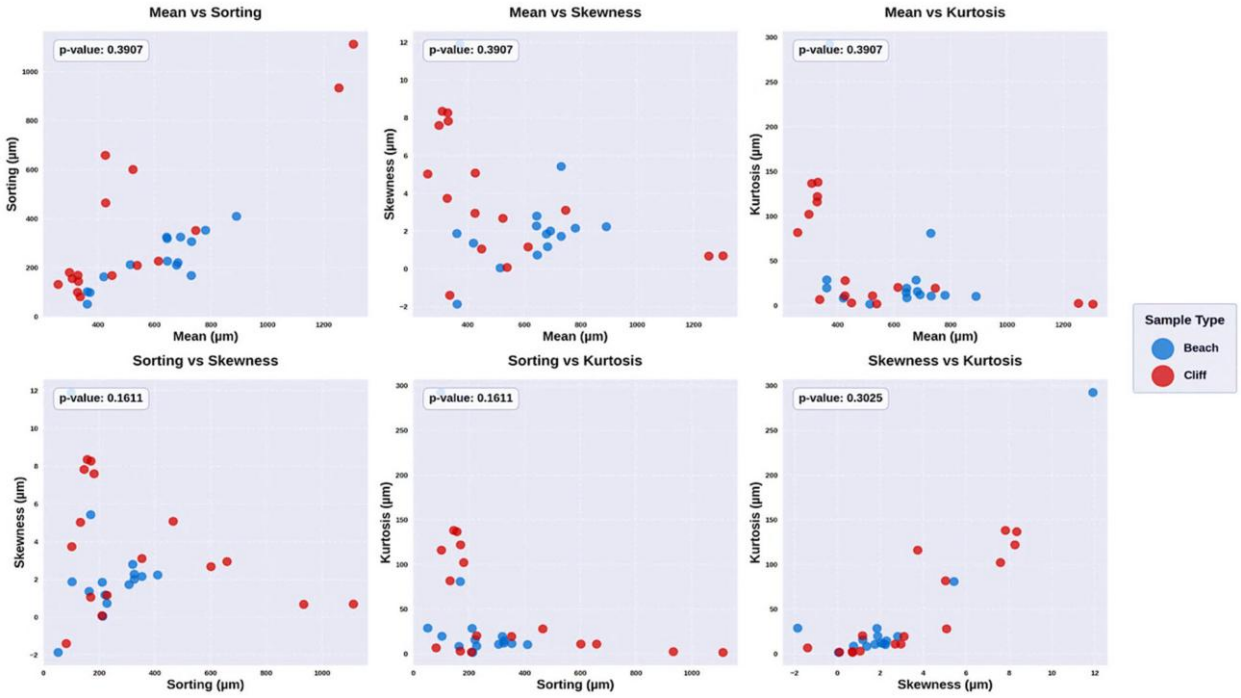

Figure A.3.2. Bivariate plots comparing grain-size parameters across all samples (cliff/bluff and beach), including (a) Mean vs Sorting; (b) Mean vs Skewness; (c) Mean vs Kurtosis; (d) Sorting vs Skewness; (e) Sorting vs Kurtosis; (f) Skewness vs Kurtosis. Blue points correspond to beach samples and red points to cliff/bluff samples, p-value are reported in each panel. No statistically significant correlations were observed, confirming the lack of strong inter-relationships among these grain-size descriptors across the dataset.

Appendix B

Appendix B.4.1

Table. B.4.1. The grain size analysis details

Sample	Mean	Sorting	Skewness	Kurtosis
1.1 Cliff	Coarse Sand	Moderately Sorted	Very Fine Skewed	Mesokurtic
1.2 Beach	Coarse Sand	Moderately Well Sorted	Coarse Skewed	Leptokurtic
2.1 Cliff top	Coarse Sand	Poorly Sorted	Symmetrical	Mesokurtic
2.2 Cliff Bay	Medium Sand	Poorly Sorted	Coarse Skewed	Mesokurtic
2.3 Beach	Coarse Sand	Moderately Well Sorted	Fine Skewed	Leptokurtic
3.1 Cliff	Very Coarse Sand	Poorly Sorted	Fine Skewed	Mesokurtic
3.2 Beach	Coarse Sand	Moderately Well Sorted	Fine Skewed	Platykurtic
4.1 Cliff	Medium Sand	Moderately Well Sorted	Coarse Skewed	Mesokurtic
4.2 Beach	Coarse Sand	Moderately Well Sorted	Symmetrical	Leptokurtic
5.1 Cliff	Medium Sand	Moderately Well Sorted	Symmetrical	Platykurtic
5.2 Beach	Medium Sand	Well Sorted	Fine Skewed	Mesokurtic
6.1 Cliff	Medium Sand	Well Sorted	Fine Skewed	Leptokurtic
6.2 Beach	Medium Sand	Well Sorted	Fine Skewed	Leptokurtic
6.3 Old Meander	Fine Sand	Moderately Sorted	Coarse Skewed	Leptokurtic
7.1 Cliff	Medium Sand	Moderately Well Sorted	Very Fine Skewed	Leptokurtic
7.2 Beach	Coarse Sand	Moderately Well Sorted	Fine Skewed	Leptokurtic
8.1 Cliff	Medium Sand	Moderately Well Sorted	Very Fine Skewed	Mesokurtic
8.2 Beach	Coarse Sand	Moderately Well Sorted	Fine Skewed	Leptokurtic
9.1 Cliff	Medium Sand	Moderately Well Sorted	Fine Skewed	Leptokurtic
9.2 Beach	Coarse Sand	Moderately Sorted	Fine Skewed	Platykurtic
10.1 Cliff	Medium Sand	Moderately Sorted	Fine Skewed	Platykurtic
10.2 Beach	Medium Sand	Well Sorted	Fine Skewed	Mesokurtic
11.1 Cliff	Medium Sand	Moderately Well Sorted	Fine Skewed	Platykurtic
11.2 Beach	Coarse Sand	Well Sorted	Fine Skewed	Mesokurtic
12.1 Cliff	Coarse Sand	Moderately Well Sorted	Fine Skewed	Leptokurtic
12.2 Beach	Medium Sand	Moderately Sorted	Symmetrical	Mesokurtic
13.1 Cliff	Medium Sand	Moderately Well Sorted	Very Fine Skewed	Leptokurtic
13.2 Beach	Coarse Sand	Moderately Well Sorted	Fine Skewed	Mesokurtic
14.1 Cliff	Fine Sand	Poorly Sorted	Very Coarse Skewed	Very Leptokurtic
14.2 Beach	Medium Sand	Moderately Well Sorted	Symmetrical	Leptokurtic
15.1 Cliff	Fine Sand	Moderately Sorted	Symmetrical	Mesokurtic
15.2 Beach	Coarse Sand	Moderately Sorted	Fine Skewed	Mesokurtic

Appendix B.4.2

Table B.4.2.1 and B.4.2.2 show three most and least significant periods of geomorphic activities and its interpretations.

Table.B.4.2.1 The three most significant periods for each year

Year	Date	ω	ωcritical	Difference	Interpretation
2009 (1)	2009-12-04	0.91571445	0.0144	0.90131445	Moderate events; just above the threshold
2009 (2)	2009-12-05	0.8762292	0.0144	0.8618292	
2009 (3)	2009-12-06	0.7588035	0.0144	0.7444035	
2011 (1)	2011-04-29	6.139098	0.0144	6.124698	High-energy events; strong geomorphic potential
2011 (2)	2011-04-30	5.4489645	0.0144	5.4345645	
2011 (3)	2011-05-01	4.703895	0.0144	4.689495	
2016 (1)	2016-04-02	5.713344	0.0144	5.698944	Consistent high activity; significant energy excess
2016 (2)	2016-04-23	5.2498215	0.0144	5.2354215	
2016 (3)	2016-04-03	4.916772	0.0144	4.902372	
2017 (1)	2017-04-17	7.299621	0.0144	7.285221	Very high intensity; peak geomorphic conditions
2017 (2)	2017-04-18	6.0120585	0.0144	5.9976585	
2017 (3)	2017-05-03	5.548536	0.0144	5.534136	
2018 (1)	2018-05-04	7.2206505	0.0144	7.2062505	Sustained high energy over consecutive days
2018 (2)	2018-05-05	7.1107785	0.0144	7.0963785	
2018 (3)	2018-05-06	7.0421085	0.0144	7.0277085	
2019 (1)	2019-04-24	7.96572	0.0144	7.95132	The highest recorded differences; very vigorous activity
2019 (2)	2019-04-25	7.8455475	0.0144	7.8311475	
2019 (3)	2019-04-27	7.670439	0.0144	7.656039	
2020 (1)	2020-04-14	5.177718	0.0144	5.163318	Significant, yet slightly lower than peak periods
2020 (2)	2020-04-15	4.8172005	0.0144	4.8028005	
2020 (3)	2020-05-02	4.7416635	0.0144	4.7272635	
2021 (1)	2021-07-01	4.2472395	0.0144	4.2328395	Lower energy surplus; moderate geomorphic changes
2021 (2)	2021-06-30	3.927924	0.0144	3.913524	
2021 (3)	2021-03-29	3.666978	0.0144	3.652578	

2022 (1)	2022-04-16	4.360545	0.0144	4.346145	Relatively moderate; less extreme geomorphic potential
2022 (2)	2022-04-15	4.3227765	0.0144	4.3083765	
2022 (3)	2022-04-17	3.8901555	0.0144	3.8757555	
2023 (1)	2023-04-18	7.1588475	0.0144	7.1444475	A return to higher energy events; significant activity
2023 (2)	2023-05-02	6.530517	0.0144	6.516117	
2023 (3)	2023-04-17	6.228369	0.0144	6.213969	

Table. B.4.2.2 The three least significant geomorphic periods for each year

Year	Date	ω	ωcritical	Difference	Interpretation
2009 (1)	2009-12-31	0.3014613	0.0144	0.2870613	Minimal geomorphic activity, stable conditions.
2009 (2)	2009-12-30	0.30592485	0.0144	0.29152485	
2009 (3)	2009-12-29	0.3103884	0.0144	0.2959884	
2011 (1)	2011-09-29	0.270250785	0.0144	0.255850785	Very low activity despite an overall energetic year.
2011 (2)	2011-09-28	0.271830195	0.0144	0.257430195	
2011 (3)	2011-03-04	0.2719332	0.0144	0.2575332	
2016 (1)	2016-10-12	0.17126298	0.0144	0.15686298	Extremely low stream energy, stable channel.
2016 (2)	2016-10-15	0.17531451	0.0144	0.16091451	
2016 (3)	2016-10-13	0.175829535	0.0144	0.161429535	
2017 (1)	2017-10-03	0.198627975	0.0144	0.184227975	Limited geomorphic potential, stable period.
2017 (2)	2017-10-02	0.20305719	0.0144	0.18865719	
2017 (3)	2017-10-04	0.20758941	0.0144	0.19318941	
2018 (1)	2018-07-22	0.207486405	0.0144	0.193086405	Consistently low activity, minimal erosion or sediment transport.
2018 (2)	2018-07-23	0.20758941	0.0144	0.19318941	
2018 (3)	2018-07-24	0.218610945	0.0144	0.204210945	
2019 (1)	2019-08-27	0.14592375	0.0144	0.13152375	Lowest recorded stream power, exceptionally stable.
2019 (2)	2019-08-26	0.15285942	0.0144	0.13845942	
2019 (3)	2019-08-25	0.16103115	0.0144	0.14663115	
2020 (1)	2020-07-06	0.206181675	0.0144	0.191781675	Stable hydrological conditions, low geomorphic activity.
2020 (2)	2020-07-26	0.20662803	0.0144	0.19222803	
2020 (3)	2020-07-07	0.20971818	0.0144	0.19531818	
2021 (1)	2021-09-04	0.1359666	0.0144	0.1215666	Minimal stream energy surplus, negligible geomorphic changes.
2021 (2)	2021-09-05	0.13692798	0.0144	0.12252798	
2021 (3)	2021-09-03	0.140945175	0.0144	0.126545175	
2022 (1)	2022-02-08	0.2705598	0.0144	0.2561598	Low energy surplus, stable channel conditions.

2022 (2)	2022-02-07	0.27158985	0.0144	0.25718985	
2022 (3)	2022-02-06	0.2753667	0.0144	0.2609667	
2023 (1)	2023-10-06	0.149803605	0.0144	0.135403605	Stable and quiet conditions, limited geomorphic processes.
2023 (2)	2023-10-05	0.15231006	0.0144	0.13791006	
2023 (3)	2023-10-04	0.153168435	0.0144	0.138768435	

Appendix C

Appendix C.5.1. Procedure for calculating the PDSI

Additional insights can be gained from the works of Palmer (1965), Dai (2011), and Wells et al. (2004). In developing the PDSI, Palmer (1965) initially introduced the concept of the Climatically Appropriate for Existing Conditions (CAFEC) values. These values were derived using water-balance coefficients, denoted as $\alpha, \beta, \gamma, \delta$, which were calculated using local climate data for each month *i*:

$$\alpha_i = \frac{\overline{E_i}}{\overline{PEi}} \qquad \beta_i = \frac{\overline{R_i}}{\overline{PR_i}} \qquad \gamma_i = \frac{\overline{Roi}}{\overline{PRO_i}} \quad \delta_i = \frac{\overline{L_i}}{\overline{PL_i}} \tag{1}$$

In equation 1, $\overline{E_i}$, $\overline{R_i}$, $\overline{Ro_i}$, and $\overline{L_i}$ represents water fluxes, denoting evapotranspiration, recharge to soils, runoff and water loss to the soil layers, respectively. In addition, $\overline{PEi}$, $\overline{PR_i}$, $\overline{PRO_i}$,and $\overline{PL_i}$ signify potential evapotranspiration, potential recharge, potential runoff, and potential loss, respectively.

Equation 2 illustrates the CAFEC precipitation, which integrates the potential values of CAFEC to depict the amount of precipitation necessary to maintain a specified level of average soil moisture within a single month.

$$\hat{P} = \alpha iPE + \beta_i PR + \gamma_i PRO - \delta_i PL \tag{2}$$

According to equation 3, moisture departure, represented by *d*, is calculated as the disparity between actual precipitation and CAFEC precipitation:

$$d = P - \hat{P} = P - (\alpha iPE + \beta_i PR + \gamma_i PRO - \delta_i PL) \tag{3}$$

Moisture departure served as a measure to ascertain whether there existed a shortfall or excess of precipitation compared to the CAFEC precipitation. Specifically, *d* carries varied implications for surface water balance across different seasons and geographical regions. To address this variability, the moisture departure is weighted by *K* or climatic factors to generate the moisture anomaly index or the *Z* index. (*Z=D.K*)

Palmer's general approximation for a location's climate characteristic based on equation 4 is *K′*, wherein *K* is a refinement of *K′*.

$$k_i = k_0 k_i' = \frac{17.67}{\sum_{i=1}^{12} \bar{D}_i k_i'} k_i' \quad \text{and} \tag{4}$$

$$k_i' = 1.5\, log_{10}\left(\frac{\frac{\overline{PE_i}+\overline{R_i}+\overline{ROi}}{\overline{Pi}+\overline{L_i}}+2.8}{\bar{D}_i}\right) + 0.5$$

The PDSI value is then calculated for the time *t(Xt)* predicted by equation 5 using the *Z* index. $X_t = PX_{t-1} + qz_{t=}0.897X_{t-1} + {}^{z_t}/_3$ (5)

In equation 5, *Xt-1* represents the PDSI for the preceding month. In addition, *p* and *q* are entitled duration factors that determine sensitivity of PDSI to the monthly moisture anomaly *Zt,* as well as measure the autocorrelation of PDSI.

Appendix C.5.2. Procedure for obtaining sc-PDSI based on PDSI

Based on the first part of equation 4, K' and $\widetilde{K}$ were assumed. K' reflects the monthly average precipitation and soil conditions, thus varying from one month to the next. Meanwhile, $\widetilde{K}$ only varies across various locations. The deficiency of PDSI arises from spatial inconsistencies in seasonal climate changes (Wells et al. 2004). Equation 6 illustrates these concepts.

$$\widetilde{K} = \frac{17.67}{\sum_{i=1}^{12} |\overline{d}_i| k_i'}. \tag{6}$$

Furthermore, to obtain the moisture anomaly $\tilde{Z}$ for a given month, the product of d and K' is crucial, as indicated by equation 7. This equation shows the approximation of the annual sum of the average absolute value of $\tilde{Z}$ over 12 months.

$$\tilde{Z} = \sum_{i=1}^{12} |\overline{d}_i| k_i'. \tag{7}$$

The value of 17.67 from equation 6 was replaced by the average value of $\tilde{Z}$ shown in equation 7, utilizing nine various climate divisions. Therefore, the expected value of $\tilde{Z}$ relative to the observed value of $\tilde{Z}$ can be introduced as a new formulation of $\tilde{K}$, according to equation 8.

$$\tilde{k} = \frac{expected\ average\ PDSI}{observed\ average\ PDSI}. \tag{8}$$

The challenge of employing equation 8 is the likelihood of obtaining an average PDSI value of zero. Instead of relying on its central tendency, the PDSI distribution's tails can be utilized to address this issue. Palmer (1965) defined the range of nonextreme PDSI values between -4.00 to 4.00. Therefore, if *fe* denotes the occurrences of extreme events *f,* then the *fe th* percentile is defined by -4.00 and the (100- *fe) th* percentile equals to 4.00. Equation 9 represents the aforementioned considerations applied to $\tilde{K}$.

$$\tilde{k} = \begin{cases} \frac{expected\ f e th\ percentile\ of\ the\ PDSI}{observed\ f e\ percentile\ of\ the\ PDSI} \\ \frac{expected(100-\ fe)th\ percentile\ of\ the\ PDSI}{observed(100-\ fe)th\ percentile\ of\ the\ PDSI} \end{cases} \tag{9}$$

The value of *fe* for adaptation to climate characteristics was defined as 2% based on equation 10.

$$k = \begin{cases} k' \left(\frac{-4.00}{2th\ percentile}\right), & if\ d < 0 \\ k' \left(\frac{4.00}{98th\ percentile}\right), & if\ d \geq 0 \end{cases} \tag{10}$$

To calculate K based on equation 10, first, the PDSI should be computed using the first-order approximation of Z or the formula $Z = Dk'$, where K' was calculated using the second part of equation 4. Then, the percentile of the 2d and 98th PDSI values for the calculation of K was utilized according to equation 10, and finally, PDSI was recomputed.

Appendix C.5.3. Procedure for calculating Mann-Kendall test

The M.K. test is calculated following the procedures outlined (Zaiontz 2020; Kendall 1975; Alemu and Dioha 2020). The time series *x1*, *x2*, *x3*… *xn* represents *n* data points.

$$= \sum_{i=1}^{n-1} \sum_{j=i+1}^{n} sign(X_j - X_i) \tag{11}$$

$$sgn(x) = \begin{cases} 1 & if\ x > 0 \\ 0 & if\ x = 0 \\ -1 & if\ x < 0 \end{cases} \tag{12}$$

In equation 11, S>0 indicates an increasing trend, while S<0 represents decreasing trend.

E[S] = 0 is equal to the mean of *S* and the variance of *S* or $(\bar{\sigma^2})$, is defined by equation 13.

$$\sigma^2 = \frac{1}{18}\{n(n-1)(2n+5) - \sum_{j=1}^{P} tj(tj-1)(2tj+5)\} \tag{13}$$

In the above equation, *tj* is the number of data points in the *jth* tied group, and *p* is the number of linked groups in the dataset. The *Z*-transformation is then concluded hereunder, whereby the statistic *S* is typically distributed for more than ten values and few tied values.

$$Z = \begin{cases} \frac{S-1}{\sqrt{\sigma^2}} & if \quad S > 0 \\ 0 & if \quad S = 0 \\ \frac{S+1}{\sqrt{t}} & if \quad S < 0 \end{cases} \tag{14}$$

If no null hypothesis exists, a standard normal distribution is assumed for time series containing more than ten elements. The probability density function is defined according to a standard deviation of 1 and a mean of 0 for the normal distribution, as described by further equations.

$$f(z) = \frac{1}{\sqrt{2\pi}} e^{\frac{-z^2}{2}} \tag{15}$$

The value of *S* is relatively close to Kendall's Tau, according to equation 16.

$$\tau = \frac{S}{D}$$

Where,

$$D = \left[\frac{1}{2}n(n-1) - \frac{1}{2}\sum_{j=1}^{P} tj(tj-1)\right]^{1/2} \left[1/2\, n(n-1)\right]^{1/2} \tag{16}$$

Appendix C.5.4. Procedure for calculating seasonal Mann-Kendall test

The seasonal M.K. statistic, *Sk,* for the entire series, as described by Hirsch et al. (1982), is computed using equation 17.

$$s_k = \sum_{i=1}^{m} s_i \quad (17)$$

Kendall's *S* statistic for each season, *Si,* is summed to form the overall statistic *Sk*. Under the null hypothesis, *Sk* is assumed to have a normal distribution with an expectation value equal to the sum of the expected values (zero) of the *Si* when the product of the number of years and seasons exceeds 25 years. *Sk* can, therefore, be rewritten as equation 18 at this stage.

$$Zsk = \begin{cases} \frac{Sk-1}{\sigma sk} & if \quad Sk > 0 \\ 0 & if \quad Sk = 0 \\ \frac{Sk+1}{\sigma sk} & if \quad Sk < 0 \end{cases} \quad (18)$$

According to equation 18, by subtracting *Sk* from its expectation $\mu_k = 0$ and dividing by its standard derivation σsk the standardized *Sk* was obtained as *Zsk*. In addition, the value of σsk can be calculated using equation 19.

$$\sigma sk = \sqrt{\sum_{i=1}^{m} \left({}^{nj}/_{18}\right)(nj-1)(2nj+5)} \quad (19)$$

In the above equation, *nj* presents the amount of data in the *ith* season.

Appendix C.5.5. Procedure for calculating Kendall coefficient.

The procedure of calculating Kendall coefficient is outlined in equations 20 to 23.

Tau-b coefficient is defined based on equation 20.

$$\tau_b = \frac{n_c - n_d}{\sqrt{(n_0 - n_1)(n_0 - n_2)}} \quad (20)$$

Where,

$$n_0 = \frac{n(n-1)}{2} \quad (21)$$

$$n_1 = \sum_i \frac{t_i(t_i-1)}{2} \quad (22)$$

$$n_2 = \sum_j \frac{u_i(u_i-1)}{2} \quad (23)$$

In the above equations, n_c and n_d stands for the concordant number and pairs of discordant, respectively. In addition, t_i and u_i are the number of tied values in the *ith* group of ties for the first quantity and in the *jth* group of ties for the second quantity, sequentially.

Appendix C.5.6. Procedure for calculating Sen's slope.

The calculation procedure for Sen's slope is outlined by equations 24 to 26.

$$f(x) = Q_x + B \tag{24}$$

In equation 24, Q is defined as a slope value, and the value of B is constant. Furthermore, a set of linear slopes is obtained, as shown in equation 25.

$$Q_i = \frac{x_j - x_k}{j-k} \quad for\ j = 1,2,3 \ldots N \tag{25}$$

In this equation, X represents the variable indicating the amount of data. Moreover, j and k are indices where $j > k$. In this test, the slope value is estimated for each observation along with the corresponding intercept and the median of all intercepts. For Sen's Slope estimator calculation, the median is calculated from the N observation of the slope based on equation 26.

$$Q = \begin{bmatrix} Q_{\frac{N+1}{2}} & if\ N\ is\ odd \\ 1/2\left(Q_{N/2} + Q_{\frac{N+1}{2}}\right) & if\ N\ is\ even \end{bmatrix} \tag{26}$$

And,

$$N = \frac{n(n-1)}{2}$$

Based on the above equations, N is the slope observations, while n is the value of Xk within a time series. To determine the appropriate slope for the non-parametric tests within the series, a two-sided test is conducted at the $100(1-\alpha)\ \%$ confidence interval.

The procedure outlined above draws from research by Drápela and Drápelová (2011), Pohlert (2020), and Mondal et al. (2012). Equation 25 distinguishes three types of trends: an upward trend is indicated by a positive slope Qi, a negative slope Qi identifies a downward trend, and a zero trend is represented by a slope of zero.

LISTE DES RÉFÉRENCES

Abbas, A., Waseem, M., Ullah, W., Zhao, C. and Zhu, J. (2021) Spatiotemporal analysis of meteorological and hydrological droughts and their propagations. Water, 13(16), 2237. https://doi.org/10.3390/w13162237

Abrahams, A. D. and Gao, P. (2006) A bed-load transport model for rough turbulent open-channel flows on plane beds. Earth Surface Processes and Landforms, 31, 910-928.

Abu El-Magd, S.A., Orabi, H.O. and Ali, S.A. (2021) An integrated approach for evaluating the flash flood risk and potential erosion using the hydrologic indices and morpho-tectonic parameters. Environmental Earth Sciences, 80, 694. https://doi.org/10.1007/s12665-021-10013-0

Abyani, M., Asgarian, B. and Zarrin, M. (2019) Sample geometric mean versus sample median in closed form framework of seismic reliability evaluation: A case study comparison. Earthquake Engineering and Engineering Vibration, 18, 187-201. https://doi.org/10.1007/s11803-019-0498-5

Agresti, A. (2010) Analysis of Ordinal Categorical Data. Second Edition. John Wiley and Sons, Hoboken, NJ, USA. https://doi.org/10.1002/9780470594001

Akay, S.S., Özcan, O. and Şanlı, F.B. (2022) Quantification and visualization of flood-induced morphological changes in meander structures by UAV-based monitoring. Engineering Science and Technology, an International Journal, 27, 101016. https://doi.org/10.1016/j.jestch.2021.05.020

Alemu, Z.A. and Dioha, M.O. (2020) Climate change and trend analysis of temperature: the case of Addis Ababa, Ethiopia. Environmental Systems Research, 9, 27. https://doi.org/10.1186/s40068-020-00190-5

Alexander, L. and Herold, N. (2016) ClimPACT2. Indices and software. A document prepared on behalf of The Commission for Climatology (CCI) Expert Team on Sector-Specific Climate Indices (ET-SCI), 46.

Ali, G., Oswald, C., Spence, C. and Wellen, C. (2018) The T-TEL method for assessing water, sediment, and chemical connectivity. Water Resources Research, 54, 634-662. https://doi.org/10.1002/2017WR020707

Alifu, H., Hirabayashi, Y., Imada, Y. and Shiogama, H. (2022) Enhancement of river flooding due to global warming. Scientific Reports, 12, 20687. https://doi.org/10.1038/s41598-022-25182-6

Allawi, M. F., Sulaiman, S. O., Sayl, K. N., Sherif, M. and El-Shafie, A. (2023) Suspended sediment load prediction modelling based on artificial intelligence methods: The tropical region as a case study. Heliyon, 9(7), e18506.

Alsafadi, K., Al-Ansari, N., Mokhtar, A., Mohammed, S., Elbeltag, A., Sammen, S.S. and Bi, S. (2022) An evapotranspiration deficit-based drought index to detect variability of terrestrial carbon productivity in the Middle East. Environmental Research Letters, 17, 014051. https://doi.org/10.1088/1748-9326/ac4765

Ampomah, A. B., Osei, G. and Baidoo, R. N. (2020) Evaluating sediment transport in river systems using multiple linear regression analysis. Water Resources Research, 56(3), e2019WR026083.

Ampomah, R., Hosseiny, H., Zhang, L., Smith, V. and Sample-Lord, K. (2020) A regression-based prediction model of suspended sediment yield in the Cuyahoga River in Ohio using historical satellite images and precipitation data. Water, 12, 881. https://doi.org/10.3390/w12030881

An, J.H., Lim, B.S., Seol, J., Kim, A.R., Lim, C.H. and Moon, J.S. (2022) Evaluation on the restoration effects in the river restoration projects practiced in South Korea. Water, 14, 2739. https://doi.org/10.3390/w14172739

Ancey, C. (2020a) Bedload transport: a walk between randomness and determinism. Part 1. The state of the art. Journal of Hydraulic Research, 58(1), 1-17. https://doi.org/10.1080/00221686.2019.1702594

Ancey, C. (2020b) Bedload transport: a walk between randomness and determinism. Part 2. Challenges and prospects. Journal of Hydraulic Research, 58(1), 18-33. https://doi.org/10.1080/00221686.2019.1702595

Andreazzini, M.J., Degiovanni, S.B., Benito, M.E. and Echevaria, K.V. (2021) Development and application of a sediment connectivity index to small fluvial catchments: A case study in Arenoso stream, Cordoba, Argentina. Environmental Earth Sciences, 80, 301. https://doi.org/10.1007/s12665-021-09585-8

Andualem, T.G., Hewa, G.A., Myers, B.R., Peters, S. and Boland, J. (2023) Erosion and sediment transport modeling: A systematic review. Land, 12, 1396. https://doi.org/10.3390/land12071396

Armanini, A., Cavedon, V. and Righetti, M. (2015) A probabilistic/deterministic approach for the prediction of the sediment transport rate. Advances in Water Resources, 81, 10-18. https://doi.org/10.1016/j.advwatres.2014.09.008

Arnell, N.W. and Gosling, S.N. (2016) The impacts of climate change on river flood risk at the global scale. Climatic Change, 134, 387-401. https://doi.org/10.1007/s10584-014-1084-5

Asadi, H., Dastorani, M. T. and Sidle, R. C. (2023) Estimating index of sediment connectivity using a smart data-driven model. Journal of Hydrology, 620(A), 129467. https://doi.org/10.1016/j.jhydrol.2023.129467

Asadi, M.A.Z., Mokhtari, L.G., Zandi, R. and et al. (2025) Modeling, evaluation and forecasting of suspended sediment load in Kal-e Shur River, Sabzevar Basin, in northeast of Iran. Applied Water Science, 15, 44. https://doi.org/10.1007/s13201-025-02361-0

Ashida, K. and Michiue, M. (1972) Study on hydraulic resistance and bedload transport rate in alluvial streams. Transactions, Japan Society of Civil Engineering, 206, 59-64. https://doi.org/10.2208/jscej1969.1972.206_59

Ashmore, P. E. (1988) Bedload transport in braided gravel bed stream models. Earth Surface Processes and Landforms, 13, 677-695. https://doi.org/10.1002/esp.3290130803

Asong, Z.E., Wheater, H.S., Bonsal, B., Razavi, S. and Kurkute, S. (2018) Historical drought patterns over Canada and their teleconnections with large-scale climate signals. Hydrology and Earth System Sciences, 22(6), 3105-3124. https://doi.org/10.5194/hess-22-3105-2018

Aucoin, F., Caissie, D., El-Jabi, N. and Turkkan, N. (2011) Flood frequency analyses for New Brunswick rivers. Canadian Technical Report of Fisheries and Aquatic Sciences, 2920, xi + 77p.

Aygün, O., Kinnard, C. and Campeau, S. (2020) Impacts of climate change on the hydrology of northern midlatitude cold regions. Progress in Physical Geography, 44, 1-20. https://doi.org/10.1177/0309133319878123

Baartman, J.E.M., Masselink, R., Keesstra, S.D. and Temme, A.J.A.M. (2013) Linking landscape morphological complexity and sediment connectivity. Earth Surface Processes and Landforms, 38, 1457-1471. https://doi.org/10.1002/esp.3434

Ballantyne, C. K. (2002) Paraglacial geomorphology. Quaternary Science Reviews, 21(18-19), 1935-2017. https://doi.org/10.1016/S0277-3791(02)00005-7

Baronetti, A., Fratianni, S., Acquaotta, F. and Fortin, G. (2019) A quality control approach to better characterize the spatial distribution of snow depth over New Brunswick, Canada. International Journal of Climatology, 39(14), 5470-5485. https://doi.org/10.1002/joc.6166

Batista, P.V.G., Fiener, P., Scheper, S. and Alewell, C. (2022) A conceptual-model-based sediment connectivity assessment for patchy agricultural catchments. Hydrology and Earth System Sciences, 26, 3753-3770. https://doi.org/10.5194/hess-26-3753-2022

Beck, H. E., Van Dijk, A. I., Larraondo, P. R., McVicar, T. R., Pan, M., Dutra, E., & Miralles, D. G. (2022). MSWX: Global 3-hourly 0.1 bias-corrected meteorological data including near-real-time updates and forecast ensembles. Bulletin of the American Meteorological Society, 103(3), E710-E732.

Beguería, S., Vicente-Serrano, S.M., Reig, F. and Latorre, B. (2014) Standardized precipitation evapotranspiration index (SPEI) revisited: parameter fitting, evapotranspiration models, tools, datasets and drought monitoring. International Journal of Climatology, 34(10), 3001-3023. https://doi.org/10.1002/joc.3887

Beltaos, S. (ed.) (2008) River ice breakup. Water Resources Publications. https://www.wrpllc.com/books/rib.html

Beltaos, S. and Burrell, B. C. (2021) Effects of river-ice breakup on sediment transport and implications to stream environments: A review. Water, 13(18), 2541. https://doi.org/10.3390/w13182541

Beltaos, S. and Prowse, T. (2009) River-ice hydrology in a shrinking cryosphere. Hydrological Processes, 23, 122-144. https://doi.org/10.1002/hyp.7165

Blåfield, L., Calle, M., Kasvi, E. and Alho, P. (2024) Modelling seasonal variation of sediment connectivity and its interplay with river forms. Geomorphology, 463, 109346. https://doi.org/10.1016/j.geomorph.2024.109346

Bobee, B., Cavadias, G., Ashkar, F., Bernier, J. and Rasmussen, P. (1993) Towards a systematic approach to comparing distributions used in flood frequency analysis. Journal of Hydrology, 142, 121-136. https://doi.org/10.1016/0022-1694(93)90008-W

Bonsal, B. and Liu, Z. (2020) Historical and projected changes to the stages and other characteristics of severe Canadian Prairie droughts. Water, 12(12), 3370. https://doi.org/10.3390/w12123370

Bonsal, B. and Regier, M. (2007) Historical comparison of the 2001/2002 drought in the Canadian prairies. Climate Research, 33, 229-242. https://doi.org/10.3354/cr033229

Bonsal, B. and Shabbar, A. (2008) Impacts of large-scale circulation variability on low streamflows over Canada: a review. Canadian Water Resources Journal, 33(2), 137-154. https://doi.org/10.4296/cwrj3302137

Bonsal, B.R., Aider, R., Gachon, P. and Lapp, S. (2013) An assessment of Canadian prairie drought: past, present, and future. Climate Dynamics, 41, 501-516. https://doi.org/10.1007/s00382-012-1422-0

Bonsal, B., Koshida, G., O'Brien, E.G. and Wheaton, E. (2004) Droughts. In Threats to Water Availability in Canada. Chapter 3. NWRI Scientific Assessment Report Series no. 3 and ACSD Science Assessment Series no. 1, National Water Research Institute, Burlington, ON, Canada.

Bonsal, B., Wheaton, E.E., Chipanshi, A.C., Lin, C., Sauchyn, D.J. and Wen, L. (2011) Drought research in Canada: A review. Atmosphere-Ocean, 49(4), 303-319. https://doi.org/10.1080/07055900.2011.555103

Borrelli, L., Conforti, M. and Mercuri, M. (2019) LiDAR and UAV system data to analyse recent morphological changes of a small drainage basin. ISPRS International Journal of Geo-Information, 8, 536. https://doi.org/10.3390/ijgi8120536

Borselli, L., Cassi, P. and Torri, D. (2008) Prolegomena to sediment and flow connectivity in the landscape: A GIS and field numerical assessment. CATENA, 75(3), 268-277. https://doi.org/10.1016/j.catena.2008.07.006

Borselli, L., Salvador Sanchis, P., Bartolini, D., Cassi, P. and Lollino, P. (2011) PESERA-L model: an addendum to the PESERA model for sediment yield due to shallow mass movement in a watershed. CNR-IRPI Italy Report, n.82.

Bracken, L. J. and Croke, J. (2007) The concept of hydrological connectivity and its contribution to understanding runoff-dominated geomorphic systems. Hydrological Processes, 21(13), 1749-1763. https://doi.org/10.1002/hyp.6313

Bracken, L.J., Turnbull, L., Wainwright, J. and Bogaart, P. (2015) Sediment connectivity: A framework for understanding sediment transfer at multiple scales. Earth Surface Processes and Landforms, 40(2), 177-188. https://doi.org/10.1002/esp.3635

Brandão, A. R. A., Schwamback, D., de Menezes Filho, F. C. M. and et al. (2025) Artificial neural networks for flood prediction in current and CMIP6 climate change scenarios. Journal of Flood Risk Management, 18(1), e70029. https://doi.org/10.1111/jfr3.70029

Brasington, J. and Richards, K. (2007) Reduced-complexity, physically-based geomorphological modelling for catchment and river management. Geomorphology, 90(3-4), 171-177. https://doi.org/10.1016/j.geomorph.2006.10.028

Brierley, G. and Fryirs, K. (2022) Truths of the riverscape: Moving beyond command-and-control to geomorphologically informed nature-based river management. Geoscientific Letters, 9, 14. https://doi.org/10.1186/s40562-022-00223-0

Brooks, G. R., Evans, S. G., Clague, J. J., & Flooding, A. (2001). Synthesis of Natural Geological Hazards in Canada. Geological Survey of Canada Bulletin. Natural Resources Canada. https://doi. org/10.4095/212210

Brogan, B., McDonald, J., Lyons, B., Johnston, P. and Stewart-Robertson, G. (2020) Climate change adaptation plan for Saint John. Published by Atlantic coastal action program [ASAP] Saint John.

Bullock, J.A., Haddow, G.D. and Coppola, D.P. (2018) Hazards Homeland Security (Second Edition). Butterworth-Heinemann, 45-66. https://doi.org/10.1016/B978-0-12-804465-0.00003-0

Buttle, J. M., Allen, D. M., Caissie, D., Davison, B., Hayashi, M., Peters, D. L., ... & Whitfield, P. H. (2016). Flood processes in Canada: Regional and special aspects. Canadian Water Resources Journal/Revue canadienne des ressources hydriques, 41(1-2), 7-30.

Burn, D. H. and Whitfield, P. H. (2016) Changes in floods and flood regimes in Canada. Canadian Water Resources Journal / Revue canadienne des ressources hydriques, 41(1-2), 139-150. https://doi.org/10.1080/07011784.2015.1026844

Burrell, B.C. and Anderson, J.E. (1991) Regional hydrology of New Brunswick. Canadian Water Resources Journal, 16(4), 317-330. https://doi.org/10.4296/cwrj1604317

Burrell, B. C., Beltaos, S. and Newton, B. (2024) Environmental effects of river ice, The Saint John (Wolastoq) River, New Brunswick, Canada. International Journal of River Basin Management. Advance online publication. https://doi.org/10.1080/15715124.2024.2349020

Burrell, B.C., Huokuna, M., Beltaos, S., Kovachis, N., Turcotte, B. and Jasek, M. (2015) Flood Hazard and Risk Delineation of Ice-Related Floods: Present Status and Outlook. CGU HS Committee on River Ice Processes and the Environment, 18th Workshop on the Hydraulics of Ice-Covered Rivers, Quebec City, QC, Canada.

Bush, E. and Lemmen, D.S. (eds) (2019) Canada's Changing Climate Report. Government of Canada, 444 p.

Buter, A., Heckmann, T., Filisetti, L., Savi, S., Mao, L., Gems, B. and Comiti, F. (2022) Effects of catchment characteristics and hydro-meteorological scenarios on sediment connectivity in glacierised catchments. Geomorphology, 402, 108128. https://doi.org/10.1016/j.geomorph.2022.108128

Butler, D.R. and Malanson, G.P. (2005) The geomorphic influences of beaver dams and failures of beaver dams. Geomorphology, 71, 1-2. https://doi.org/10.1016/j.geomorph.2004.08.016

Buttle, J. M., Allen, D. M., Caissie, D., Davison, B., Hayashi, M., Peters, M. D. L., Pomeroy, J. W., Simonovic, S., St-Hilaire, A. and Whitfield, P. H. (2016) Flood processes in Canada: Regional and special aspects. Canadian Water Resources Journal, 41(1-2), 7-30. https://doi.org/10.1080/07011784.2015.1131629

Buttle, J. M., Creed, I. F. and Pomeroy, J. W. (2000) Advances in Canadian forest hydrology, 1995-1998. Hydrological Processes, 14(9), 1551-1578. https://doi.org/10.1002/1099-1085(20000630)14:9<1551::AID-HYP74>3.0.CO;2-J

Camenen, B., Bayram, A. and Larson, M. (2006) Equivalent roughness height for plane bed under steady flow. Journal of Hydraulic Engineering, 132(11), 1146-1158. https://doi.org/10.1061/(ASCE)0733-9429(2006)132:11(1146

Camici, S., Brocca, L., Melone, F. and Moramarco, T. (2014) Impact of climate change on flood frequency using different climate models and downscaling approaches. Journal of Hydrologic Engineering, 19(8), 04014002. https://doi.org/10.1061/(ASCE)HE.1943-5584.0000959

Capito, L.M., Pandrin, E., Bertoldi, W., Surian, N. and Bizzi, S. (2024) Path length and sediment transport estimation from DEMs of difference: A signal processing approach. Earth Surface Dynamics, 12, 321-345. https://doi.org/10.5194/esurf-12-321-2024

Cavalli, M. and Marchi, L. (2008) Characterisation of the surface morphology of an alpine alluvial fan using airborne LiDAR. Natural Hazards and Earth System Sciences, 8, 323-333. https://doi.org/10.5194/nhess-8-323-2008

Cavalli, M., Trevisani, S., Comiti, F. and Marchi, L. (2013) Geomorphometric assessment of spatial sediment connectivity in small Alpine catchments. Geomorphology, 188, 31-41. https://doi.org/10.1016/j.geomorph.2012.05.007

CCCR2019 (2019) Canada's Changing Climate Report Chapter 6. https://changingclimate.ca/CCCR2019/chapter/6-0/

Cerpa Reyes, L.J., Ávila Rangel, H. and Herazo, L.C.S. (2022) Adjustment of the Standardized Precipitation Index (SPI) for the evaluation of drought in the Arroyo Pechelín Basin, Colombia, under zero monthly precipitation conditions. Atmosphere, 13(2), 236. https://doi.org/10.3390/atmos13020236

Champagne, O., Arain, M.A., Leduc, M., Coulibaly, P. and McKenzie, S. (2020) Future shift in winter streamflow in southern Ontario. Hydrology and Earth System Sciences, 24, 3077-3096. https://doi.org/10.5194/hess-24-3077-2020

Chassiot, L., Lajeunesse, P. and Bernier, J.-F. (2020) Riverbank erosion in cold environments: Review and outlook. Earth-Science Reviews, 207, 103231. https://doi.org/10.1016/j.earscirev.2020.103231

Chattopadhyay, N. and Hulme, M. (1997) Evaporation and potential evapotranspiration in India under conditions of recent and future climate change. Agricultural and Forest Meteorology, 87, 55-73. https://doi.org/10.1016/S0168-1923(97)00006-3

Chen, W. and Thomas, K. (2020) Revised SEDD (RSEDD) model for sediment delivery processes at the basin scale. Sustainability, 12, 4928. https://doi.org/10.3390/su12124928

Chipanshi, A.C., Findlater, K.M., Hadwen, T. and O'Brien, E.G. (2006) Analysis of consecutive droughts on the Canadian prairies. Climate Research, 30, 175-187. https://doi.org/10.3354/cr030175

Cho, S. J., Karwan, D. L., Skalak, K., Pizzuto, J. and Huffman, M. E. (2023) Sediment sources and connectivity linked to hydrologic pathways and geomorphic processes: a conceptual model to specify sediment sources and pathways through space and time. Frontiers in Water, 5, 1241622. https://doi.org/10.3389/frwa.2023.1241622

Chouaib, W. and Caissie, D. (2021) Regional disparities in water availability and low flow conditions in rivers across Canada. Journal of Hydrology, 598, 126195. https://doi.org/10.1016/j.jhydrol.2021.126195

Church, M. (2006) Bed material transport and the morphology of alluvial river channels. Annual Review of Earth and Planetary Sciences, 34, 325-354. https://doi.org/10.1146/annurev.earth.33.092203.122721

Church, M. (2010) The trajectory of geomorphology. Progress in Physical Geography: Earth and Environment, 34, 265-286. https://doi.org/10.1177/0309133310363992

Church, M. and Ryder, J. M. (1972) Paraglacial sedimentation: a consideration of fluvial processes conditioned by glaciation. Geological Society of America Bulletin, 83(10), 3059-3072. https://doi.org/10.1130/0016-7606(1972)83[3059:PSACOF]2.0.CO;2

Ciarapica, L. and Todini, E. (2002) TOPKAPI: a model for the representation of the rainfall-runoff process at different scales. Hydrological Processes, 16, 207-229. https://doi.org/10.1002/hyp.342

Cienciala, P. (2021) Vegetation and geomorphic connectivity in mountain fluvial systems. Water, 13, 593. https://doi.org/10.3390/w13050593

Cislaghi, A. and Bischetti, G. B. (2019) Source areas, connectivity, and delivery rate of sediments in mountainous-forested hillslopes: A probabilistic approach. Science of The Total Environment, 652, 1168-1186. https://doi.org/10.1016/j.scitotenv.2018.10.318

Clarke, B., Otto, F., Stuart-Smith, R. and Harrington, L. (2022) Extreme weather impacts of climate change: an attribution perspective. Environmental Research: Climate, 1(1), 012001. https://doi.org/10.1088/2752-5295/ac6e7d

Clifton, Z.J., Cashman, M.J., Gellis, A.C., Katoski, M.P., Nibert, L.A. and Noe, G.B. (2022) Quantifying connectivity and its effects on sediment budgeting for an agricultural basin, Chesapeake Bay Watershed, United States. Hydrological Processes, 36, e14777. https://doi.org/10.1002/hyp.14777

Coles, S. (2001) An introduction to statistical modeling of extreme value. Springer, 224 p.

Collins, M. J., Kirk, J. P., Pettit, J., DeGaetano, A. T., McCown, M. S., Peterson, T. C., Means, T. N. and Zhang, X. (2014) Annual floods in New England (USA) and Atlantic Canada: synoptic climatology and generating mechanisms. Physical Geography, 35(3), 195-219. https://doi.org/10.1080/02723646.2014.888510

Conrad, C. (2009) Severe and hazardous weather in Canada: the geography of extreme events. Oxford University Press.

Conrad, O., Bechtel, B., Bock, M., Dietrich, H., Fischer, E., Gerlitz, L., Wehberg, J., Wichmann, V. and Böhner, J. (2015) System for Automated Geoscientific Analyses (SAGA) v. 2.1.4. Geoscientific Model Development, 8, 1991-2007. https://doi.org/10.5194/gmd-8-1991-2015

Cook, B.I., Mankin, J.S. and Anchukaitis, K.J. (2018) Climate change and drought: From past to future. Current Climate Change Reports, 4, 164-179. https://doi.org/10.1007/s40641-018-0093-2

Corenblit, D., Piégay, H., Arrignon, F., González-Sargas, E., Bonis, A., Davies, N. S., Ebengo, D. M., Garófano-Gómez, V., Gurnell, A. M., Henry, A. L., Hortobágyi, B., Martínez-Capel, F., Steiger, J., Tabacchi, E., Tooth, S., Vautier, F. and Walcker, R. (2024) Interactions between vegetation and river morphodynamics. Part I: Research clarifications and challenges. Earth-Science Reviews, 253, 104769. https://doi.org/10.1016/j.earscirev.2024.104769

Corenblit, D., Tabacchi, E., Steiger, J. and Gurnell, A. M. (2007) Reciprocal interactions and adjustments between fluvial landforms and vegetation dynamics in river corridors: A review of complementary approaches. Earth-Science Reviews, 84(1-2). https://doi.org/10.1016/j.earscirev.2007.05.004

Cossart, E. and Fressard, M. (2017) Assessment of structural sediment connectivity within catchments: insights from graph theory. Earth Surface Dynamics, 5, 253-268. https://doi.org/10.5194/esurf-5-253-2017

Cossart, E., Mercier, D., Decaulne, A. and Feuillet, T. (2013) An overview of the consequences of paraglacial landsliding on deglaciated mountain slopes: typology, timing and contribution to cascading fluxes. Quaternaire, 24, 13-24. https://doi.org/10.4000/quaternaire.6444

Cossart, E., Viel, V., Lissak, C., Reulier, R., Fressard, M. and Delahaye, D. (2018) How might sediment connectivity change in space and time? Land Degradation & Development, 29, 2595-2613. https://doi.org/10.1002/ldr.3022

Cowherd, M., Leung, L.R. and Girotto, M. (2023) Evolution of global snow drought characteristics from 1850 to 2100. Environmental Research Letters, 18(6), 064043. https://doi.org/10.1088/1748-9326/acd804

Crema, S. and Cavalli, M. (2018) SedInConnect: a stand-alone, free and open source tool for the assessment of sediment connectivity. Computers & Geosciences, 111. https://doi.org/10.1016/j.cageo.2017.10.009

Crema, S., Llena, M., Calsamiglia, A., Estrany, J., Marchi, L., Vericat, D. and Cavalli, M. (2020) Can inpainting improve digital terrain analysis? Comparing techniques for void filling, surface reconstruction and geomorphometric analyses. Earth Surface Processes and Landforms, 45, 736-755. https://doi.org/10.1002/esp.4739

Czuba, J.A. and Foufoula-Georgiou, E. (2014) A network-based framework for identifying potential synchronizations and amplifications of sediment delivery in river basins. Water Resources Research, 50, 3826-3851. https://doi.org/10.1002/2013WR014227

Czuba, J.A. and Foufoula-Georgiou, E. (2015) Dynamic connectivity in a fluvial network for identifying hotspots of geomorphic change. Water Resources Research, 51, 1401-1421. https://doi.org/10.1002/2014WR016139

Czuba, J. A., Foufoula-Georgiou, E., Gran, K. B., Belmont, P. and Wilcock, P. R. (2017) Interplay between spatially explicit sediment sourcing, hierarchical river-network structure, and in-channel bed material sediment transport and storage dynamics. Journal of Geophysical Research: Earth Surface, 122, 1090-1120. https://doi.org/10.1002/2016JF003965

Dai, A. (2011) Characteristics and trends in various forms of the Palmer Drought Severity Index during 1900-2008. Journal of Geophysical Research, 116, D12115. https://doi.org/10.1029/2010JD015541

De Rose, R.C. and Basher, L.R. (2011) Measurement of river bank and cliff erosion from sequential LiDAR and historical aerial photography. Geomorphology, 126, 132-147. https://doi.org/10.1016/j.geomorph.2010.10.037

de Souza Cruz, A. M. (2021) Les impacts des changements climatiques sur le réseau de drainage: Le cas de la portion urbanisée du bassin versant de Mill Creek, Nouveau-Brunswick. Master Thesis, Université de Moncton, Canada.

Deltares (2018) Delft3D-Flow User Manual. Delft, Deltares.

Déry, S. J., Stahl, K., Moore, R. D., Whitfield, P. H., Menounos, B. and Burford, J. E. (2009) Detection of runoff timing changes in pluvial, nival, and glacial rivers of western Canada. Water Resources Research, 45, W04426. https://doi.org/10.1029/2008WR006975

Dietrich, W.E. and Dunne, T. (1978) Sediment budget for a small catchment in mountainous terrain. Zeitschrift für Geomorphologie, 29, 191-206. https://doi.org/10.1130/0091-7613(2001)029

Diffenbaugh, N.S. and Ashfaq, M. (2010) Intensification of hot extremes in the United States. Geophysical Research Letters, 37, L1570. https://doi.org/10.1029/2010GL043888

Ding, Y., Gong, X., Xing, Z., Cai, H., Zhou, Z., Zhang, D., Sun, P. and Shi, H. (2021) Attribution of meteorological, hydrological and agricultural drought propagation in different climatic regions of China. Agricultural Water Management, 255, 106996. https://doi.org/10.1016/j.agwat.2021.106996

Dolan, T.J., Castens, P.G., Sonu, C.J. and Egense, A.K. (1987) Review of sediment budget methodology: Oceanside Littoral Cell, California. In Proceedings, Coastal Sediments, ASCE, Reston, VA, 1289-1304.

Douglas, M. M., Dunne, K. B. J. and Lamb, M. P. (2023) Sediment entrainment and slump blocks limit permafrost riverbank erosion. Geophysical Research Letters, 50, e2023GL102974. https://doi.org/10.1029/2023GL102974

Drápela, K. and Drápelová, I. (2011) Application of Mann-Kendall test and the Sen's slope estimates for trend detection in deposition data from Bílý Kříž (Beskydy Mts., the Czech Republic) 1997-2010. Beskydy, Mendelova univerzita v Brně, 4(2), 133-146.

Dubreuil, V. (1997) La sécheresse dans la France de l'Ouest: une contrainte climatique trop souvent oubliée. Sécheresse, 8(1), 47-55.

Dubreuil, V. (2005) Un risque climatique à géographie variable: la sécheresse dans la France de l'ouest. In Les risques climatiques, sous la direction de D. Lamarre, Belin-Sup, GDR RICLIM, 147-173.

Dumanski, S., Pomeroy, J.W. and Westbrook, C.J. (2015) Hydrological regime changes in a Canadian Prairie basin. Hydrological Processes, 29, 3893-3904. https://doi.org/10.1002/hyp.10567

Dwivedi, D., Poeppl, R. E. and Wohl, E. (2025) Hydrological connectivity: A review and emerging strategies for integrating measurement, modeling, and management. Frontiers in Water, 7, 1496199. https://doi.org/10.3389/frwa.2025.1496199

Efthymiou, N.P., Palt, S., Annandale, G.W. and Karki, P. (2017) Reservoir Conservation Model Rescon 2 Beta., Economic and engineering evaluation of alternative sediment management strategies. User Manual. Washington, DC, World Bank.

Ehteram, M., Ahmed, A. N., Latif, S. D., Huang, Y. F., Alizamir, M., Kisi, O., Mert, C. and El-Shafie, A. (2021) Design of a hybrid ANN multi-objective whale algorithm for suspended sediment load prediction. Environmental Science and Pollution Research, 28(2), 1596-1611.

Einstein, H. A. (1942) Formulas for the transportation of bedload. Transactions of the American Society of Civil Engineers, 107.

Einstein, H. A. (1950) The bed-load function for sediment transportation in open-channel flows. U.S. Department of Agriculture, Soil Conservation Service, Technical Bull., No. 1026.

El-Jabi, N., Caissie, D. and Turkkan, N. (2016) Flood analysis and flood projections under climate change in New Brunswick. Canadian Water Resources Journal, 41(1-2), 319-330. https://doi.org/10.1080/07011784.2015.1071205

El-Jabi, N., Turkkan, N. and Caissie, D. (2013) Regional climate index for floods and droughts using Canadian Climate Model (CGCM3.1). American Journal of Climate Change, 2(2), 106-115. https://doi.org/10.4236/ajcc.2013.22011

Engelund, F. and Fredsoe, J. (1976) A sediment transport model for straight alluvial channels. Nordic Hydrology, 7, 294-298. https://doi.org/10.2166/nh.1976.0019

Engelund, F. and Hansen, E. (1967) A monograph on sediment transport in alluvial streams. Technical University of Denmark, T. Forlag, editor, 62.

Environment and Climate Change Canada (2010) https://www.canada.ca/en/environment-climate-change.html.

Environment and Climate Change Canada (2011) https://www.canada.ca/en/environment-climate-change.html.

Environment and Climate Change Canada (2018) https://www.canada.ca/en/environment-climate-change.html.

Environment Climate Change Canada (2026) Historical data. Available online : Historical Data - Climate - Environment and Climate Change Canada

Environment Canada and New Brunswick Department of Municipal Affairs and Environment (1987) Flood frequency analyses, New Brunswick, A guide to the estimation of flood flows for New Brunswick rivers and streams. 49 p.

ETH Zurich (2021) BASEMENT Basic Simulation Environment for Computation of Environmental Flow and Natural Hazard Simulation. Version 3.1.1 ETH Zurich, VAW, 2021.

Ettema, R. and Daly, S.F. (2004) Sediment Transport Under Ice. U.S. Army Engineer Research and Development Center, Hanover, NH, USA.

Ety, N.J. and Rashid, M.S. (2020) Spatiotemporal variability of erosion and accretion in Ganges River using GIS and RS: A comparative study overlapping Rennell's map of 1760s. Environment, Development and Sustainability, 22, 3757-3775. https://doi.org/10.1007/s10668-019-00317-4

Faghfouri, A., Hentati, A., Fortin, G. and Germain, D. (2023) A novel statistical model for flood prediction in the Eel River watershed, New Brunswick, Canada. Water Science, 37(1), 251-268. https://doi.org/10.1080/23570008.2023.2243693

Fan, W., Wei, S., Haijun, Y., Guangyuan, K., Xiaoyan, H., Dawei, Z., Minglei, R. and Gang, W. (2020) Re-evaluation of the power of the Mann-Kendall test for detecting monotonic trends in hydrometeorological time series. Frontiers in Earth Science, 8, 14. https://doi.org/10.3389/feart.2020.00014

Fang, X. and Pomeroy, J. W. (2020) Diagnosis of future changes in hydrology for a Canadian Rockies headwater basin. Hydrology and Earth System Sciences, 24, 2731-2754. https://doi.org/10.5194/hess-24-2731-2020

Farooq, M., Shafique, M. and Khattak, M.S. (2018) Flood frequency analysis of river swat using Log Pearson type 3, Generalized Extreme Value, Normal, and Gumbel Max distribution methods. Arabian Journal of Geosciences, 11, 216. https://doi.org/10.1007/s12517-018-3553-z

Faulkner, D., Warren, S. and Burn, D. (2016) Design floods for all of Canada. Canadian Water Resources Journal / Revue canadienne des ressources hydriques, 41(3), 398-411. https://doi.org/10.1080/07011784.2016.1141665

Fernandez, L. R. and Beek, V. R. (1976) Erosion and transport of bedload sediment. Journal of Hydraulic Research, 14(2), 127-144.

Ferro, V. and Porto, P. (2000) Sediment Delivery Distributed (SEDD) model. Journal of Hydrologic Engineering, 5(4), 411-422. https://doi.org/10.1061/(ASCE)1084-0699(2000)5:4(411

Flow Science, Inc. (2018) FLOW-3D® Version 12.0 Users Manual. Santa Fe, NM, USA.

Folk, R.L. and Ward, W.C. (1957) Brazos River bar: A study in the significance of grain size parameters. Journal of Sedimentary Petrology, 27, 3-26. https://doi.org/10.1306/74D70646-2B21-11D7-8648000102C1865D

Fortin, G. and Dubreuil, V. A. (2020) A geostatistical approach to create a new climate types map at regional scale: case study of New Brunswick, Canada. Theoretical and Applied Climatology, 139, 323-334. https://doi.org/10.1007/s00704-019-02961-2

Franz, M., Lopes, C.T., Huck, G., Dong, Y., Sumer, O. and Bader, G.D. (2016) Cytoscape.js: a graph theory library for visualisation and analysis. Bioinformatics, 32(2), 309-311. https://doi.org/10.1093/bioinformatics/btv557

Frey, A. E., Connell, K. J., Hanson, H., Larson, M., Thomas, R. C., Munger, S. and Zundel, A. (2012) GenCade version 1 Model theory and user's guide. US Army, Engineer Research and Development Center, ERDC/CHL TR-12-25, 169 pp.

Frings, R.M. and Ten Brinke, W.B.M. (2018) Ten reasons to set up sediment budgets for river management. International Journal of River Basin Management, 16(1). https://doi.org/10.1080/15715124.2017.1345916

Fryirs, K. (2013) (Dis)Connectivity in catchment sediment cascades: A fresh look at the sediment delivery problem. Earth Surface Processes and Landforms, 38(1), 30-46. https://doi.org/10.1002/esp.3242

Fryirs, K. A. (2017) River sensitivity: a lost foundation concept in fluvial geomorphology. Earth Surface Processes and Landforms, 42(1), 55-70. https://doi.org/10.1002/esp.3940

Fryirs, K.A. and Brierley, G.J. (2013) Geomorphic analysis of river systems: An approach to reading the landscape. Wiley, Chichester.

Fryirs, K.A. and Brierley, G.J. (2016) Assessing the geomorphic recovery potential of rivers: forecasting future trajectories of adjustment for use in management. WIREs Water, 3, 727-748. https://doi.org/10.1002/wat2.1158

Furbish, D. J., Haff, P. K., Roseberry, J. C. and Schmeeckle, M. W. (2012) A probabilistic description of the bed load sediment flux: 1. Theory. Journal of Geophysical Research, 117, F03031. https://doi.org/10.1029/2012JF002352

Gaeuman, D., Andrews, E. D., Krause, A. and Smith, W. (2009) Predicting fractional bed load transport rates: Application of the Wilcock-Crowe equations to a regulated gravel bed river. Water Resources Research, 45, W06409. https://doi.org/10.1029/2008WR007320

Gallerand, G., Couturier, A., Archambaut, C., René, A. and Choné, G. (2015) Diagnostic des problématiques d'érosion en milieu agricole dans la MRC des Laurentides. OBV RPNS et AGIR pour la Diable, Québec, Canada.

García-Ruiz, J. M., Beguería, S., Nadal-Romero, E., González-Hidalgo, J. C., Lana-Renault, N. and Sanjuán, Y. (2017) A meta-analysis of soil erosion rates across the world. Geomorphology, 293, 103-120. https://doi.org/10.1016/j.geomorph.2015.03.008

Gaur, A., Gaur, A. and Simonovic, S.P. (2018) Future changes in flood hazards across Canada under a changing climate. Water, 10, 1441. https://doi.org/10.3390/w10101441

Gautam, P.K., Singh, D.S., Singh, A.K. and Kumar, D. (2022) Geomorphic analysis of Baghain River, Yamuna Basin, and its implication for drainage characteristic and tectonics using remote sensing and GIS techniques. Journal of the Geological Society of India, 98, 1573-1584. https://doi.org/10.1007/s12594-022-2214-8

Gautier, E., Dépret, T., Cavero, J., Costard, F., Virmoux, C., Fedorov, A., Konstantinov, P., Jammet, M. and Brunstein, D. (2021) Fifty-year dynamics of the Lena River islands (Russia): Spatio-temporal pattern of large periglacial anabranching river and influence of climate change.

Science of the Total Environment, 783, 147020. https://doi.org/10.1016/j.scitotenv.2021.147020

Gay, A., Cerdan, O., Mardhel, V. and Desmet, M. (2016) Application of an index of sediment connectivity in a lowland area. Journal of Soils and Sediments, 16(1), 280-293. https://doi.org/10.1007/s11368-015-1235-y

Gerard, R. and Davar, K.S. (1995) Chapter 1: Introduction. In Beltaos, S. (ed.) River Ice Jams. Water Resources Publications, Highlands Ranch.

Germain, D., Luciano, J., Milot, J.-F. and Faghfouri, A. (2022) The predator-prey relationship from a zoogeomorphic perspective: A study of the red fox (Vulpes vulpes) and bank swallow (Riparia riparia) in eastern Canada. Geomorphology, 414, 108378. https://doi.org/10.1016/j.geomorph.2022.108378

Ghotbi, S., Wang, D., Singh, A., Blöschl, G. and Sivapalan, M. (2020) A new framework for exploring process controls of flow duration curves. Water Resources Research, 56, e2019WR026083. https://doi.org/10.1029/2019WR026083

Gilbert, J. T. and Wilcox, A. C. (2020) Sediment routing and floodplain exchange (SeRFE): A spatially explicit model of sediment balance and connectivity through river networks. Journal of Advances in Modeling Earth Systems, 12, e2020MS002048. https://doi.org/10.1029/2020MS002048

Gouvernement du Québec (2025, June) Regulation to amend the transitional rules that apply to boundary changes for flood zones and channel migration zones (Gazette officielle du Québec, Partie 2). Publications du Québec, 25. https://www.publicationsduquebec.gouv.qc.ca/fileadmin/gazette/pdf_encrypte/lois_reglements/2025A/107527.pdf

Government of Canada (2017) Canada's top 10 weather stories 2017. https://www.canada.ca/en/environment-climate-change/services/top-ten-weather-stories/2017.html

Government of New Brunswick (2022) https://www2.gnb.ca/content/gnb.

Graf, W. H. (1998) Hydraulics of Sediment Transport. Water Resources Publications, Third Printing, 123-159.

Graf, W. H. and Suszka, L. (1987) Sediment transport in steep channels. Journal of Hydrosciences and Hydraulic Engineering, 5(1), 11-26.

GRASS Development Team (2022) Geographic Resources Analysis Support System (GRASS) Programmer's Manual. Open Source Geospatial Foundation. https://grass.osgeo.org/programming8/

Grauso, S., Pasanisi, F., Tebano, C. and et al. (2021) A multiple regression model to estimate the suspended sediment yield in Italian Apennine rivers by means of geomorphometric

parameters. Modeling Earth Systems and Environment, 7, 363-371. https://doi.org/10.1007/s40808-020-01077-1

Greenwood, J. A., Landwehr, J. M., Matalas, N. C. and Wallis, J. R. (1979) Probability weighted moments: definition and relation to parameters of several distributions expressable in inverse form. Water Resources Research, 15(5), 1049-1054. https://doi.org/10.1029/WR015i005p01049

Hairsine, P. B. and Rose, C. W. (1992a) Modeling water erosion due to overland flow using physical principles: 1. Sheet flow. Water Resources Research, 28(1), 237-243. https://doi.org/10.1029/91WR02380

Hairsine, P. B. and Rose, C. W. (1992b) Modeling water erosion due to overland flow using physical principles: 2. Rill flow. Water Resources Research, 28(1), 245-250. https://doi.org/10.1029/91WR02381

Hajdukiewicz, M., Wyżga, B., Hajdukiewicz, H. and Mikuś, P. (2019) Photogrammetric reconstruction of changes in vertical river position using archival aerial photos: Case study of the Czarny Dunajec River, Polish Carpathians. Acta Geophysica, 67, 1205-1221. https://doi.org/10.1007/s11600-019-00307-0

Hamel, P., Chaplin-Kramer, R., Sim, S. and Mueller, C. (2015) A new approach to modeling the sediment retention service (InVEST 3.0): Case study of the Cape Fear catchment, North Carolina, USA. The Science of the Total Environment, 524-525, 166-177. https://doi.org/10.1016/j.scitotenv.2015.04.027

Haron, N.A., Yusuf, B., Sulaiman, M.S., Razak, M.S.A. and Nurhidayu, S. (2022) Morphological assessment of river stability: Review of the most influential parameters. Sustainability, 14, 10025. https://doi.org/10.3390/su141610025

Harun, M. A., Safari, M. J. S., Gul, E. and Ghani, A. A. (2021) Regression models for sediment transport in tropical rivers. Environmental Science and Pollution Research, 28(38), 53097-53115.

Hassanjabbar, A., Nezaratian, H. and Wu, P. (2022) Climate change impacts on the flow regime and water quality indicators using an artificial neural network (ANN): a case study in Saskatchewan, Canada. Journal of Water and Climate Change, 13(8), 3046-3060. https://doi.org/10.2166/wcc.2022.106

Haughton, G., Bankoff, G. and Coulthard, T.J. (2015) In search of 'lost' knowledge and outsourced expertise in flood risk management. Transactions of the Institute of British Geographers, 40, 375-386. https://doi.org/10.1111/tran.12082

Hay, L.E., Wilby, R.L. and Leavesley, G.H. (2000) A comparison of delta change and downscaled GCM scenarios for three mountainous basins in the United States. JAWRA Journal of the American Water Resources Association, 36, 387-397. https://doi.org/10.1111/j.1752-1688.2000.tb04276.x

Heckmann, T., Cavalli, M., Cerdan, O., Förster, S., Javaux, M., Lode, E., Smetanová, A., Vericat, D. and Brardinoni, F. (2018) Indices of sediment connectivity: Opportunities, challenges and limitations. Earth-Science Reviews, 187, 77-108. https://doi.org/10.1016/j.earscirev.2018.08.004

Heckmann, T., Haas, F., Wichmann, V. and Morche, D. (2008) Sediment budget and morphodynamics of an Alpine talus cone on different timescales. Zeitschrift für Geomorphologie Supplementary Issues, 52, 103-121. https://doi.org/10.1127/0372-8854/2008/0052S1-0103

Heckmann, T. and Schwanghart, W. (2013) Geomorphic coupling and sediment connectivity in an alpine catchment - exploring sediment cascades using graph theory. Geomorphology, 182, 89-103. https://doi.org/10.1016/j.geomorph.2012.10.033

Heng, S. and Suetsugi, T. (2013) Using artificial neural network to estimate sediment load in ungauged catchments of the Tonle Sap River Basin, Cambodia. Journal of Water Resource and Protection, 5, 111-123. https://doi.org/10.4236/jwarp.2013.52013

Henry, S., Laroche, A. M., Hentati, A. and Boisvert, J. (2020) Prioritizing flood-prone areas using spatial data in the province of New Brunswick, Canada. Geosciences, 10(12), 478. https://doi.org/10.3390/geosciences10120478

Hidayati, N., Suntoyo and Pratikto, W.A. (2023) IOP Conference Series: Earth and Environmental Science, Volume 1198, 10th International Seminar on Ocean, Coastal Engineering, Environmental and Natural Disaster Management, 29/11/2022, Surabaya, Indonesia. 1198, 012036.

Hirsch, R. and Slack, J. (1984) Nonparametric trend test for seasonal data with serial dependence. Water Resources Research, 20, 727-732. https://doi.org/10.1029/WR020i006p00727

Hirsch, R.M., Slack, J.R. and Smith, R.A. (1982) Techniques of trend analysis for monthly water quality data. Water Resources Research, 18(1), 107-121. https://doi.org/10.1029/wr018i001p00107

Hirschberg, J., Fatichi, S., Bennett, G. L., Badoux, A. and McArdell, B. W. (2021) Climate change impacts on sediment yield and debris-flow activity in an Alpine catchment. Journal of Geophysical Research: Earth Surface, 126(6), e2020JF005739. https://doi.org/10.1029/2020JF005739

Ho, S., Tian, L., Disse, M. and Tuo, Y. (2021) A new approach to quantify propagation time from meteorological to hydrological drought. Journal of Hydrology, 603, 127056. https://doi.org/10.1016/j.jhydrol.2021.127056

Hodge, R., Brasington, J. and Richards, K. (2009) Analysing laser-scanned digital terrain models of gravel bed surfaces: linking morphology to sediment transport processes and hydraulics. Sedimentology, 56, 2024-2043. https://doi.org/10.1111/j.1365-3091.2009.01068.x

Hood, G.A. and Bayley, S.E. (2008) Beaver (Castor canadensis) mitigate the effects of climate on the area of open water in boreal wetlands in western Canada. Biological Conservation, 141(3), 556-567. https://doi.org/10.1016/j.biocon.2007.12.003

Hooke, J. and Souza, J. (2021) Challenges of mapping, modelling and quantifying sediment connectivity. Earth-Science Reviews, 223, 103847. https://doi.org/10.1016/j.earscirev.2021.103847

Hosking, J.R.M. (1990) L-moments: analysis and estimation of distributions using linear combinations of order statistics. Journal of the Royal Statistical Society: Series B, 52, 105-124. https://doi.org/10.1111/j.2517-6161.1990.tb01775.x

Hosking, J.R.M. (1994) The four-parameter kappa distribution. IBM Journal of Research and Development, 38(3), 251-258. https://doi.org/10.1147/rd.383.0251

Hosking, J.R.M. and Wallis, J.R. (1997) Regional frequency analysis: an approach based on L-moments. Cambridge University Press. https://doi.org/10.1017/CBO9780511529443

Hosseiny, H., Masteller, C. C., Dale, J. E. and Phillips, C. B. (2023) Development of a machine learning model for river bed load. Earth Surface Dynamics, 11, 681-693. https://doi.org/10.5194/esurf-11-681-2023

Huang, H. Q. (2010) Reformulation of the bed load equation of Meyer-Peter and Müller in light of the linearity theory for alluvial channel flow. Water Resources Research, 46, W09533. https://doi.org/10.1029/2009WR008974

Huang, Y., Weis, J., Vereecken, H. and Hendricks Franssen, H.J. (2021) Long-term trends in agricultural droughts over Netherlands and Germany: how extreme was the year 2018? Hydrology and Earth System Sciences Discussions, 2021, 1-27. https://doi.org/10.5194/hess-2021-569

Javadi, F., Qaderi, K., Ahmadi, M.M. and et al. (2022) Application of classical and novel integrated machine learning models to predict sediment discharge during free-flow flushing. Scientific Reports, 12, 19390. https://doi.org/10.1038/s41598-022-23781-x

Jiang, Q., Qi, Z., Tang, F., Xue, L. and Bukovsky, M. (2020) Streams response to snowmelt under climate in Nicolet River watershed, Quebec. Computers and Electronics in Agriculture, 178, 105756. https://doi.org/10.1016/j.compag.2020.105756

Jones, B. M., Tape, K. D., Clark, J. A., Bondurant, A. C., Ward Jones, M. K., Gaglioti, B. V., Elder, C. D., Witharana, C. and Miller, C. E. (2021) Multi-dimensional remote sensing analysis documents beaver-induced permafrost degradation, Seward Peninsula, Alaska. Remote Sensing, 13(23), 4863. https://doi.org/10.3390/rs13234863

Jordan, P. (2006) The use of sediment budget concepts to assess the impact on watersheds of forestry operations in the southern interior of British Columbia. Geomorphology, 79(1-2), 27-44.

Julien, P. Y. (1995) Erosion and sedimentation. Cambridge University Press, 280.

Julien, P. Y. (2002) River mechanics. Cambridge University Press, 434.

Keesstra, S., Nunes, J., Novara, A., Finger, D., Avelar, D., Kalantari, Z. and Cerdà, A. (2018) The superior effect of nature based solutions in land management for enhancing ecosystem services. The Science of the Total Environment, 610-611, 997-1009. https://doi.org/10.1016/j.scitotenv.2017.08.077

Keesstra, S.D., Bagarello, V., Ferro, V., Finger, D. and Parsons, A.J. (2020) Connectivity in hydrology and sediment dynamics. Land Degradation & Development, 31, 2525-2528. https://doi.org/10.1002/ldr.3401

Keller, A.A., Garner, K.L., Rao, N., Knipping, E. and Thomas, J. (2022) Downscaling approaches of climate change projections for watershed modeling: Review of theoretical and practical considerations. PLOS Water, 1(9), e0000046. https://doi.org/10.1371/journal.pwat.0000046

Kendall, M.G. (1938) A new measure of rank correlation. Biometrika, 30, 81-93.

Kendall, M.G. (1975) Rank correlation methods, fourth edition. Charles Griffin, London.

Kennedy, G.W., Drage, J. and Check, G. (2017) Development of indices to assess the potential impact of drought to private wells in Nova Scotia. GEO Ottawa.

Khosravi, G., Majidi, A. and Nohegar, A. (2012) Determination of suitable probability distribution for annual mean and peak discharges estimation (case study: Minab river-barantin gage, Iran). International Journal of Statistics and Probability, 1, 160-163. https://doi.org/10.5923/j.ijps.20120105.03

Kim, D. and Rhee, J.A. (2016) Drought index based on actual evapotranspiration from the Bouchet hypothesis. Geophysical Research Letters, 43, 10-277. https://doi.org/10.1002/2016GL070302

Kim, D., Lee, W., Kim, S.T. and Chun, J.A. (2019) Historical drought assessment over the contiguous United States using the generalized complementary principle of evapotranspiration. Water Resources Research, 55(7), 6244-6267. https://doi.org/10.1029/2019WR024991

Kingumbi, A. and Mailhot, A. (2010) Courbes Intensité-Durée-Fréquence (IDF): comparaison des estimateurs des durées partielles et des maximums annuels. Hydrological Sciences Journal, 55(2), 162-176.

Kiss, T., Tóth, M., Török, G.T. and Sipos, G. (2024) Reconstruction of a long-term, reach-scale sediment budget using lateral channel movement data as a proxy: A case study on the lowland section of the Tisza River, Hungary. Hydrology, 11, 67. https://doi.org/10.3390/hydrology11050067

Klaassen, J.A. (2000) Climatological assessment of major 20th Century drought years in the Grand River Basin. Contracted Report for the Grand River Conservation Authority, Meteorological Service of Canada-Ontario-Region, Environment Canada.

Klaassen, J.A. (2002) Climatological assessment of major 20th Century drought in Southern Ontario, Canada. In Proceedings of the 13th Conference on Applied Climatology, Portland, OR, USA.

Knuth, F., Shean, D., Bhushan, S., Schwat, E., Alexandrov, O., McNeil, C., Dehecq, A. and Florentine, C. (2023) Historical structure from motion (HSfM): Automated processing of historical aerial photographs for long-term topographic change analysis. Remote Sensing of Environment, 285, 113379. https://doi.org/10.1016/j.rse.2022.113379

Kokelj, S. V., Zajdlik, B. and Thompson, M. S. (2009) The impacts of thawing permafrost on the chemistry of lakes across the subarctic boreal tundra transition, Mackenzie Delta region, Canada. Permafrost and Periglacial Processes, 20, 185-199. https://doi.org/10.1002/ppp.641

Koohafkan, M.C. and Gibson, S. (2018) Geomorphic trajectory and landform analysis using graph theory: A panel data approach to quantitative geomorphology. Progress in Physical Geography: Earth and Environment, 42, 679-696. https://doi.org/10.1177/0309133318783143

Köppen, W. and Geiger, R. (1930) Handbuch der klimatologie (Vol. 1). Gebrüder Borntraeger, Berlin.

Kour, R., Patel, N. and Krishna, A.P. (2016) Climate and hydrological models to assess the impact of climate change on hydrological regime: a review. Arabian Journal of Geosciences, 9, 544. https://doi.org/10.1007/s12517-016-2561-0

Kumanlioglu, A.A. (2020) Characterizing meteorological and hydrological droughts: A case study of the Gediz River Basin, Turkey. Meteorological Applications, 27, e1857. https://doi.org/10.1002/met.1857

Kumar, A., Hossain, S., Sen, S., Mohan, S. and Ghoshal, K. (2024) Grain-size distribution in suspension under non-equilibrium conditions. International Journal of Sediment Research, 39(5), 774-794. https://doi.org/10.1016/j.ijsrc.2024.06.003

Kundzewicz, Z.W., Kanae, S., Seneviratne, S. I., Handmer, J., Nicholls, N., Peduzzi, P., Mechler, R., Bouwer, L. M., Arnell, N., Mach, K., Muir-Wood, R., Brakenridge, G. R., Kron, W., Benito, G., Honda, Y., Takahashi, K. and Sherstyukov, B. (2013) Flood risk and climate change: global and regional perspectives. Hydrological Sciences Journal, 59(1), 1-28. https://doi.org/10.1080/02626667.2013.857411

Laio, F. (2004) Cramer-von Mises and Anderson-Darling goodness of fit tests for extreme value distributions with unknown parameters. Water Resources Research, 40(9), W09308. https://doi.org/10.1029/2004WR003204

Lamy, C. and Dubreuil, V. (2013) Impact potentiel du changement climatique sur les sécheresses pédologiques en Bretagne au 21eme siècle. Climatologie, 10, 107-121. https://doi.org/10.4267/climatologie.96

Lane, S.N., Richards, K.S. and Chandler, J.H. (1996) Discharge and sediment supply controls on erosion and deposition in a dynamic alluvial channel. Geomorphology, 15(1), 1-15. https://doi.org/10.1016/0169-555X(95)00113-J

Laplante, P. and Simard, M. (2013) Les enjeux et les défis du développement territorial durable dans une région à problèmes: le cas du comté de Restigouche au Nouveau-Brunswick. Revue de l'Université de Moncton, 44(1), 111-143.

Larocque, M., Levison, J., Martin, A. and Chaumont, D. (2019) A review of simulated climate change impacts on groundwater resources in Eastern Canada. Canadian Water Resources Journal, 44(1), 22-41. https://doi.org/10.1080/07011784.2018.1503066

Latif, S.D., Chong, K.L., Ahmed, A.N. and et al. (2023) Sediment load prediction in Johor river: deep learning versus machine learning models. Applied Water Science, 13, 79. https://doi.org/10.1007/s13201-023-01874-w

Le Minor, M., Davy, P., Howarth, J. and Lague, D. (2022) Multi grain-size total sediment load model based on the disequilibrium length. Journal of Geophysical Research: Earth Surface, 127, e2021JF006546. https://doi.org/10.1029/2021JF006546

Li, J., Wang, G., Song, C., Sun, S., Ma, J., Wang, Y., Guo, L. and Li, D. (2024) Recent intensified erosion and massive sediment deposition in Tibetan Plateau rivers. Nature Communications, 15, 722. https://doi.org/10.1038/s41467-024-44982-0

Li, J., Wang, Z., Wu, X., Chen, J., Guo, S. and Zhang, Z. (2020) A new framework for tracking flash drought events in space and time. Catena, 194, 104763. https://doi.org/10.1016/j.catena.2020.104763

Li, L. and Cai, H. (2024) A comparative study of various drought indices at different timescales and over different record lengths in the arid area of northwest China. Environmental Science and Pollution Research, 31(17), 25096-25113. https://doi.org/10.1007/s11356-024-32803-2

Li, Z., Yan, C. and Boota, M.W. (2022) Review and outlook of river morphology expression. Journal of Water and Climate Change, 13, 1725-1747. https://doi.org/10.2166/wcc.2022.449

Lin, H., Mo, R., Vitart, F. and Stan, C. (2019) Eastern Canada flooding 2017 and its subseasonal predictions. Atmosphere-Ocean, 57(3), 195-207. https://doi.org/10.1080/07055900.2018.1547679

Lin, Y.C., Kuo, E.D. and Chi, W.J. (2021) Analysis of meteorological drought resilience and risk assessment of groundwater using signal analysis method. Water Resources Management, 35, 179-197.

Lindenschmidt, K.E., Huokunab, M., Burrellc, B. C. and Beltaosd, S. (2018) Lessons learned from past ice-jam floods concerning the challenges of flood mapping. Journal of River Basin Management, 16(4), 457-468. https://doi.org/10.1080/15715124.2018.1439496

Lininger, K. B. and Wohl, E. (2019) Floodplain dynamics in North American permafrost regions under a changing climate. Earth-Science Reviews, 193, 24-44. https://doi.org/10.1016/j.earscirev.2019.02.024

Liu, C., Yang, C., Yang, Q. and Wang, J. (2021) Spatiotemporal drought analysis by the standardized precipitation index (SPI) and standardized precipitation evapotranspiration index (SPEI) in Sichuan Province, China. Scientific Reports, 11, 1280. https://doi.org/10.1038/s41598-020-80527-3

Liu, Z. and Todini, E. (2002) Towards a comprehensive physically-based rainfall-runoff model. Hydrology and Earth System Sciences, 6(5), 859-881. https://doi.org/10.5194/hess-9-347-2005

Liu, Z., Martina, M.L.V. and Todini, E. (2005) Flood forecasting using a fully distributed model: application of the TOPKAPI model to the Upper Xixian Catchment. Hydrology and Earth System Sciences, 9(4), 347-364.

López-Vicente, M. and Ben-Salem, N. (2019) Computing structural and functional flow and sediment connectivity with a new aggregated index: A case study in a large Mediterranean catchment. Science of The Total Environment, 651(Pt 1), 179-191. https://doi.org/10.1016/j.scitotenv.2018.09.170

Lu, H., Moran, C. J., Prosser, I. P. and DeRose, R. (2004) Investment prioritization based on broadscale spatial budgeting to meet downstream targets for suspended sediment loads. Water Resources Research, 40, W09501. https://doi.org/10.1029/2003WR002966

Ma, L., Liu, D., Luan, J., Ming, G., Meng, X. and Huang, Q. (2024) Connecting flow duration curve and precipitation duration curve based on the relationship deduced from machine learning in the watersheds of northern China. Journal of Hydrology, 635, 131235. https://doi.org/10.1016/j.jhydrol.2024.131235

Macklin, M.G., Brewer, P.A., Hudson-Edwards, K.A., Bird, G., Coulthard, T.J., Dennis, I.A., Lechler, P.J., Miller, J.R. and Turner, J.N. (2006) A geomorphological approach to the management of rivers contaminated by metal mining. Geomorphology, 79(3-4), 423-447. https://doi.org/10.1016/j.geomorph.2006.06.024

Macurová, T. and Škarpich, V. (2024) Assessment of sediment connectivity using modelling and field-based approaches in the Slavíč River catchment (Moravskoslezské Beskydy Mts, Czech Republic). Journal of Mountain Science, 21, 734-753. https://doi.org/10.1007/s11629-023-8399-5

Madsen, O. S. (1991) Mechanics of cohesionless sediment transport in coastal waters. Proceedings Coastal Sediments. ASCE, New York, USA, 15-27.

Magilligan, F.J., Buraas, E.M. and Renshaw, C.E. (2015) The efficacy of stream power and flow duration on geomorphic responses to catastrophic flooding. Geomorphology, 228, 175-188. https://doi.org/10.1016/j.geomorph.2014.08.016

Mailhot, A., Kingumbi, A., Talbot, G. and Poulin, A. (2010) Future changes in intensity and seasonal pattern of occurrence of daily and multi-day annual maximum precipitation over Canada. Journal of Hydrology, 388(3-4), 173-185. https://doi.org/10.1016/j.jhydrol.2010.04.038

Mallet, J., Fortin, G. and Germain, D. (2018) Extreme weather events in northeastern New Brunswick (Canada) for the period 1950-2012: Comparison of newspaper archive and weather station data. The Canadian Geographer, 62(2), 130-143. https://doi.org/10.1111/cag.12411

Mancini, D. and Lane, S. N. (2020) Changes in sediment connectivity following glacial debuttressing in an alpine catchment, Switzerland. Geomorphology, 370, 107385. https://doi.org/10.1016/j.geomorph.2019.106987

Mann, H.B. (1945) Nonparametric test against trend. Econometrica, 13, 245-259. http://dx.doi.org/10.2307/1907187

McClenaghan, S.H., Lentz, D.R. and Fyffe, L.R. (2006) Chemostratigraphy of volcanic rocks hosting massive sulfide clasts within the Meductic Group, N.B. Exploration and Mining Geology, 15(3-4), 241-261. https://doi.org/10.2113/gsemg.15.3-4.241

McEwen, L.J. and Jones, O. (2012) Building local/lay flood knowledges into community flood resilience planning after the July 2007 floods, Gloucestershire, UK. Hydrology Research, 43, 675-688. https://doi.org/10.2166/nh.2012.022

McGrath, H., Stefanakis, E. and Nastev, M. (2015) Sensitivity analysis of flood damage estimates: A case study in Fredericton, New Brunswick. International Journal of Disaster Risk Reduction, 14(4), 379-387. https://doi.org/10.1016/j.ijdrr.2015.09.003

Meyer-Peter, E. and Muller, R. (1948) Formulas for Bed Load Transport. 2nd Conference IAHR Congress, International Association for Hydraulic Research, Stockholm, 39-64.

Mladjic, B., Sushama, L., Khaliq, M.N., Laprise, R., Caya, D. and Roy, R. (2011) Canadian RCM projected changes to extreme precipitation characteristics over Canada. Journal of Climate, 24, 2565-2584. https://doi.org/10.1175/2010JCLI3937.1

Mondal, A., Kundu, S. and Mukhopadhyay, A. (2012) Rainfall trend analysis by Mann-Kendall test: a case study of Northeastern part of Cuttack district, Orissa. International Journal of Geology, Earth and Environmental Sciences, 2(1), 70-78.

Monsalve, A., Yager, E. M., Turowski, J. M. and Rickenmann, D. (2016) A probabilistic formulation of bed load transport to include spatial variability of flow and surface grain size distributions. Water Resources Research, 52, 3579-3598. https://doi.org/10.1002/2015WR017694

Moody, J. A. and Martin, D. A. (2009) Synthesis of sediment yields after wildland fire in different rainfall regimes in the western United States. International Journal of Wildland Fire, 18(1), 96-115. https://doi.org/10.1071/WF07162

Moore, R. D. and Wondzell, S.M. (2005) Physical hydrology and the effects of forest harvesting in the Pacific Northwest: a review. Journal of the American Water Resources Association, 41(4), 763-784.

Morin, S., Boucher, E. and Buffin-Belanger, T. (2015) The spatial variability of ice-jam bank morphologies along the Mistassini River (Quebec, Canada): an indicator of the ice-jam regime?. Natural Hazards, 77, 2117-2138. https://doi.org/10.1007/s11069-015-1693-y

Mousavi, R., Johnson, D., Kroebel, R. and Byrne, J. (2023) Analysis of historical drought conditions based on SPI and SPEI at various timescales in the South Saskatchewan River Watershed, Alberta, Canada. Theoretical and Applied Climatology, 153, 873-887. https://doi.org/10.1007/s00704-023-04495-0

Mtilatila, L., Bronstert, A., Bürger, G. and Vormoor, K. (2020) Meteorological and hydrological drought assessment in Lake Malawi and Shire River basins (1970-2013). Hydrological Sciences Journal, 65(16), 2750-2764. https://doi.org/10.1080/02626667.2020.1837384

Mueller, J.E. (1968) An introduction to the hydraulic and topographic sinuosity indexes. Annals of the Association of American Geographers, 58, 371-385. https://doi.org/10.1111/j.1467-8306.1968.tb00650.x

Mukherjee, R., Bilas, R., Biswas, S.S. and Pal, R. (2017) Bank erosion and accretion dynamics explored by GIS techniques in lower Ramganga River, Western Uttar Pradesh, India. Spatial Information Research, 25, 23-38. https://doi.org/10.1007/s41324-016-0074-2

Najafi, S., Dragovich, D., Heckmann, T. and Sadeghi, S.H. (2021) Sediment connectivity concepts and approaches. Catena, 196, 104880. http://dx.doi.org/10.1016/j.catena.2020.104880

Ndetei, C., Opere, A. and Mutua, F. (2007) Flood frequency analysis in lake Victoria basin based on tail behaviour of distributions. Kenya Meteorological Society (KMS), 1, 44-54.

Nelson, J. M. (1988) Mechanics of flow and sediment transport over nonuniform erodible beds. Ph.D. dissertation, University of Washington, Geophysics Program.

Nerantzaki, S. D., Giannakis, G. V., Efstathiou, D., Nikolaidis, N. P., Sibetheros, I. A., Karatzas, G. P. and Zacharias, I. (2015) Modeling suspended sediment transport and assessing the impacts of climate change in a karstic Mediterranean watershed. Science of the Total Environment, 538, 288-297.

Nino, Y. and Garcia, M. H. (1994) Gravel saltation-2, Modeling. Water Resources Research, 30(6), 1915-1924.

Noguera, I., Vicente-Serrano, S.M., Domínguez-Castro, F. and Reig, F. (2022) Assessment of parametric approaches to calculate the Evaporative Demand Drought Index. International Journal of Climatology, 42(2), 834-849. https://doi.org/10.1002/joc.7275

Nolin, A.F., Tardif, J.C., Conciatori, F. and Bergeron, Y. (2021) Spatial coherency of the spring flood signal among major river basins of eastern boreal Canada inferred from flood rings. Journal of Hydrology, 596, 126084. https://doi.org/10.1016/j.jhydrol.2021.126084

Notebaert, B., Verstraeten, G., Govers, G. and Poesen, J. (2009) Qualitative and quantitative applications of LiDAR imagery in fluvial geomorphology. Earth Surface Processes and Landforms, 34, 217-231. https://doi.org/10.1002/esp.1705

Nova Scotia Department of Agriculture and Fisheries (2001) Estimated impact of 2001 drought on agriculture in Nova Scotia. Agriculture Services Branch, Halifax, Canada, 27.

Nuth, C. and Kääb, A. (2011) Co-registration and bias corrections of satellite elevation data sets for quantifying glacier thickness change. The Cryosphere, 5, 271-290. https://doi.org/10.5194/tc-5-271-2011

Önöz, B. and Bayazit, M. (1995) Best-fit distributions of largest available flood samples. Journal of Hydrology, 167(1-4), 195-208. https://doi.org/10.1016/0022-1694(94)02633-M

Orwin, J. F., Lamoureux, S. F., Warburton, J. and Beylich, A. (2010) A framework for characterizing fluvial sediment fluxes from source to sink in cold environments. Geografiska Annaler: Series A, Physical Geography, 92(2), 155-176. https://doi.org/10.1111/j.1468-0459.2010.00387.x

Owens, P. N. (2005) Conceptual models and budgets for sediment management at the river basin scale. Journal of Soils and Sediments, 5, 201-212. https://doi.org/10.1065/jss2005.05.133

Owens, P.N. (2020) Soil erosion and sediment dynamics in the Anthropocene: a review of human impacts during a period of rapid global environmental change. Journal of Soils and Sediments, 20, 4115-4143. https://doi.org/10.1007/s11368-020-02815-9

Owens, P.N., Petticrew, E.L. and van der Perk, M. (2010) Sediment response to catchment disturbances. Journal of Soils and Sediments, 10, 591-596. https://doi.org/10.1007/s11368-010-0235-1

Palagiri, H. and Pal, M. (2024) Parametric and non-parametric indices for agricultural drought assessment using ESACCI soil moisture data over the Southern Plateau and Hills, India. International Journal of Applied Earth Observation and Geoinformation, 134, 104175. https://doi.org/10.1016/j.jag.2024.104175

Palmer, W.C. (1965) Meteorological drought. Research Paper No. 45. U.S. Weather Bureau, Washington, DC, USA.

Parker, G. (1979) Hydraulic geometry of active gravel rivers. Journal of Hydraulic Engineering, 105(9), 1185-1201.

Parsons, A. J. (2012) How useful are catchment sediment budgets?. Progress in Physical Geography, 36, 60-71. https://doi.org/10.1177/0309133311424591

Paul, A. and Bhattacharji, M. (2022) Assessing land erosion and accretion dynamics and river bank line shifting of upper reach of Hooghly River of West Bengal, India. Sustainable Water Resources Management, 8, 136. https://doi.org/10.1007/s40899-022-00732-y

Pearson, S. G., van Prooijen, B. C., Elias, E. P. L., Vitousek, S. and Wang, Z. B. (2020) Sediment connectivity: A framework for analyzing coastal sediment transport pathways. Journal of Geophysical Research: Earth Surface, 125, e2020JF005595. https://doi.org/10.1029/2020JF005595

Peel, M.C., Finlayson, B.L. and McMahon, T.A. (2007) Updated world map of the Köppen-Geiger climate classification. Hydrology and Earth System Sciences, 11, 1633-1644. https://doi.org/10.5194/hess-11-1633-2007

Pellicone, G., Caloiero, T. and Guagliardi, I. (2019) The De Martonne aridity index in Calabria (Southern Italy). Journal of Maps, 15(2), 788-796. https://doi.org/10.1080/17445647.2019.1673840

Pestal, G.P. and Carr-Harris, C. (2025) Biological benchmarks and building blocks for aggregate-level management targets for Skeena and Nass sockeye salmon (Oncorhynchus nerka). DFO Canadian Science Advisory Secretariat Research Document, 2024/056.

Petts, G.E. (1984) Impounded rivers: perspectives for ecological management. John Wiley, Chichester. xviii + 326 pp.

Piqué, G., Batalla, R.J., López, R. and Sabater, S. (2017) The fluvial sediment budget of a dammed river (Upper Muga, Southern Pyrenees). Geomorphology, 293, 211-226. https://doi.org/10.1016/j.geomorph.2017.05.018

Poeppl, R. E., Keesstra, S. D., Maroulis, J., McKergow, L. A. and Parsons, A. J. (2017) A conceptual connectivity framework for understanding geomorphic system response to disturbance. Geomorphology, 277, 237-250. https://doi.org/10.1016/j.geomorph.2016.07.033

Poeppl, R.E., Fryirs, K. A., Tunnicliffe, J. and Brierley, G. J. (2020) Managing sediment (dis)connectivity in fluvial systems. Science of The Total Environment, 736, 139627. https://doi.org/10.1016/j.scitotenv.2020.139627

Pohlert, T. (2020) Nonparametric Trend Tests and Change-Point Detection. https://creativecommons.org/licenses/by-nd/4.0/

Poirier, C. (2022) Portrait historique des sécheresses au Nouveau-Brunswick (1971-2020): analyses climatologiques et médiatiques. Master thesis, Université de Moncton, 77.

Poirier, C., Fortin, G. and Dubreuil, V. (2023) Spatial and temporal characteristics of past droughts in New Brunswick (1971-2020). International Journal of Climatology, 43(15), 7183-7198.

Pomeroy, J. W., Fang, X. and Marks, D. G. (2016) The cold rain-on-snow event of June 2013 in the Canadian Rockies - characteristics and diagnosis. Hydrological Processes, 30, 2899-2914. https://doi.org/10.1002/hyp.10905

Pons, F., Delgado, J.L., Guéro, P. and Berthier, E. (2010) EXZECO: a GIS and DEM based method for pre-determination of flood risk related to direct runoff and flash floods. 9th International Conference on Hydroinformatics, HIC 2010, Tianjin, China.

Prowse, T. D. (1993) Suspended sediment concentration during river ice breakup. Canadian Journal of Civil Engineering, 20(5), 874-878.

Prowse, T. D. (2001) River-ice ecology. I: Hydrologic, geomorphic, and water-quality aspects. Journal of Cold Regions Engineering, 15(1), 1-16. https://doi.org/10.1061/(ASCE)0887-381X(2001)15:1(1

Prugne, M., Corenblit, D., Boivin, M. and Buffin-Bélanger, T. (2025) Vegetation and channel adjustment trajectories in cold regions: The effects of ice disturbances in two Gaspesian rivers. Earth Surface Processes and Landforms, 50, e70051. https://doi.org/10.1002/esp.70051

Prugne, M., Corenblit, D., Boivin, M., Evette, A. and Buffin-Bélanger, T. (2024) Soil and water bioengineering in cold rivers: A biogeomorphological perspective. Ecological Engineering, 204, 107261. https://doi.org/10.1016/j.ecoleng.2024.107261

Public Safety of Canada (2013) https://www.publicsafety.gc.ca/cnt/mrgnc-mngmnt/ntrl-hzrds/fld-en.aspx

Pulley, S. and Collins, A.L. (2018) SIFT: SedIment Fingerprinting Tool v.1.0.1. Rothamsted Research. https://doi.org/10.23637/model-SIFT-1-0

Pyarali, K., Peng, J., Disse, M. and Tuo, Y. (2022) Development and application of high resolution SPEI drought dataset for Central Asia. Scientific Data, 9, 172. https://doi.org/10.1038/s41597-022-01279-5

Rashmi, I., Karthika, K. S., Roy, T., Shinoji, K. C., Kumawat, A., Kala, S. and Pal, R. (2022) Soil erosion and sediments: A source of contamination and impact on agriculture productivity. In Naeem, M., Bremont, J.F.J., Ansari, A.A. and Gill, S.S. (eds) Agrochemicals in Soil and Environment. Springer, Singapore. https://doi.org/10.1007/978-981-16-9310-6_14

Rathburn, S. L., Shahverdian, S. M. and Ryan, S. E. (2018) Post-disturbance sediment recovery: Implications for watershed resilience. Geomorphology, 305, 61-75. https://doi.org/10.1016/j.geomorph.2017.08.039

Reaney, S.M., Milledge, D., Lane, S.N., Heathwaite, L., Shore, M., Melland, A. and Jordan, P. (2011) Understanding nutrient connectivity at the landscape scale: The use of the SCIMAP approach in the UK and Ireland. American Geophysical Union Fall Meeting, abstract id. H41H-1157.

Reid, L.M. and Dunne, T. (2016) Sediment budgets as an organizing framework in fluvial geomorphology. In Kondolf, G.M. and Piégay, H. (eds) Tools in Fluvial Geomorphology, 2nd ed. Wiley-Blackwell, pp. 357-387. https://doi.org/10.1002/9781118648551.ch16

Renard, K., Foster, G., Weesies, G., McCool, D. and Yoder, D. (1997) Predicting soil erosion by water: A guide to conservation planning with the Revised Universal Soil Loss Equation (RUSLE). US Department of Agriculture, Agriculture Handbook No. 703, Washington DC.

Riahi, K., Rao, S., Krey, V., Cho, C., Chirkov, V., Fischer, G., Kindermann, G., Nakicenovic, N. and Rafaj, P. (2011) RCP 8.5-A scenario of comparatively high greenhouse gas emissions. Climatic Change, 109, 33. https://doi.org/10.1007/s10584-011-0149-y

Ribberink, J. S. (1998) Bed load transport for steady and unsteady oscillatory flow. Coastal Engineering, 34, 59-82. https://doi.org/10.1016/S0378-3839(98)00013-1

Richardson, J. S., Naiman, R. J. and Bisson, P. A. (2012) How did fixed-width buffers become standard practice for protecting freshwaters and their riparian areas from forest harvest practices? Freshwater Science, 31(1), 232-238.

Robson, A. and Reed, D. (1999) Statistical procedures for flood frequency estimation. Flood Estimation Handbook, Wallingford: Centre for Ecology and Hydrology, Vol 3.

Rokaya, P., Budhathoki, S. and Lindenschmidt, K.E. (2018) Trends in the timing and magnitude of ice-jam floods in Canada. Scientific Reports, 8, 5834. https://doi.org/10.1038/s41598-018-24057-z

Rosati, J.D. and Kraus, N.C. (2001, revised 2003) Sediment budget analysis system (SBAS): Upgrade for regional applications. Coastal and Hydraulics Engineering Technical Note ERDC/CHL CHETN-XIV-3. Vicksburg, MS, US Army Engineer Research and Development Center. http://chl.erdc.usace.army.mil/library/publications/chetn/pdf/chetn-xiv-3.pdf

Roy, P. and Huard, D. (2016) Future Climate Scenarios - Province of New Brunswick. Ouranos, Montreal, 46.

Saf, B. (2009) Regional flood frequency analysis using L-moments for the West Mediterranean region of Turkey. Water Resources Management, 23(3), 531-551. https://doi.org/10.1007/s11269-008-9287-z

Safari, H., Montaseri, M. and Hejabi, S. (2024) Spatiotemporal changes in snow cover and their relationship with drought events in the Lake Urmia basin. Hydrological Sciences Journal, 69(1), 46-62. https://doi.org/10.1080/02626667.2023.2276737

Salas, J. (1993) Analysis and modeling of hydrologic time series. Handbook of hydrology. McGraw-Hill, New York, 19, 1-72.

Saleem, A., Dewan, A., Rahman, M.M., Nawfee, S.M., Karim, R. and Lu, X.X. (2020) Spatial and temporal variations of erosion and accretion: A case of a large tropical river. Earth Systems and Environment, 4, 167-181. https://doi.org/10.1007/s41748-019-00143-8

Schafer, J.L. (1997) The analysis of incomplete multivariate data. Chapman and Hall, London. http://dx.doi.org/10.1201/9781439821862

Schmidt, K.-H. and Morche, D. (2006) Sediment output and effective discharge in two small high mountain catchments in the Bavarian Alps, Germany. Geomorphology, 80(1-2), 131-145. https://doi.org/10.1016/j.geomorph.2005.09.013

Schneider, J. M., Rickenmann, D., Turowski, J. M., Schmid, B. and Kirchner, J. W. (2016) Bed load transport in a very steep mountain stream (Riedbach, Switzerland): Measurement and prediction. Water Resources Research, 52, 9522-9541. https://doi.org/10.1002/2016WR019308

Schwanghart, W. and Kuhn, N. J. (2010) TopoToolbox: A set of Matlab functions for topographic analysis. Environmental Modelling & Software, 25(6), 770-781. https://doi.org/10.1016/j.envsoft.2009.12.002

Schwanghart, W. and Scherler, D. (2014) Short Communication: TopoToolbox 2 - MATLAB-based software for topographic analysis and modeling in Earth surface sciences. Earth Surface Dynamics, 2(1), 1-7. https://doi.org/10.5194/esurf-2-1-2014

Schwenk, J., Khandelwal, A., Fratkin, M., Kumar, V. and Foufoula-Georgiou, E. (2017) High spatiotemporal resolution of river planform dynamics from Landsat: The RivMAP toolbox and results from the Ucayali River. Earth and Space Science, 4, 46-75. https://doi.org/10.1002/2016EA000196

Sen, P.K. (1968) Estimates of the regression coefficient based on Kendall's tau. Journal of the American Statistical Association, 63, 1379-1389. https://doi.org/10.1080/01621459.1968.10480934

Serinaldi, F., Kilsby, C.G. and Lombardo, F. (2018) Untenable nonstationarity: An assessment of the fitness for purpose of trend tests in hydrology. Advances in Water Resources, 111, 132-155. https://doi.org/10.1016/j.advwatres.2017.10.015

Shekhar, S. and Xiong, H. (2008) Soil and water assessment tool "SWAT". Encyclopedia of GIS, 1068.

Shen, H.T. (2010) Mathematical modeling of river ice processes. Cold Regions Science and Technology, 62, 3-13. https://doi.org/10.1016/j.coldregions.2010.02.007

Shepard, D. (1968) A two-dimensional interpolation function for irregularly spaced data. In Proceedings of the 23rd ACM National Conference, 517-524. https://doi.org/10.1145/800186.810616

Shi, C., Liang, Y., Qin, W., Ding, L., Cao, W., Zhang, M. and Zhang, Q. (2025) Review of sediment connectivity: Conceptual connotations, characterization indicators, and their relationships with soil erosion and sediment yield. Earth-Science Reviews, 264, 105091. https://doi.org/10.1016/j.earscirev.2023.105091

Shields, A. (1936) Application of similarity principles and turbulence research to bed-load movement. Mitteilungen der Preussischen Versuchsanstalt für Wasserbau und Schiffbau, Heft 26, Berlin.

Shin, J. h., Grabowski, R. C. and Holman, I. (2023) Catchment and climatic influences on spatio-temporal variations in suspended sediment transport dynamics in rivers. Hydrology Research, 54(8), 901-923. https://doi.org/10.2166/nh.2023.127

Shojaeezadeh, S. A., Nikoo, M. R., McNamara, J. P., AghaKouchak, A. and Sadegh, M. (2018) Stochastic modeling of suspended sediment load in alluvial rivers. Advances in Water Resources, 119, 188-196.

Shuster, W. D., Bonta, J., Thurston, H., Warnemuende, E. and Smith, D. R. (2005) Impacts of impervious surface on watershed hydrology: A review. Urban Water Journal, 2(4), 263-275.

Singh, K. and Singh, V.P. (1991) Derivation of bivariate probability density functions with exponential marginals. Stochastic Hydrology and Hydraulics, 5, 55-68. https://doi.org/10.1007/BF01544178

Singh, V.P. (1998) Three-parameter lognormal distribution, entropy-based parameter estimation in hydrology. Water Science and Technology Library, Springer, Vol 30. https://doi.org/10.1007/978-94-017-1431-0_7

Sinnakaudan, S. K., Ghani, A. A., Ahmad, M. S. and Zakaria, N. A. (2006) Multiple linear regression model for total bed material load prediction. Journal of Hydraulic Engineering, 132(5), 521-528. https://doi.org/10.1061/(ASCE)0733-9429(2006)132:5(521

Slaymaker, O. (2003) The sediment budget as a conceptual framework and management tool. Hydrobiologia, 494, 71-82. https://doi.org/10.1023/A:1025437509525

Soleimani-Motlagh, M., Soleimani-Sardo, M. and Mossivand, A.M. (2022) The efficiency of the Standardized Evapotranspiration Deficit Index (SEDI) in assessing the impact of drought on vegetation cover. Environmental Monitoring and Assessment, 194, 299. https://doi.org/10.1007/s10661-022-09972-z

Soulsby, R. L. (1997) Dynamics of marine sands: A manual for practical applications. Thomas Telford, London, UK.

Spiekermann, R., Betts, H., Dymond, J. and Basher, L. (2017) Volumetric measurement of river bank erosion from sequential historical aerial photography. Geomorphology, 296, 193-208. https://doi.org/10.1016/j.geomorph.2017.08.047

Stagge, J.H., Tallaksen, L.M., Gudmundsson, L., Van Loon, A.F. and Stahl, K. (2015) Candidate distributions for climatological drought indices (SPI and SPEI). International Journal of Climatology, 35(13), 4027-4040. https://doi.org/10.1002/joc.4267

St-Laurent, D., M. Mesfioui, and G. Evin. 2009. Hydroclimatic variability and relation with flood events (Southern Québec, Canada). Water Resources 36: 43–56.

Statistic Canada (2017) New Brunswick [Province] and Canada [Country] (table). Census Profile. 2016 Census. Statistics Canada Catalogue no. 98-316-X2016001.

Statistic Canada (2023) Profile table, Census Profile, 2021 Census of Population - Eel River Crossing, Village (VL) [Census subdivision], New Brunswick. https://statcan.gc.ca

Statistics Canada (2010) Canada at a glance 2010. https://www150.statcan.gc.ca/n1/pub/12-581-x/12-581-x2010000-eng.pdf

Statistics Canada (2016) Census of Agriculture, 2017. https://www150.statcan.gc.ca/n1/daily-quotidien/170510/dq170510a-eng.htm

Statistics Canada (2022) Population and dwelling counts: Canada, provinces and territories. https://www150.statcan.gc.ca/t1/tbl1/en/tv.action?pid=9810000101

Stedinger, J.R. and Lu, L.H. (1995) Appraisal of regional and index flood quantile estimators. Stochastic Hydrology and Hydraulics, 9(1), 49-75. https://doi.org/10.1007/BF01581758

Svensson, C., Hannaford, J. and Prosdocimi, I. (207) Statistical distributions for monthly aggregations of precipitation and streamflow in drought indicator applications. Water Resources Research, 53(2), 999-1018. https://doi.org/10.1002/2016WR019276

Szeto, K., Zhang, X., White, R.E. and Brimelow, J. (2016) The 2015 extreme drought in western Canada. Bulletin of the American Meteorological Society, 97(12), S42-S46. https://doi.org/10.1175/BAMS-D-16-0147.1

Tan, X. and Gan, T.Y. (2017) Non-stationary analysis of the frequency and intensity of heavy precipitation over Canada and their relations to large-scale climate patterns. Climate Dynamics, 48, 2983-3001. https://doi.org/10.1007/s00382-016-3246-9

Tan, Z., Li, Y., Zhang, Q., Liu, X., Song, Y., Xue, C. and Lu, J. (2021) Assessing effective hydrological connectivity for floodplains with a framework integrating habitat suitability and sediment suspension behavior. Water Research, 201, 117253. https://doi.org/10.1016/j.watres.2021.117253

Tananaev, N. and Lotsari, E. (2022) Defrosting northern catchments: Fluvial effects of permafrost degradation. Earth-Science Reviews, 228, 103996. https://doi.org/10.1016/j.earscirev.2022.103996

Tangi, M., Bizzi, S., Fryirs, K. and Castelletti, A. (2022) A dynamic, network scale sediment (dis)connectivity model to reconstruct historical sediment transfer and river reach sediment budgets. Water Resources Research, 58, e2021WR030784. https://doi.org/10.1029/2021WR030784

Tangi, M., Schmitt, R., Bizzi, S. and Castelletti, A. (2019) The CASCADE toolbox for analyzing river sediment connectivity and management. Environmental Modelling & Software, 119. https://doi.org/10.1016/j.envsoft.2019.07.008

Thomson, A.M., Calvin, K.V., Smith, S.J., Page Kyle, G., Volke, A., Patel, P., Delgado, A. S., Bond-Lamberty, B., Wise, M. A., Clarke, L. E. and Edmonds, J. A. (2011) RCP4.5: a pathway for stabilization of radiative forcing by 2100. Climatic Change, 109, 77. https://doi.org/10.1007/s10584-011-0151-4

Tonini, F. and Liu, J. (2017) Telecoupling Toolbox: spatially explicit tools for studying telecoupled human and natural systems. Ecology and Society, 22(4), 11. https://doi.org/10.5751/ES-09696-220411

Toone, J., Rice, S.P. and Piégay, H. (2014) Spatial discontinuity and temporal evolution of channel morphology along a mixed bedrock-alluvial river, upper Drôme River, southeast France: Contingent responses to external and internal controls. Geomorphology, 205, 5-16. https://doi.org/10.1016/j.geomorph.2012.05.033

Tsakiris, G. and Vangelis, H. (2005) Establishing a drought index incorporating evapotranspiration. European Water, 9(10), 3-11.

Turcotte, B., Morse, B., Bergeron, N. E. and Roy, A. G. (2011) Sediment transport in ice-affected rivers. Journal of Hydrology, 409(1-2), 561-577. https://doi.org/10.1016/j.jhydrol.2011.08.009

Turley, M. and Hassan, M. A. (2023) Spatial patterns of disconnectivity explain catchment-scale sediment dynamics and transfer efficiencies. Journal of Geophysical Research: Earth Surface, 128, e2023JF007111. https://doi.org/10.1029/2023JF007111

Turkkan, N., El-Jabi, N. and Caissie, D. (2011) Floods and droughts under different climate change scenarios in New Brunswick. Canadian Technical Report of Fisheries and Aquatic Sciences, 2928, xii+55p.

Valois, P., Anctil, F., Cloutier, G., Tessier, M. and Herpin-Saunier, N. (2023) Following up on flood adaptation in Québec households four years later: A prospective exploratory study. International Journal of Disaster Risk Reduction, 94, 103782. https://doi.org/10.1016/j.ijdrr.2023.103782

Van Der Kamp, G., Keir, D. and Evans, M.S. (2008) Long-term water level changes in closed-basin lakes of the Canadian prairies. Canadian Water Resources Journal, 33, 23-38. https://doi.org/10.4296/cwrj3301023

van der Schrier, G., Barichivich, J., Briffa, K.R. and Jones, P.D. (2013) A scPDSI based global data set of dry and wet spells for 1901-2009. Journal of Geophysical Research: Atmospheres, 118(10), 4025-4048. https://doi.org/10.1002/jgrd.50355

Van der Schrier, G., Jones, P.D. and Briffa, K.R. (2011) The sensitivity of the PDSI to the Thornthwaite and Penman-Monteith parameterizations for potential evapotranspiration. Journal of Geophysical Research, 116, D03106. https://doi.org/10.1029/2010JD015001

van Hamel, A., Molnar, P., Janzing, J. and Brunner, M. I. (2025) Suspended sediment concentrations in Alpine rivers: from annual regimes to sub-daily extreme events. Hydrology and Earth System Sciences, 29, 2975-2995. https://doi.org/10.5194/hess-29-2975-2025

Van Rijn, L. C. (1993) Principles of sediment transport in rivers, estuaries and coastal seas. Aqua Publications, Amsterdam, the Netherlands.

van Rooijen, E. and Lotsari, E. (2024) The spatiotemporal distribution of river bank erosion events and their drivers in seasonally frozen regions. Geomorphology, 454, 109140. https://doi.org/10.1016/j.geomorph.2024.109140

Vergara, I., Garreaud, R., Delaney, I. and Ayala, A. (2024) Deglaciation in the subtropical Andes has led to a peak in sediment delivery. Communications Earth & Environment, 5, 630. https://doi.org/10.1038/s43247-024-01815-8

Vessella, F. and Schirone, B. (2022) Forest conservation and restoration using the Emberger index: Cork oak as study case. Forests, 13(2), 252. https://doi.org/10.3390/f13020252

Vicente-Serrano, S.M. and Beguería, S. (2016) Comment on "Candidate distributions for climatological drought indices (SPI and SPEI)" by Stagge JH. et al. International Journal of Climatology, 36, 2120-2131. https://doi.org/10.1002/joc.4474

Vicente-Serrano, S.M., Miralles, D.G., Domínguez-Castro, F., Azorin-Molina, C., El Kenawy, A., MeVicar, T.R., Tomás-Burguera, M., Beguería, S., Maneta, M. and Peña-Gallardo, M. (2018) Global assessment of the Standardized Evapotranspiration Deficit Index (SEDI) for drought analysis and monitoring. Journal of Climate, 31, 5371-5393. https://doi.org/10.1175/JCLI-D-17-0775.1

Vicente-Serrano, S.M., Peña-Angulo, D., Beguería, S., Domínguez-Castro, F., Tomás-Burguera, M., Noguera, I., Gimeno-Sotelo, L. and El Kenawy, A. (2022) Global drought trends and future projections. Philosophical Transactions of the Royal Society, 380(2238), 20210285. https://doi.org/10.1098/rsta.2021.0285

Vincent, L. A. and Mekis, É. (2006) Changes in daily and extreme temperature and precipitation indices for Canada over the twentieth century. Atmosphere-Ocean, 44, 177-193. https://doi.org/10.3137/ao.440205

Vincent, L. A., Zhang, X., Brown, R. D., Feng, Y., Mekis, E., Milewska, E. J., Wan, H. and Wang, X. L. (2015) Observed trends in Canada's climate and influence of low-frequency variability modes. Journal of Climate, 28, 4545-4560. https://doi.org/10.1175/JCLI-D-14-00697.1

Wainwright, J., Turnbull, L., Ibrahim, T. G., Lexartza-Artza, I., Thornton, S.F. and Brazier, R.E. (2011) Linking environmental régimes, space and time: Interpretations of structural and functional connectivity. Geomorphology, 126(3-4), 387-404. https://doi.org/10.1016/j.geomorph.2010.07.027

Wang, P., Fu, K., Huang, J., Duan, X. and Yang, Z. (2020) Morphological changes in the lower Lancang River due to extensive human activities. PeerJ, 8, e9471. https://doi.org/10.7717/peerj.9471

Wang, T., Tu, X., Singh, V.P., Chen, X., Lin, K., Zhou, Z. and Zhu, J. (2023) A CMIP6-based framework for propagation from meteorological and hydrological droughts to socioeconomic drought. Journal of Hydrology, 623, 129782. https://doi.org/10.1016/j.jhydrol.2023.129782

Wang, X., Gualtieri, C. and Huai, W. (2023) Grain shear stress and bed-load transport in open channel flow with emergent vegetation. Journal of Hydrology, 618, 129204. https://doi.org/10.1016/j.jhydrol.2023.129204

Wang, X.L., Chen, H., Wu, Y., Feng, Y. and Pu, Q. (2010) New techniques for detection and adjustment of shifts in daily precipitation data series. Journal of Applied Meteorology and Climatology, 49, 2416-2436. https://doi.org/10.1175/2010JAMC2376.1

Wells, N., Goddard, S. and Hayes, M.J. (2004) A self-calibrating Palmer Drought Severity Index. Journal of Climate, 17, 2335-2351. https://doi.org/10.1175/1520-0442(2004)017<2335:ASPDSI>2.0.CO;2

Westoby, M.J., Brasington, J., Glasser, N.F., Hambrey, M.J. and Reynolds, J.M. (2012) 'Structure-from-Motion' photogrammetry: A low-cost, effective tool for geoscience applications. Geomorphology, 179, 300-314. https://doi.org/10.1016/j.geomorph.2012.08.021

Wheaton, E., Kulshreshtha, S., Wittrock, V. and Koshida, G. (2008) Dry times: Hard lessons from the Canadian drought of 2001 and 2002. The Canadian Geographer, 52, 241-262. https://doi.org/10.1111/j.1541-0064.2008.00211.x

Wheaton, J.M., Brasington, J., Darby, S.E. and Sear, D.A. (2010) Accounting for uncertainty in DEMs from repeat topographic surveys: improved sediment budgets. Earth Surface Processes and Landforms, 35, 136-156. https://doi.org/10.1002/esp.1886

Whitfield, P. H. and Shook, K. R. (2019) Changes to rainfall, snowfall, and runoff events during the autumn-winter transition in the Rocky Mountains of North America. Canadian Water Resources Journal / Revue Canadienne Des Ressources Hydriques, 45(1), 28-42. https://doi.org/10.1080/07011784.2019.1685910

Wiberg, P. and Smith, J. D. (1989) Calculation of the critical shear stress for motion of uniform and heterogeneous sediments. Water Resources Research, 23(8), 1471-1480. https://doi.org/10.1029/WR023i008p01471

Wilcock, P. R. (2001) Toward a practical method for estimating sediment-transport rates in gravel-bed rivers. Earth Surface Processes and Landforms, 26, 1395-1408. https://doi.org/10.1002/esp.301

Wilcock, P. R. and Crowe, J. C. (2003) Surface-based transport model for mixed-size sediment. Journal of Hydraulic Engineering, 129(2), 120-128. https://doi.org/10.1061/(ASCE)0733-9429(2003)129:2(120

Wild, T.B., Loucks, D.P. and Annandale, G.W. (2019) SedSim: A river basin simulation screening model for reservoir management of sediment, water, and hydropower. Journal of Open Research Software, 7, 22. https://doi.org/10.5334/jors.261

Wilks, D.S. and Livezey, R.E. (2013) Performance of alternative "normal" for tracking climate changes, using homogenized and non-homogenized seasonal U.S. surface temperatures.

Journal of Applied Meteorology and Climatology, 52, 1677-1687. https://doi.org/10.1175/JAMC-D-13-026.1

Williams, R., Brasington, J., Vericat, D., Hicks, M., Labrosse, F. and Neal, M. (2011) Monitoring braided river change using terrestrial laser scanning and optical bathymetric mapping. Developments in Earth Surface Processes, vol. 15, Elsevier, pp. 507-532. https://doi.org/10.1016/B978-0-444-53446-0.00020-3

Wilson, B., Trépanier, I. and Beaulieu, M. (2002) The western Canadian drought of 2001- how dry was it? Vista on the Agri-food industry and the farm community. Statistics Canada, 21-004.

Wilson, K. C. (1966) Bed load transport at high shear stress. Journal of the Hydraulics Division, ASCE, 92(6).

Wohl, E. (2013) Landscape-scale carbon storage associated with beaver dams. Geophysical Research Letters, 40, 3631-3636. https://doi.org/10.1002/grl.50710

Wohl, E. (2017) Connectivity in rivers. Progress in Physical Geography, 41(3), 345-362. https://doi.org/10.1177/0309133317714972

Wohl, E. (2018) Geomorphic context in rivers. Progress in Physical Geography: Earth and Environment, 42, 841-857. https://doi.org/10.1177/0309133318776488

Wohl, E., Magilligan, F. J. and Rathburn, S. L. (2017) Introduction to the special issue: Connectivity in geomorphology. Geomorphology, 277, 1-5. https://doi.org/10.1016/j.geomorph.2016.11.005

Wohl, E., Marshall, A. E., Scamardo, J., White, D. and Morrison, R. R. (2022) Biogeomorphic influences on river corridor resilience to wildfire disturbances in a mountain stream of the Southern Rockies, USA. Science of the Total Environment, 820, 153321. https://doi.org/10.1016/j.scitotenv.2022.153321

Wong, M. and Parker, G. (2006) Re-analysis and correction of bed load relation of Meyer-Peter and Muller using their own database. Journal of Hydraulic Engineering, 132, 1159-1168. https://doi.org/10.1061/(ASCE)0733-9429(2006)132:11(1159

Wu, R., Liu, Y. and Xing, X. (2021) Evaluation of evapotranspiration deficit index for agricultural drought monitoring in North China. Journal of Hydrology, 596, 126057. https://doi.org/10.1016/j.jhydrol.2021.126057

Yalin, M. S. (1963) An expression for bed-load transportation. Journal of the Hydraulics Division, ASCE, 89(3), 221-250.

Yihdego, Y., Vaheddoost, B. and Al-Weshah, R.A. (2019) Drought indices and indicators revisited. Arabian Journal of Geosciences, 12, 69. https://doi.org/10.1007/s12517-019-4237-z

Yildirim, G., Rahman, A. and Singh, V.P. (2022) A bibliometric analysis of drought indices, risk, and forecast as components of drought early warning systems. Water, 14(2), 253. https://doi.org/10.3390/w14020253

Yochum, S. E., Sholtes, J. S., Scott, J. A. and Bledsoe, B. P. (2017) Stream power framework for predicting geomorphic change: The 2013 Colorado Front Range flood. Geomorphology, 292, 178-192. https://doi.org/10.1016/j.geomorph.2017.03.004

Yozgatligil, C., Aslan, S., Iyigun, C. and Batmaz, I. (2013) Comparison of missing value imputation methods in time series: the case of Turkish meteorological data. Theoretical and Applied Climatology, 112, 143-167. https://doi.org/10.1007/s00704-012-0723-x

Yue, S. and Wang, C.Y. (2004) Possible regional probability distribution type of Canadian annual streamflow by L-moments. Water Resources Management, 18, 425-438. https://doi.org/10.1023/B:WARM.0000049145.37577.87

Zaiontz, C. (2020) Mann-Kendall test. Real Statistics Using Excel. https://www.real-statistics.com/

Zanandrea, F., Michel, G. and Kobiyama, M. (2021) Guidelines on the hydrosedimentological connectivity ArcGIS 10.3 toolbox. https://doi.org/10.13140/RG.2.2.14284.74880

Zang, C.S., Buras, A., Esquivel-Muelbert, A., Jump, A.S., Rigling, A. and Rammig, A. (2020) Standardized drought indices in ecological research: Why one size does not fit all. Global Change Biology, 26(2), 322-324. https://doi.org/10.1111/gcb.14809

Zargar, A., Sadiq, R., Bahman, N. and Khan, F.I. (2011) A review of drought indices. Environmental Reviews, 19, 333-349. https://doi.org/10.1139/a11-013

Zhang, T., Li, D., East, A. E., Kettner, A. J., Best, J., Ni, J. and Lu, X. (2023) Shifted sediment-transport regimes by climate change and amplified hydrological variability in cryosphere-fed rivers. Science Advances, 9(45), eadi5019. https://doi.org/10.1126/sciadv.adi5019

Zhang, T., Li, D., East, A. E., Walling, D. E., Lane, S. N., Overeem, I., Beylich, A. A., Koppes, M. and Lu, X. (2022) Warming-driven erosion and sediment transport in cold regions. Nature Reviews Earth & Environment, 3(12), 832-851. https://doi.org/10.1038/s43017-022-00362-0

Zhang, T., Li, D., Kettner, A. J., Zhou, Y. and Lu, X. (2021) Constraining dynamic sediment-discharge relationships in cold environments: The sediment-availability-transport (SAT) model. Water Resources Research, 57, e2021WR030690. https://doi.org/10.1029/2021WR030690

Zhang, X., Li, M., Ma, Z., Yang, Q., Lv, M. and Clark, R. (2019) Assessment of an evapotranspiration deficit drought index in relation to impacts on ecosystems. Advances in Atmospheric Sciences, 36, 1273-1287. https://doi.org/10.1007/s00376-019-9061-6

Zhang, Y., Cabilio, P. and Nadeem, K. (2016) Improved seasonal Mann-Kendall tests for trend analysis in water resources time series. In Li, W., Stanford, D. and Yu, H. (eds) Advances in Time Series Methods and Applications. Fields Institute Communications, Springer, New York, NY, 78. https://doi.org/10.1007/978-1-4939-6568-7_10

Zhang, Z., Stadnyk, T. A. and Burn, D. H. (2020) Identification of a preferred statistical distribution for at-site flood frequency analysis in Canada. Canadian Water Resources Journal

/ Revue canadienne des ressources hydriques, 45(1), 43-58. https://doi.org/10.1080/07011784.2019.1691942

Zhao, K., Coco, G., Gong, Z., Darby, S. E., Lanzoni, S., Xu, F., Zhang, K. and Townend, I. (2022) A review on bank retreat: Mechanisms, observations, and modeling. Reviews of Geophysics, 60(2), e2021RG000761. https://doi.org/10.1029/2021RG000761

Zhao, P., He, S., Wang, D., Qi, Y., Pei, Z., Yang, Y. and Zhang, Z. (2025) Unraveling the impacts of geomorphic indicators on sediment connectivity in a typical debris-flow prone small watershed. Journal of Hydrology, 659, 133256. https://doi.org/10.1016/j.jhydrol.2025.133256

Zhou, Y., Zhou, P., Jin, J., Wu, C., Cui, Y., Zhang, Y. and Tong, F. (2022) Drought identification based on Palmer drought severity index and return period analysis of drought characteristics in Huaibei Plain China. Environmental Research, 212, 113163. https://doi.org/10.1016/j.envres.2022.113163

Zounemat-Kermani, M., Fadaee, M., Adarsh, S. and Hinkelmann, R. (2020) Predicting sediment transport in sewers using integrative harmony search-ANN model and factor analysis. IOP Conference Series: Earth and Environmental Science, 491(1), 012004.